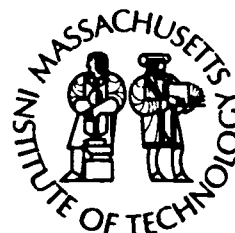AD-A258 429

WHOI-89-15

Woods Hole Oceanographic Institution
Massachusetts Institute of Technology

Joint Program
in Oceanography
and
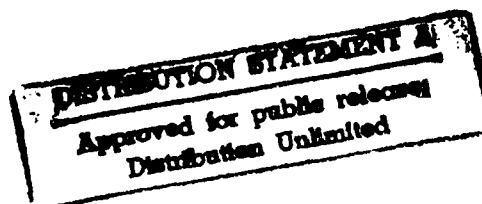Oceanographic Engineering

DOCTORAL DISSERTATION

Diffusion of Helium Isotopes in Silicate Glasses and Minerals: Implications for Petrogenesis and Geochronology
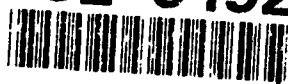
by

Thomas W. Trull

June 1989

DTIC
ELECTE
DEC 18 1992
B

92-31920

92 12 17 044

Diffusion of Helium Isotopes in Silicate Glasses and Minerals: Implications for Petrogenesis and Geochronology

by

Thomas W. Trull

Woods Hole Oceanographic Institution
Woods Hole, Massachusetts 02543

and

The Massachusetts Institute of Technology
Cambridge, Massachusetts 02139

June 1989

Doctoral Dissertation
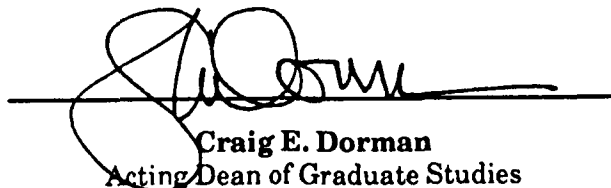
Approved for Distribution:

Frederick L. Sayles, Chairman
Department of Chemistry

Craig E. Dorman
Acting Dean of Graduate Studies

DIFFUSION OF HELIUM ISOTOPES IN SILICATE GLASSES AND MINERALS: IMPLICATIONS FOR PETROGENESIS AND GEOCHRONOLOGY

by

THOMAS W. TRULL

B.S., University of Michigan, 1981

submitted in partial fulfillment
of the requirements for the degree of

DOCTOR OF PHILOSOPHY

at the

MASSACHUSETTS INSTITUTE OF TECHNOLOGY

and the

WOODS HOLE OCEANOGRAPHIC INSTITUTION

April, 1989

© Thomas W. Trull

The author hereby grants to MIT and WHOI permission to reproduce and
distribute copies of this thesis document in whole or in part.

Signature of Author: _____
Joint Program in Oceanography, Massachusetts Institute
of Technology/Woods Hole Oceanographic Institution,
and the Department of Earth, Atmospheric, and
Planetary Sciences, Massachusetts Institute of
Technology.

Certified by: _____
Dr. Mark D. Kurz, Thesis Supervisor

Accepted by: _____
Dr. Philip M. Gschwend, Chair, Joint Committee for Chemical
Oceanography, Massachusetts Institute of Technology/Woods Hole
Oceanographic Institution.

DIFFUSION OF HELIUM ISOTOPES IN SILICATE GLASSES AND MINERALS: IMPLICATIONS FOR PETROGENESIS AND GEOCHRONOLOGY

by

THOMAS W. TRULL

ABSTRACT

Helium mobility in geologic materials is a fundamental constraint on the petrogenetic origins of helium isotopic variability and on the application of radiogenic and cosmogenic helium geochronology.

^{3}He and ^{4}He volume diffusivities determined at 25-600°C in basaltic glasses by incremental-heating and powder storage experiments (using a diffusion model incorporating grain size and shape information to obtain high precision) are three to four orders of magnitude greater than for common cations. Diffusion in tholeiitic glass can be described by an Arrhenius relation with activation energy $= 16.85\pm.13$ Kcal/mole and log $D_o = -2.37\pm.06$, although low temperature data are better described by a distribution of activation energies model. The best estimate for D at 0°C in tholeiitic glass is $5\pm2 \times 10^{-16}$ cm^2/s, an order of magnitude higher than the results of Kurz and Jenkins (1981) but lower than suggested by Jambon, Weber and Begemann (1985). Measurements in an alkali basalt show that helium diffusion is composition dependent ($E_a = 14.4\pm.5$ Kcal/mole; log $D_o = -3.24\pm.2$), and roughly five times faster than in tholeiites at seafloor temperatures. The corresponding timescales for 50% helium loss or exchange with seawater (1 cm spheres) are about one million years for mid-ocean-ridge-basalts, and about 100,000 years in seamount alkali basalts. Radiogenic ^{4}He diffusion has a higher activation energy (27 ± 2 Kcal/mole; log $D_o = +2.4\pm1.0$) than inherited (magmatic) helium, suggesting very low mobility ($D = 3\times10^{-19}$ cm^2/s at 0°C; factor of 5 uncertainty) and that U+Th/^{4}He geochronology of fresh seafloor basalt glasses is unlikely to be hampered by helium loss.

Measured isotopic diffusivity ratios, D^3He/D^4He, are not composition dependent, average $1.08\pm.02$, and vary slightly with temperature, consistent with an activation energy difference of 60 ± 20 cal/mole. This result differs from the inverse-square-root of mass prediction of 1.15, and may be explained by quantization of helium vibrational energies. These results suggest preferential loss of ^{3}He will be minimal at low temperature ($D^3He/D^4He = 1.02\pm.03$ at 0°C). Therefore, alteration of magmatic ^{3}He/^{4}He ratios in basaltic glasses on the seafloor will occur only by helium exchange with seawater, and be important only for samples with low helium contents ($<10^{-8}$ ccSTP/g), such as those found in island arc environments. Extrapolating the glass results to magmatic temperatures yields diffusivities similar to melt values, and suggests D^3He/D^4He approaches 1.15 at these and higher temperatures.

Helium diffusivities in olivine and pyroxene at magmatic and mantle temperatures (900-1400°C) are higher than for cations, ($E_a = 100\pm5$ Kcal/mole, log $D_o = +5.1\pm.7$; and 70 ± 10 Kcal/mole, log $D_o = +2.1\pm1.2$, respectively), but are still too low to transport or homogenize helium in the mantle

3

or even in magma chambers. However, diffusion equilibrates melts and mantle minerals within decades, and interaction with wall-rocks may be enhanced for helium in comparison to other isotopic tracers because of its greater mobility. Rapid exchange of helium within xenoliths and with their host magmas set limits on origin depths and transport times for xenoliths which exhibit helium isotopic disequilibrium between minerals, or between the magma and the xenolith. Phenocrysts equilibrate helium too rapidly to exhibit zoned isotopic compositions, and are likely to retain magmatic helium quantitatively in rapidly cooled volcanic extrusives. The 100-fold higher He diffusivity in pyroxene than olivine at 1000°C allows diffusive loss effects to be evaluated in more slowly cooled rocks, when cogenetic minerals can be measured.

Diffusivities of cosmic-ray produced ^{3}He in surface exposed rocks are several orders of magnitude higher than for inherited helium. However, activation energies for olivine and quartz, 25 ± 4 Kcal/mole (log D_o = -3.7$\pm$.8) and $25.2\pm.9$ Kcal/mole (log D_o = +.2$\pm$.4) respectively, still suggest low diffusivities at surface temperatures of approximately 10^{-22} and 10^{-20} cm^2/s. Equations for simultaneous helium production and diffusive loss allow model ages for surface exposure to be corrected for helium loss, and demonstrate that cosmogenic ^{3}He geochronology will not be limited by helium loss for timescales of approximately 1 million years in quartz and 10 million years or more in olivine. The measurements also suggest that radiogenic ^{4}He produced by U and Th decay may be a useful dating method in quartz.

Application of the diffusion measurements demonstrates that part of the wide range of ^{3}He/^{4}He ratios (.01 to 9 R_a) of a suite of dredged basalts and andesites from the Woodlark Basin, (western Pacific) reflects post-eruptive helium addition, from seawater in glasses with low He contents and from U and Th decay in mafic mineral separates. In unaltered samples, ^{3}He/^{4}He ratios for tholeiites from the Woodlark Spreading Center are 8-9 R_a, similar to mid-ocean-ridges, but distinctly different than the ratio of $6.9\pm.2$ R_a observed in Kavachi submarine volcano basaltic andesites. Helium isotopic systematics in cogenetic pyroxenes and olivines from these samples demonstrate that this is a magmatic signature, and not the result of preferential ^{3}He loss by diffusion. Coupled Sr and He isotopic systematics in these and other samples from the region suggest the sub-arc mantle has been enriched in radiogenic helium supplied by subducted Pacific lithosphere.

Thesis Supervisor: Dr. Mark D. Kurz, Associate Scientist.

ACKNOWLEDGEMENTS

TABLE OF CONTENTS

LIST OF TABLES

LIST OF FIGURES

CHAPTER 4 (contd.)

CHAPTER 5

CHAPTER 6

CHAPTER 6 (contd.)

Chapter 1. Introduction

1.1 OVERVIEW

Helium isotopes provide a unique combination of properties for the study of igneous petrogenesis. Helium is one of the few volcanic volatiles for which there are both a primordial stable isotope, ^{3}He, and a radiogenic stable isotope, ^{4}He. This combination allows the timescales of mantle and magma degassing processes to be investigated, and the presence of juvenile, (i.e dating from the time of Earth's formation) volatiles to be identified. The generation of radiogenic helium is intimately tied to the heat budget of the Earth and to Pb isotopic systematics because the same nuclear decay chains that generate ^{4}He produce a large proportion of the heat presently being lost from the deep Earth, and terminate in stable lead isotopes. This means that the loss of heat, gaseous elements, and less volatile species during the chemical differentiation of the earth can be investigated by comparing helium isotopic systematics to other elements and to present-day heat flow estimates. In addition, because both isotopes are lost to space, the low concentration of helium in the atmosphere makes determining the isotopic composition of helium in rocks relatively free from contamination.

Helium isotopic studies have had important impacts on understanding the formation of Earth's atmosphere, the internal structure and dynamics of the mantle, and basaltic volcanism. However, an often poorly constrained aspect of these studies has been the mobility of helium in geologic materials. This is an important issue in the interpretation of isotopic variability as resulting from closed system evolution or bulk mixing of different source materials. The rate at which helium, as a light neutral atom, can permeate rocks or the silicate mantle is generally assumed to be fast, but has not been thoroughly investigated. In addition, the possible diffusive separation of ^{3}He from ^{4}He because of their large mass difference and different origins has not been previously quantified. Diffusive mobility of helium in individual crystals and basaltic glasses is also important to geochronology efforts using radiogenic ^{4}He and cosmogenic ^{3}He.

For these reasons, this thesis focuses on determining the diffusivities of ^{3}He and ^{4}He in silicate minerals and glasses. The results are used to interpret helium isotopic variability in rocks from mid-oceanic-ridges, island arcs, seamounts, and hotspot volcanos. In addition, the impact of helium mobility on radiogenic helium (^{*4}He) dating of basaltic glasses and cosmogenic helium (^{3}He$_c$) surface exposure dating of lava flows and other rocks is considered and quantified.

1.2 TERRESTRIAL HELIUM ISOTOPIC SYSTEMATICS AND DIVERSITY

Two stable isotopes of helium exist in the universe, ^{3}He, and ^{4}He which is by far the most abundant. For example, stars, meteorites, and our solar wind, have ratios of a few times 10^{-4} (e.g. Mamyrin$_a$ and Tolstikhin, 1984). On Earth, the isotopic composition of helium varies from these high values to several orders of magnitude further depletion of ^{3}He (figure 1.1). This variability is related to the different origins of the two isotopes. Almost all of the ^{3}He presently in the earth's interior remains from planetary formation. However, ^{4}He is continuously produced by decay of ^{235}U, ^{238}U, and ^{232}Th and their radioactive daughters. These decays (listed in figure 1.2) also produce very small amounts of ^{3}He through secondary nuclear reactions (predominantly with ^{6}Li), yielding a ^{3}He/^{4}He radiogenic production ratio of 10^{-8} to 10^{-7} for common silicate rocks (e.g. Morrison and Pine, 1955; Mamyrin and Tolstikhin, 1984).

Over the age of the Earth, addition of radiogenic ^{4}He has reduced the ^{3}He/^{4}He ratio of silicate rocks relative to likely initial compositions (figure 1.2). For example, most continental rocks, degassed and enriched in U and Th during their formation, contain virtually no primordial ^{3}He and exhibit ^{3}He/^{4}He ratios corresponding to the radiogenic production ratio (figure 1.2). Other rock types, such as young oceanic volcanics, still retain significant ^{3}He, suggesting their sources have not been completely degassed, and reflecting their relatively low U and Th contents. The exact helium isotopic composition of a sample reflects its initial composition, time-integrated U and Th

Figure 1.1 Comparison of ^{3}He/^{4}He ratios for terrestrial rocks with
likely primordial sources and Earth's atmosphere. The lowered ratios
reflect ^{3}He loss, and ^{4}He gain by radiodecay of U and Th. Continental
rocks have isotopic compositions similar to the radiogenic production
^{3}He/^{4}He ratio, and have retained far less ^{3}He than samples from the
oceanic mantle. The large range in ^{3}He/^{4}He ratios allows different
components involved in petrogenesis and mantle mixing to be
distinguished (data fields are approximate, for a compilation see
Mamyrin and Tolstikhin, 1984; figure adapted from M.D. Kurz,
unpublished).

Figure 1.1

Terrestrial Helium
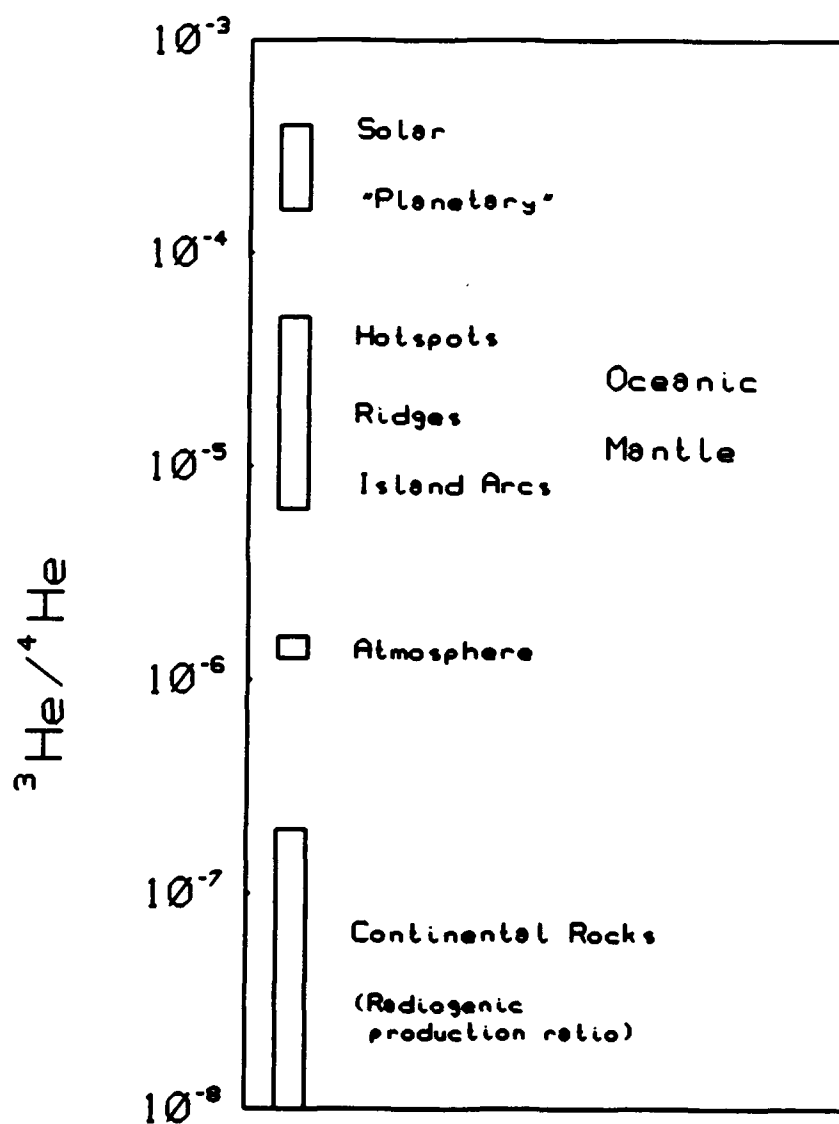
Figure 1.2   Radioactive decay series for the production of ^{4}He from U and Th isotopes.   Decay half-lives and alpha-particle energies (MeV) are also shown.

Figure 1.2

contents, and the degree to which it has exchanged helium with other reservoirs.

For a closed system, the helium isotopic composition at some time, t, is related to its initial composition by:

$$(^3He/^4He)_t = (^3He_o + ^{*3}He)/(^4He_o + ^{*4}He) \qquad (1.1)$$

where o indicates initial helium contents, and * denotes helium produced by radioactive decay over the time, t. Provided the geologic system is in secular equilibrium, the production of $^{*4}He$ is given by:

$$^{*4}He = 8[^{238}U(1-e^{-\lambda t})] + 7[^{235}U(1-e^{-\lambda t})] + 6[^{232}Th(1-e^{-\lambda t})] \qquad (1.2)$$

in which the parent nuclide concentrations are those at the start of production. In terms of final U and Th contents, as are usually measured, this equation can be rewritten:

$$^{*4}He = 8[^{238}U(e^{\lambda t}-1)] + 7[^{235}U(e^{\lambda t}-1)] + 6[^{232}Th(e^{\lambda t}-1)] \qquad (1.3)$$

The decay constants are 1.55125×10^{-10}, 9.8485×10^{-10}, and 4.9475×10^{-11} decays per year for ^{238}U, ^{235}U and ^{232}Th respectively (Steiger and Jager, 1977). For short times and the present day $^{238}U/^{235}U$ ratio of 137.8, is sometimes linearized (e.g. Graham et al, 1987):

$$^{*4}He = 2.80 \times 10^{-8}\{[U](4.35+Th/U\}\lambda t \qquad (1.4)$$

where Th/U is the atom ratio, [U] is concentration is ppm, and $^{*4}He$ is in $cm^3 STP/g$ (Graham et al, 1987). The radiogenic production of ^3He is:

$$^{*3}He = R_p \, ^{*4}He \qquad (1.5)$$

where R_p designates the radiogenic production ratio, $^{*3}He/^{*4}He$. As mentioned above, R_p is very small and varies from 10^{-8} to 10^{-7} depending primarily on lithium content and on the matrix composition.

Equations 1.1 and 1.5 can be combined to obtain an expression for fractional change in the closed system's ^{3}He/^{4}He ratio with time, designating ^{3}He/^{4}He ratios by R, leads to::

$$F = R_t/R_o = (^3He/^4He)_t/(^3He/^4He)_o$$

$$= [1 + Q^o (R_p/R_o)] / [1 + Q^o] \qquad (1.6)$$

where Q^o is written for $^{*4}He/^4He_o$ for convenience; Q^o is the quotient of radiogenic to initial helium. This equation shows that radiogenic production of ^{*3}He will have a negligible effect (less than .1%) on F for systems such as oceanic rocks, where R_o is much (1000 times) larger than R_p . In these cases, taking R_p equal to zero gives the approximation:

$$F = 1/(1+Q^o) = {}^4He_o/ ({}^4He_o + {}^{*4}He) \qquad (1.7)$$

These expressions can be used to predict the timescales over which different geologic materials will change their ^{3}He/^{4}He ratios by radiodecay.

F can also be written in terms of measured (rather than initial) helium contents and used to calculate initial ^{3}He/^{4}He ratios, when age estimates can be made. Defining Q^t as the ratio of radiogenic to total helium in the sample:

$$Q^t = {}^{*4}He/^4He_t \qquad (1.8)$$

allows F to be written:

$$F = \{1 + [Q^t/(1-Q^t)][1-(R_p/R_t)]\}^{-1} \qquad (1.9)$$

This form of F makes clear that ^{*3}He production is not important when

the measured ratio, R_t, is large in comparison to the production ratio, R_p, giving the approximation:

$$\tilde{F} = 1 - Q^t = ({}^4He_t - {}^{*4}He) / {}^4He_t \qquad (1.10)$$

Given measured U and Th contents and an age, ${}^{*4}He$ can be obtained from equation 1.2, and used along with the measured helium content to calculate F from equation 1.9. The initial ratio is then obtained by multiplying the measured ${}^3He/{}^4He$ ratio by F.

F values for different U and He contents ratios are plotted in figure 1.3. This figure reveals that the timescales to change the ${}^3He/{}^4He$ ratio of different rocks and source regions varies dramatically, from 1000 years to 10^8 years, primarily because of large variations in He contents. This phenomenon offers the advantage that many different processes in petrogenesis can be investigated through helium isotopic systematics, but the concomitant disadvantage that the ${}^3He/{}^4He$ ratios of even relatively young rocks may have changed since eruption. In addition, it is clear that departures from closed system behavior, such as loss of helium by degassing from the mantle or a magma, or by diffusion from an erupted rock have a large influence on the subsequent evolution of helium isotopic compositions.

Earth's atmosphere is an open reservoir for He. Its helium content is quite low (5.24 ppm, e.g. Mamyrin and Tolstikhin, 1984) in comparison to other noble gases because helium is lost to space. Control of the helium isotopic composition of the atmosphere is quite complex and reflects a balance between radiogenic additions from continental crust, primordial additions from active volcanic regions, and several upper atmosphere processes, including accretion of helium from solar wind, helium production by cosmic ray spallation, and both thermal and photo-ionization losses to space (Johnson and Axford, 1969; Lupton, 1973; Mamyrin and Tolstikhin, 1984). These processes maintain the atmospheric ${}^3He/{}^4He$ ratio above that for radiogenic production (figure 1.1). Both the low helium concentration of air and its distinct isotopic composition are important to helium isotope geochemistry of silicate rocks, because contamination problems are minimized and readily

Figure 1.3 Fractional change in ^{3}He/^{4}He ratios as a function of time for varying U and He contents. Curves are calculated for Th/U = 3, ^{3}He/^{4}He radiogenic production ratio of 10^{-8}, and initial ^{3}He/^{4}He of 1.38 x 10^{-6}, but are accurate to better than 1% for all initial ^{3}He/^{4}He ratios greater than 1 Ra (see text). The individual curves correspond to initial U and He contents as follows:

	U ppm	He ccSTP/g	Example
1	0.3	10^{-7}	Back-arc basin basaltic glass
2	1.0	10^{-7}	
3	0.3, 3.0	10^{-8}	Island arc basaltic glass (Chap. 6)
4	1.0	10^{-8}	Island arc andesitic glass (Chap.6)
5	0.3, 3.0	10^{-9}	
6	1.0	10^{-9}	Dacite glass
7	3.0	10^{-9}	

Curves for mid-ocean-ridge basalt glasses and mantle source regions are not shown, but with He contents on the order of 10^{-5} to 10^{-6} cc/g and low U contents of 100 to 10 ppb, the timescales are 10^8 to 10^{10} years. (figure adapted from Graham, 1987)

24

Figure 1.3
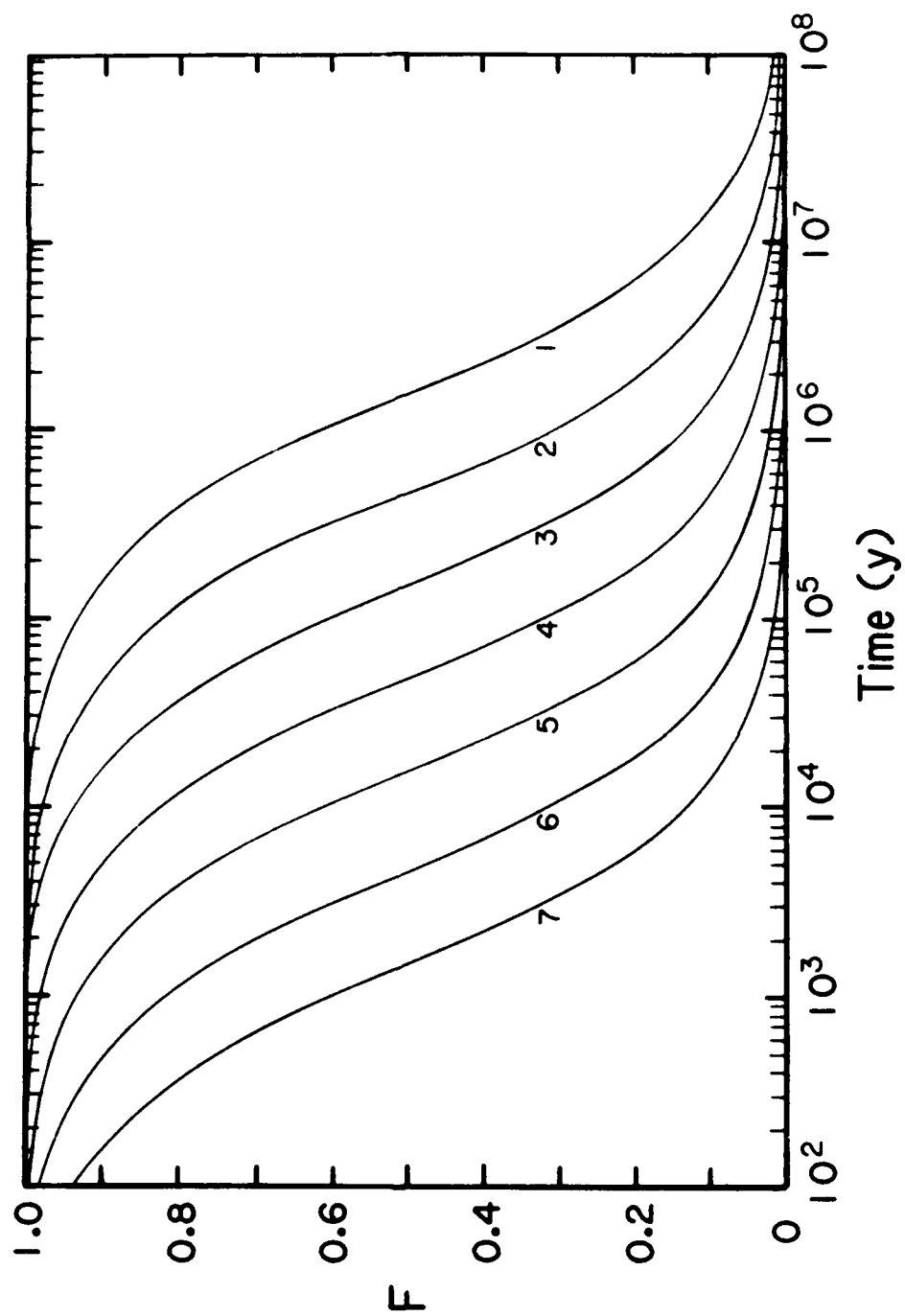
identified. This is true more generally, in that large differences in helium isotopic compositions allow the petrogenetic involvement of crustal rocks, mantle sources, and the atmosphere and oceans to be readily distinguished.

In addition to their impact on the atmosphere, cosmic rays produce some ^{3}He in terrestrial rocks directly. As discussed below, this process provides an important geochronometer, and can lead to misinterpretations in petrogenetic studies, if unrecognized. Interplanetary dust particles also contribute some helium which is high in ^{3}He, as has been recognized in oceanic sediment studies (Merrihue, 1964; Krylov et al, 1973; Ozima et al, 1984). These ^{3}He sources are not important to the helium isotopic composition of the earth's interior or erupted rocks because weathering releases most of it before it is subducted into the mantle, and because the global flux is small.

Finally, the reactions which produce radiogenic helium terminate in stable isotopes of lead, and produce a large proportion of the present heat flow from the earth. Thus radiogenic production of ^{4}He provides a connection between helium isotopic compositions and terrestrial heat flow (e.g. O'Nions and Oxburgh, 1983) and between gaseous (He) and solid-state (Pb) isotopic tracers of mantle processes (e.g. Graham, 1987).

1.3 ORIGINS OF HELIUM ISOTOPIC VARIABILITY IN OCEANIC BASALTS.

Helium isotopic differences between different types of oceanic volcanic rocks, such as the higher ratios observed in hotspot volcanos (e.g. Hawaii, Iceland) than in mid-ocean-ridge basalts (figure 1.1) have been interpreted as reflecting fundamentally different mantle source regions that have remained separate for much of Earth's history (e.g. Kaneoka and Takaoka, 1978; Kurz et al, 1983; Rison and Craig, 1983; Condomines et al, 1983; Kurz, Meyer and Sigurdsson, 1985; Allegre et al, 1983). In this view, the mid-ocean-ridge-basalt (MORB) source has lost primordial helium over time and decay has lowered its ^{3}He/^{4}He ratio to a greater degree than in the source region of hotspot volcanos. This interpretation assumes that parts of the mantle remain isolated from

26

each other for long times and that helium does not migrate within the mantle at faster rates than bulk convection. The few measurements available for mafic minerals (Gramlich and Naughton, 1972; Hart, 1984) suggest helium diffusion rates are too slow to homogenize helium isotopic compositions on mantle length scales (i.e. km), even over the age of the earth. This result is confirmed by further measurements in chapter 4 on olivine and pyroxene crystals. Thus both the relative homogeneity of the MORB helium isotopic compositions ($7-9R_a$) and the difference between hotspots and mid-ocean ridge basalts must represent characteristics of the mixing process (e.g. Kurz and Jenkins, 1981) or possibly the relative nature of U, Th and He extraction during melt generation (Lupton, 1983).

In addition to these large differences, there are helium isotopic variations within hotspot volcanos and along oceanic ridges which are well outside measurement error. For example, Kurz et al (1987) have shown that the $^3He/^4He$ ratio of lavas erupted from Hawaiian volcanos vary with time, generally decreasing from the initial hotspot values of 20 to 30 R_a to values near 8 R_a as the volcanos age. This has been interpreted as a change of magma source from hotspot plume to residual heated lithosphere as the Pacific tectonic plate moves away from the plume source (op. cit.). However, other interpretations are possible, including sequential tapping of a magma chamber which is steadily degassing helium and accumulating radiogenic ^4He, or preferential degassing of ^3He by diffusion (e.g. Condomines et al, 1983; Zindler and Hart, 1986).

Similarly, while Mid-oceanic-ridge-basalts have generally uniform helium isotopic compositions ($6-9 R_a$) there are significant local and regional variations. For example, $^3He/^4He$ ratios along the mid-Atlantic-ridge display smooth variations that may represent mixing of mantle components with different U contents and degassing histories (Kurz et al, 1982; Poreda et al, 1980; Lupton, 1983). In addition, the helium isotopic composition of spreading ridge basalts in the southwestern Pacific may be relatively enriched in ^3He in comparison to other regions (Craig and Poreda, 1986; data in chapter 6). These differences may offer important information about mantle heterogeneity

or melt segregation and transport processes, particularly with respect
to separation of a gas phase. If these variations reflect source
differences, understanding the mobility of helium in the mantle in the
presence of melt is essential to determining mantle structure. However,
it is possible that part or all of this variability derives from
isotopically fractionating gas loss from the magmas or the basalts after
eruption (Zindler and Hart, 1986; Craig and Lupton, 1976).

Another aspect of interpreting helium isotopic studies of rocks is
accounting for processes that may affect the samples measured, which are
usually small basaltic glass fragments, or separated mineral grains.
Helium loss by diffusion during magma transport, lava cooling, or from
the subsamples can affect helium concentration determinations and
isotopic compostitions if the loss process is isotopically
fractionating. Thus, helium diffusion rates in glasses are important in
assessing contamination of samples on the seafloor, especially when the
samples contain very little helium so that a small amount of helium from
seawater can drastically alter their isotopic compositions. Because low
helium contents are common in samples from island arc regions and
seamounts and subaerial volcanics, extending helium isotopic tracer
studies to these regions requires a better understanding of helium
diffusion rates.

1.4 RADIOGENIC AND COSMOGENIC HELIUM GEOCHRONOLOGY

The production of radiogenic helium, ^{*4}He, by uranium and thorium
series nuclear decay provides a method for dating rocks. However, ages
obtained by this method have often been unreasonably young given
geologic settings (e.g. Hurley, 1954; Fanale, 1964; Leventhal, 1975)
This problem generally reflects radiogenic helium loss by diffusion,
often exacerbated because U and Th tend to be located on grain
boundaries or in fine-grained accessory minerals. Recently radiogenic
helium geochronology has been applied to alkali basalt glasses where
heterogeneous uranium and thorium distribution is not a problem, but in
which corrections for inherited magmatic helium must be made (Graham et
al, 1987). The ^{3}He/^{4}He ratio measured in gas-filled vesicles is assumed

to represent magmatic helium and combined with the ^{3}He content of helium dissolved within the glass to correct the total ^{4}He of the glass for inherited helium. Therefore, both the loss of radiogenic helium and the exchange of helium between vesicles and glass can lead to incorrect age estimates.

Graham et al (1987) considered this problem using a diffusivity measured for tholeiitic basalt (Kurz and Jenkins, 1981). However, higher diffusivities have been measured in similar rocks (Jambon, Weber, and Begemann, 1985) and the mobility of radiogenic helium may differ from inherited helium because of the nature of its generation. Thus, the accuracy of this technique remains uncertain. A similar problem is the determination of magmatic ^{3}He/^{4}He ratios from phenocryst fluid inclusion studies in older rocks which contain significant radiogenic helium. Determining the diffusive mobility of ^{*4}He in these samples allows the contamination of the fluid inclusions to be constrained.

In addition to the dominantly primordial origin of ^{3}He in the silicate earth, small amounts of ^{3}He (^{3}He$_c$) are produced in surface rocks by interactions with energetic cosmic rays (Kurz et al, 1985; Kurz, 1986a,b; Craig and Poreda, 1986). This process is significant to the study of silicate rocks in two ways. The presence of ^{3}He$_c$ can interfere with the determination of magmatic ^{3}He/^{4}He ratios, although this problem can be avoided simply by sampling rocks at depth (approximately a meter; Kurz, 1986b). More importantly, ^{3}He$_c$ production provides a means of obtaining surface exposure ages and erosion rates (Kurz, 1986b; Craig and Poreda, 1986).

Several nuclear reactions contribute to the ^{3}He$_c$ production. Most important is spallation of major element target atoms by high energy neutrons, which are produced as secondary particles in the atmosphere when the primary cosmic rays (predominantly protons, but containing some neutrons and heavier nuclei) collide with atmospheric atoms. Another production reaction is the interaction of thermalized secondary neutrons (from cosmic ray interactions) with ^{6}Li to yield equal amounts of ^{3}He and ^{4}He. For rocks with lithium contents of a few parts per million this mechanism is only about 1% as effective as spallation. A third mechanism produces much less ^{3}He and only becomes relatively important

at depths below where the secondary neutrons have been largely absorbed (on the order of a meter). This is the interaction of cosmic muons with major element nuclei to produce neutrons which then interact with lithium by the reaction already described. More detailed discussion of these production processes, the energies involved, and attenuation depths are presented in chapter 5, and have been recently reviewed by Lal (1987,1988).

Using cosmogenic helium contents as an indicator of surface exposure duration requires determining its production rate, that inherited and cosmogenic helium can be distinguished and that no cosmogenic helium has been lost since formation. Accounting for inherited helium appears to be possible in basaltic phenocrysts by separating helium contained in fluid inclusions from that in the crystal matrix (Kurz, 1986a,b). However, the diffusivity of cosmogenic helium has not yet been determined for any minerals, and may differ significantly from diffusivity of inherited helium because of the particle energies involved in its generation. For this reason, the effect of $^3\text{He}_c$ loss on surface exposure and erosion studies is unknown.

1.5 OBJECTIVES

The objectives of this research are 1) to quantify the diffusive mobility of helium isotopes in silicate glasses and minerals important to petrogenesis and geochronology studies, and 2) to apply the results in interpreting helium isotopic variability in oceanic volcanic rocks and evaluating model ages based on radiogenic and cosmogenic helium contents. Chapter 3 addresses the diffusivity of inherited ^3He, inherited ^4He and radiogenic ^4He in basaltic glasses, with implications for low temperature loss of helium, exchange of helium with seawater, and alteration of inherited helium isotopic compositions via preferential ^3He loss. It also discusses the mobility of helium in basaltic melts as a guide to quantifying volcanic degassing processes, including the separation of helium from other elements, and the relative loss rates of helium and heat from magma bodies. Chapter 4 examines helium mobility in mafic minerals at high temperature to quantify the

mobility of helium in the mantle and the extent to which phenocrysts and xenoliths retain magmatic helium. Chapter 5 discusses the mobility of cosmogenic ^3He_c in olivine and quartz crystals to constrain the effects of diffusive loss on surface exposure dating. Chapter 6 is a study of the helium (and strontium) isotopic compositions of volcanic rocks from the Woodlark Basin/Solomon Islands lithospheric subduction region in the western Pacific. The large helium isotopic variability observed is considered in light of the diffusion measurements for contamination affects occuring on the seafloor in addition to source variations.

REFERENCES

ALLEGRE C.J., STAUDACHER T., SARDA P. and KURZ M. (1983) Constraints on evolution of earth's mantle from rare gas systematics. Nature 303, 762-766.

CONDOMINES M., GRONVOLD K., HOOKER P.J., MUEHLENBACHS K., O'NIONS R.K., OSKARSSON N. and OXBURGH E.R. (1983) Helium, oxygen, strontium and neodymium isotopic relationships in Icelandic volcanics. Earth Plan. Sci. Let. 66, 125-136.

CRAIG H. and LUPTON J.E. (1976) Promordial neon, helium and hydrogen in oceanic basalts. Earth Plan. Sci. Let. 31, 369-385.

CRAIG H. and POREDA R. (1986) Papatua Expedition Legs V and VI: Studies of methane and helium in hydrothermal vent plumes, spreading-axis basalts, and volcanic island lavas and gases in southwest Pacific marginal basins. Scripps Institute of Oceanography Reference 87-14.

FANALE F.P. (1964) Helium in magnetite. Columbia University Ph.D., (Geology), 135 p.

GRAHAM D.V., JENKINS W.J., KURZ M.D. and BATIZA R. (1987) Helium isotope disequilibrium and geochronology of glassy submarine basalts. Nature 326(6111), 384-386.

GRAMLICH J.W. and NAUGHTON J.J. (1972) Nature of source material for ultramafic minerals from Salt Lake Crater, Hawaii, from measurment of helium and argon diffusion. J. Geophys. Res. 77-17, 3032-3042.

HART S.R. (1984) He diffusion in olivine. Earth Plan. Sci. Let. 70, 297-302. HESS P.C. (1980) Polymerization model for silicate melts. In Physics of Magmatic Processes (ed. R.B. HARGRAVES) pp.3-44. Princeton Univ. Press, Princeton, N.J.

HURLEY P.M. (1954) The helium age method and the distribution and migration of helium in rocks. In Nuclear Geology (ed. H. FAUL) pp. 301-329. J. Wiley and Sons, New York.

JAMBON A., WEBER H.W. AND BEGEMANN F. (1985) Helium and Argon from an Atlantic MORB glass: concentration, distribution and isotopic composition. Earth Plan. Sci. Let. 73 255-267.

JOHNSON H.E. and AXFORD W.I. (1969) Production and loss of ^{3}He in the earth's atmosphere. J. Geophy. Res. 74, 2433.

KANEOKA I. and TAKAOKA N. (1978) Excess ^{129}Xe and high ^{3}He/^{4}He ratios in olivine phenocrysts of Kapuho lava and xenolithic dunites from Hawaii. Earth Plan. Sci. Let. 39, 382–386.

KRYLOV A.Y.,MAMYRIN B.A., SILIN, Y.I. and KHABARIN L.V. (1973) Helium isotopes in ocean sediments. Geochem. Int. 10, 202.

KURZ M.D. and JENKINS W.J. (1981) The distribution of helium in oceanic basalt glasses. Earth Plan. Sci. Let. 53, 41–54.

KURZ M.D., JENKINS W.J., SCHILLING J.G. and HART S.R. (1982) Helium isotopic variations beneath the central North Atlantic Ocean. Earth Plan. Sci. Let. 58, 1–14.

KURZ M.D., JENKINS W.J., HART S.R. and CLAGUE D. (1983) Helium isotopic variations in the volcanic rocks from Loihi Seamount and the island of Hawaii. Earth Plan. Sci. Let. 66,

KURZ M.D., MEYER P.S. and SIGGURDSON H. (1985) Helium isotopic systematics within the neovolcanic zones of Iceland. Earth Plan. Sci. Let. 74, 291–305.

KURZ M.D. (1986a) Cosmogenic helium in a terrestrial igneous rock. Nature 320, 435–439.

KURZ M.D. (1986b) In situ production of terrestrial cosmogenic helium and some applications to geochronology. Geochim. Cosmo. Acta 50, 2855–2862.

KURZ M.D., GARCIA M.O., FREY F.A. and O'BRIAN P.A. (1987) Temporal helium isotopic variations within Hawaiian volcanoes: basalts from Mauna Loa and Haleakala. Geochim Cosmo. Acta 51, 2905–2914.

LAL D. (1987) Production of ^{3}He in terrestrial rocks. Chemical Geology (Isotope Geoscience Section) 66, 89–98.

LAL D. (1988) In situ-produced cosmogenic isotopes in terrestrial rocks. Ann. Rev. Earth Planet. Sci. 16, 355–388.

LEVENTHAL J.S. (1975) An evaluation of the U-Th-He method for dating young basalts. J. Geophys. Res. 80, 1911–1914.

LUPTON J.E. (1983) Terrestrial inert gases: isotope tracer studies and clues to primordial components in the mantle. Ann. Rev. Earth Planet. Sci. 11, 371-414.

LUPTON J.E. (1973) Direct accretion of ^{3}He and ^{3}H from cosmic rays. J. Geophys. Res. 78, 8330-8337.

MAMYRIN B.A. and TOLSTIKHIN I.N. (1984) Helium Isotopes in Nature. Elsevier, Amsterdam.

MERRIHUE C. (1964) C. Ann. N.Y. Acad. Sci. 119, 351-367.

MORRISON P. and PINE J. (1955) Radiogenic origin of the helium isotopes in rock. Ann. N.Y. Acad. Sci. 62, 71-92.

O'NIONS R.K. and OXBURGH E.R. (1983) Heat and helium in the earth. Nature 306, 429-431.

OZIMA M., TAKAYANAGI M., ZASHU S. and AMARI S. (1984) High ^{3}He/^{4}He ratio in ocean sediments. Nature 311, 448-450.

POREDA R., CRAIG H. and SCHILLING J.G. (1980) ^{3}He/^{4}He variations along the Reykjanes Ridge. EOS, Trans. Am. Geophys. Union 61, 1158.

RISON W. and CRAIG H. (1983) Helium isotopes and mantle volatiles in Loihi Seamount and Hawaiian Island basalts and xenoliths. Earth Plan. Sci. Let. 66, 407-426.

STEIGER R.H. and JAGER E. (1977) Subcommission on geochronology: convention on the use of decay constants in geo- and cosmochronology. Earth Plan. Sci. Let. 36, 359-362.

ZINDLER A. and HART S. (1986) Helium: problematic primordial signals. Earth Plan. Sci. Let. 79, 1-8.

Chapter 2. Experimental Methods

2.1 INTRODUCTION

This chapter describes the selection and preparation of rock samples, techniques for releasing helium from rocks, and details of helium isotope mass spectrometry. It also reviews the assumptions and deficiencies of standard equations for determining diffusivities from emanation data, and presents a refined calculation scheme incorporating grain shape and size variations developed to improve the accuracy of diffusivity estimates for basaltic glasses (chapter 3).

2.2 SAMPLE PREPARATION

The main sample types used were submarine basaltic glasses, phenocryst separates from both submarine and subaerial basaltic and andesitic rocks, and mineral separates from ultramafic xenoliths. In all cases the whole rock samples were examined in hand specimen and by preparing a thin section prior to dissection. Interior portions of the whole rocks were chosen for study to avoid weathered or thermally altered margins; when necessary altered portions were removed by abrasive sawing or with hammer and chisel. The fresh rock interior pieces were broken with a hydraulic sample splitter to produce centimeter size pieces which were then crushed with a ceramic jaw crusher to approximately .5 to 3mm fragments. The rock chips were then sieved and directly hand-picked for mafic minerals when abundant .5 to 2mm crystals were present. For samples with less abundant, smaller phenocrysts a preliminary separation of minerals from fine-grained rock matrix fragments was carried out with a Frantz Isodynamic Separator, prior to hand-picking.

In some cases the first mineral separates were further crushed using a hardened steel mortar and pestle to obtain grain fragments without adhering matrix or to produce smaller grain sizes for diffusion studies. Glass samples and xenolith minerals were crushed directly with the mortar and pestle, without preliminary steps. Glass and mineral separates were sieved in standard stainless sieves (Newark Wire Cloth Co., N.J.) and cleaned by ultrasonic agitation in water, acetone and

methanol and dried in air at room temperature. Final selection of
sample grains was done by individual examination in reflected and
transmitted light in air and in ethanol at 20 to 80x magnification.
Polished grain mounts were prepared from splits of the samples analysed
to examine fluid inclusion or vesicle abundances and extent of internal
fracturing. These mounts were also used for chemical analysis with the
JEOL electron microprobe under the direction of Dr. Steve Recca at MIT.
Multiple spot analyses were always performed, and appropriate
calibration standards used. Other details of sample selection and
preparation are given in individual chapters as appropriate.

2.3 HELIUM ANALYSES

2.3.1 Releasing helium

Helium was released from the rock samples using three different
extraction methods, all of which were performed under high vacuum while
attached to the processing line for the noble gas mass spectrometer used
for rocks (MS2). Helium contained in gas or fluid inclusions was
released by crushing glass and mineral separates in 3/4" diameter
stainless cylinders connected to the processing lines with VCR fittings
and copper gaskets. Crushing was accomplished with a magnetic
stainless-steel cylindrical slug that was lifted and driven down onto
the sample by three stacked electromagnetic coils. This was done in an
automated mode by computer control. Fifty cycles generally were enough
to reduce millimeter sized phenocrysts to powders of less than 100
microns, although a few larger grains (250 um or so) often remained, and
some very fine powder was produced. Crushing efficiency dropped as
sample size was increased, particularly if more than 200-300 mg of
material was used. The ram is quite forceful and diamonds have been
successfully fractured.

Cleaning of the crusher canisters and rams was extensive to avoid
inter-sample contamination and to reduce pump out times. Cleaning steps
included polishing of the slugs, high-speed wire brushing of the
canisters and a sequence of washings and sonic agitations in water, 8N

nitric acid, acetone and methanol of both canisters and slugs. In addition, small disk inserts of non-magnetic stainless steel were used to protect the bottom of the sample container, and were replaced for each analysis to minimize memory effects. The crushers have been previously described by Kurz et al (1987). The only important improvement was the replacement of four VCR^{TM} vacuum fittings with welds and one Mini-Conflat^{TM} connections in the crusher manifold, which reduced the leak background.

Helium release was also achieved by sample heating and/or fusion in a resistively-heated furnace. The furnace consists of a tantalum crucible sealed to the gas processing line with a gold wire o-ring and isolated from the secondary vaccum jacket with a second gold o-ring. The vacuum jacket contains a basket-shaped tungsten resistance element along with a series of concentric tungsten and molybdenum heat shields isolated from each other with high temperature ceramic spacers. The water cooled copper feedthroughs are electrically insulated with teflon and the vacuum seal is achieved with viton o-rings. The secondary vacuum is maintained at less than $2x10^{-7}$ torr with a dedicated 200/s oil diffusion pump. The power supply is a 220v line controlled by a large variable transformer which supplies current to a secondary transformer. Temperature control relies on a constant power input and has been calibrated using pyrometry, and the melting of metal standards. The furnace can achieve temperatures up to 2000 ^{o}C, can reach basaltic fusion temperatures (1200 ^{o}C) in about 5 minutes, and will remain at constant temperature within 5-8 degrees for days on end without regulation. The furnace has been described before by Kurz et al (1987) and is similar to the design presented by Staudacher et al (1978).

Samples were loaded into the furnace with either a rotary "six-shooter" or a magnetic-piston "four-shooter". Both are thermally-isolated sample holders which sit above the crucible, from which multiple samples can be delivered to the hot zone without breaking vacuum. In this way, the furnace can be baked out, and a blank determination performed prior to sample analysis. The six-shooter has been described before (Kurz et al, 1987). The four-shooter was built for the diffusion experiments and has the advantage of a viewing port

Figure 2.1. The "Four-shooter" device for loading furnace samples. Construction is welded stainless steel with copper gasket knife-edge seals. Samples can be loaded either as loose grains or wrapped in aluminum or tantalum foil. Loose grains are first loaded into a small cup made from a permanent magnet (ALNICO), which is then lowered into the central tube and magnetically connected to the permanent magnet push ram. Foil wrapped samples are simply pushed into the sample arms with forceps. Loading samples requires venting the furnace (there is no valve between the sample holder and the crucible), and unbolting the flange between the window section and the sample section. Cleaning the sapphire window (Varian), shutter and sample loader is done by swabbing with a solution of 45% conc. Nitric acid, 5% conc. HF and 50% water, followed by copious water rinsing, and a final methanol rinse. Care must be taken not to expose the knife-edges and especially the bronze window seal to the acid. Sample loading is done by repelling the permanent magnet push rods towards the axial tubes using an external cylindrical magnet. For the loose grains, the cup is first repelled into the center and then rotated by rolling the external magnet around the loading arm. Similarly, the stainless steel shutter is actuating with an external magnet, and protects the viewing window from becoming coated by fine particles from the crucible, although gases can still reach the port and coat it.

Figure 2.1
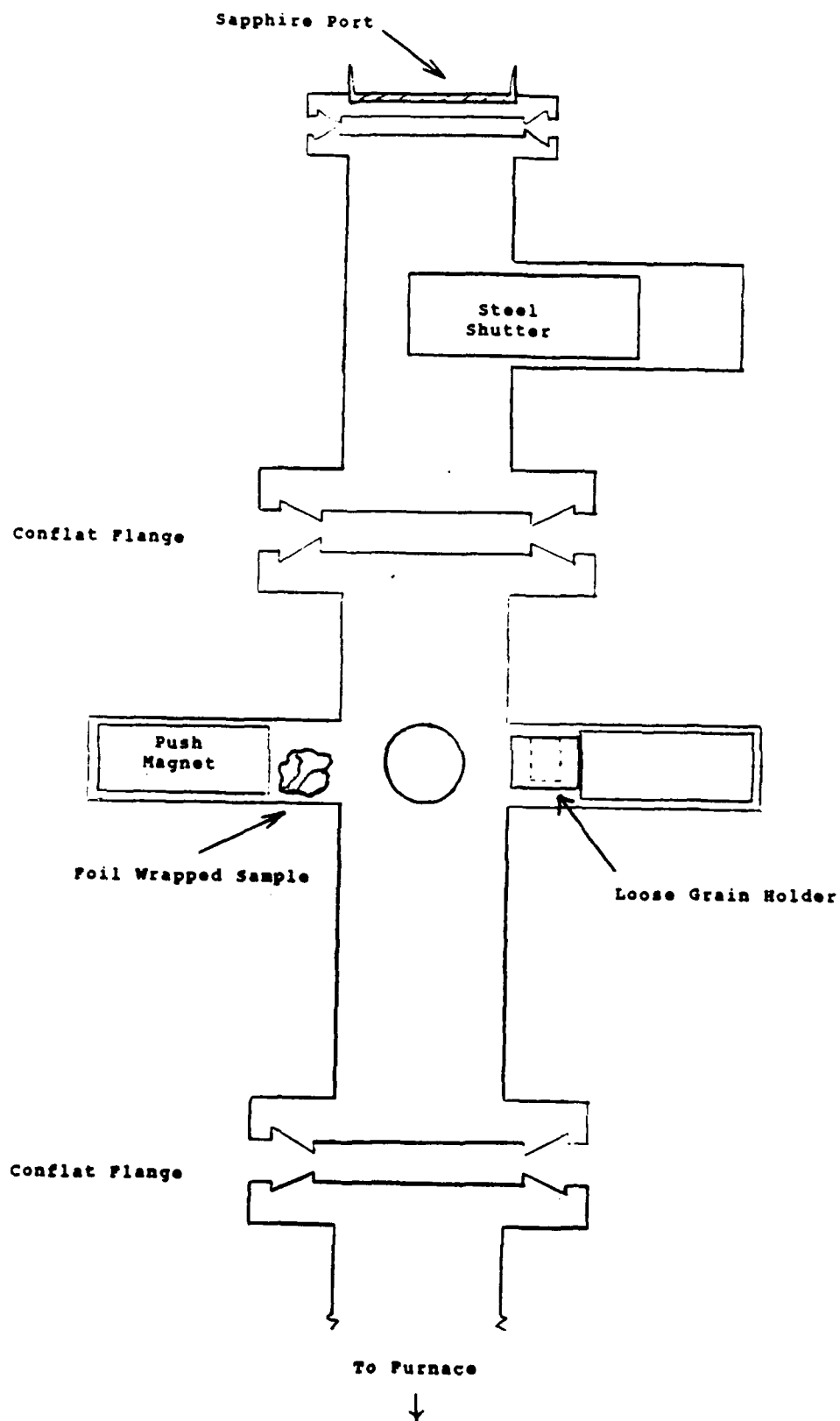
(figure 2.1). In general, the furnace was operated with a tantalum thin-walled inner crucible. This insert was replaced between samples during step-heating experiments to avoid chemical reactions that might release gases, and protected the outer crucible from direct contact with molten silicates during fusion studies. However, the outer tantalum crucibles are subject to hardening and fracture by recrystallization, and this required their replacement after roughly 100 heat cycles. Aspects of the furnace that have not been described before include the addition of the four-shooter, temperature calibration using standard metals, new copper feedthroughs, and a nitrogen venting line which allows the primary vacuum side of the furnace to be vented without bringing the processing line up to atmospheric pressure.

Measurements to determine the helium diffusivity of silicate glasses and crystals at low temperature used a specially constructed vessel designed for incremental heating of small samples in the temperature range or $20 - 600^{\circ}C$. This diffusion vessel consists of a copper sample holder inserted in a .065" wall stainless steel canister, with an exterior thermocouple and resistance heater (figure 2.2). Good thermal contact is provided by the copper insert which surrounds the sample grains. The surfaces between the insert and the vessel bottom are polished to improve thermal contact between the sample and the thermocouple. In order to examine thermal equilibrium between the sample and the external thermocouple, a test was performed in which a second thermocouple was installed in the copper sample holder, and the temperature between the two was compared. In these tests the internal temperature was slightly lower, the differences ranged from $0\ ^{\circ}C$ at 25 $^{\circ}C$ to 14 $^{\circ}C$ at 600 $^{\circ}C$ and the subsequent experiments were corrected for this offset. This temperature differential was reproducible and does not represent an important uncertainty in the experimental temperatures. The .015" Cr-Al bare wire thermoc⌐ 'es were insulated with high temperature ceramic tubing and glass wool, to avoid strong temperature gradients along the leads, and the junction was well within the heater's hot zone (see figure 2.2). The thermocouples were calibrated to 1 $^{\circ}C$ at the endpoints 0 $^{\circ}C$ and 600 $^{\circ}C$ using a distilled water/ice bath and a specially constructed DC millivolt supply, providing a factory-specified

Figure 2.2. Diffusion Vessel schematic showing sample chips enclosed in a copper sample holder with copper lid, which is attached to the stainless vessel with a central screw. Outside the vacuum, a Cr-Al .15" bare-wire thermocouple insulated with high-temperature ceramic tubes is attached to the vessel floor. The vessel wall thickness is .065". Both the vessel floor and the copper sample holder are highly polished to promote good thermal contact. Surrounding the sample hoder and the glass wool insulated thermocouple well is a Nichrome wire heater (20 ohm) constructed in the laboratory by winding the wire around an asbestos-wrapped stainless steel sleeve and insulating with high temperature ceramic (Ceramacast Inc.). The heater and thermocouple leads are run to a microprocessor-based controller (Omega 4002) and a variable power supply (0-140V, Variac.).

Figure 2.2

To Vacuum Line

Stainless Steel Vessel

Sample Grains in
Copper Insert

Nichrome Heater
Cast in Ceramic

Polished Contact
Surfaces

Glass Wool Insulation

Thermocouple Leads
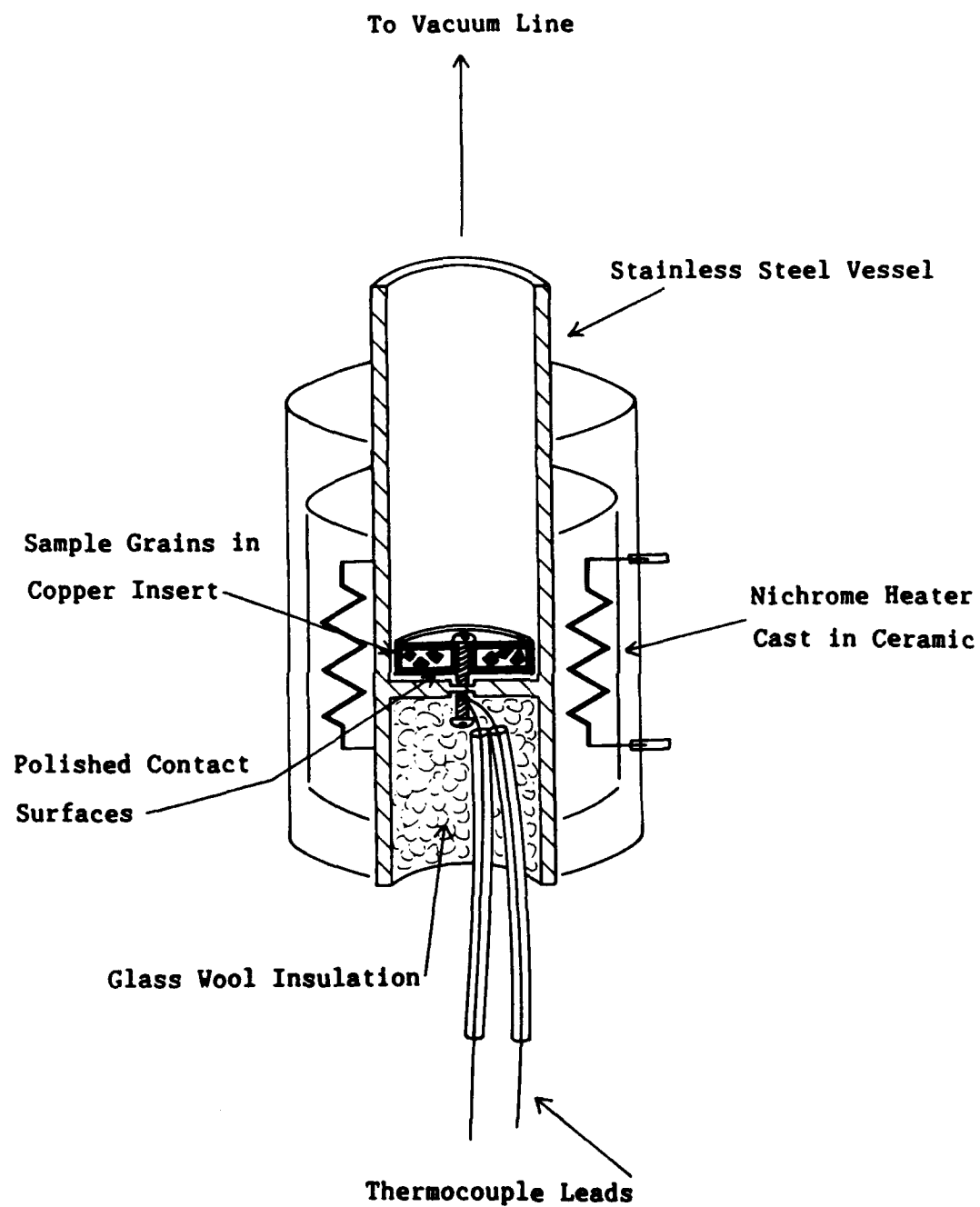
accuracy of better than 3 ^{o}C over this temperature range. The combination of a variable power supply (0-140v AC) and a time-proportional controller (OMEGA model 4002) allowed rapid temperature ramping (50 ^{o}C/min) and precise temperature regulation ($\pm$ 2 ^{o}C) over long periods (days).

2.3.2 Gas processing

The gas processing line used for rock analyses (MS2) has been recently described in detail (figure 2.3; Kurz et al. 1987; Graham, 1987). For this reason the discussion presented here focuses on aspects of gas processing not discussed previously, or which differed from the methods presented earlier. Helium from both the air standard volumes and samples was sequentially exposed to a temperature cycled titanium sponge and SAES^{TM} Zr-Al getter. A small fraction of the sample was then measured for approximate helium content using an on-line quadrupole mass spectrometer. The sample volume was split based on this determination to limit the amount of helium inlet to the mass spectrometer. After splitting, the noble gases were sequentially exposed to a stainless steel frit at 26K and coconut-charcoal chips at less than 15K, which concentrates the gases from the processing line volume and separates heavy noble gases from neon and helium. More than 99.7% of the helium was drawn from the line during this "cryopumping stage". These two species were then separated by warming the low temperature trap to 36+1 K and releasing helium into the mass spectrometer. In general, 10^{-9} to 10^{-8} ccSTP of helium were inlet. After inlet both traps were warmed to 65 K and desorbed gases were pumped away. The cryogenic systems are very similar to those described by Lott and Jenkins (1984).

For the diffusion experiments, the diffusion vessel was constantly exposed to in-line flow-through traps of charcoal at liquid N_2 temperature and Ti sponge at room temperature to remove reactive gases as they were released. The effective emanation volume (vessel and traps) was about 130cc, which guaranteed that helium release from the glass or crystal grains occured into an effectively zero concentration surrounding space. Another difference from standard processing for the

Figure 2.3. Gas Processing Line for Mass Spectrometer 2, designed by
M.D. Kurz and D.E. Lott. LTCT=low temperature cryogenic trap
(charcoal), HTCT=high temperature cryogenic trap (steel frit),
RGA=residual gas analyzer (quadrupole mass spectrometer),
TP=turbomolecular pump, IP=ion pump, RP=rotary pump (figure from Graham,
1987).

Figure 2.3
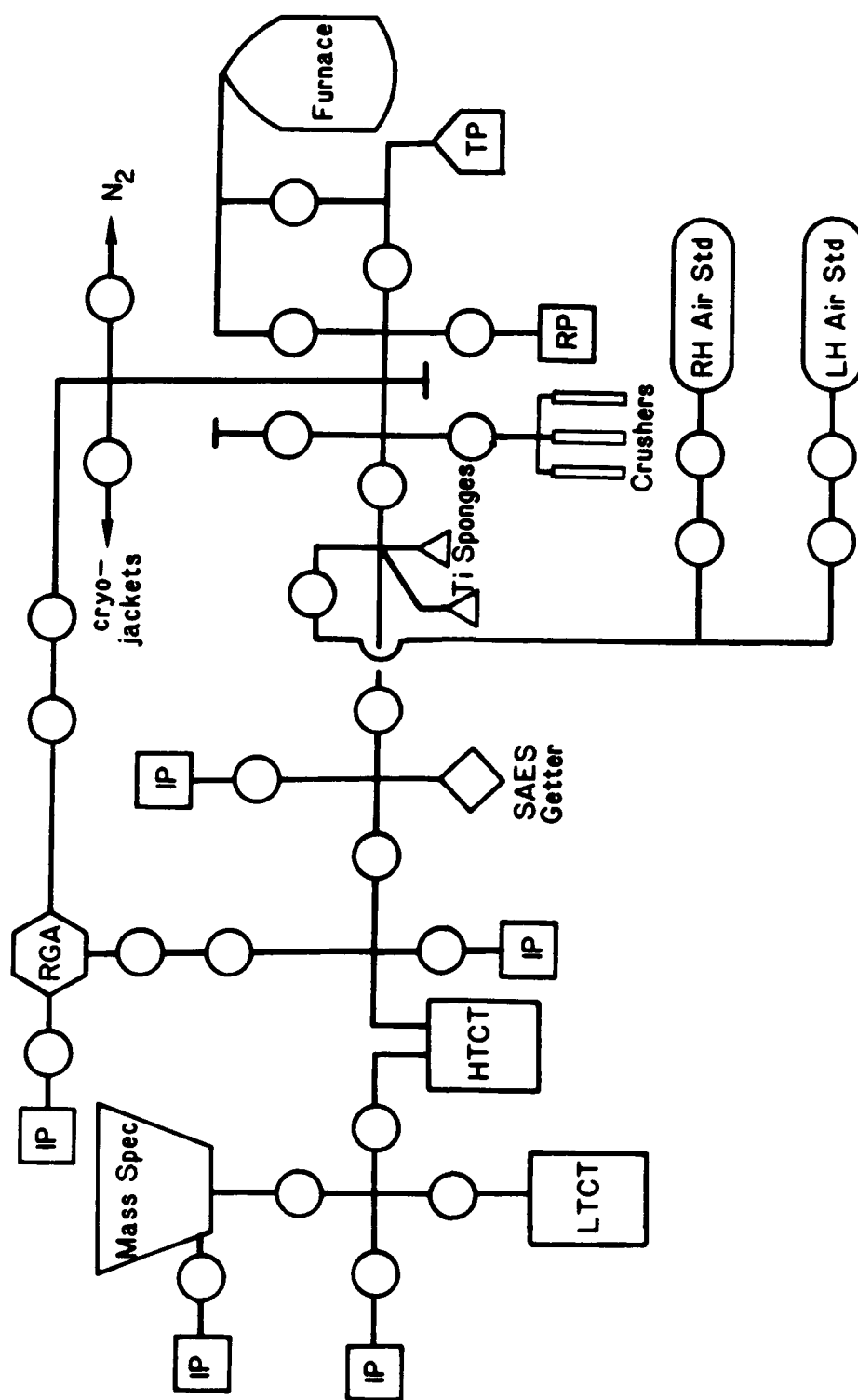
diffusion me surements was that the samples could not be split without losing some of the continuously emanating gas, so relatively large amounts of helium were occasionally inlet to the mass spectrometer.

The entire gas processing operation as well as the mass spectrometry has been automated using solenoid actuated pneumatic valves (thanks to Dr. W.J. Jenkins, Mr. D.E. Lott III and Dr. M.D. Kurz). This is an important aspect of the analysis because automation allows highly reproducible run conditions, including expansion, cryopumping, and inlet times; as well as pumping times between samples. Gas processing and analysis follows an approximately 30 minute cycle, with two samples being processed at any time, one in the mass spectrometer, the other in the processing line. Computer control is via a PDP11/23, recently upgraded from the previous 11/03 CPU to allow the use of multitasking software (TSX-Plus version 6.31; S&H computer systems, Inc.).

Gas processing and mass spectrometry are controlled by different software jobs (Fortran 77) which run at different priorities, providing uninterrupted servicing of analysis routines (program RATIO5), while allowing the computer to be used for real time data analysis. The gas processing program (SMPLR5) was specifically tailored for the diffusion experiments. Data is recorded on a hard disk and on paper, and is automatically backed up to floppy disks every 24 hours. The dedicated PDP11 computer is networked to a central computer for the laboratory (a PDP11 173). This connection provides access to graphics routines, plotters, laser printers, other computers and communication lines. Modem access to the mass spectrometer at all hours greatly relieved the machine-side duties required during the long duration diffusion experiments. Data transfer to a SUN 3/260 computer made the computationally intensive diffusion coefficient determinations possible.

2.3.3 Mass spectrometry

The mass spectrometer dedicated to rock analyses (MS2) has a 10 inch radius, 90° sector electromagnet and an all metal branched flight-tube. The source is a modified Nier design with a half-circle filament, and a source electromagnet outside the vacuum, to extend the electrons'

flight paths through the ionizing chamber. A faraday cup is used to measure ^{4}He with a resolution of 1:230 and a electron-multiplier (JLI model MM-2) operated in analog mode with its entrance slit set to a resolution of 625 to separate ^{3}He from the much larger HD-H$_3$ peak. The instrument has been described before (Kurz, 1982; Graham, 1987) and is of the general design outlined by Jenkins (1974) and Clarke et al (1976). It was constructed in the Woods Hole laboratory. Measurement of the ion beams is done under computer control. Peak-switching is done by adjusting the accelerating voltage rather than the magnetic field strength. After sample inlet (duration 30 seconds), the machine is centered on the HD peak, and then offset to ^{3}He. The ^{3}He peak height (56 second integration) and baseline (14 second integration) are measured in 15 voltage switching cycles. During each on-peak cycle ^{4}He is also measured, but the ^{4}He baseline is measured only once (25 second integration) prior to inlet of the sample, because secondary electrons from the large ^{4}He ion beam lead to incorrect baseline estimates. Baseline corrections are done for each cycle, using the mean of adjacent baseline measurements for ^{3}He and the initial baseline determination for ^{4}He.

Because both depletion and "grow-in" of background occur during the static analysis, the sequential peak determinations (and their ratio at each cycle) are fit to a linear trend and extrapolated to the time of sample inlet to obtain the peak heights prior to depletion. The ratios determined at each cycle display a more linear time dependence than the individual peaks, so the extrapolated ratio is a more reliable determination of the isotopic ratio of a sample than the ratio of individually extrapolated ^{3}He and ^{4}He peaks. The extrapolated ratio is then combined with the extrapolated ^{4}He contents to obtain the best determination of the ^{3}He contents. For a wide range of ^{3}He/^{4}He ratios, this ^{3}He estimate is found to be within the uncertainty (associated with linear regression) of the directly extrapolated ^{3}He peak value, but with smaller uncertainties (by 20 to 50%).

The mass spectrometer is capable of detecting small amounts of helium and in practice is limited by the ability to reduce the atmospheric background, or processing blank, rather than absolute

sensitivity. Detection limits (estimated as twice the uncertainty in the determination of line blanks) are 5×10^{-12} ccSTP ^{4}He and about 3×10^{-16} ccSTP ^{3}He. Under normal run conditions, the processing blanks range as follows, with uncertainties at any time of 10% or so: $2-3 \times 10^{-11}$ ccSTP He for the "dry" section of the line (that is the mass spectrometer, inlet line and cryotraps), and $3-5 \times 10^{-11}$ ccSTP He including the "wet" line (getters, quadrupole inlet line, crushers and/or furnace). It is not possible to precisely determine the isotopic composition of individual processing blanks, but their daily and longer term average has an atmospheric ^{3}He/^{4}He ratio. This isotopic composition and the increased blank associated with increased line sections is consistent with the blank being caused by very small leaks of atmospheric gases into the line at VCR^{TM} and Mini-Conflat^{TM} connections. In this regard, replacing VCR fittings with Mini-Conflats in the crusher manifold section reduced the processing blank from $5-6 \times 10^{-11}$ to $3-4 \times 10^{-11}$ ccSTP He. There are additional backgrounds associated with long term closures of both the diffusion vessel (owing to several VCR connections) and the furnace when the Varian 5/8" diameter sapphire viewing port is used, of $8\pm1 \times 10^{-16}$ cc/s and $1.5\pm1 \times 10^{-16}$ cc/s respectively, both with atmospheric isotopic composition.

Calibration of both sample size and isotopic composition is by comparison to air aliquots. An aliquot of approximately 1.6×10^{-8} ccSTP He with atmospheric isotopic composition is automatically analyzed repeatedly throughout the day (usually 15-25 times) and is alternated with blank, sample, and other size air aliquot determinations. The size and ratio of this daily air standard may vary by a few percent during a 24 hour period (primarily due to changes in filament characteristics), so temporal trends are examined and used to calibrate sample determinations based on when they were run.

The dependence of apparent isotopic composition on sample size is examined on a roughly monthly basis from accumulated determinations on air standards of different sizes, or whenever instrumental modifications are made, or failures occur. In contrast to the strong dependence of ^{3}He/^{4}He ratio on size observed in large samples (10^{-7} to 10^{-6} ccSTP He) by Kurz (1982), no size effect is detectable in the much smaller sample

range now used (generally less than a few times 10^{-8}ccSTP; figure 2.4). However, on the order of 3% decrease in the ^{3}He/^{4}He ratio with increasing size was found for samples larger than 10^{-7} cc STP (figure 2.5).

A few diffusion experiment releases were this large (and could not be readily split) and have been corrected for this "linearity" effect. Possible "memory" effects for these large samples were explored by examining the size and isotopic composition of adjacent air standards and processing blanks, and were found to be unimportant. The uncertainties reported for the ^{4}He contents and ^{3}He/^{4}He ratios were derived from the statistical errors of measuring the ion beams and extrapolating to time of inlet combined with uncertainties propagated through the standard calibration, blank subtraction and linearity correction equations. Typical one sigma errors for a sample of 10^{-8}ccSTP He with a ^{3}He/^{4}He ratio of 1.2 x 10^{-5} (8.4 Ra, typical of MORB) are .1% on the size and 1% on the ratio.

Primary air standards are taken in a stainless-steel canister (about 40 ml) with copper stem-tipped stainless steel bellows valve. Its volume has been calibrated by weighing before and after filling with water and more recently by measuring the N_2 content of the canister with a quadropole mass spectrometer. These determinations are in good agreement and provide a calibration volume precision of .05%. The air standard volume is corrected to standard temperature and pressure (including humidity) using values measured at the collection site, which is located well away from laboratory influences (Chemotaxis beach, Quissett Campus).

The air standard is then exposed to a charcoal trap at liquid N_2 temperature to remove argon, H_2O, CO_2, O_2, etc. and expanded into a 10 L reservoir. Standard aliquots are taken from the reservoir during automated running for use in size and isotopic ratio calibration. The standard aliquot volumes were calibrated by comparison with a mercury calibrated glass volume using ^{4}He peak height measurements. Two of these large reservoirs with separate aliquotting valves are used to allow cross-calibration between old and new air standards. The number of aliquots removed from each tank since its most recent filling is used

Figure 2.4. Relationship between sample size and measured ratio for typical sample sizes (data from July, 1987). Samples used are splits of the air standard, obtained by isolating different sections of the processing line prior to cryotrapping helium. Errors in measuring small samples increase because of ion-counting statistics. There is no evidence for any dependence of the observed ^{3}He/^{4}He ratio on size in this range. This data is typical of normal running conditions.

Figure 2.4
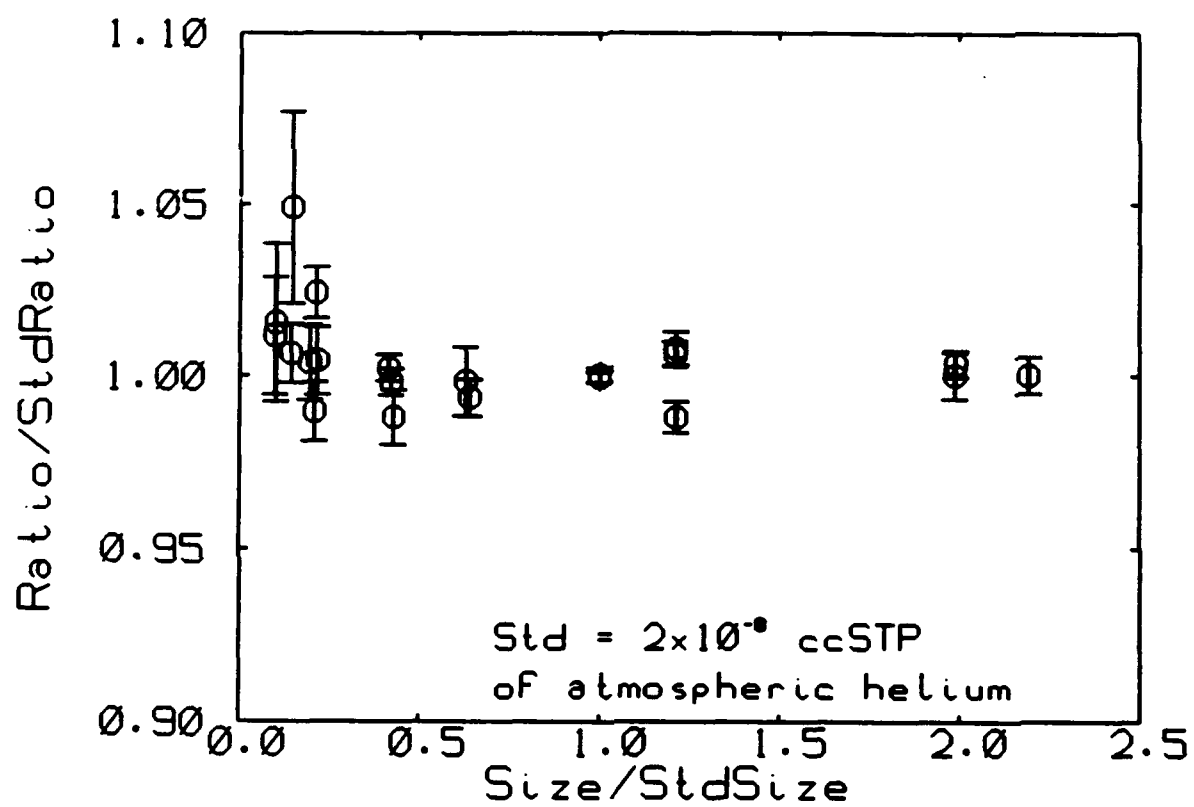
Figure 2.4

Figure 2.5. "Linearity" relationship for very large samples (data from August, 1987). In contrast to smaller samples, the apparent ^{3}He/^{4}He ratio varies with size for samples greater than about 8 x 10^{-9} ccSTP, decreasing by 3% or so over the range of 2 x10^{-8} to 2 x 10^{-7} ccSTP (the large size data points were determined twice each, and the mean is shown).

Figure 2.5

Figure 2.5
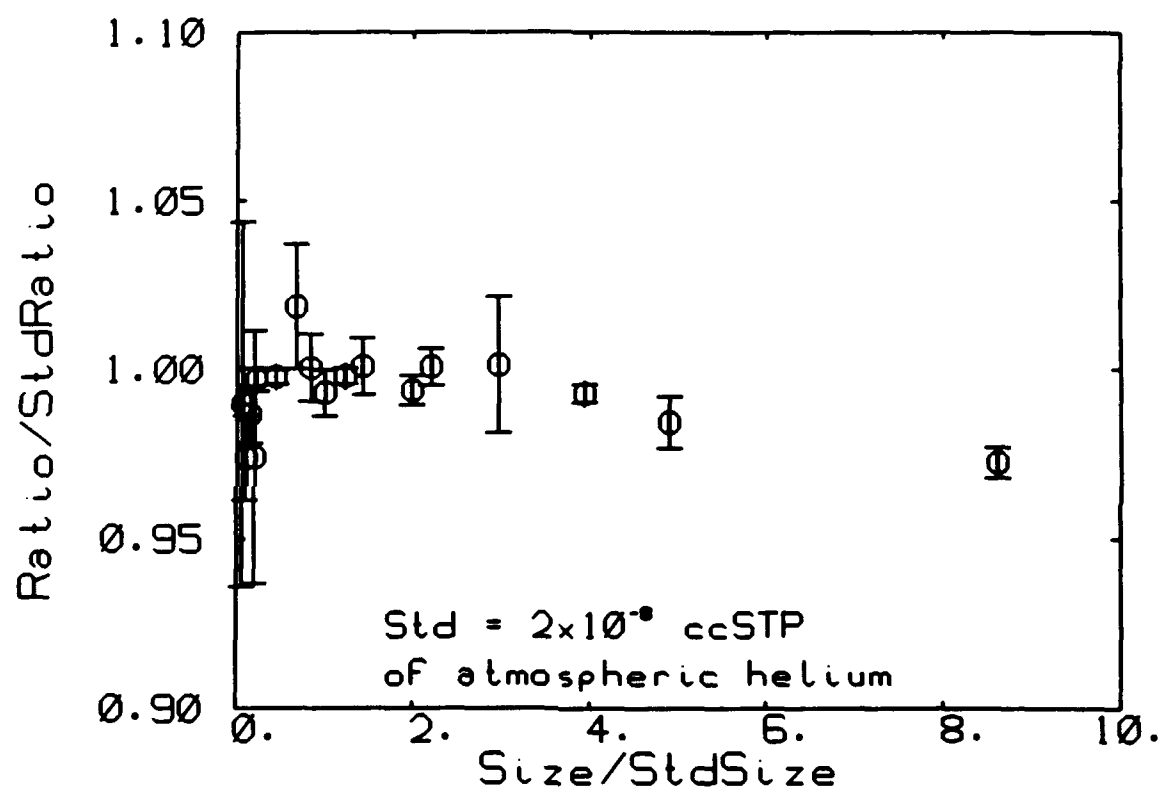
in correcting each standard's size for depletion. Overall, the
precisions involved in calibrating the standard volume, aliquotting
volumes, reservoir volumes, and expansion line volumes suggest an
uncertainty of less than <.5% in the absolute size of the air standards.
This uncertainty is much smaller than errors associated with sample
analyses

2.4 THE DETERMINATION OF DIFFUSION COEFFICIENTS FROM EMANATION DATA

2.4.1 Assumptions and associated errors of the standard spherical model

Emanation experiments measure the rate of release of a gas from a
condensed phase, in this case a collection of solid particles. The
release may occur by one or more mechanisms and may be controlled by
processes that occur within the solid, at its surface, or in the
surrounding medium. In order to use emanation data to characterize
transport of the gas within the solid, it is neccesary to establish the
physical nature of the release. This generally requires knowledge of
the physical properties of the solid, diffusing gas, surrounding medium,
and experimental setup, but to some degree the systematics of the
measured release (for instance its time dependence) can distinguish
different release processes. In these experiments, we desired to
determine the rate of volume diffusion of helium isotopes within
silicate glasses and minerals. In order to do this it was necessary to
establish that helium release was governed by volume diffusion within
the solid and not by processes such as diffusion along cracks, leaks
from vesicles, surface desorption, or passage through a surface layer on
the particles. This was done by comparing the time and temperature
dependence of release from different grain sizes and from samples with
and without vesicles over large extents of fractional release, as
discussed in Chapter 3.

Volume diffusion, or diffusion in a locally isotropic medium,
provides the fundamental hypothesis that the rate of transfer of a

diffusing substance through a section is proportional to the
concentration gradient normal to the section. This is Fick's first law:

$$F = -D dC/dx \qquad (2.1)$$

where x is measured normal to the section (e.g. Crank, 1975). This
equation is the basis of the determination of diffusion coefficients in
steady-state experiments. Conservation of the diffusing substance leads
to the diffusion equation:

$$dC/dt = - \text{div}[D \, \text{grad}(C)] \qquad (2.2)$$

which expresses the temporal change in concentration in terms of the
spatial variations in both C and D that drive diffusive fluxes and
allows the determination of diffusion coefficients in time dependent
situations. Both equations 2.1 and 2.2 can be derived from the vantage
of statistical mechanics by envisioning a random walk with
characteristic step length and frequency (Einstein, 1905).

If D is independent of concentration and does not vary with
location in the material of interest then equation 2.2 reduces to:

$$dC/dt = - D \, \text{div}^2[C] \qquad (2.3)$$

When D varies with time, as in a step-heating experiment, solutions to
this equation yield diffusivities defined by the mean value theorem,
that is D becomes

$$D = 1/(t - t_0) \int_{t_0}^{t} D(t)dt \qquad (2.4)$$

For diffusion of a trace component such as helium in an isotropic
material like basaltic glass the assumption that D varies only with time
and temperature is extremely reasonable. In addition, since fast-
diffusing helium is a neutral species and interacts only minimally with
other atoms its diffusivity will not be coupled to other species by

electroneutrality or mutual diffusion conditions so that a tracer diffusion coefficient may be directly obtained.

Evaluating equation 2.3 requires a description of the spatial nature of the system. Spherical geometry provides a useful limiting case because this is the shape with the lowest surface to volume ratio, the property which controls the rate of emanation for low extents of releases. For a sphere, considering only radial diffusion, equation 2.3 becomes:

$$dC/dt = D\{d^2C/dr^2 + 2/r(dC/dr)\} \tag{2.5}$$

where D is defined by equation 2.4. The initial condition is given by the concentration profile , $C(r)$ at time zero, and loss from the grain can be described by either evaporation or constant surface concentration boundary conditions.

For evaporation: the flux from the surface is proportional to the concentration difference at the boundary:

$$-D \cdot dC/dr = h(C_s - C_o) \tag{2.6a}$$

where C_s is the concentration just inside the sphere, C_o is the concentration in the surrounding medium, and h is a proportionality constant, essentially determined by the impedence to evaporation into the medium. As h increases, C_s and C_o tend to approach each other and for the limit of h=infinity the evaporation condition is equivalent to the constant surface concentration boundary condition:

$$C_s = C_o \tag{2.6b}$$

In the helium emanation experiments, the greatest impedence to helium loss is likely to occur within the solid rather than at the surface (i.e. h is very large because there is little resistance to release of a helium atom from the surface to the surrounding medium) so that 2.6b is a reasonable boundary condition. In addition, the diffusion vessel was designed so that the helium concentration in the space

surrounding the grains was always negligible so that C_o can be taken as zero (the vessel volume was about 130 cc, and less than 10^{-6} cc He were present in any sample volume of about 1 cc). Together with the initial distribution $C_i(r)$ this leads to the solution, for a sphere of radius a :

$$C(t) = \sum_1^\infty A_n \exp(-n^2\pi^2/a^2 \, Dt) \tag{2.7}$$

with:

$$A_n = 6/a^3 \int_0^a \left(\int_0^a r \, C_i(r) \sin(n\pi r/a) \, dr \right) r/a \, \sin(n\pi r/a) dr \tag{2.8}$$

Provided the initial helium distribution is known, this solution gives the fractional loss as a function of time, which is the relation needed to obtain diffusivities from emanation data. For $C_i(r)$ constant, equations 2.7 and 2.8 yield:

$$F = 1 - 6/\pi^2 \sum_1^\infty 1/n^2 \exp(-n^2\pi^2/a^2 \, Dt) \tag{2.9}$$

where F is the fraction released. This equation reveals that loss is governed by the ratio D/a^2 for a sphere, and is a frequent starting point for analyses of emanation data. However, helium distributions in natural minerals and glasses can differ from homogeneity for two fundamental reasons, the grains may have formed with heterogeneous distributions, or the helium content of the grains may have evolved away from an initial constant concentration profile.

Vesicles and fluid inclusions contain large fractions of the total helium in some of the basaltic glasses studied in chapter 3, and in the olivine and pyroxene mineral grains studied in chapter 4. Thus, a homogeneous initial distribution is clearly an approximation, but will be a reasonable one provided the vesicles and inclusions are small in comparison to grain sizes and the rate-limiting step for loss is passage through the glass or mineral volume. Emanation rates for glasses with approximately 1% and 50% vesicle helium contents were very similar

(chapter 3), suggesting the approximation is reasonable for these samples, and that dissolution at the gas-solid interface is not a rate-limiting process.

In the mineral studies, 50 to 90% of the helium was contained in the fluid inclusions, which tended to be aligned in planar arrays. It is possible this geometry enhances loss, so that derived diffusivities may be upper limits (chapter 4). If helium loss were dominated by passage from a large vesicle or inclusion through a surrounding glass or mineral "membrane", the release behavior would differ from volume diffusion. Initial releases of helium permeating the membrane would increase with time, and steady-state loss would display a constant release rate, rather than the linear in $t^{1/2}$ behavior of volume diffusion (see below). In addition, the initial "transient permeation" of the solid by the vesicle helium can greatly enhance isotopic fractionation (Rama and Hart, 1965). These characteristics were not observed (chapter 4), suggesting the release process and helium distributions were more akin to volume diffusion and an approximately homogeneous initial condition.

Heterogeneous radiogenic helium distributions may be generated by variations in parent uranium and thorium contents, which are known to primarily reside in fine-grained accessory minerals in basaltic minerals (Polve, 1985). However, in glasses (as studied in chapter 3) these elements, and thus radiogenic helium (^{*4}He), are likely to be isotropically distributed. Cosmogenic helium (^{3}He$_c$) distributions in the rocks studied here should also be homogeneous, because the dominant production mechanism is spallation of major elements (chapter 5). However, in some situations, secondary production through reactions on lithium could lead to ^{3}He$_c$ heterogeneities. The energies associated with ^{*4}He and ^{3}He$_c$ generation may also redistribute these atoms, however, as discussed in chapter 5, most rocks will not be strongly affected by this process, because ejection losses will generally be balanced by injection gains. Exceptions would be rocks with dramatically varying parent nuclide compositions. Recoil related redistribution problems have been recognized in ^{40}Ar studies (e.g.

Hunecke, 1976) but are unlikely to significantly affect the results presented here.

The most important departure from homogeneous distribution is the occurrence of prior diffusive loss. This can lead to large errors in diffusivity estimates, if unaccounted for. In particular, D values will be highly underestimated at low fractional losses, because initial release rates are much lower for a grain which has already depleted its near surface helium contents. At higher F, both distributions will suggest similar diffusivities. This can be seen by approximating the series in equation 2.9 by its first term at high F (Huneke, 1976):

$$C(t) = A_1 \cdot \exp(-1^2 \pi^2/a^2 \; Dt) \qquad (2.10)$$

which after taking logarithms and differentiating yields, (because A_1 is independent of t):

$$d \; (\ln C(t))/dt = 1/C(t) \; dC(t)/dt = -\pi^2 \; D/a^2 \qquad (2.11)$$

This equation shows that the fractional release rate dC/C at high F (long time) depends only on D and a and not the initial distribution, even though the amount of helium remaining is a function of the initial distribution (equation 2.10). Thus, diffusivities obtained at sufficiently high F will be unaffected by problems associated with unknown initial conditions. Numerical simulations of prior loss effects on apparent diffusivities confirm this behavior, and reveal that D values can be underestimated by more than an order of magnitude at low F, even for relatively small prior losses (figure 2.6). D values approach the correct diffusivity at F values greater than approximately twice the prior loss amount. The numerical experiments also revealed that diffusive prior loss does not have a large effect on the determination of isotopic diffusivity ratios, essentially because both isotopes have similar initial profiles.

In the glass experiments (chapter 3), prior loss problems were minimized by preparing glass grains from the center of large pieces, but in experiments with fine powders helium was lost between preparation and

60

Figure 2.6. Effect of prior diffusive loss on apparent diffusivities. Curves derived by discarding successive amounts of synthetic release data (spherical model with homogeneous initial condititon, 2% release intervals and log D = -15) and processing the remaining release data (F versus time) as if it constituted the entire helium content. Prior loss leads to apparent diffusion coefficients that are strongly underestimated at low F, but which trend toward correct values at high F. This is because helium is initially lost far more slowly from a grain with a smooth, diffusive profile than one with an initially discontinuous (step) profile at the grain surface, yet loss is similar at high F once both grains have established diffusive profiles. Prior diffusive loss produces only small errors in estimating isotopic diffusivity ratios, and as with absolute diffusivities, only at low F.. For a true D^3He/D^4He ratio of 1.08 the apparent ratio at low F is 1.081 for 2% loss, 1.082 at 5%, 1.084 at 10% and 1.089 at 20% loss.

Figure 2.6
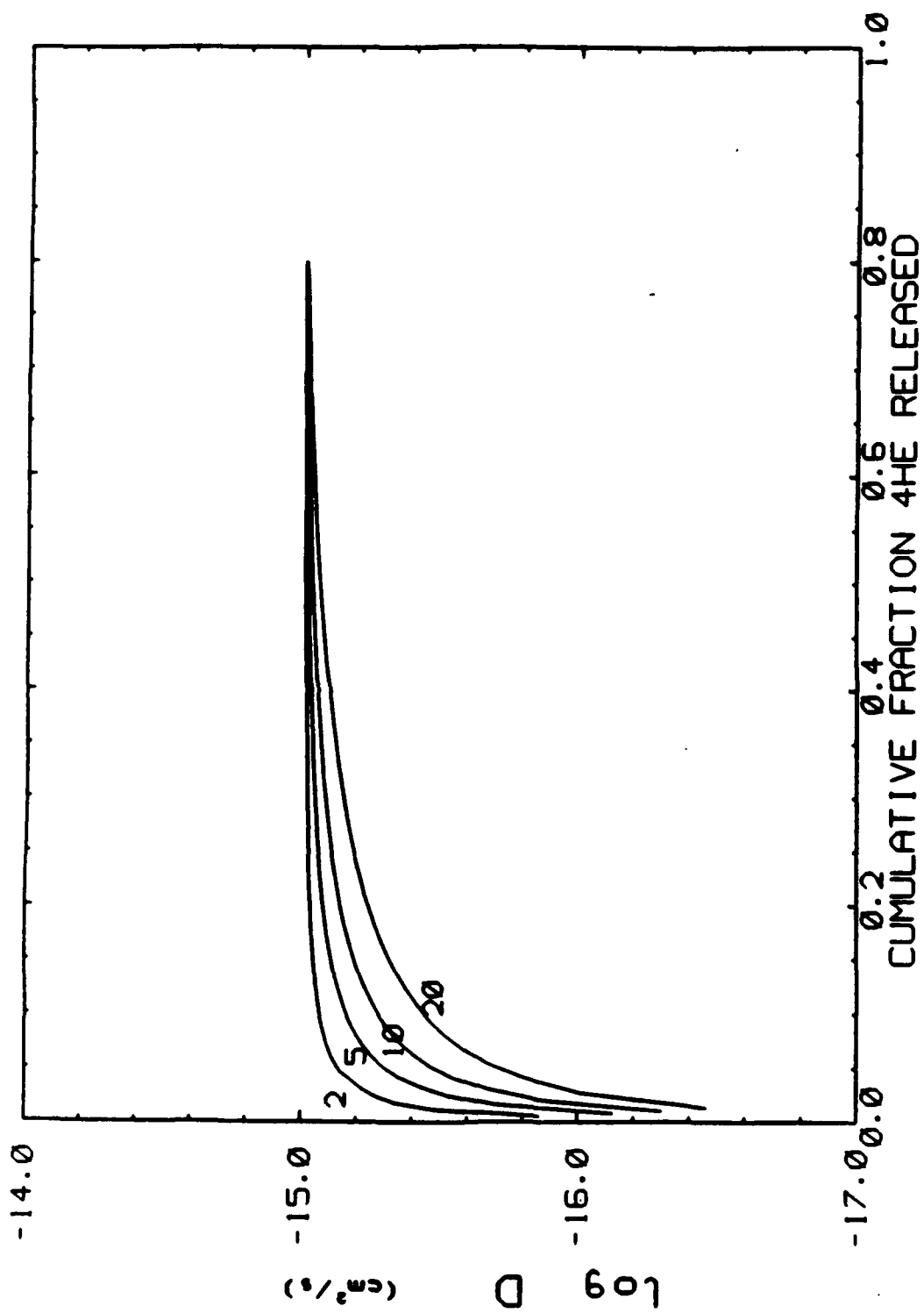
analysis. This problem was easily recognized by increasing trends of D versus F at constant temperature which did not continue at high F. As discussed in chapter 3, prior loss problems can be corrected for, either by comparison of the D versus F trends to figure 2.6, or more directly when emanation data is obtained at the temperature at which prior loss is likely to have occured. When the extent of prior loss can not be readily determined, D estimates at higher F are more reliable than those at lower F, especially if an assymptotic trend can be verified (e.g. data for helium diffusion in olivine, chapter 4). This is one important instance of the advantage of multiple aliquot experiments; release systematics can be used to identify potential errors in estimating diffusivities.

Equation 2.9 is rarely used to obtain diffusion coefficients because it converges slowly at low F and requires an iterative solution. However, approximation equations have been developed which give diffusion coefficients directly from sequential release data for spherical geometry (Inthoff and Ziemen, 1956; Fechtig and Kalbitzer, 1966,):

$$\text{for } F < .1 \ : \quad D_i = \pi a^2/36/(t_i - t_{i-1})\ (F_i^2 - F_{i-1}^2) \qquad (2.12a)$$

$$\text{for } .1 < F < .9 \ : \quad D_i = a^2/\pi^2/(t_i - t_{i-1}) \qquad (2.12b)$$

$$X\ \left[-\pi^2/3\ (F_i - F_{i-1})\ -\ 2\pi\left\{(1-\pi/3\ F_i)^{1/2} - (1-\pi/3\ F_{i-1})^{1/2}\right\}\right]$$

$$\text{for } F > .9 \ : \quad D_i = a^2/\pi^2/(t_i - t_{i-1})\ \ln\ \{(1-F_{i-1})/(1-F_i)\} \qquad (2.12c)$$

These approximations have small numerical errors when compared to the full series solution for a sphere (figure 2.7). The first equation readily shows the proportionality between F and $(Dt)^{1/2}$ expected for

Figure 2.7. Apparent diffusivities obtained by processing exact emanation data for diffusive loss ($D = 10^{-10}$) from a sphere (with homogeneous initial distribution, equation 2.9) with approximation equations 2.12a (+), 2.12b (o) and 2.12c (▼). The approximations yield numerically accurate D estimates, provided they are used over limited ranges of F. Approximation 2.12a progressively underestimates D. Approximation 2.12b is accurate below F of about .9, at which point 2.12c is better until very high F. Typical analytical uncertainties are shown, and dominate the numerical errors.

Figure 2.7
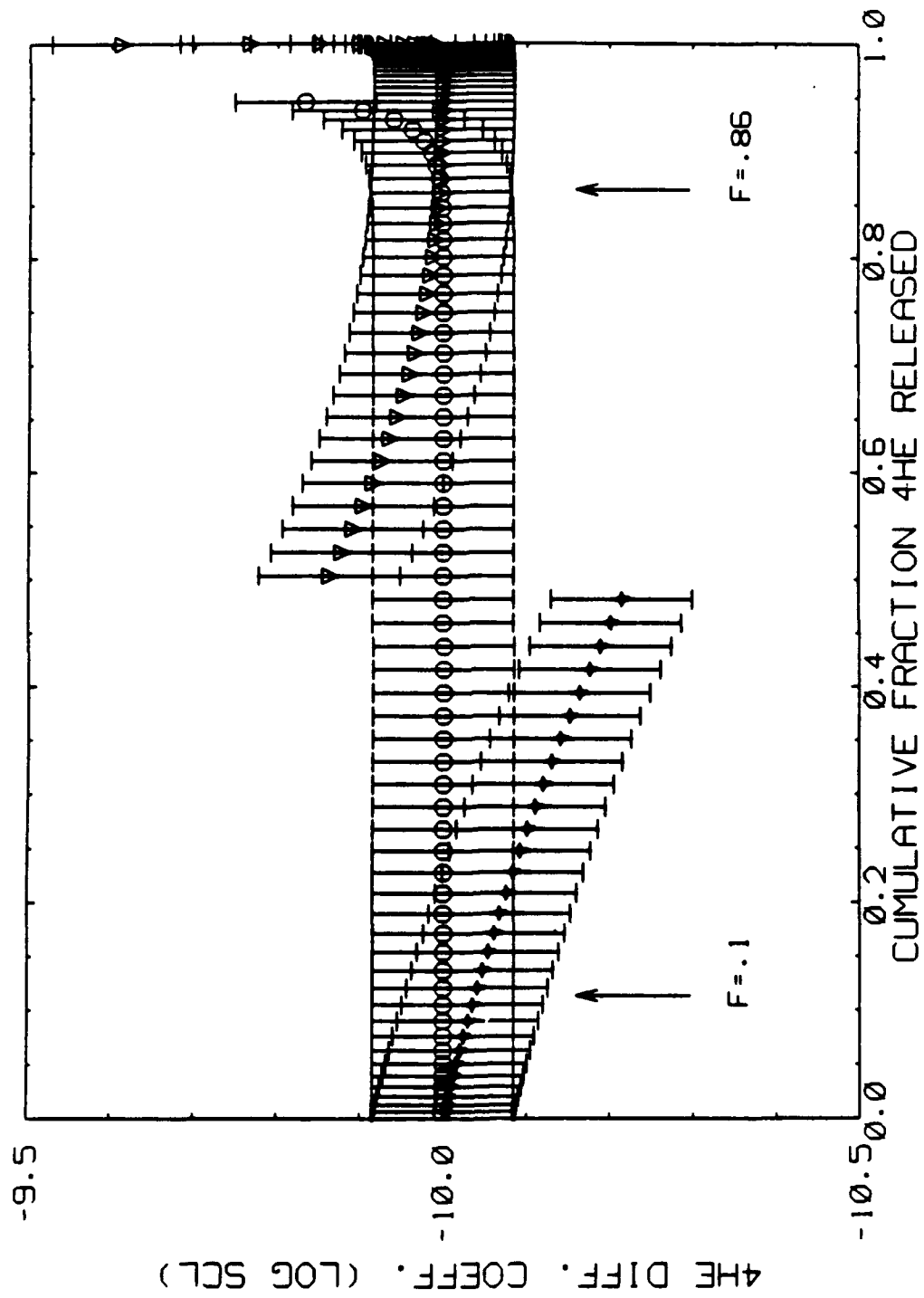
volume diffusion at low F. This expression can be written more
generally for all geometries at low F as:

$$F_i = 2/\sqrt{\pi} \ S/V \ \sqrt{Dt} \qquad\qquad (2.12a')$$

where S/V is the surface to volume ratio (Inthoff and Zimen, 1956).
Thus, the slope of a plot of F versus $t^{1/2}$ can be used to determine D at
low F.

However, use of these approximations (or the full series solution
for a sphere) for grains of varying sizes and shapes can produce
diffusivity estimates that are in considerable error. These errors are
of two types which usually occur together, 1) apparent diffusivities may
be offset from true values, and 2) false variations of D with F can be
induced. Shape errors are generally smaller than those from size
distribution, and fall primarily into the first type. Figure 2.8 shows
apparent diffusivities calculated with the spherical approximations for
emanation data from right prisms, including a cube and both plate and
bar shapes. Apparent D values decrease approximately linearly with
increasing F, but do not vary by more than a factor of two.
Nonetheless, this can have a significant effect on the determination of
activation energies. For example, accounting for the roughly cubic
shape of a single basaltic glass chip suggests an activation energy 4%
higher than obtained with the spherical equations, a difference roughly
twice analytical errors (chapter 3). Because most shapes exhibit
relatively high releases at low F in comparison to spheres which have
minimal surface to volume ratios, fractional releases at high F are
correspondingly small and activation energies determined with the
spherical model must be considered lower limits.

Shape variations may produce much larger offset errors (up to an
order of magnitude), depending on the "effective" radius chosen for the
grain (figure 2.8). For basaltic glasses, which tend to fracture into
rough prisms or plates, typical square-holed sieves tend to select
grains with two similar short sides and a range of long side lengths
(chapter 3). These bar shapes lead to overestimated D values when the
spherical routines are used and the sieve size is chosen as the

Figure 2.8. Effect of shape variations on apparent diffusivities. The solid lines show diffusivities calculated from synthetic fractional release data (generated using equation 2.14) for several different parellelpipeds, using the approximation equations for a sphere. The dotted horizontal lines simply provide a reference to make the slopes of the solid lines more visible. Note that using the spherical model can result in large offsets in apparent diffusivities from the correct value of 1×10^{-9} cm^2/s used to generate the fractional release data, as well as apparent decreases in diffusivities with increasing gas loss of up to a factor of 2. This means that both absolute D estimates and activation energies can be in error when grain shapes are not appropriately represented in diffusion calculations. However, as with prior losses, errors in determining the isotopic diffusivity ratio are small, the shapes with the steepest D versus F curves lead to underestimates of D^{3}He/D^{4}He of only .4 to .5%. The shapes corresponding to curves 1 to 5 are parallepipeds with side lengths as follows:

Shape	Side lengths			"Spherical radius"
1	1	.25	.25	1
2	1	.5	.5	1
3	1	1	1	1
4	1	1.45	1.45	1
5	1	2	2	1

Figure 2.8
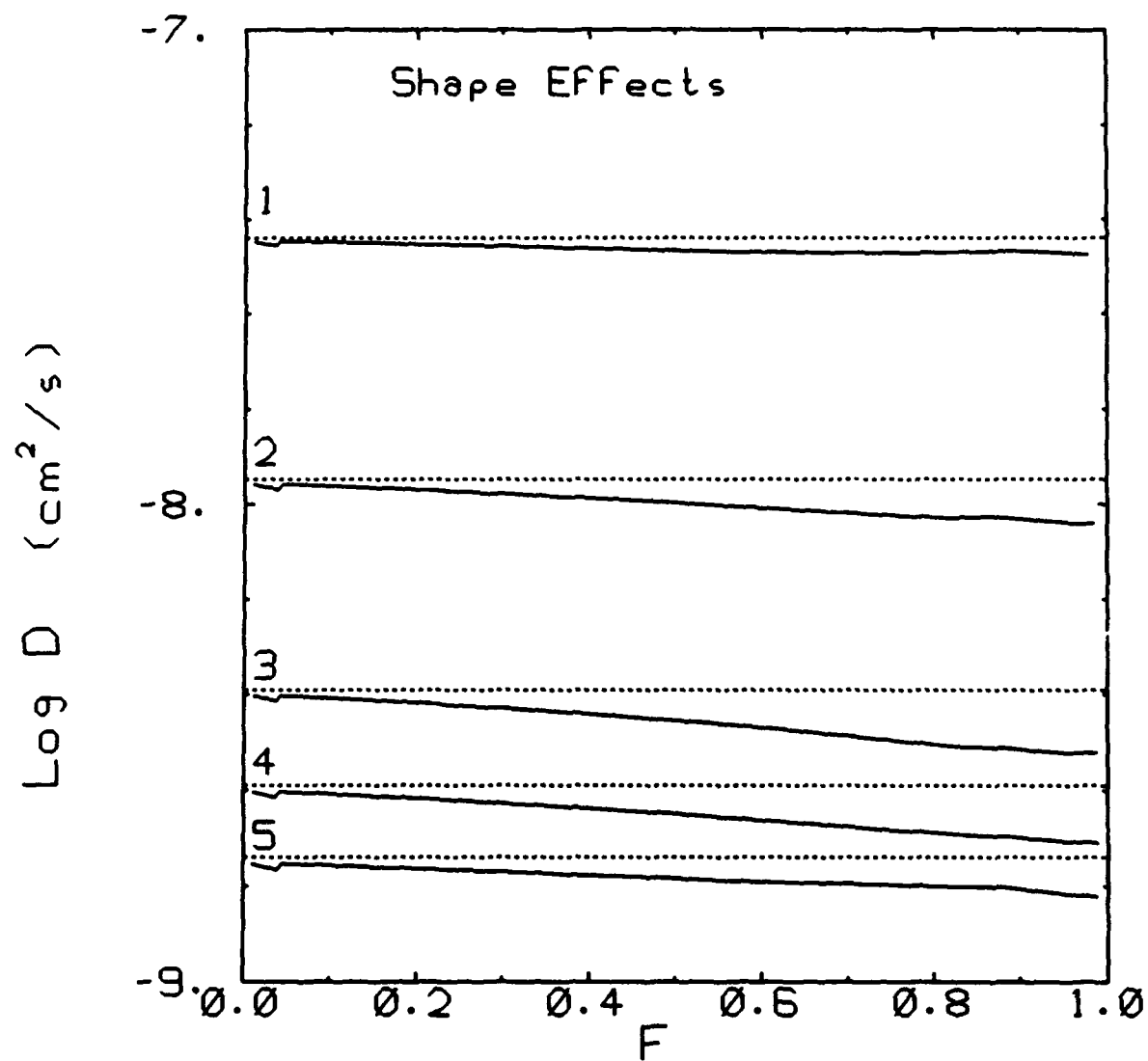
effective diameter (e.g. a factor of 4 overestimate for a cube, figure 2.8). Because both isotopes experience the same release geometry, shape errors are not a significant problem in determining isotopic diffusivity ratios. Jagged-edged and porous geometries produce release patterns that are roughly similar to those for a collection of many small and one large particle, and many small particles, respectively.

Size variations in grain assemblies produce offset errors in apparent diffusivities for the same reasons that shape errors do - it is difficult to assign an effective spherical radius. However, size distribution can lead to much larger decreases in D values at high F. This occurs because the larger grains lose their helium far more slowly (loss scales with a^2) and because relatively few grains contribute helium after smaller grains have released all their gas. Thus, D values at high F can be underestimated well beyond that expected from the overall range in sizes, because it is the helium mass distribution that controls emanation rates and not just the spread in grain size. Gallager (1965) has discussed this problem for log normal size distributions and developed correction equations for this specific distribution. More generally, Shaked (1965) pointed out that this effect becomes important at F values that correspond to large releases for the smallest particles which contain significant fractions of the total helium.

Numerical experiments with several simple distributions reveal that errors in relative diffusivities increase with F, particularly above F of .8 to .9 (figure 2.9). The presence of a single large grain in an otherwise tightly clustered sample produces particularly large errors. As for shapes, not accounting for size distributions will lead to underestimated activation energies. This problem can be identified by decreasing D values in multiple release experiments at high F, and can be minimized by avoiding data collection at high F when possible. In contrast to shape errors, grain size distribution does have significant effects on the determination of isotopic diffusivity ratios, as shown in figure 2.10. This figure also demonstrates that helium release from a rock or mineral sample with a wide range of grain sizes can mimic the presence of components with different diffusivities and isotopic

Figure 2.9. Effects of grain size distributions on apparent
diffusivities. Note scale changes between top and bottom figures! The
curves were obtained by processing synthetic release data for
$D=10^{-9} cm^2/s$ with the spherical approximation equations. The slope
breaks at fractional releases (F) of .04 and .86 are the result of
changing approximation equations. Distributions 1-5 and A were
calculated using 7 spherical grain sizes with radii ranging from .7 to
1.3 cm as follows: .7, .8, .9, 1., 1.1, 1.2, 1.3, with grain
distributions among these bins of:

Curve	Distribution Type	Bins:
1	Normal (approx.)	1 2 5 8 5 2 1
2	Single grain	1
3	Decreasing	7 6 5 4 3 2 1
4	Uniform	1 1 1 1 1 1 1
5	Increasing	1 2 3 4 5 6 7
A	Flyer	100 0 0 0 0 0 1
B	High Flyer	100 parallepipeds with side lengths of 1,.5,.5 and one parallelpiped with side lengths of 4,2,2.

Curve B combines the effects of size and shape variations.

Figure 2.9
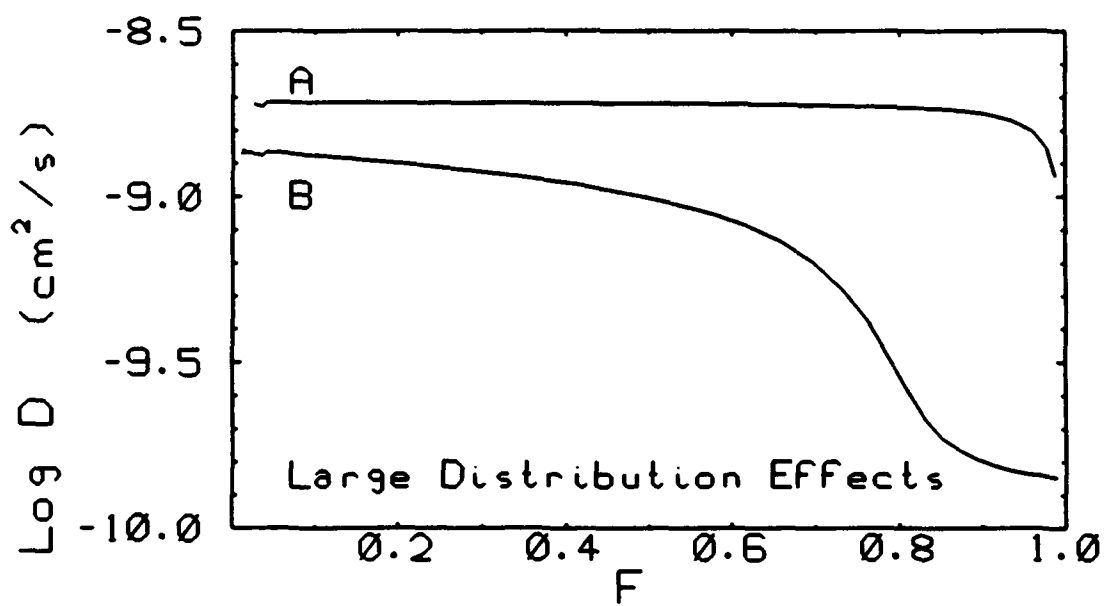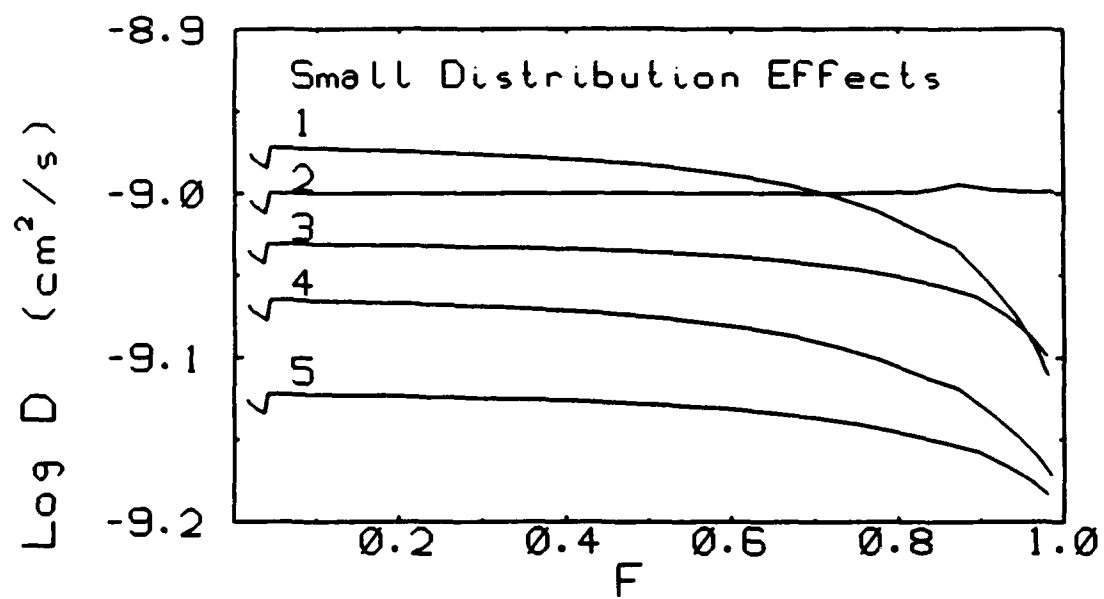
Figure 2.10. Isotopic effects of grain size distribution. The top plot shows the variation of ^{3}He/^{4}He ratios of released gas aliquots as a function of increasing fractional loss. Only the extreme distribution (B, see caption figure 8) is noticeably different than for a single grain. The dotted line references the bulk composition. However, the small differences in relative release of the two isotopes have large effects when a spherical model is used to obtain the apparent isotopic diffusivity ratio, D^3He/D^4He, as shown in the bottom plot. D^3He/D^4He values are underestimated at high F for all distributions, with large errors for distributions A and B. The dotted reference line shows the correct diffusivity ratio (1.08) used to generate the emantion data. The breaks in slope in the lines reflect changing between different spherical approximation equations.

Figure 2.10
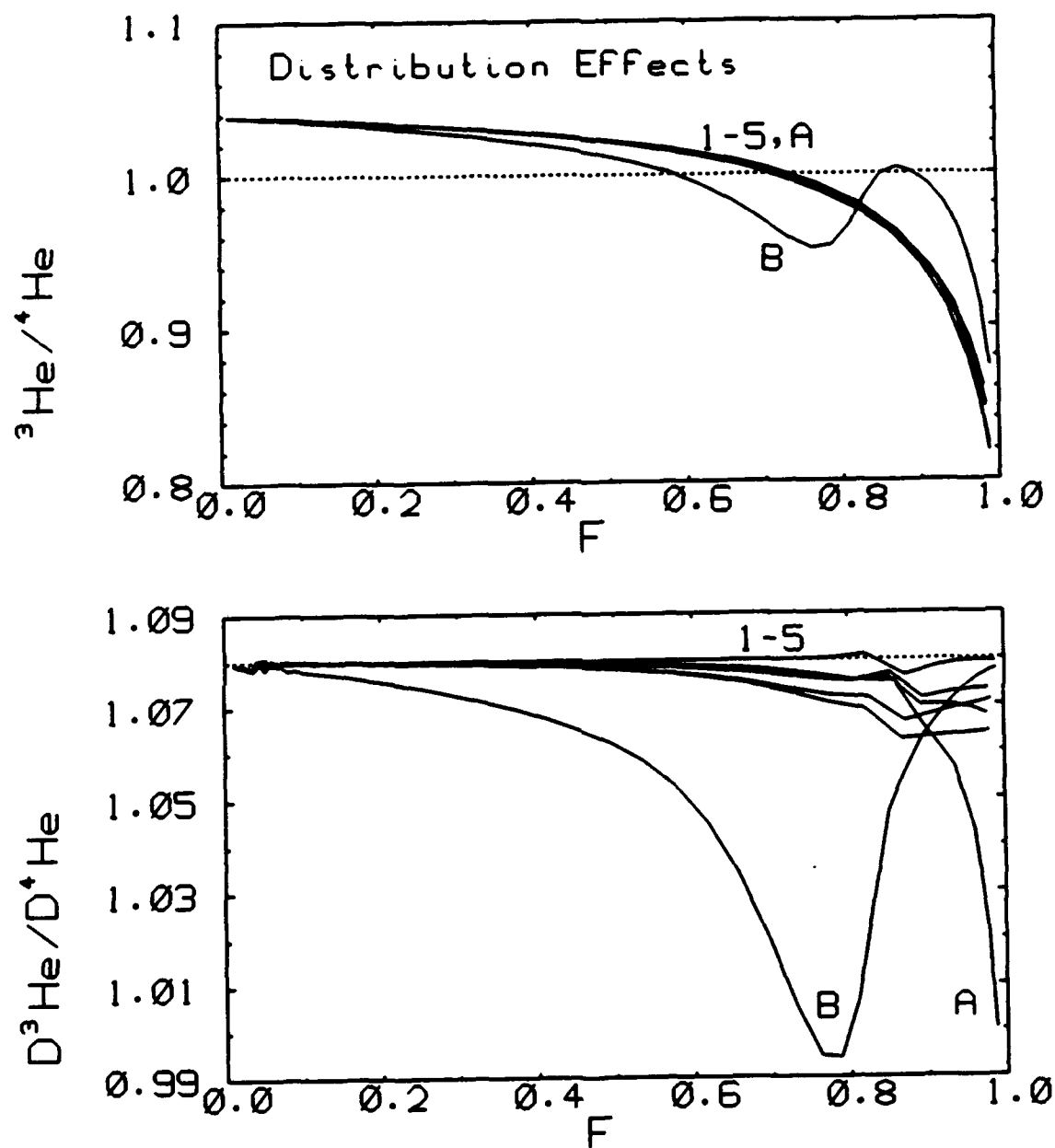
compositions. For this reason, studies which attempt to determine the spatial distribution of isotopically variable noble gas components by inverting emanation data (e.g. Albarede, 1978) are very prone to errors induced by grain size variations.

To summarize, the equisized-sphere model offers the advantage of easy-to-use approximation equations, but suffers from its inability to describe varying grain shapes and sizes. Multiple release experiments often reveal these problems, as variations in constant temperature diffusivities with extent of fractional release. Once the problem is recognized, a best diffusivity estimate can be made by examining these release systematics. However, if precise and accurate diffusivities are desired it is neccesary to account for shape and size variations directly. For this reason, a refined diffusivity model and calculation scheme incorporating shape and size variations was developed, and applied to the determination of helium diffusivities in basaltic glasses (chapter 3).

2.4.2 Refined Model incorporating shape and size variations.

In the refined model, the particles are treated as a collection of rectangular parallelpipeds. This formulation has three advantages: an analytical form is available, grains of varying size can be accounted for, and fairly broad shape variations can be encompassed by using three size parameters per grain. For the basaltic glass experiments, the model is particularly successful because these particles are generally smooth and flat-sided. Roughness and jagged edges can, in principle, be treared by considering the particle to be composed of a collection of smaller shapes plus a central core.

Fractional loss from a parallelpiped can be described by (Inthoff and Zimen, 1956):

$$F = 1 - \{ \sum (a) \cdot \sum (b) \cdot \sum (c) \} \tag{2.13}$$

where a, b and c are the side lengths, and the summation signs

represent:

$$\sum (a) = \sum_0^\infty 8/\pi^2/(2n + 1)^2 \exp\{ - (2n+1)^2 \pi^2/q^2 \, Dt)\}$$

For step-heating experiments D is given by equation 2.4. For a collection of particles, this becomes:

$$1 - F = \frac{\sum_p \left\{ \overset{q=a,b,c}{\prod} \left(\sum(q)\right)\right\}}{\sum_p (a \cdot b \cdot c)} \tag{2.14}$$

In this expression the denominator represents the volume of each grain summed over all the grains, and the numerator expresses the amount of helium remaining in each grain summed over all the grains.

Solving this expression for D (by iteration) at the points (F_i, t_i) and (F_{i-1}, t_{i-1}) yields mean value diffusivities $(\bar{D})$ for the intervals $(t_i - t_o)$ and $(t_{i-1} - t_o)$, respectively, of:

$$\text{at } F_{i-1}, \quad \bar{D}_{i-1} = 1/(t_{i-1} - t_o) \int_{t_o}^{t_{i-1}} D(t)dt \tag{2.15}$$

$$\text{at } F_i, \quad \bar{D}_i = 1/(t_i - t_o) \int_{t_o}^{t_i} D(t)dt \tag{2.16}$$

The effective diffusivity, $D_{\Delta i}$, in the interval $(t_i - t_{i-1})$ can then be obtained from:

$$D_{\Delta i} = \{\bar{D}_i(t_i - t_o) - \bar{D}_{i-i}(t_{i-1} - t_o)\}/(t_i - t_{i-1}). \tag{2.17}$$

For constant temperature steps, $D_{\Delta i}$ represents an estimate of the true diffusion coefficient, but for temperature ramp aliquots $D_{\Delta i}$ is itself a mean value on the interval.

The problem is computationally intensive for two reasons. The series converges slowly (particularly at low F) so that up to a million

75

terms may be required to obtain an absolute error of 1×10^{-6} in F or about 1% error for the low temperature emanation experiments which measured small fractional releases at low temperature. The second problem is that the precision of $D_{\Delta i}$ estimates depends on small differences between $\bar{D}_i$ and $\bar{D}_{i-1}$, so that the iteration must be performed until the $\bar{D}$ are obtained with precisions of .00001% for precision of .1% in $D_{\Delta i}$.

These tasks were performed by a series of nested subroutines which are provided in appendix A, along with the driver program that calculates fractional releases and their associated errors from aliquot measurements. The programs are written in Fortran 77, but with some non-ANSI-standard statements, and are well documented (see Appendix A). They were run on a Sun 3/260 computer with floating point acceleration and required a few hours to complete processing for a typical experiment involving two isotopes and a few tens of aliquots.

Use of the refined model with measured grain sizes and shapes (as represented by three side lengths) lead to significantly different helium diffusivity and activation energy estimates for basaltic glasses than initially obtained with the spherical model (chapter 3). The improved grain size description also demonstrated that Arrhenius temperature plots for these glasses were more closely linear than suggested by the spherical model. This lends confidence in the extrapolation of laboratory determined diffusivities to other temperatures using these relations (see chapter 3). This model is the first general scheme (to my knowledge) to account for arbitrary size and (limited) shape variations in diffusion experiments, and should be useful in future studies.

REFERENCES

ALBAREDE F. (1978) The recovery of spatial isotope distributions from stepwise degassing data. Earth Plan. Sci. Let. 39, 387-397.

CLARKE W.B., JENKINS W.J. and TOP Z. (1976) Determination of tritium by mass spectrometric measurement of ^{3}He. Inter. J. Appl. Rad. and Isotopes 27, 515-522.

CRANK J. (1975) The Mathematics of Diffusion, 2nd edition, Oxford Press.

EINSTEIN A. (1905) Ann. Physik 17, 549.

FECHTIG H. and KALBITZER S. (1966) Diffusion of argon in potassium bearing solids. In: Potassium-Argon Dating (ed. O. SCHAEFFER)

GALLAGHER K.J. (1965) The effect of particle size distribution on the kinetics of diffusion reactions in powders. In Reactivity of Solids. 5th International Symposium on the reactivity of solids. Munich, August 2-8, 1964. (ed. G.M. SCHWAB), Elsevier, New York, 192-203.

GRAHAM D. V. (1987) Helium and lead isotope geochemistry of oceanic volcanic rocks from the East Pacific and South Atlantic. WHOI/MIT Ph.D., 252 p.

HUNEKE J.C. (1976) Diffusion artifacts by dating in stepwise thermal release of rare gases. Earth Plan. Sci. Let. 28, 407-417.

INTHOFF W. and ZIMEN K.E. (1956) Kinetik der Diffusion radioaktiver Edelgase aus festen Stoffen nach Bestrahlung (Edelgasdiffusion in Festkorpern 2). Trans. Chalmers. Univ. Techn. (Goteborg) 176, 16p.

JENKINS W.J. (1974) Helium isotope and rare gas ocaenology. PhD. Diss., McMaster Univ.

KURZ M.D. (1982) Helium isotope geochemistry of oceanic volcanic rocks: implications for heterogeneity and degassing. PhD. Diss. MIT/WHOI.

KURZ M.D., GURNEY J.J., JENKINS W.J.and LOTT D.E. (1987) Helium isotopic variability within single diamonds from the Orapa kimberlite pipe. Earth Plan. Sci. Let. 86, 57-68.

LOTT D.E. and JENKINS W.J. (1984) An automated cryogenic charcoal trap
system for helium isotope mass spectromtry. Rev. Sci. Instr. 55,
1982-1988.

POLVE M. (1985) Fission track mapping of U in alkali basalts:
implications for U behavior during crystallization. EOS 66, 404.

RAMA S.N.I. and HART S.R. (1965) Neon isotope fractionation during
transient permeation. Science 147, 737-738.

SHAKED H. (1965) Simple theory for the release of fission gas from
powders. J. Nucl. Materials 17, 136-141.

STAUDACHER T., JESSBERGER E.K.,DORFLINGER D.and KIKO J. (1978) A
refined ultra-high vacuum furnace for rare gas analysis. J. Phys.
E 11, 781-784.

CHAPTER 3.

The Diffusivity of ^{3}He and ^{4}He

in basaltic glasses.

3.1 INTRODUCTION

Basaltic glasses, which form in submarine, subglacial, and to a lesser extent, subaerial environments are an important sample type for studying the elemental and isotopic variability of helium and other noble gases in igneous systems because they trap magmatic gases (e.g. Fisher, 1971). Thus, it is essential to understand the rates at which helium can be lost from or added to samples of this type. In addition, glass is a reasonable, if limited, analog for the structure of melts (e.g Mysen, Virgo and Scarfe, 1980; Stolper, 1982 and references therein), and studying helium transport in glasses can provide estimates for its behavior in magmas.

Diffusion may lead to the alteration of basaltic glass isotopic compositions by either preferential loss of one isotope or diffusive exhange of helium with the surrounding seawater or atmosphere. The effectiveness of these processes depends on the rate of helium exchange, the extent to which helium isotopes are fractionated by diffusion, and the glass helium concentration at eruption and after equilibration with the surrounding medium. Unfortunately, none of these factors are very well known, and some are in dispute. The rate of helium diffusion has been measured in two previous studies. Kurz and Jenkins (1981) estimated the ^{4}He diffusion coefficient to be very low at seafloor temperatures ($1.\underline{+}.6$ x 10^{-17}cm^2/s at 0°C and 1.6 x 10^{-16} at 20°C), from extrapolation of emanation measurements at elevated temperatures, and concluded that "diffusion is an insignificant mechanism for helium loss" from mid-ocean-ridge-basalts (MORB) glasses. In contrast, Jambon, Weber and Begemann (1985) observed significant helium loss from powdered and sieved basaltic glass stored in their laboratory, and estimated the diffusion coefficient to be 40 times higher (6 x 10^{-15} cm^2/s at 20°C). The difference in these values has great significance for the interpretation of helium isotope measurements in basaltic glasses. As an example, the timescale to lose 1/2 of the initial helium content of a 1cm sphere of basaltic glass decreases from several million years to less than 100,000 years, if the higher diffusivity is correct. This is

an important difference, because most dredged MORB samples will be less than than a million years old (at a 1cm/year plate separation rate this corresponds to samples dredged within 10 km of the ridge crest), but many could be 100,000 years old. Thus it is essential to determine which of these previous helium diffusivity estimates is correct. Interestingly, the two studies found a similar Arrhenius dependence of the diffusion coefficient on temperature, although only Kurz and Jenkins (1981) obtained an activation energy with reasonable precision ($Ea=19.9\pm1.0$ Kcal/mole). Determining the precise nature of the temperature dependence of helium diffusion in basaltic glasses is essential to their study and the work presented here, because measurements made at elevated temperatures in the laboratory are extrapolated to obtain diffusivity estimates at lower environmental temperatures.

No previous study has measured the diffusivity of ^{3}He in basaltic or other natural glasses, so the extent to which diffusion fractionates helium isotopes is unknown. From a theoretical viewpoint, diffusion is expected to fractionate helium isotopes because of their large mass difference. Simple heuristic models, such as pure gas kinetic theory ($E=1/2mv^2$) or one-dimensional harmonic oscillation of an isolated atom (frequency proportional to $(m)^{-1/2}$), suggest that the relative rates of ^{3}He and ^{4}He diffusion will correspond to the square-root of the mass ratio of ^{4}He to ^{3}He (i.e the isotopic diffusivity ratio, D^3He/D^4He would equal $(m^4He/m^3He)^{1/2}$, which is 1.154). This predicts that ^{3}He will be diffuse about 15% more rapidly than ^{4}He. More sophisticated theory reveals that the diffusity ratio for two isotopes depends on properties of the solid in addition to the diffusing species, and allows for the possibility of a larger isotope effect (Prigogine and Bak, 1959; Stoneham and Flynn, 1971), a somewhat smaller diffusivity ratio because of quantum effects (Le Claire, 1966), and even preferential ^{4}He mobility (Ebisuzaki, Kass and O'Keefe, 1967).

Measurements made in synthetic glasses observed a temperature dependent helium isotopic diffusivity ratio (D^3He/D^4He) ranging from 1.12 at 600°C down to 1.07 at 300°C (Shelby, 1971). However, the applicability of this result to basalt glasses is uncertain because of

the large compositional differences, which are known to lower the diffusivity for ^{4}He in basalts in comparison to synthetic glasses by several orders of magnitude (Jambon and Shelby, 1980). Unfortunately, network-modifier/network-former theory, which does offer a qualitative explanation for the lower natural glass diffusivities (e.g Jambon and Shelby, 1980; Kurz and Jenkins, 1981), can be used to predict isotopic fractionation variations. Small differences in D^3He/D^4He are important because this ratio governs the fraction of helium which must be lost by a glass to lower its initial ratio significantly. For example, to reduce an initial $^3He/^4He$ ratio by 10% requires 80% gas loss for D^3He/D^4He equal to 1.08, but only 65% loss (which occurs in half the time) for D^3He/D^4He of 1.15. Craig and Lupton (1976) have suggested that preferential diffusive loss of ^3He accounts for the low $^3He/^4He$ ratios of two oceanic basalt glasses with low helium contents, but assumed a high diffusivity based on synthetic glass studies and an isotopic diffusivity ratio of 1.15. Determining the true diffusion rate and D^3He/D^4He ratio is essential to understanding whether samples such as these represent primary magma characteristics or contamination effects.

The timescales for loss of helium from a sample also apply to helium exchange with seawater. The effect of this contamination process on observed $^3He/^4He$ ratios is obviously most severe for those samples which were erupted with less helium than expected for basalt-seawater equilibrium, because helium with atmospheric composition can be added to the sample. Samples with more helium than this level will lose helium until the equilibrium level is obtained. Of course ^3He and ^4He behave independently in this equilibration process. The equilibrium concentration level can be estimated from the helium partial pressure in seawater (P_{he}^{Sw}) which is essentially in equilibrium with air at one atmosphere total pressure (Weiss, 1971) and the Henry's law constant for helium solubility in basaltic glass (K_{He}) from the definition:

$$[He]_g^{Sw} = K_{He} \times P_{He}^{Sw} \qquad (3.1)$$

Henry's law coefficients have been estimated for basaltic melts and glasses in laboratory studies and from natural distributions, and

average 5×10^{-4} ccSTP/g-atm (table 3.1). The temperature dependence is very small, similar to experimental errors in the melt studies, but favors higher solubilities as temperature increases (Jambon, Weber and Braun, 1986; Lux, 1987). No measurements of the ^{3}He solubility have been made, but indistinguishable isotopic compositions of helium in vesicles and dissolved in MORB glasses suggest the two isotopes have identical solubilities (Kurz and Jenkins, 1981) although data precision allows a 1% difference, similar to that observed for seawater, which favors ^{3}He dissolution by 1.7% (Weiss, 1971). Assuming these Henry's law constants apply to glasses at low temperature on the seafloor, the equilibrium value for helium dissolved in basalt is $2-3\times10^{-9}$ ccSTP/g (i.e. $4-5\times10^{-4}$ ccSTP/g-atm x 5.3×10^{-6} atm). This can be compared to typical seawater concentrations (e.g 2×10^{-8} ccSTP/g in deepwater in the Galapagos; Jenkins, Edmond and Corliss, 1987) and to basaltic glass concentrations which are on the order of 10^{-5} to 10^{-8} ccSTP/g in MORB (e.g. Lupton and Craig, 1975; Kurz and Jenkins, 1981), but which range as low as 10^{-8} to 10^{-10} ccSTP/g in rocks from seamounts and island arcs (Graham et al, 1987; Trull, Perfit and Kurz, 1989). Therefore, contamination by helium addition on the seafloor is a concern in extending helium isotopic studies to these sample types, particularly if the helium diffusivity is relatively high. In this regard, helium isotopic disequilibrium within basaltic glasses from Loihi seamount has been interpreted as the result of diffusive exchange with seawater (Rison and Craig, 1983) and the low ^{3}He/^{4}He ratios of some glasses from the Woodlark basin probably are also contaminated by this process (see chapter 6).

The production of radiogenic ^{4}He by alpha-decay of U and Th series nuclides is another mechanism by which the isotopic composition of basaltic glasses can be altered after eruption (e.g. Graham et al, 1987; Trull, Perfit and Kurz, 1989) and which provides a promising dating method for seamount basalts (Graham et al, 1987). Helium loss by diffusion bears directly on the utility of this method, because apparent ages will be lowered in proportion to the fraction of helium lost, and because helium exhange between glass and vesicles affects the correction

Table 3.1 Henry's law coefficients for Helium solubility in
basaltic melts and glasses.

Experiment and Reference	K_{He}
Equilibration of tholeiitic melts at 1250–1600°C followed by analysis of quenched glasses. Jambon, Weber and Braun, 1986.	5.6+1.1 ($\times 10^{-4}$ ccSTP/$\overline{g}$-atm)
Equilibration of tholeiitic melt at 1350°C followed by analysis of quenched glass. Lux, 1987.	6.4+.8
Comparison of vesicle and glass helium contents of mid-ocean-ridge-basalts. Kurz and Jenkins, 1981; Kurz, 1982; Graham et al, 1988.	3.7+.8
Permeability measurement of basaltic glass at 200–300°C. Jambon and Shelby, 1980.	4

required for inherited helium (Graham et al, 1987). The mobility of in-situ produced radiogenic helium (denoted ^{*4}He here) may differ from inherited helium because of the nature of its generation. Keevil (1940) suggested, on theoretical grounds, that the disruption of bonds associated with alpha-particle ejection and daughter nuclide recoil is insufficient to enhance diffusion of ^{*4}He, at least in silicate crystals. However, many studies have documented elevated losses of radionuclides, including ^{222}Rn from rocks and crystals (e.g. Giletti and Kulp, 1955; Rama and Moore, 1984; Fleischer, 1988) and ^{234}Th and ^{234}U from granites (Fleischer and Raabe, 1978) where release is enhanced by recoil energies. ^{*4}He has a much higher energy/mass ratio than these elements, resulting in a stopping range of 20-30 microns in basalt (e.g. Graham, 1986), and suggesting that its release may be similarly, and perhaps more strongly affected. Many efforts to use ^{*4}He acccumulation as a gechronometer have documented helium loss (e.g. Hurley, 1954 for zircon and granitic minerals; Fanale, 1964 for magnetite; Bender, 1970 for corals; Leventhal, 1975 for holocrystalline basalts). However, it is unclear that these losses result from enhanced mobility related to radioactive decay, rather than preferential siting of the parent nuclides on grain boundaries and surfaces.

In summary, because of the potential role of diffusion in releasing and exhanging helium and thereby affecting their isotopic compositions, the work described in this chapter was designed to determine the diffusivity of inherited ^{3}He and ^{4}He, and ^{*4}He in several basaltic glasses. The large discrepancy between previous studies (Kurz and Jenkins, 1981; Jambon, Weber and Begemann, 1985) and the desire to extend helium isotopic analysis to low helium samples from new tectonic terrains, such as island arcs and seamounts, made a reassessment of this problem particularly important.

3.2 SAMPLES

All the samples analyzed were basaltic glasses produced by the rapid quenching that occurred when the lavas erupted on the seafloor. The sample numbers, their provenance, rock type, and bulk helium

contents are listed in table 3.2a. Chemical compositions are given in tables 3.2b and 3.2c. Charco 98-11T is a tholeiitic basalt typical of those recovered from normal mid-ocean-ridges (Bougault and Treuil, 1981), and is very similar in chemical composition to another sample from the same dredge studied for He diffusion by Jambon, Weber and Begemann (1985, sample Charco 98-DR11). The letter T designates the split from the bulk dredge sample prepared in this study from the center of a 3cm drop-shaped lobe which appears to have been cooled as it was extruded from a larger lava volume. Chemically, sample Alv892-1a is also in the range of normal mid-ocean-ridge-basalts (MORB) although it has been described as iron and titanium rich, perhaps reflecting its origin in the relatively fast-spreading Galapagos rift (Byerly, Melson and Vogt, 1976). A similar sample from the same dive (Alv892-2) was among those studied by Kurz and Jenkins (1981). The sub-sample prepared for Alv892-1a came from the center of a 20cm long, 5cm diameter, cylindrically-shaped, entirely vitreous lava tube. These two samples were chosen because they have chemical compositions representive of many mid-ocean-ridge basalts and allow ready comparison with previous work. Aftermath D9 and Alv1389-1854B are alkali basalt glasses recovered from off-axis seamounts (Graham et al 1987, 1988). D9 was selected to examine the compositional dependence of helium diffusion by comparison with the tholeiites. Sample 1854B contains predominantly radiogenic ^{4}He (97% ^{*4}He), and has been dated at 680($\pm$140) thousand years using the U+Th/He method (Graham et al, 1987). It was studied in order to examine the effect of diffusive ^{*4}He loss on on this dating method. In contrast to the tholeiites, both alkali basalt samples were prepared from the glassy margins of pillow lava fragments.

For all samples, large glass fragments (.5 to 1 cm chunks) were broken from the rocks using a stainless-steel mortar and in some cases a small steel chisel. The glasses were examined in thin section before crushing to identify sections of the samples that were free from spherulites, varioles, and other devitrification textures. These fragments were then further broken, sieved on a shaker table with repeated acetone washings to disperse electrostatic aggregates and remove fines (ISO/USA standard stainless steel sieves), and handpicked

Table 3.2a. Sample descriptions and bulk helium contents.

SAMPLE	TYPE	PROVENANCE	VES. (%)	HELIUM COMPOSITION [He] cc/g	R/Ra	METHOD
ALV892-1A	TH	Galapagos Spreading Center 0 49'N, 86 08'W 2750m depth	0	3.21x10-7 8.60x10-7 8.92x10-6	8.48(.04) 8.51(.06) 8.32(.07)	1 1 2
CHARCO 98-11T	TH	Mid-Atlantic-Ridge 30 41'N, 41 49'W 3500-3600m depth	.5	6.93x10-6 9.42x10-6	8.57(.07) 8.73(.06)	1 2
AFTERMATH D9 station glass #1	FAB	Mathematicians Rift, Pacific 17N, 110W 1800-2000m	2	2.79x10-6 7.95x10-7 4.97x10-7	6.62(.05) 7.24(.12) 7.14(.06)	1 1 2
ALV1389-1854B	FAB	Seamount 6 12 44'N, 102 35'W East Pacific Rise approx. 2000m	1	6.19x10-9 2.16x10-7 2.1x10-7	1.67(.03) 0.06(.01) *4He	1 2 3

a. FAB=fractionated alkali basalt TH = tholeiite
b. Ves. denotes the vesicle content estimated visually from thin sections.
c. Method: 1 - helium released by crushing (from vesicles)
   2 - release by melting the crushed powder (from within glass)
   3 - radiogenic helium generated in the sample since eruption, derived
   from: *4He = [He]m (1-Rm/Rc), c denotes crushing and m, melting.
d. 3He/4He ratios are normalized to the atmospheric ratio, Ra = 1.38 x 10-6.
e. 1 sigma errors for the 3He/4He ratios are shown in parentheses.
f. Analyses for D9 and 1854B from Graham et al, 1987, 1988, respectively.

Table 3.2b. Chemical compositions of basaltic glasses.

Sample:	D9		D9 (dvs)		1854B		Alv892		Charco98	
MgO	6.90	(.10)	6.88	(.09)	5.96	(.06)	7.98	(.09)	8.64	(.11)
Al2O3	15.73	(.02)	15.98	(.14)	17.84	(.06)	14.19	(.07)	14.66	(.07)
SiO2	47.84	(.13)	48.33	(.19)	49.88	(.25)	50.95	(.32)	50.28	(.20)
CaO	9.35	(.10)	9.54	(.05)	8.19	(.12)	11.99	(.11)	11.13	(.10)
TiO2	2.47	(.05)	2.47	(.04)	2.47	(.10)	1.23	(.03)	1.42	(.04)
Cr2O3	.07	(.01)	.08	(.03)	.06	(.01)	0.09	(.01)	.11	(.02)
MnO	.18	(.04)	.18	(.03)	.10	(.05)	0.18	(.03)	.17	(.04)
FeO	11.08	(.10)	11.35	(.16)	8.21	(.15)	10.50	(.08)	9.95	(.09)
P2O5	.36	(.03)	.37	(.02)	.68	(.03)	.15	(.02)	.18	(.02)
Na2O	3.45	(.11)	3.45	(.11)	4.47	(.10)	2.14	(.11)	2.56	(.06)
K2O	.94	(.02)	.98	(.05)	1.98	(.02)	.04	(.01)	.06	(.01)
Total	98.35	(.27)	99.63	(.34)	99.84	(.39)	99.44	(.35)	99.15	(.43)
Mg#	52.6	(.4)	51.9	(.2)	56.4	(.7)	57.4	(.4)	60.7	(.3)

a. Electron microprobe analyses done at M.I.T. with Dr. Steve Recca. (errors) are 1 s.d. of the mean of 10 analyses on 2 glass chips.
b. D9 (dvs) was heated at 600C for several hours during experiment #9 and may have lost volatiles, although its higher total could also represent analytical variability. Other samples were not heated.
c. Mg# = Mg/(Mg+Fe).

Table 3.2c. Molar compositions of major network formers/modifiers.

Sample:	D9	1854B	Alv892	Charco98
Type	AB	AB	TH	TH
SiO2	.536	.558	.548	.541
Al2O3	.104	.117	.090	.092
TiO2	.021	.021	.010	.012
CaO	.112	.098	.138	.129
FeO	.076	.056	.069	.066
MgO	.115	.099	.128	.138
Na2O	.030	.038	.017	.021
K2O	.006	.012	.0003	.0004
NF	66.1	69.6	64.8	64.5
CD	2.68	2.61	2.69	2.68

AB = alkali basalt, TH = tholeiite
NF = mole percent network formers
        (SiO2+Al2O3+TiO2)
CD = density calculated from compositions
        (Stebbins et al, 1984).

(in both reflected and transmitted light in air and in ethanol,which reveals surface features) to completely eliminate adhering alteration minerals, phenocrysts, and devitrification textures. Grains (200 microns or larger) were individually examined; smaller sizes were obtained by crushing handpicked .5-1mm grains. All samples were cleaned by brief ultrasonic agitation in distilled water, acetone and methanol, followed by drying in air at room temperature. The glass powders were examined extensively in thin section for alteration and devitrification and during electron microprobe analyses for evidence of glass immiscibility, none was found, with the exception of one Alv892-1a subsample which was specifically prepared from a spherulitic glass fragment.

The total helium contents of the MORB glasses (about 10^{-5}ccSTP) are typical for this rock type (e.g. Kurz and Jenkins, 1981) and are 3 to 5 times higher than for the alkali basalts (table 3.2a). In general, the relative releases of He by crushing large (2mm) chips and melting the resulting powder are consistent with the vesicularities determined in thin section and the partitioning relation found for MORB samples by Kurz and Jenkins (1981). Alkali basalt sample D9 had the highest vesicularity at 2%, which suggests the two-fold variation in vesicle helium concentrations obtained from replicate analysis derives from heterogeneous vesicle distributions. No vesicles were observed in sample Alv892-1a, and with only about 1% of the helium released by crushing (suggesting .04% vesicles by volume) this is consistent with either sub-micron vesicles, or with the presence of rare larger vesicles not intersected by a thin section. Alternatively, it is possible that this small fractional release results from diffusion of He from new surfaces produced by crushing. To investigate this, the fraction of helium that could diffuse from new grains during a typical 1 hour crushing and analysis period was calculated by assuming that the crushing process produces cubic grains of a uniform size. Figure 3.1 shows that the fraction released is much less than one percent for likely room temperature helium diffusivities (10^{-15} to 10^{-16} cm^2/s) except when 10um or smaller powders are produced. Because much of the powdered glass samples are in the 20-100um size range, the helium released during crushing sample Alv892-1a probably derives from rare larger vesicles.

Figure 3.1 Approximate fraction of helium in a glass sample that may be released by diffusion during a crushing analysis, for several values of the diffusion coefficient, given as Log D in cm^2/s on the curves. The calculation assumes crushing produces cubic particles of uniform size (x-axis), and that diffusve loss occurs over a typical 1 hour crushing and analysis period. For example, if D is $1 \times 10^{-13} cm^2/s$ and the crushed powder size is 20um, approximately 5% of the helium contained in the glass will be diffusively released, and will contribute to the helium released by fracturing vesicles.

Figure 3.1
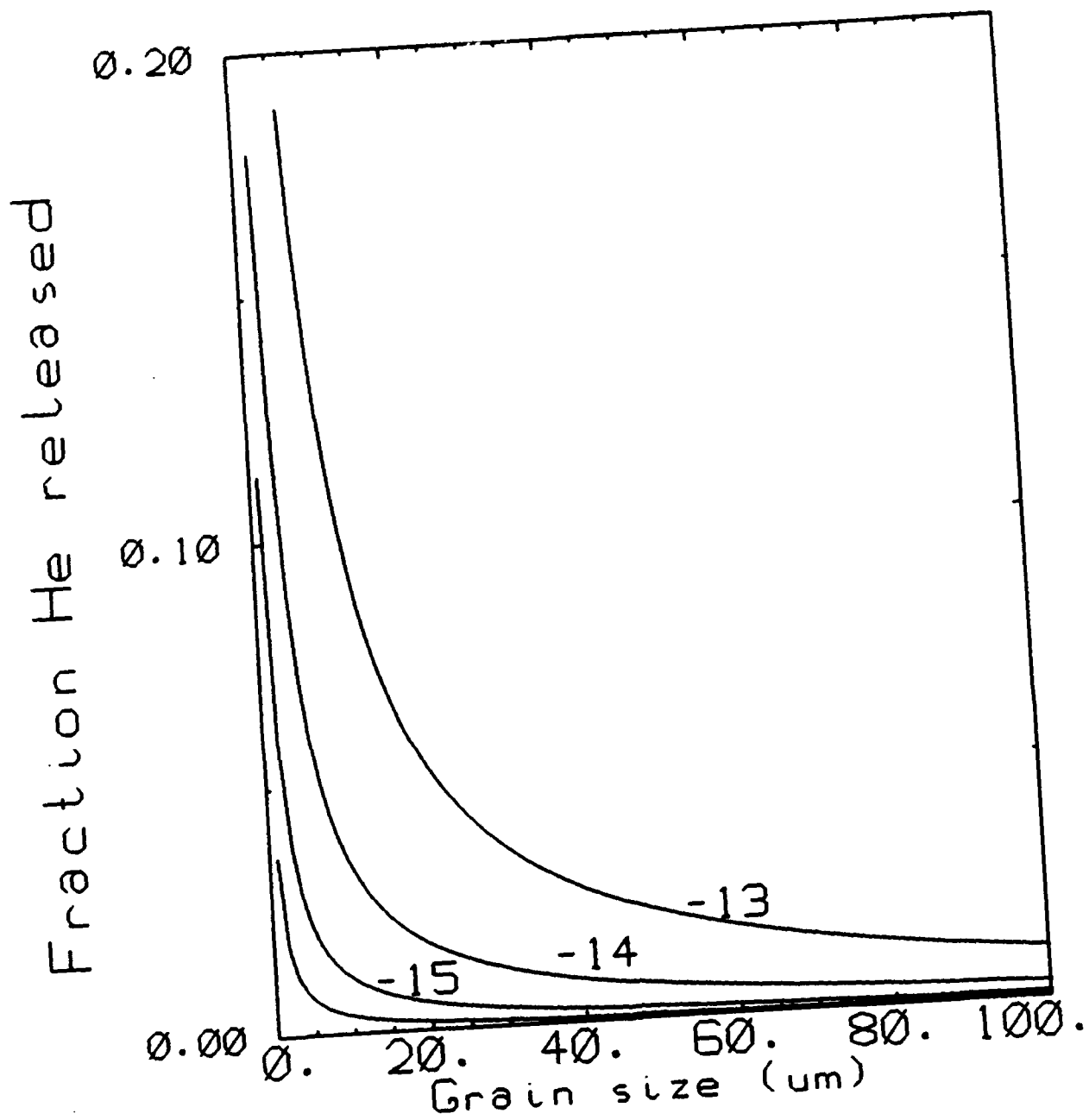
In any case, it is clear that the helium contained in this sample is predominantly dissolved in the glass. In contrast, the other tholeiite (Charco 98-11T) has half its helium in vesicles   As discussed below, the diffusivity results on these samples are almost identical, suggesting that vesicles have little effect on helium mobility after glass solidification and that transfer of helium between the vesicle gas phase and the glass is not a rate-limiting step in diffusion. As a result of the production of $*^4$He by in-situ U and Th decay, sample 1854B contains only 3% of its helium in vesicles, rather than the 90% expected for 1% vesicularity in MORB glasses (Kurz and Jenkins, 1981). As mentioned above, and calculated in table 3.2a, this sample contains 97% radiogenic helium.

The tholeiitic glasses have ^{3}He/^{4}He ratios typical of MORB samples (8-9 R_a, e.g. Lupton and Craig, 1975; Kurz and Jenkins, 1981), and higher than the alkali basalts. This relation between tholeiitic and alkali basalt helium isotopic compositions has been observed at both spreading center and hotspot related seamounts and may reflect either source compositions or petrogenetic processes (Kurz et al, 1982; Graham et al, 1988). With the exception of alkali basalt sample 1854B, the isotopic composition of helium released by crushing chips is identical to that released by melting the crushed powders, consistent with minimal fractionation accompanying partitioning (Kurz and Jenkins, 1981) and negligible ingrowth of radiogenic $*$He. The low ^{3}He/^{4}He ratio obtained by crushing 1854B was suggested to be magmatic in origin by Graham et al (1987, 1988) based on the observation that several samples from seamount 6 and other submarine volcanos give similar results despite varying $*^4$He contents. However, this ratio would be considered suspect by the criteria developed for island arc basalt glasses by Trull, Perfit and Kurz (1989, chapter 6)) because the large radiogenic helium content of the glass is readily capable of contaminating the 100-fold smaller vesicle helium content. Graham et al (1987) suggested that the diffusive timescale for this to occur was too long, using the low diffusivity estimate of Kurz and Jenkins (1981), but did not consider higher diffusivity estimates (Jambon, Weber and Begemann, 1985) or release of $*^4$He during crushing (figure 3.1). However, as shown below, the

diffusivity of ^{*4}He is quite low in this sample, which supports the interpretation that the vesicle helium represents magmatic helium.

3.3 RESULTS

Two methods were used to estimate the helium diffusivity. The simplest method was to determine the helium contents of powdered and sieved glasses by total fusion analysis before and after storage for several months in air at room temperature, and to calculate a diffusion coefficient from the fractional loss, the elapsed time and the grain size. This approach has the advantages that the helium diffusivity can be estimated at low temperature because the powder can be stored for a long time, and determining low helium emanation rates is not required. The disadvantage is that only one determination of the extent of loss as a function of time can be made, revealing little about the mechanism of release, and the temperature dependence of the diffusivity is not measured. In principle, these objectives could be achieved by storing powder splits at different temperatures for various lengths of time, but other aspects of the storage technique make the second method, measuring helium emanation in-vacuo directly, more precise. In particular, it is difficult to determine the initial helium content of powdered glasses (before storage), because of heterogeneous vesicle distributions and because helium is lost from fine powders between preparation and analysis.

3.3.1 Storage experiments.

The storage experiments were designed to examine and reproduce the work of Jambon, Weber, and Begemann (1985), who found that the helium content of powdered basaltic glass (Charco 98-DR11) decreased with grain size after storage in their laboratory for about a year. After estimating the fractional loss for the powders by comparison to the helium content of larger fragments (circa 1mm) they obtained a helium diffusivity estimate at room temperature of 6×10^{-15}cm^2/s with an error range estimate of a factor of 3. To see if part of the dependence of

helium content on grain size these researchers observed might result from the crushing process, rather than from diffusive loss, a similar sample from the same dredge (Charco 98-11T) was crushed, sieved, and immediately analyzed by melting. Figure 3.2 shows these results superimposed on the diagram of Jambon, Weber and Begemann (1985) for their sample and suggests that part of the helium loss observed in their study occured during powder preparation, because fine powders contain less helium than larger chips even before storage. This suggests that small vesicles may have contributed to the apparent loss in their study and that their diffusion coefficient is an overestimate. Both the Charco 98 sample used by Jambon, Weber and Begemann (1985) and the one studied here contained .5% vesicles, primarily.5 -1.0 mm in size.

To further examine the problem of crushing losses in powder storage experiments, sample Alv892-1a, which is extemely devoid of vesicles (table 3.2a), was powdered and analysed by melting before and after storage. Again, the powders had lower "initial" helium contents than larger grains, suggesting a loss related to crushing. Diffusive loss during the 3-5 days delay (table 2a) between crushing and analysis can not account for these low helium contents because this would require that the diffusion coefficient (D) be greater than $10^{-14} cm^2/s$, which is not compatible with previous studies or the results of the emanation experiments. After storage, the reduced helium contents suggest high diffusivities when fractional loss is calculated by comparison to the helium content of a 2mm chip (the proceedure used by Jambon, Weber and Begemann, 1985), but accounting for crushing losses by calculating fractional losses from the initial powder contents determined soon after crushing reduces D estimates by an order of magnitude (figure 3.3). The data do not determine the diffusivity with high precision because of the spread in grain size within a sieve fraction, errors in specifying grain geometry and the low fractional losses, but suggest a mean value of 5 x $10^{-16} cm^2/s$, with an error range of a factor of 2. This is considerably less than the value of 6 x10^{-15} obtained by Jambon, Weber, and Begemann (1985) but higher than the value of 1 x $10^{-16} cm^2/s$, predicted by the Arrhenius temperature relation of Kurz and Jenkins (1981).

Figure 3.2 Helium content of basaltic glass as a function of grain size (adapted from Jambon, Weber and Begemann, 1985). The horizontal bars are the helium contents measured by these workers for sieved powders after one year storage, and suggest a room temperature diffusivity of $6 \times 10^{-15} cm^2/s$ (the dashed curves are for diffusivities of 3 times lower and higher). The horizontal line at $800 \times 10^{-8} ccSTP/g$ He marks the helium content below which their study assumed no helium was contained in vesicles, corresponding to a grain size of .04cm. However, analyses of unstored powders (solid circles) reveal that powder preparation releases more helium from small particles than large grains , implying the diffusivity estimate of Jambon, Weber and Begemann (1985) is overestimated.

Figure 3.2
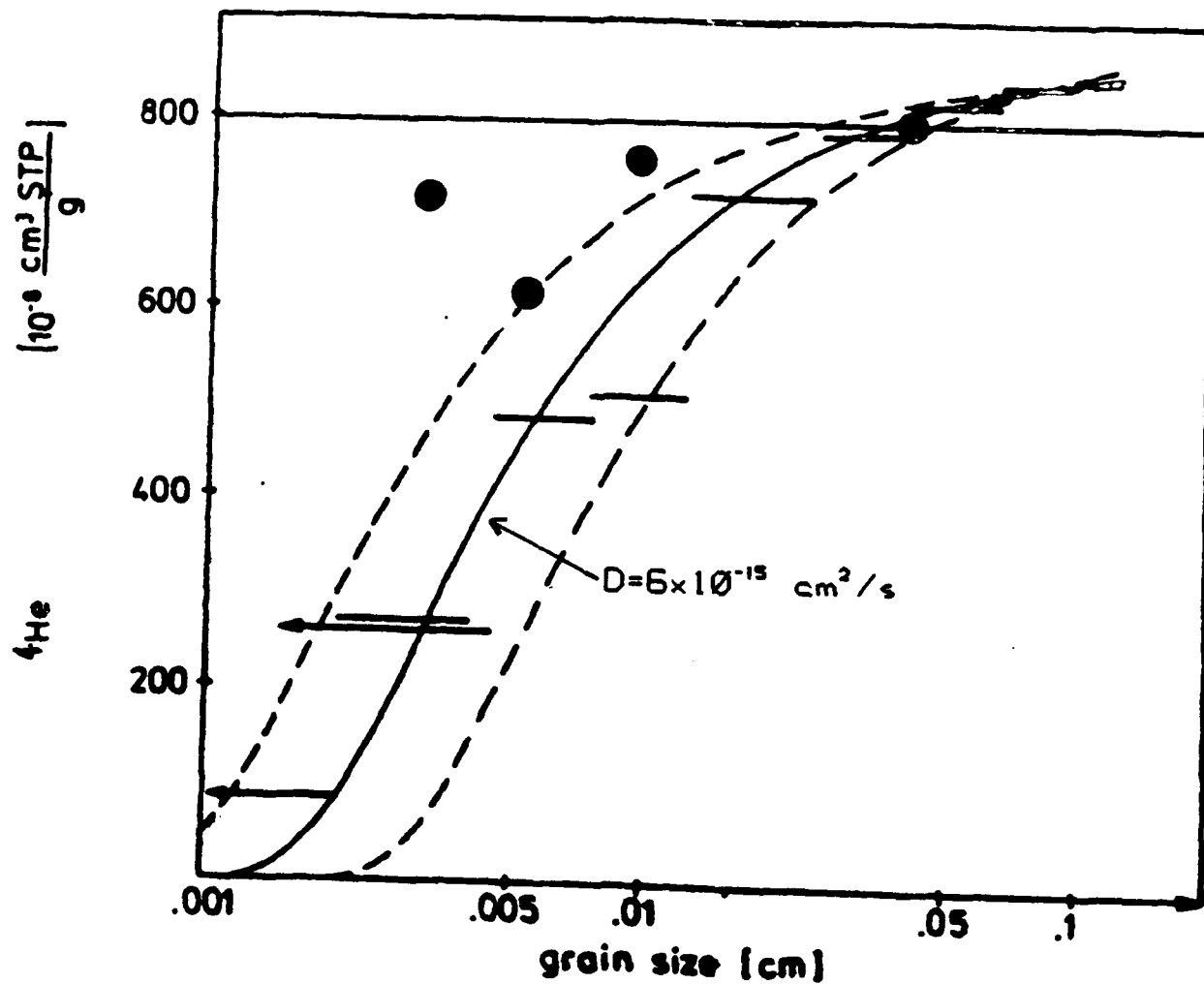
Table 3.3 Helium contents of powders stored at room temperature.

SAMPLE (glass)	GRAIN SIZE (um)	STORAGE TIME (days)	[He] (10-6 cc/g)	3He/4He (R/Ra)	(1s)
a. Total fusion analyses					
Charco 98-11T	1mm chip	years	9.42	8.73	(.06)
	38-53	5	8.63	8.51	(.08)
	53-75	5	8.95	8.76	(.05)
Alv892-1A	2mm chip	3	8.92	8.32	(.07)
	25-38	3	7.70	8.37	(.06)
	38-53	3	6.73	8.22	(.04)
	75-106	3	8.51	8.31	(.04)
	25-38	235	5.70	8.27	(.09)
	53-75	235	7.73	8.40	(.07)
	75-106	235	7.86	8.26	(.07)
	106-180	235	8.35	8.42	(.07)
	250-300	337	7.83	8.27	(.06)
	355-425	337	8.06	8.39	(.06)
	425-500	337	8.16	8.27	(.06)
b. Sums of diffusive releases for step-heating expts. in table 3.					
Alv892-1A	38-53	3	8.0(8.1)*	8.31	(.01)
	75-106	55	7.7(7.9)*	8.22	(.01)
	300-355	90	8.0(8.2)*	8.34	(.01)
	2mm shard	8	8.3	8.56	(.03)
	2mm chips	68	8.6	8.35	(.01)
	2mm chips	87	7.7 #	8.54	(.04)
Charco 98-11T	1mm chips	years	9.7	8.73	(.04)

a.   1 sigma analytical error in concentration is less than .3%
b.   Storage times are from crushing cm-sized pieces until analysis.
c.   * (values) corrected for helium loss prior to analysis - see text.
d.   # variolitic texture may contribute to low helium content.

Figure 3.3 Comparison of helium contents of _stored_ glass powders
with expected loss curves calculated assuming spherical geometry
and the diffusivities shown (e.g. the leftmost curve is for
$D=5 \times 10^{-17}$ cm^2/s). The two plots are for different storage times,
given in days. Samples are plotted for their sieve range
assuming it approximates the diameter of an equivalent sphere The
thin bars represent fractional contents calculated by comparison
to a the helium content of a 2mm chip and suggest a relatively
high diffusivity of 10^{-15} to 10^{-14} cm^2/s. In contrast, fractional
contents calculated by comparison to the helium contents of
unstored powder splits (thick bars) suggest the correct
diffusivity is an order of magnitude lower.

Figure 3.3
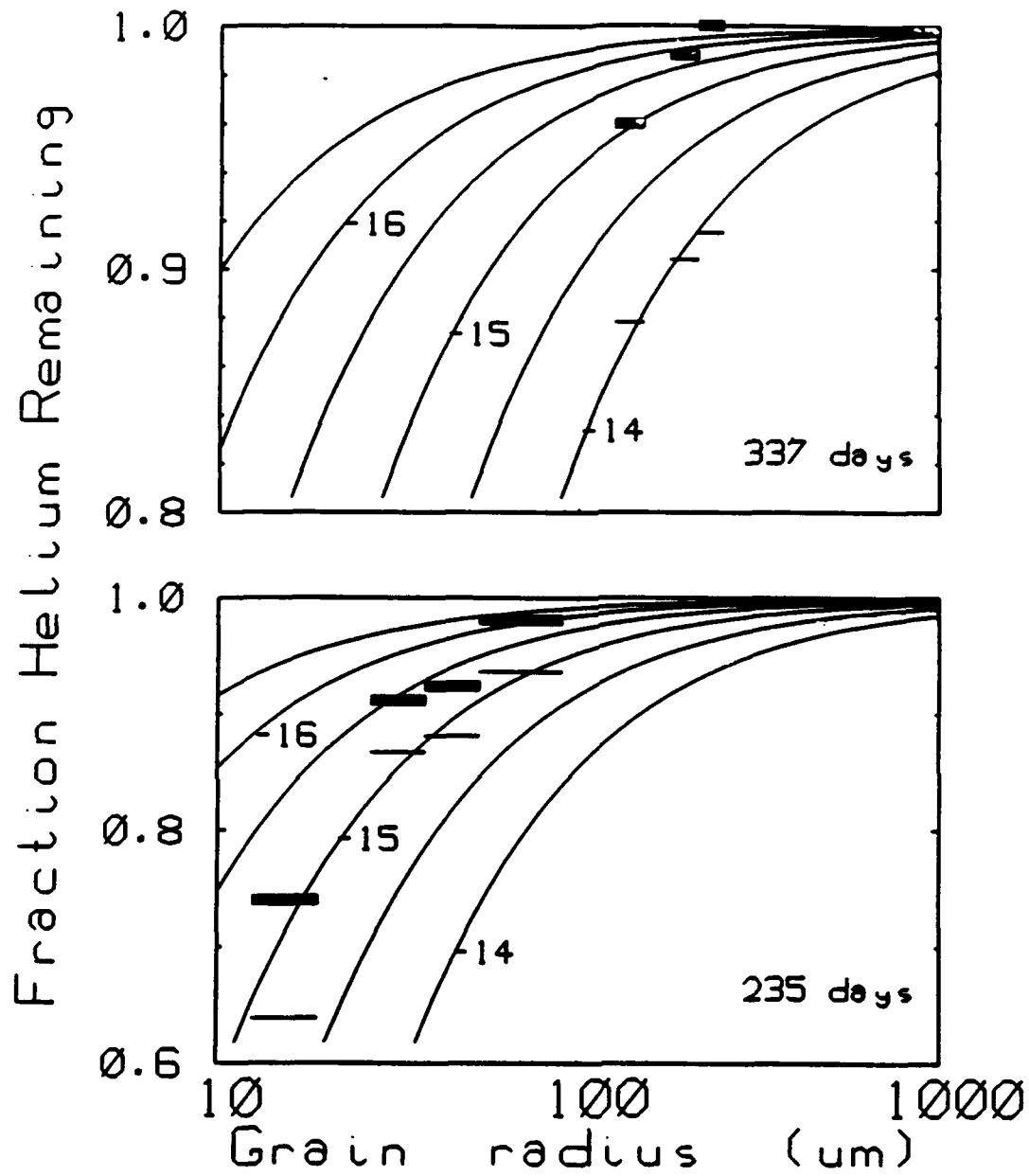
The isotopic composition of the powders showed no clear variation with grain size initially, or with extent of helium loss after storage. This is consistent with a homogeneous initial compositionn and a small diffusive fractionation; D^3He/D^4He ratios of 1.2 or less are permissable within the precision of the isotopic determinations. Because the storage method relies on analysing different splits for the initial and final concentrations of the powders it is subject to uncertainties related to natural variability in glass concentrations, which often vary between subsamples by 10 to 20% or more (table 2.3 and e.g. Graham et al, 1987, 1988;.Kurz, 1982). In summary, the storage experiments suggest that the helium diffusivity indicated by Jambon, Weber, and Begemann (1985) was overestimated, but the method is imprecise, and isotopic fractionation associated with diffusion could not be quantified.

3.3.2 Emanation Experiments.

In the in-vacuo emanation experiments the rate of release of naturally present helium from glass chips and powders was determined using a specially constructed diffusion vessel. Two major advantages of this method are the ability to vary the temperature in a single experiment and to measure sequential releases, which provides information on the release mechanism and its thermal activation. Diffusion coefficients can then be calculated for each aliquot from a diffusion model assuming appropriate boundary and initial conditions (typically spherical geometry and an initially homogeneous distribution). Because this method requires the determination of fractional loss rates, total helium release (greater than 99.9%) was verified for one experiment (#1) by melting the sample and the other samples were heated at $600^{\circ}C$ until the release rate limited the remaining helium to less than .1% of the total. The experimental conditions also ensure that the helium diffuses into a surrounding volume with essentially zero helium content, which simpliries the diffusion model boundary conditions. The temperature range investigated was $20^{\circ}C$ to $600^{\circ}C$, essentially limited by safety concerns for heating the vessel at the high end, and by the ability to distinguish small

helium releases from atmospheric leaks at low temperature. Typically, sample sizes were about 100mg, but one experiment was performed with a single 7mg chip, and the powder experiments used up to 300mg of glass. Details of the diffusion vessel construction, temperature control, gas processing, mass spectrometry and the calculation of diffusion coefficients can be found in chapter 2.

Six experiments were performed using tholeiite sample Alv892-1a to investigate reproducibility and the nature of helium release in detail (table 3.4; expts. #1-6). This included three experiments with large chips and three with powders. One experiment was done with a single glass fragment to minimize grain size distribution effects (#1) and another with slightly variolitic glass to examine the effect of glass devitrification on release (#3). The powder experiments were designed to extend the temperature range from the $100^{\circ}C$ to $600^{\circ}C$ range of the chip experiments to room temperature, and to see if the glass crushing induced any high diffusivity paths. Most of the experiments were step-heated to investigate the temperature dependence of the diffusivity, but experiment #4 was carried out isothermally (except for a few initial aliquots at low temperature). This simplifies examination of the release time dependence in terms of diffusion mechanisms because uncertainties in the temperature dependence of diffusion need not be considered. Experiments were also carried out on another tholeiite (Charco 98-11T, expt. 7 in table 3.4) and two alkali basalts to examine compositional effects (Aftermath D9, expts. 8 and 9) and the release of $^{*4}He$ (1854B, expts. 10 and 11). The six Alv892-1a experiments are described first, as a guide to understanding the nature of helium mobility and in interpreting results for the other samples.

3.3.3 Systematics of helium loss.

Calculation of diffusivities from emanation rates assumes that helium loss is controlled by volume diffusion. By measuring multiple aliquots within each experiment it was possible to investigate this assumption. All the experiments displayed smooth extents of gas release as a function of time, as shown in figure 3.4. Helium loss rates

Table 3.4   Basaltic Glass Step-heating Helium Diffusivity Results.

Experiment	Simple Model Ea (kcal) log Do	Refined Model Ea (kcal) log Do	Nominal Size (um)
A1V892-1A			
1. single tabular chip	17.4 (.3) -2.54 (.10)	18.1 (.3) -2.06 (.08)	1400 (150)
2. 13 roughly cubic chips	16.6 (.1) -2.79 (.04)	17.1 (.1) -2.30 (.03)	1300 (230)
3. 2 chips with 5% 100um varioles	17.9 (.4) -2.30 (.13)	18.2 (.4) -1.85 (.1)	1620 (100)
4. 300-355um grains prior loss: 2.6%	16.8 (.2) -2.57 (.11)	17.2 (.2) -1.90 (.1)	328 (28)
5. 75-106um powder prior loss: 5.8(.1)%	15.5 (.2) -3.33 (.07)	16.1 (.1) -2.96 (.05)	90 (16)
6. 38-53um powder prior loss: 9.3(.4)%	14.0 (.4) -3.88 (.2)	14.9 (.3) -3.38 (.2)	45 (8)
CHARCO 98-11T			
7. 8 chips	17.2 (.5) -2.56 (.21)	17.4 (.5) -2.15 (.21	820 (200)
AFTERMATH D9			
8. 17 chips	14.5 (.6) -3.07 (.26)	14.7 (.6) -2.74 (.26)	980 (200)
9. 26 chips	13.9 (.5) -3.87 (.25)	14.0 (.5) -3.75 (.25)	990 (180)
ALV1389-1854B			
10. 9 chips *4He	28.2 (1.0) +3.0 (.5)	28.3 (1.1) +3.5 (.5)	1160 (300)
11. 212-250um grains *4He	25.8 (2.2) +1.0 (1.2)	26.0 (2.4) +1.2 (1.3)	231 (20)

a. The simple (equisized-spheres) model used the nominal size given to estimate Do values. The refined model used measured sizes and shapes. Both models corrected for prior loss in expts. #4-6, using emanation data for 5 and 6 (1s fitting errors given), and a minimum estimate for #4 (see text). Expt. 4 measured release at only two temperatures., its Ea is poorly constrained.

b. 1-sigma Arrhenius line-fitting errors are given for Ea and Do values in parentheses. Including grain measurement errors estimated at 10% suggests 1-sigma errors in absolute diffusivities and Do values of 20%.

Figure 3.4 - #1-6. Fractional release (F) versus time plots for each of the Alv892-1a experiments, numbered as in table 3.4. Note the changing time scales. Experiments #1-3 used glass chips at temperatures of 200-600°C. Experiments #4-6 used sieved powders at 20-300°C. Specific temperature steps for each experiment are given in figure 3.7, here the temperature ramp steps are marked by solid symbols. Experiment #4 was run isothermally except for the first few aliquots.

Figure 3.4
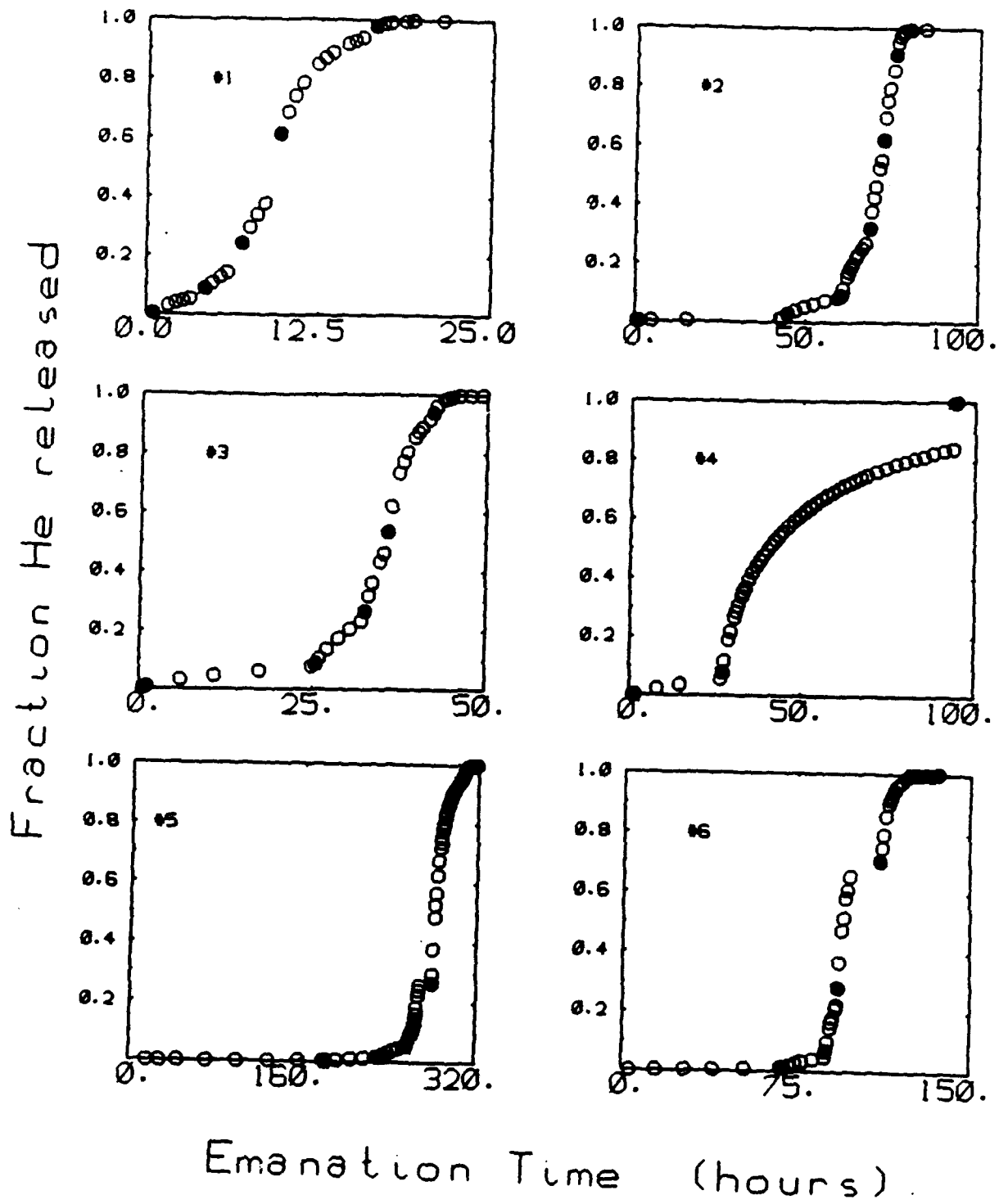
Figure 3.4 - #7-11. Fractional release (F) versus time plots for tholeiite Charco 98-11T (#7), alkali basalt Aftermath D9 (#8 and #9) and for ^{*4}He release from alkali basalt 1854B (#10 and #11). Specific temperatures for each experiment are given in figure 3.7 (the range is 200-600°C), here the temperature ramp steps are marked by solid symbols.

Fraction He Released vs Emanation Time (hours)
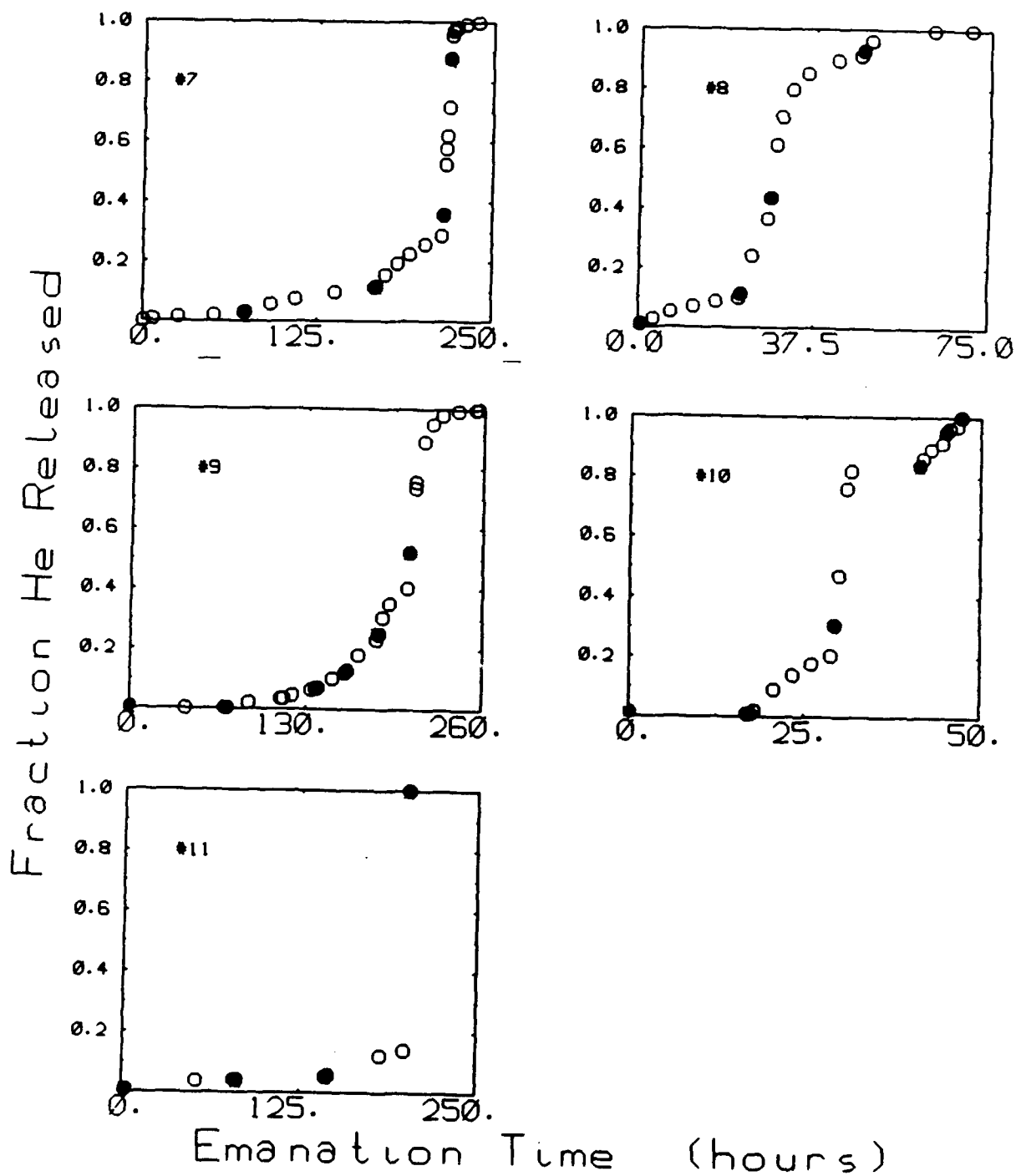
increased when the temperature was raised and leveled off at a new rate without any sudden releases. As discussed below, the isotopic compositions of sequential releases also varied smoothly. These aspects of the releases point towards continuum process such as volume diffusion, rather than events such as vesicle decrepitation or cracking. This is in agreement with examination of the samples in thin section before and after the experiments, which revealed no internal cracks or other changes. The time dependence of release can also aid in distinguishing between different loss mechanisms.

As shown analytically, volume diffusion exhibits a linear dependence between fractional release (F) and the square-root of time ($t^{1/2}$) for low extents of gas loss (e.g less than 20% for a sphere, Inthoff and Zimen, 1956; Fechtig and Kalbitzer, 1966). The F range over which this relation holds varies with grain geometry and in a sample with a distribution of grain sizes and shapes, it is reduced to that for which the smallest grains (with the largest surface to volume ratio) still retain a major portion of their gas (Shaked, 1965). At higher extents of release, plots of F versus the square-root of time will remain monotonic but exhibit concave downward curve shape as the gas release rate tapers off. Other time dependences for release are indicative of different loss mechanisms. For instance, steady-state leakage from a vesicle through a glass wall would yield a linear F versus time relation until the vesicle began to be depleted, and desorption processes exhibit sigmoidal (s-shaped) release curves (Crank, 1975).

All the experiments exhibited release rates consistent with volume diffusion (i.e linear F vs. $t^{1/2}$ relations). A particularly good example is experiment #4 which collected isothermal aliquots over a large F range. Its emanation curve demonstrates that the release is compatible with volume diffusion but not with a steady-state leak or desorption (figure 3.5). Examining the time dependence of release in the finest powders (expts. # 5 and 6) shows both that they lost helium between preparation and analysis and that the release is consistent with volume diffusion (figure 3.6a). However, the limited F range examined at room temperature prevented ruling out a linear F versus time relation (figure

Figure 3.5 Release systematics for small fractional losses in experiment #4. The rate of helium loss displays good agreement with volume diffusion (a, linear with $t^{1/2}$), and shows a distinct departure from a constant emanation rate (b). The break in slope corresponds to an increase in emanation temperature from 123°C to 236°C.

Figure 3.5
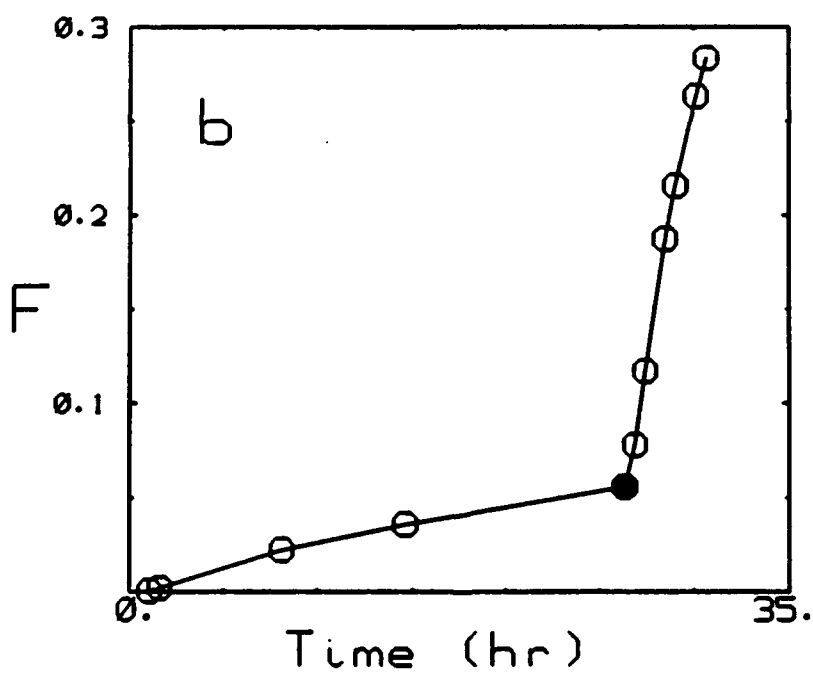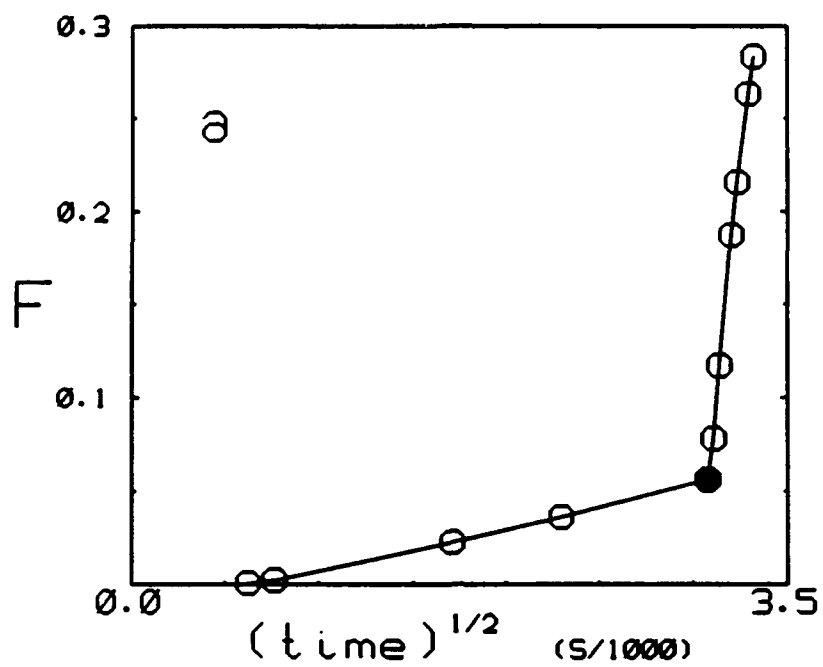
Figure 3.6 Release systematics for tholeiite glass powders at room temperature (squares: expt. #5, 75-106um; circles: expt. #6, 38-53um). The top plot shows that helium release from both powders is consistent with volume diffusion (linear F vs. $t^{1/2}$ relation). In this figure, the time axes are different (top axis for expt. 6, bottom axis for expt. 5), but both measure time from powder preparation, not from the beginning of the emanation experiments. The fact that the F vs. $t^{1/2}$ do not tend to F=0 at $t^{1/2}$=0 reveals the powders lost helium between preparation and analysis. Extrapolating the lines to $t^{1/2}$=0 yields negative F values which correspond to the fractional extent of loss (see text). The lower plot demonstrates that it is difficult to distinguish between constant release rates (F linear with t) and volume diffusion (F linear with $t^{1/2}$ as in top plot) when data is collected over a small F range.

Figure 3.6
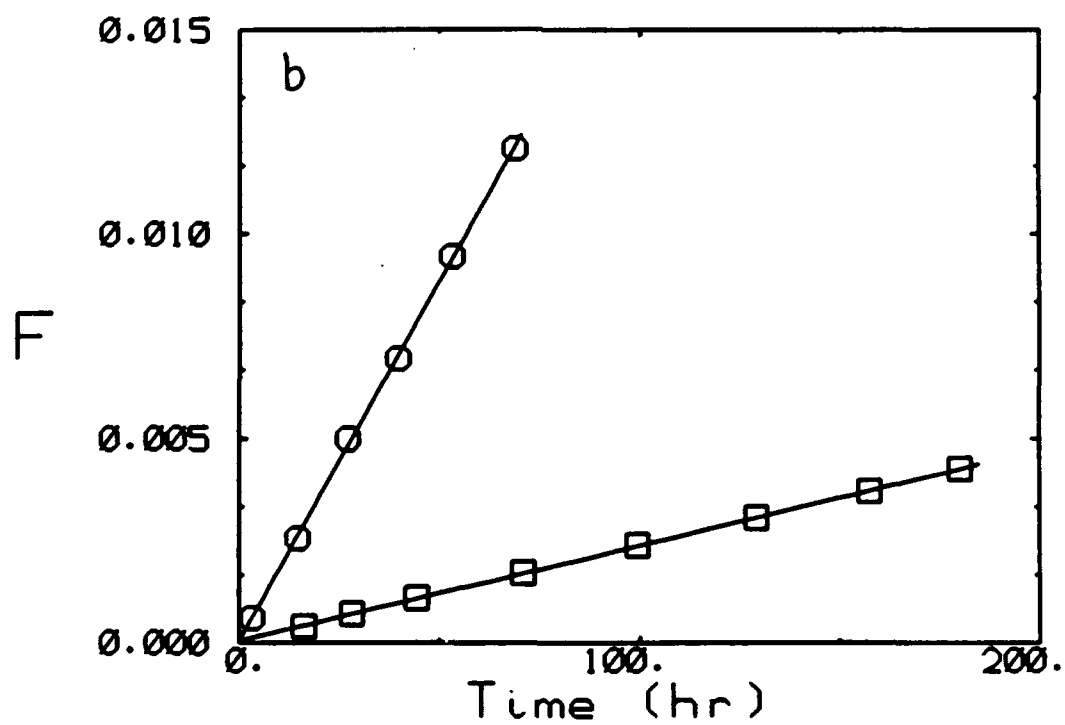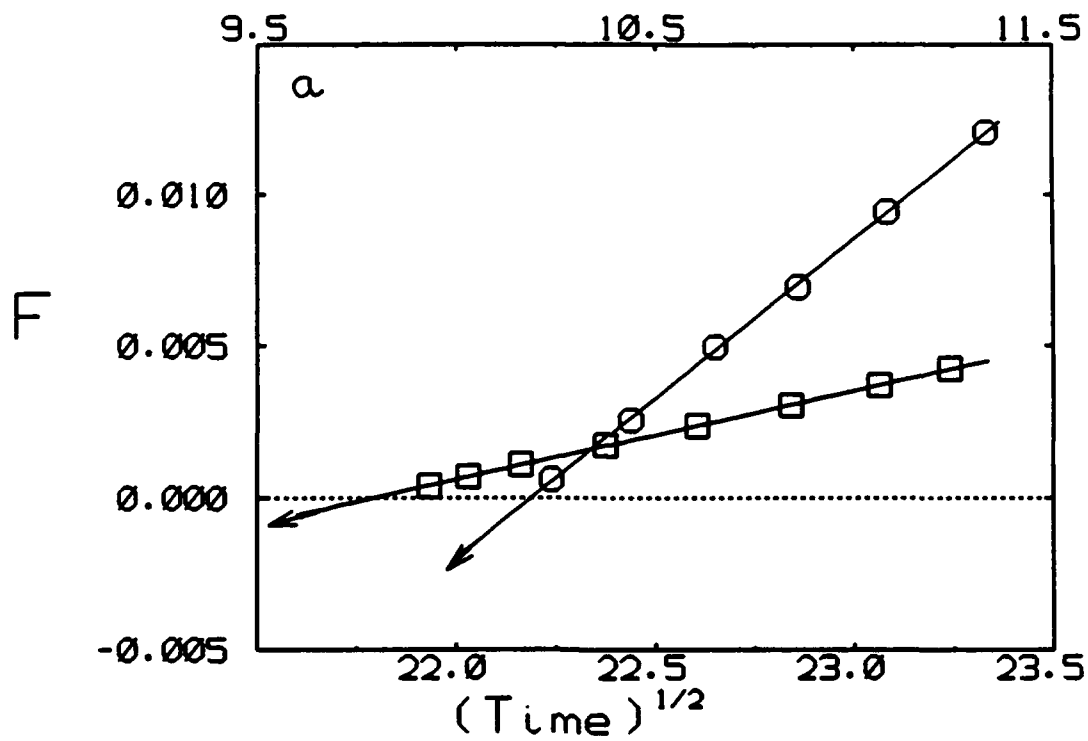
3.6b). Nonetheless, it is clear that the release process is not a steady-state one because more helium remains in stored splits of the powders than the constant loss rates suggested by figure 3.6c allow (data in table 3.3). Applying the volume diffusion time dependence relation to the fine powder data allows the amount of helium lost prior to analysis to be calculated. As shown graphically, extrapolating the F vs. $t^{1/2}$ line to the time of powder preparation ($t^{1/2}$=0) yields the apparent loss, F_a, as a fraction of the measured helium contents (figure 3.6b). The fractional loss of the initial helium contents (the total of measured and lost helium) is thus equal to $F_a x(1-F_a)$. These prior losses amount to a few percent (table 3.4), but are very important in determining diffusivity estimates, as discussed below. The precisions given for the prior losses are the errors associated with the extrapolation.

3.3.4 Calculation of Diffusion Coefficients from a Standard Model.

Helium diffusion coefficients are most easily calculated by assuming that the grains and powders are reasonably represented by equisized spheres with initially homogeneous distributions of helium. This approach has the advantage that approximation equations can be used to determine D directly from F. In contrast, iterative solutions (estimating D to calculate F and then refining D) involving rather cumbersome infinite series equations are required to account for shape and size variations. Measurement errors in determining emanation rates are usually larger than numerical errors from the spherical approximation equations, which provide D estimates within a few percent of values obtained from the full series solution for a sphere. However, as shown below, use of the spherical model leads to other errors because of its poor description of real grain shapes and size distributions. (The approximation equations and complete series solutions are presented and discussed further in chapter 2.)

Diffusive loss from a sphere is controlled by the diffusion coefficient D and the grain radius a, which combined as the parameter D/a^2 define the characteristic diffusive timescale (note its units are

1/t). D/a^2 values can be calculated directly from fractional release and elapsed time data without estimating a representative grain radius. The nature of helium loss can then be considered by examining variations in these values. In general, sequential aliquots taken at constant temperature (T) exhibit constant values of D/a^2 (figure 3.7, #1-11). This suggests that the release process is not strongly dependent on concentration or heating history, but only on temperature as expected for trace component diffusion. Experiment #4, for which helium release was measured isothermally over the greatest range of F, is the best example of this. However, there are exceptions to this behavior. In several experiments D/a^2 increases steadily within the early temperature steps. This effect is particularly pronounced in the fine powder experiments where apparent diffusivities vary by over an order of magnitude (#5 and #6 in figure 3.7), but can be seen in the larger grain runs as well (e.g in the first temperature steps of experiments 3 and 4). This feature is more related to low extents of fractional release than to temperature. For example, it is pronounced in the 113°C data of experiment #2 at very low F (less than .02), present in the 123°C data of experiment #4 at F less than .06, weakly visible in experiment #5 at 112°C for F ranging from .06 to .12, and absent in experiment #6 at 118°C, where F exceeds 10%. Similarly, the strong trends observed in the fine powders (expts. #5 and #6) occur at very low F (less than a few percent). It is clear that these increases of D/a^2 with F are not the result of slow thermal equilibration or temperature drift problems because they also occur at room temperature, and because measured thermal equilibration times for the diffusion vessel (<15 minutes) were much shorter than the emanation intervals (chapter 2).

A different type of deviation from the expected constant D at constant temperature relation occurs at high F values, where D/a^2 values exhibit smooth, and in some cases strong, decreases with increasing F. Examples include experiments using both powders and glass chips (e.g.#6,7,8, and 10). Again, this effect is more correlated with extent of fractional release than with temperature. However, the F value at which D/a^2 begins to decline varies in these experiments from as low as .6 in #10 to over .9 in #6 and #7. In addition to these large trends,

Figure 3.7 - #1-3. Spherical-model helium diffusivities
calculated for each release in the Alv892-1a tholeiite glass chip
experiments (#1-3). Filled symbols mark ramp steps between
temperature plateaus (in ^{o}C). Also shown are histograms
describing the grain assemblies. Viewing the grains as
rectangular prisms, the bars represent the short side length
(hatched), long side length (open) and mean size (filled).
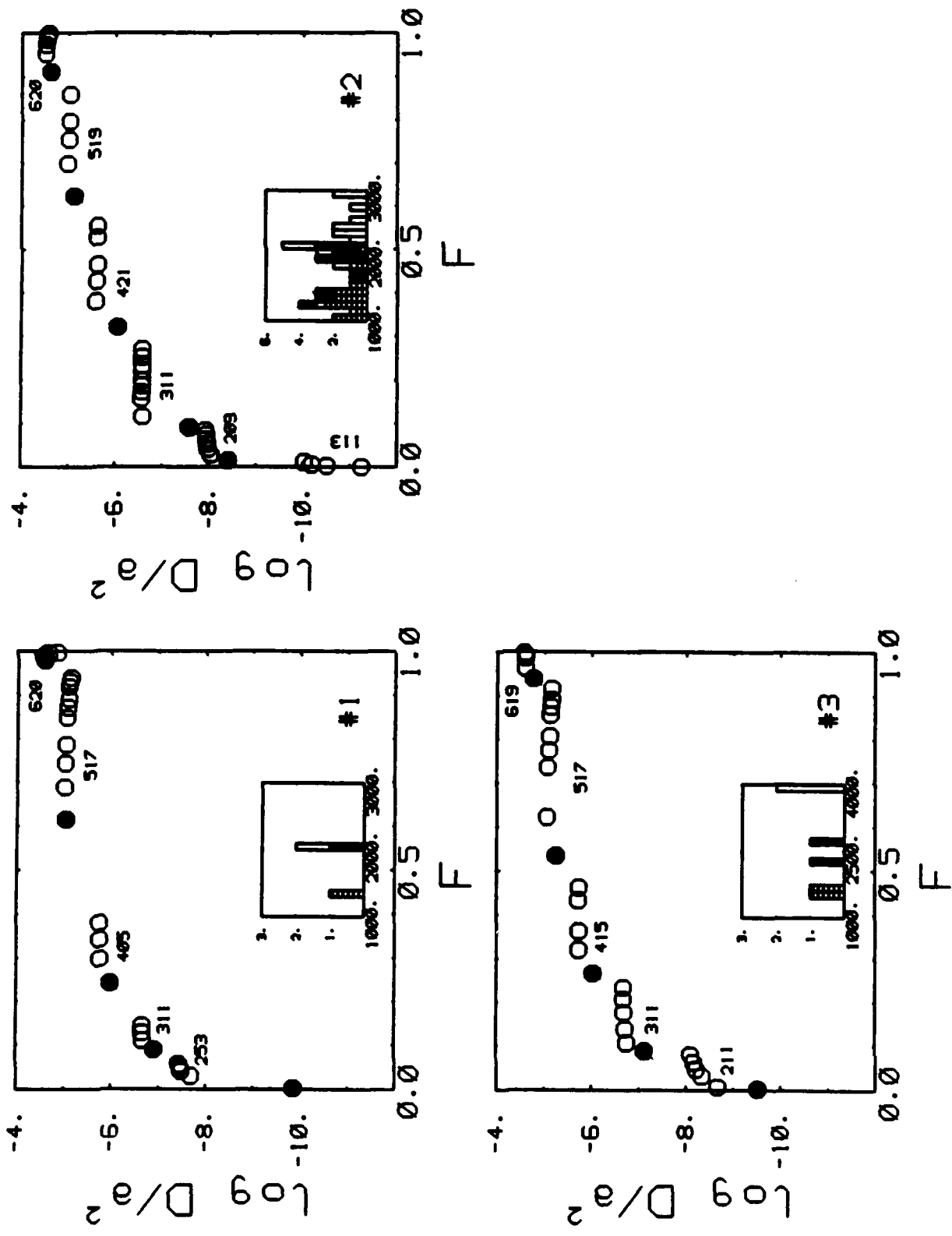
Figure 3.7

Figure 3.7 - #4-6. Spherical-model helium diffusivities
calculated for each release in the Alv892-1a tholeiite glass
powder experiments (#4-6).Filled symbols mark ramp steps between
temperature plateaus (in ^{o}C). Also shown are histograms
describing the grain assemblies. Viewing the grains as
rectangular prisms, the bars represent the short side length
(hatched), long side length (open) and mean size (filled). The
sieve ranges are shown by horizontal bars above the histograms.
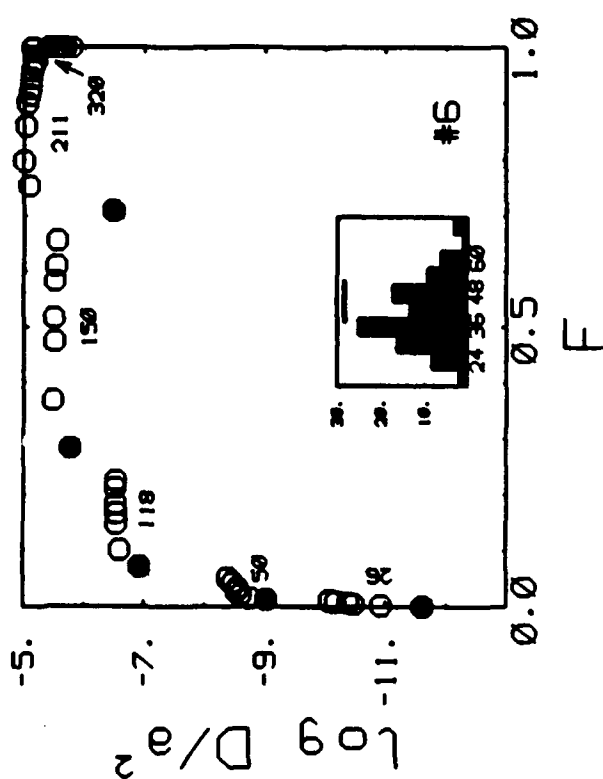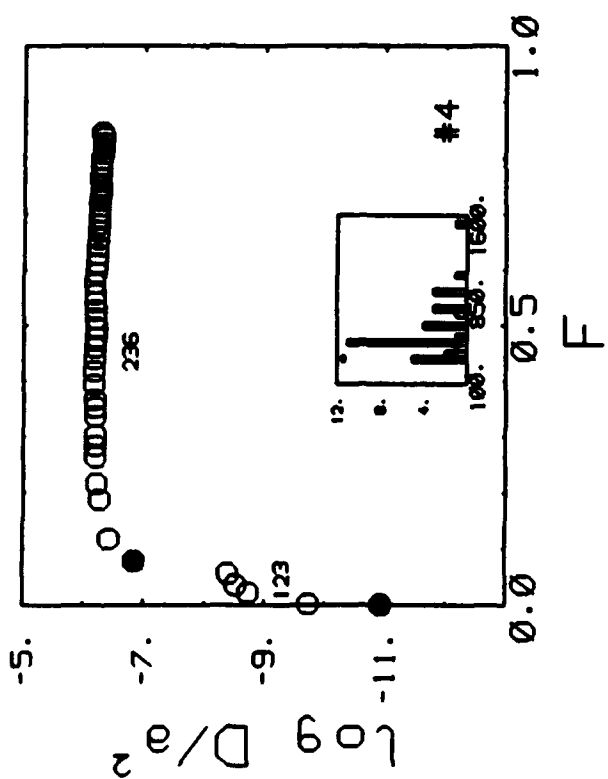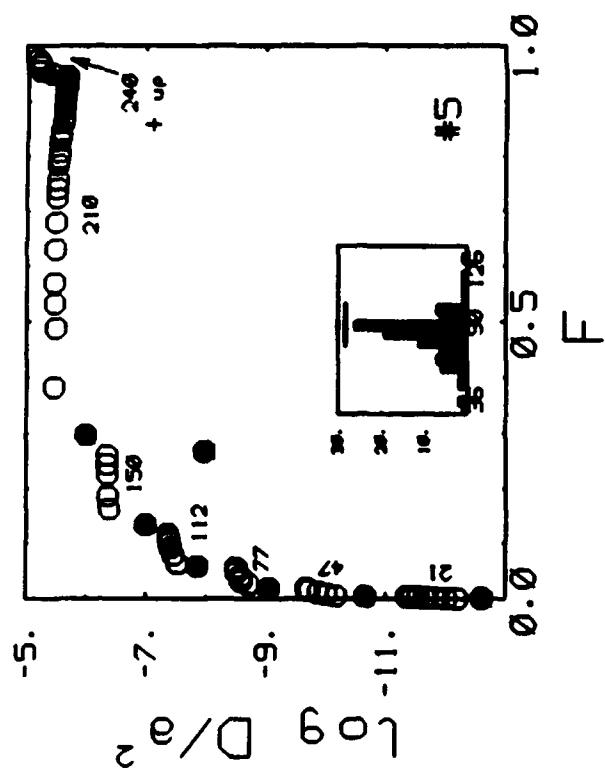
Figure 3.7 - #7-9. Spherical-model helium diffusivities
calculated for each release for Charco 98-11T tholeiite chips
(expt. #7), and two experiments with alkali basalt Aftermath D9
glass chips (#8 and #9). Filled symbols mark ramp steps between
temperature plateaus (in ^{o}C). Also shown are histograms
describing the grain assemblies. Viewing the grains as
rectangular prisms, the bars represent the short side length
(hatched), long side length (open) and mean size (filled).
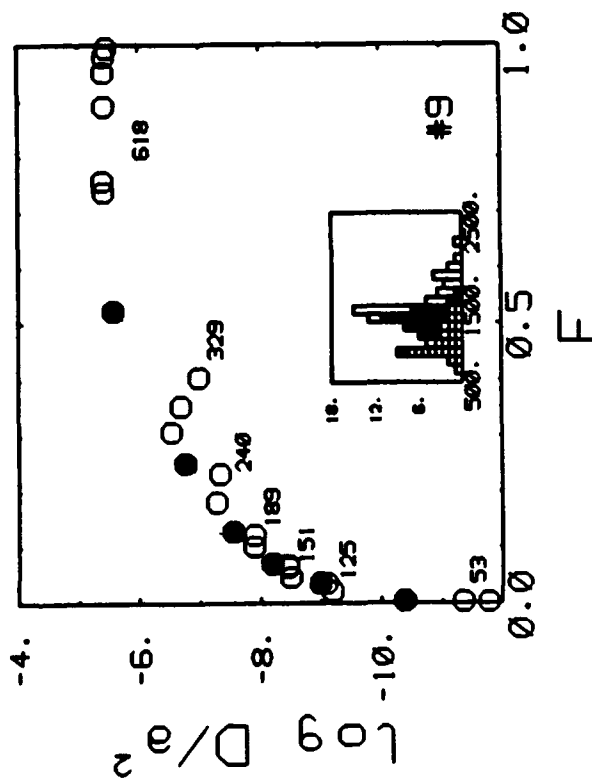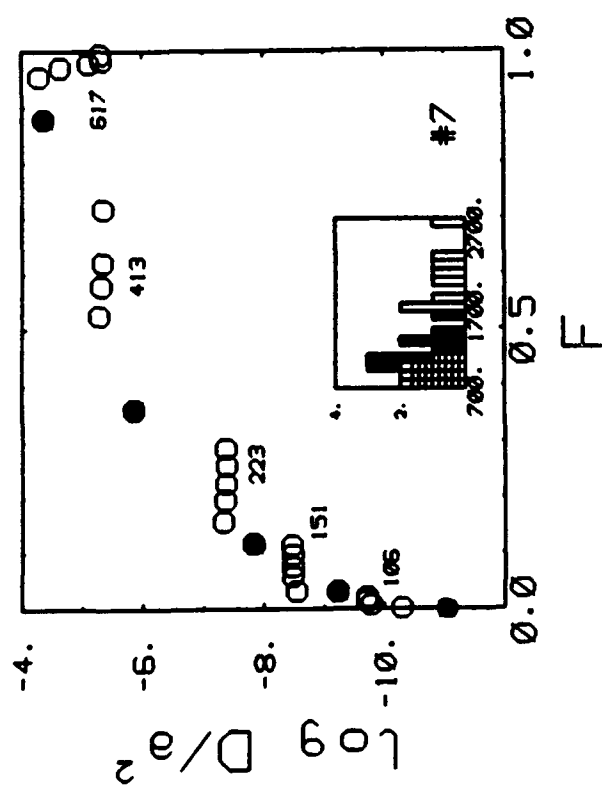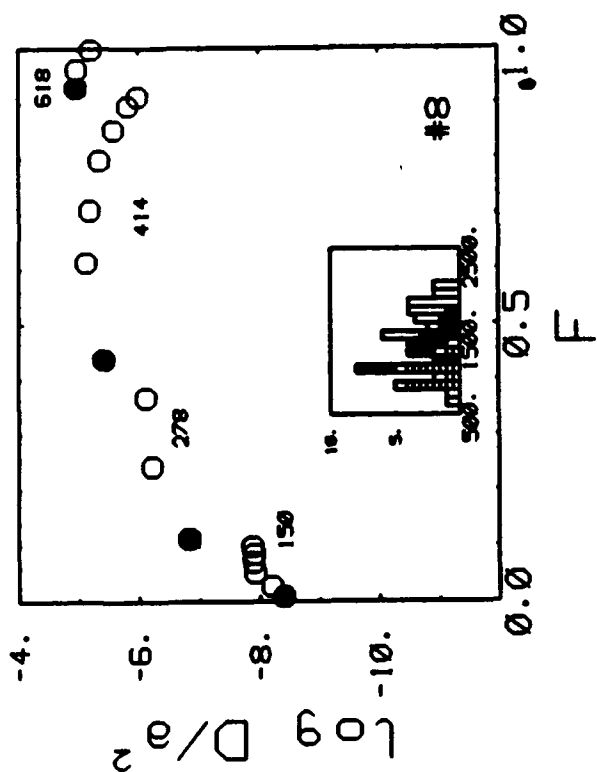
Figure 3.7 - #10-11. Spherical-model helium diffusivities calculated for each ^{*4}He release from alkali basalt 1854B in two experiments. Filled symbols mark ramp steps between temperature plateaus (in ^{o}C). Also shown are histograms describing the grain assemblies. Viewing the grains as rectangular prisms, the bars represent the short side length (hatched), long side length (open) and mean size (filled). The sieve range in expt. #11 is shown by a horizontal bar above its histogram.
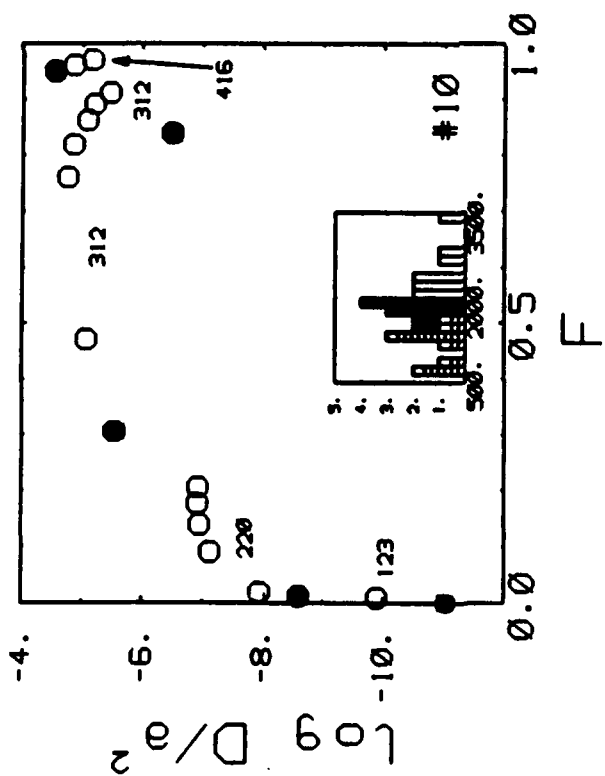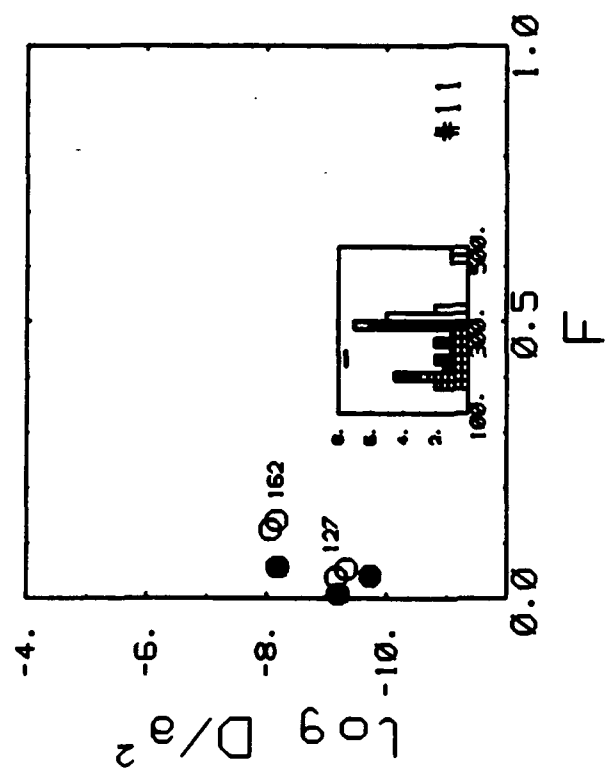
there are many smaller monotonic variations in D/a^2 with F at constant T which are not visible in the plots, but which are significantly larger than the analytical uncertainties related to measured emanation rates alone (see data in Appendix A).

In order to interpret these variations in diffusivity values, the assumptions of the standard spherical model were re-examined. Because the powders (and perhaps other samples) have lost helium prior to analysis, the correct initial condition is a diffusive profile rather than a constant helium concentration throughout the grain. Modelling synthetic isothermal emanation data shows that prior loss leads to apparent diffusion coefficients which are highly underestimated at low F but increase towards appropriate D values as more helium is released (at F values that are large in comparison to the amount of prior loss, correct D values are obtained, figure 3.8). This suggests the increasing D/a^2 values at low F (<10%) in the powder experiments (figure 3.7, #5 and #6) have their origin in not accounting for prior diffusive loss. It also implies that these and other diffusivities determined from grains or powders which have lost helium prior to analysis will be underestimated at low F but tend towards correct values at high F. Fortunately, this problem is readily visible when many aliquots are measured at constant temperature, and in some cases can be corrected for, as shown below.

The standard model assumption that the grains can be represented as a collection of equisized spheres also leads to errors and variations in D/a^2 values. As an example, D/a^2 values calculated from emanation data for cubes and other right prisms display decreasing trends (with roughly constant slope) as F increases, leading to values at high F that are lower by a factor of 2 or so (see chapter 2, figure 2.8). Essentially all shapes will display this decrease in D/a^2 with F when processed with the spherical model because spheres have the lowest surface to volume ratio of any shape and therefore lose helium relatively slowly as emanation begins, but relatively rapidly later when other grain shapes are becoming exhausted. More severe errors arise from the presence of grain size distribution. As with shape variations, D/a^2 values are underestimated at high F, with the problem increasing when size

Figure 3.8 Effect of prior diffusive loss on apparent
diffusivities. Curves derived by discarding successive amounts
of synthetic release data (spherical model with homogeneous
initial condititon, 2% release intervals and log D = -15) and
processing the remaining release data (F versus time) as if it
constituted the entire helium content. Prior loss leads to
apparent diffusion coefficients that are strongly underestimated
at low F, but which trend toward correct values at high F. Note
that the apparent diffusivity is within a factor of 2 of the
correct value for F greater than twice the prior loss amount.
This is because helium is initially lost far more slowly from a
grain with a smooth, diffusive profile than one with an initially
discontinuous (step) profile at the grain surface, yet loss is
similar at high F once both grains have established diffusive
profiles.

Figure 3.8
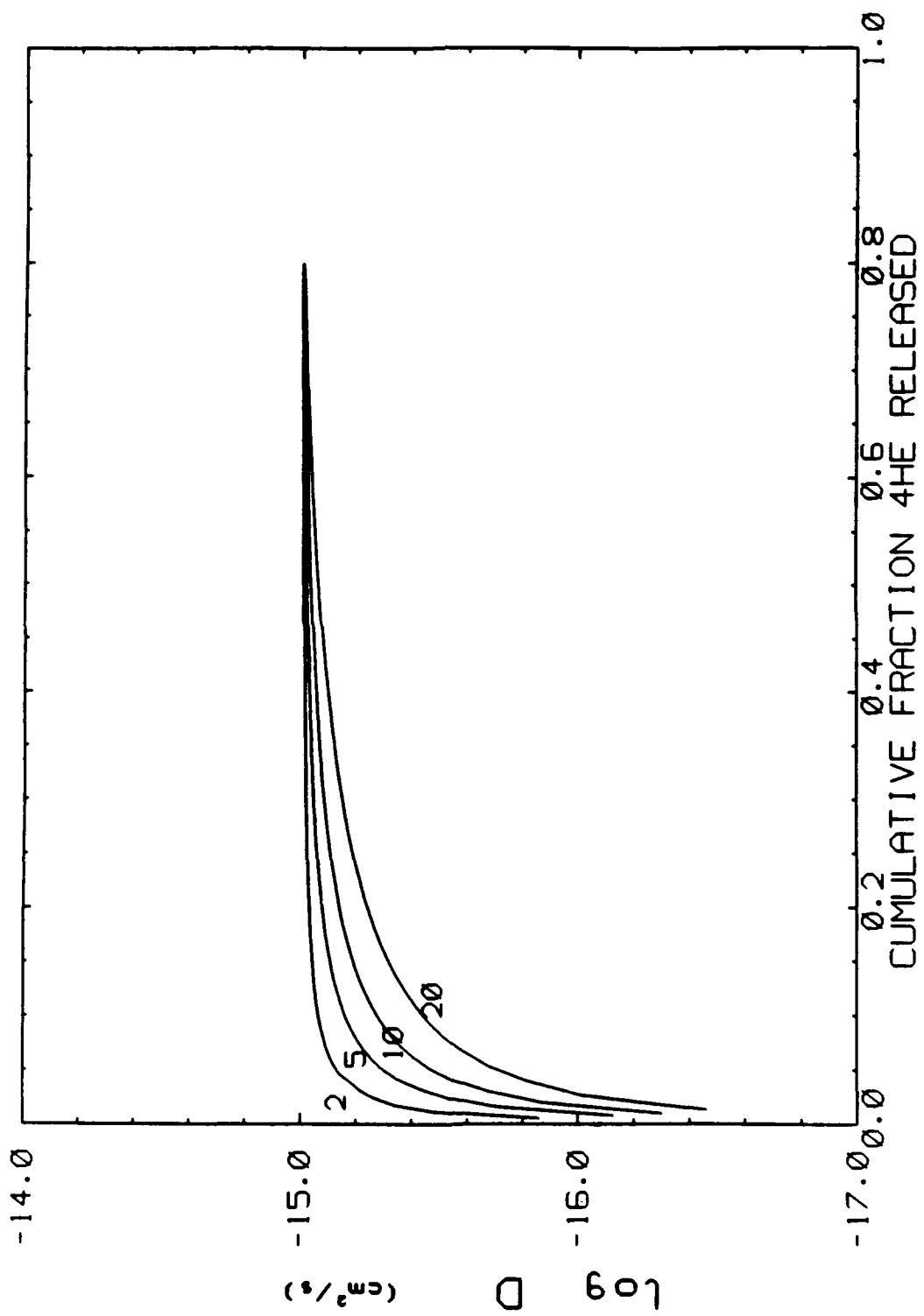
distributions are broad or include rare grains larger than the average size (D/a^2 vs. F trends for several model distributions are displayed in chapter 2, figure 2.9). The decrease in apparent diffusivities occurs because the larger grains lose their helium more slowly and because relatively few of them contribute to the gas loss. **Thus it is important to realize that D/a^2 values can be underestimated well beyond the error expected from the overall range in sizes, because it is the helium mass distribution that controls emanation rates and not just the spread in grain size.** For this reason, conversion of D/a^2 values to D values involves a choice for "a" that is not clear from the size range alone, and without knowledge of the mass distribution large errors can result since D varies with a^2. The effects of grain size distribution have been discussed previously in regard to reaction rate determinations (Gallagher, 1965) and noble gas emanation experiments (e.g. Huneke et al, 1969; Abe, Rauch and Brandt, 1971).

Examining grain size histograms for the experiments (figure 3.7) suggests that most of the decreases in D/a^2 values at high F (>.8) reflect size distribution effects not accounted for by the standard model. The effect is nearly absent in the single grain experiment (figure 3.7, #1), and in experiment #3 which used only two glass chips of very similar size and shape. Experiments #8 and #10 have broad, decreasing D/a^2 trends at high F (above .7 or so) which reflect wide distribution in the short side lengths of these grains (three grain size parameters were measured for each grain in the chip experiments – the shortest side, the "average" side, and the longest side, as shown in figure 3.7). Experiment #8 exemplifies the fact that helium mass distribution governs loss in that D/a^2 drops by an order of magnitude in sequential aliquots at 414°C although the overall short side length range is only a factor of 2. The decrease of D/a^2 in experiment #7 (617°C data) occurs only for F in excess of 90%, consistent with a tighter clustering of short and average side lengths, which in large part govern loss since they represent more direct routes to the grain exterior than the long side length. The powder experiments (# 5 and #6) do not show strong D/a^2 decreases at high F reflecting their narrow size ranges. However, not all variations agree well with the

histograms, for example D/a^2 values do not vary strongly in expt. #2 despite similar size distribution to #8, and the strongly bimodal distribution required to explain the decrease in D/a^2 at 329°C in expt. #9 which does not continue at higher temperature is not evident in the histogram.

In summary, use of the overly simple standard model can produce large errors in calculated diffusivities at both low and high extents of gas release, because of prior loss and grain size and shape distribution effects. These errors can be recognized if many sequential aliquots are measured in emanation experiments. We now address these problems with a refined model.

3.3.5 A Refined Model for Diffusion Coefficient Calculation

Because one of the goals of this research was to accurately determine the low temperature diffusivity of He, a refined model incorporating grain size and shape variations and correcting for prior loss was used. As already discussed, prior helium loss can be recognized in multiple release experiments from the presence of increasing apparent diffusivities at constant temperature, especially when this behavior occurs at low extents of gas loss but does not continue at higher F. When multiple aliquots are collected, a minimum estimate of the extent of prior loss can be made in two ways. If isothermal aliquots were collected over a large F range, the F value at which standard model diffusivites stop increasing and remain constant is a rough minimum (and also a rough maximum) estimate for prior loss, as revealed by the model calculations displayed in figure 3.8. Secondly, diffusivities can be recalculated assuming progressively larger extents of loss until constant values are obtained for constant temperature. This approach is illustrated for the data from powder experiment #5 and suggests a prior loss of about 4.5% (figure 3.9). Correcting the room temperature diffusivities in this experiment for this loss leads to a D/a^2 value of about 5×10^{-11} cm^2/s as opposed to values of 5×10^{-13} to 5×10^{-12} without correction. However, without a maximum constraint on prior loss it is possible the diffusivity is even higher.

Figure 3.9 Successive corrections (subplots a-f) for prior
helium loss in expt. #5 increase and coalesce apparent diffusion
coefficients at low F, leading to relatively constant values of
D/a^2 within temperature plateaus. Temperature ramp steps are
shown by filled symbols. The dotted lines at $D=10^{-11} cm^2/s$ are a
visual reference to reveal that apparent room temperature
diffusivities (RT) increase with the extent of prior loss
correction.

Figure 3.9
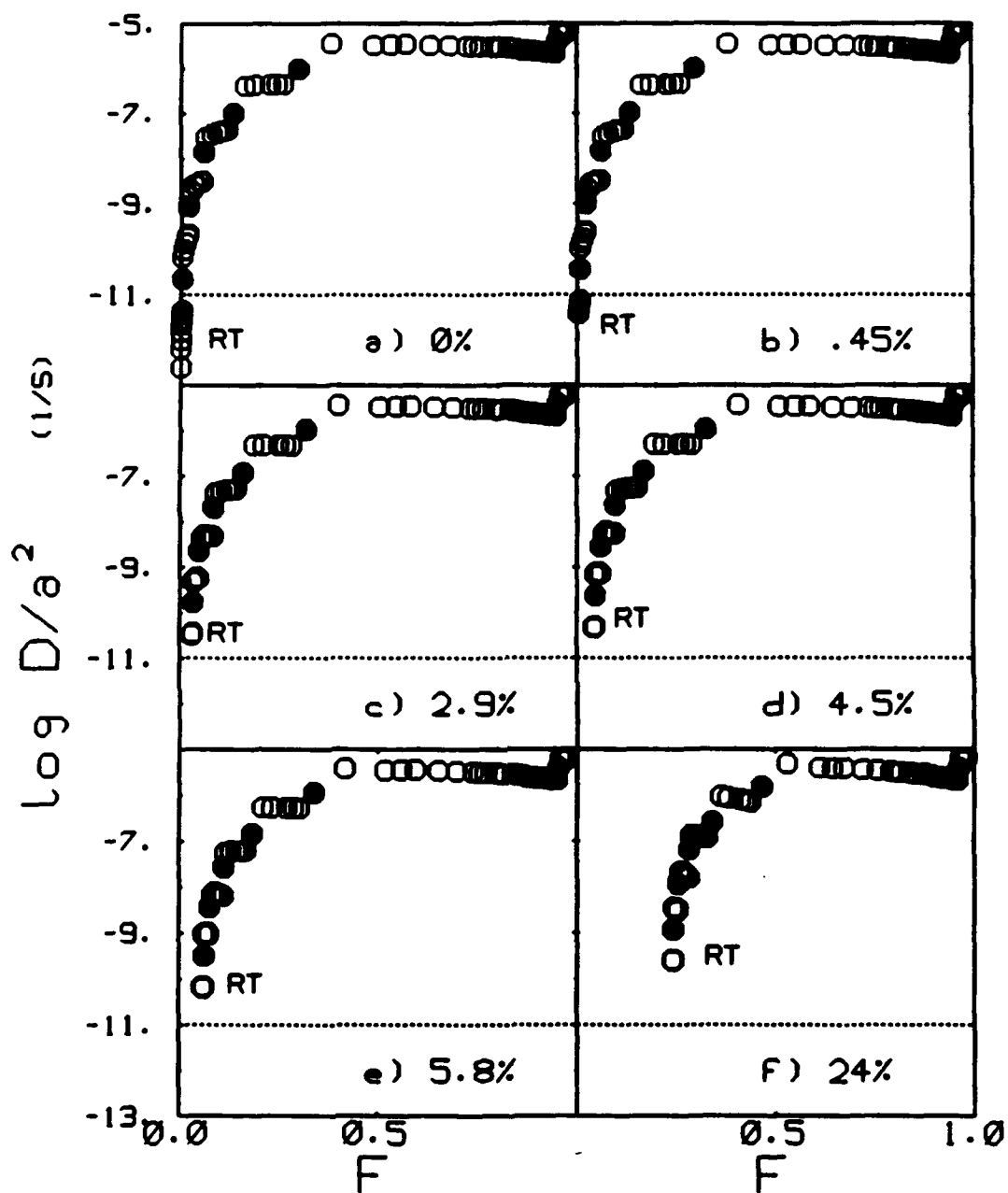
The relationship between extent of prior loss correction and apparent room temperature diffusivity is shown in figure 3.10. This figure also shows that prior loss corrections have an effect on the estimation of thermal activation energies (discussed further below). Fortunately, as discussed earlier, precise estimates of the extent of prior loss can be made for this experiment and for expt.#6, from the linear relations between F and $t^{1/2}$ observed at room temperature (the method is illustrated graphically in figure 3.10). These prior loss values are a few percent higher than suggested by the minimum estimation method (e.g. 5.8% instead of 4.5% for expt. #5). Corrected diffusivities for each aliquot in these experiments were then calculated by incorporating the prior loss amount as a first aliquot. In the other experiments, where it was not possible to accurately correct for prior loss (e.g. #2 and #3), aliquots which showed D/a^2 vs. F trends indicative of prior loss were discounted in obtaining diffusivities and activation energies. Considering the powder experiments as a case study, it is clear that prior loss can lead to highly understimated diffusivites and incorrect activation energies. Thus we believe it is essential to check for this problem by measuring multiple aliquots, particularly in experiments which use natural grain sizes from older rocks where helium loss may have occured over many years.

In addition to making prior loss corrections, the refined model accounts for a distribution of sizes and shapes by treating the grains as collections of parallelpipeds. In the chip experiments, three size parameters were used for each grain, the short side length, "average" grain width, and longest side length, determined by microscopically examining the grains with a size-calibrated grid. For the powders only the average grain width was determined (for 100 randomly selected particles) and the side lengths were assumed to be in the ratio 1,1,1.45 based on visual examination of about 20 randomly selected grains. The size parameters are given along with the emanation data in appendix A, and are displayed as histograms in figure 3.7. The errors in measuring the lengths were about 10%. The grain shapes are not actually parallelpipeds, of course, but this representation does account for major variations in both sizes and shapes and is particularly reasonable

Figure 3.10 Effect of unrecognized prior loss on apparent
diffusion coefficients and activation energies, calculated for
experiment #5 using the spherical model. The inset shows the
method used to determine the extenT of prior loss by
extrapolating release trends at room temperature to the time of
sample preparation (see also figure 3.6).

Figure 3.10
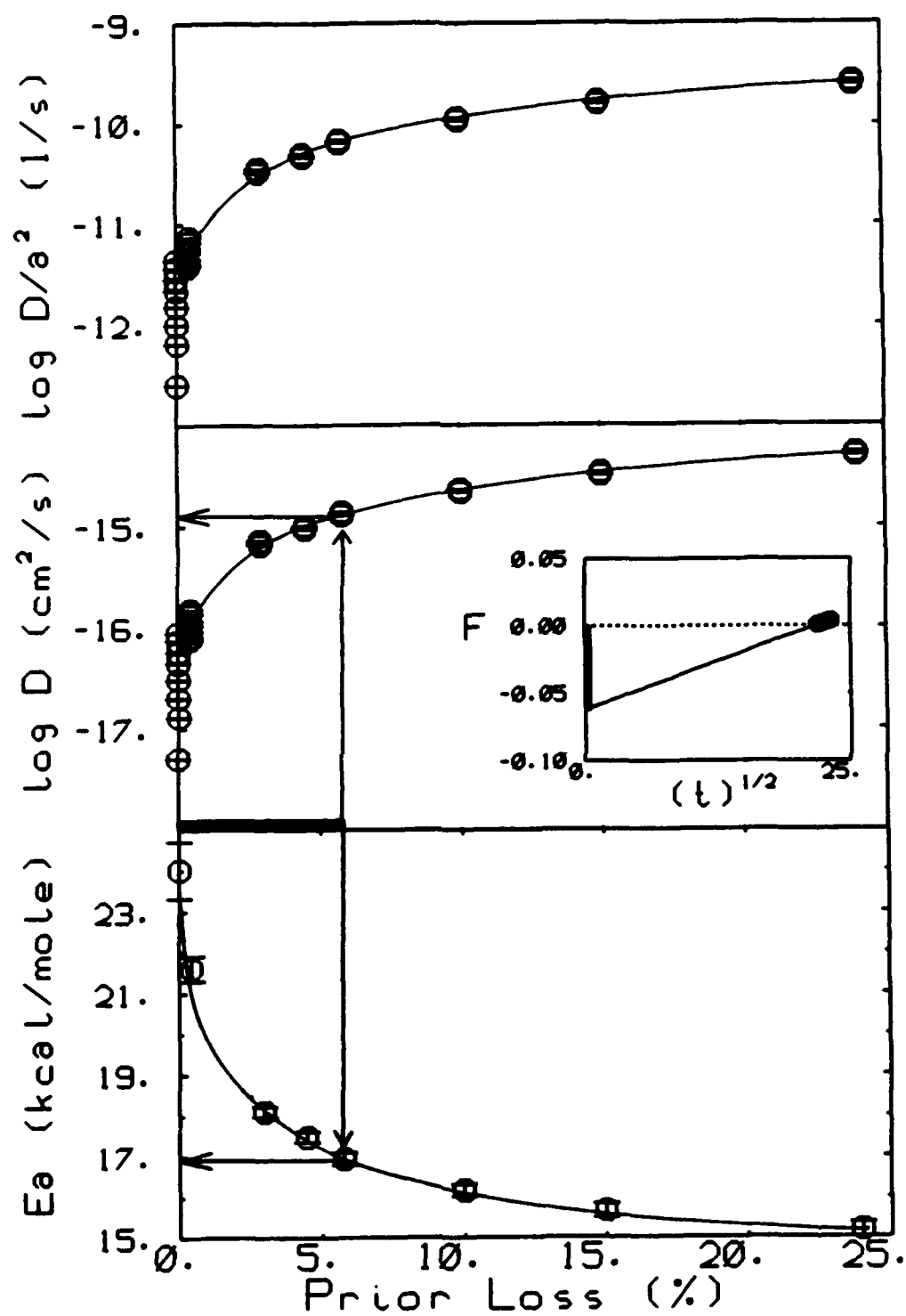
for basaltic glasses, which when fractured tend to form smooth surfaced, sharp-sided grains.

To use these grain size descriptions in calculating refined diffusivity estimates, fractional releases were calculated for each grain individually using the infinite series equations of Inthoff and Zimen (1956) and an initial diffusivity estimate from the spherical approximation equations. These individual grain releases were weighted by grain volume and combined to give the extent of release from the assembly which was then compared to the measured fractional release in each aliquot and the comparison used to iteratively refine the initial diffusivity estimate. A more complete description of the model calculations, including Fortran 77 routines is given in chapter 2. While correction factors have been tabulated for specific size distributions and spherical geometry (Gallagher, 1965; Shaked, 1965), this work represents the first general development allowing the calculation of diffusion coefficients for emanation from an arbitrary distribution of grain sizes and shapes.

Diffusivities obtained from the refined model show far less variation at constant temperature than the spherical approximation results, and in some cases are offset from the simple model values. However, some variations still occur at very high F, and may be attributed to remaining errors in grain size and shape description, estimated at 10% in the size measurements. This high F data is displayed, but discounted in the discussion that follows. For those experiments where the simple and refined model results differ significantly, both are displayed to illustrate the improvement provided by accounting for shape and size distribution.

3.3.6 Temperature dependence of the helium diffusivity.

An exponential temperature dependence or 'Arrhenius relation' :

$$D = D^o \exp(-E_a/RT), \qquad (3.2)$$

where D^o and E_a are constants independent of temperature, is often used to characterize diffusion processes. In some instances this may be an

oversimplification of the true temperature dependence, but examining the data with an Arrhenius plot of Log_{10} versus $1/T$ (^{o}K) is a good way to determine an effective activation energy, Ea, and any deviations from this simple relation.

The three Alv892-1a glass chip experiments at 200 to 600°C exhibit high linearity in Arrhenius diagrams (figure 3.11). The slopes are very similar (figure 3.14) and imply activation energies ranging from 17.1 to 18.1 Kcal/mole with errors of less than 2% (table 3.4). As expected, the refined model suggests greater temperature dependence than the simple model (16.6 to 17.9 Kcal/mole; table 3.4) because it accounts for the emanation decrease from grain exhaustion at high F, where the high temperature data was obtained. Comparing the results of the simple and refined model for experiment #1 which used a single glass chip (17.4 and 18.1 Kcal/mole, respectively) demonstrates the importance of correct shape description as well as of grain size distribution. The remaining errors in describing exact grain shapes and sizes will have the effect of reducing the apparent activation energy, so that even the refined model values must be considered minima. There was no discernible effect of variolitic texture on activation energy Ea (expt. #3), suggesting that the presence of unconnected varioles in a glass sample does not enhance helium loss. The variation in D^{o} values for these experiments (table 3.4) primarily reflects the different Ea values, as the diffusivities are essentially overlapping (figure 3.14).

Diffusivities and the activation energy (17.4$\pm$.5 Kcal/mole) for the other tholeitte, Charco98-11T, are very similar to the Alv892-1a results (figures 3.13a, 3.14b and table 3.4). The agreement between the two tholeiites is strong evidence that the measured helium loss rates are fundamental properties of the material, and not the result of extrinsic factors such as cracking or thermal history. Further, the difference in internal helium distribution between the two tholeiites (table 3.2a) did not affect release, suggesting that dissolution at vesicle walls is not a limiting process.

Arrhenius plots of the Alv892-1a powder experiments are not linear until corrected for prior loss (figure 3.12) and derived activation energies can be in considerable error if this problem goes unrecognized

Figure 3.11 Arrhenius plots for the Alv892-1a tholeiite glass
chip experiments. One sigma errors are smaller than the symbols:
circles for the spherical model, and diamonds for the refined
model. Activation energies corresponding to these regression
lines are given in table 3.4 The lowest temperature data in
experiment #2, obtained at very low F and affected by prior loss,
were not used to obtain the regression line.

Figure 3.11
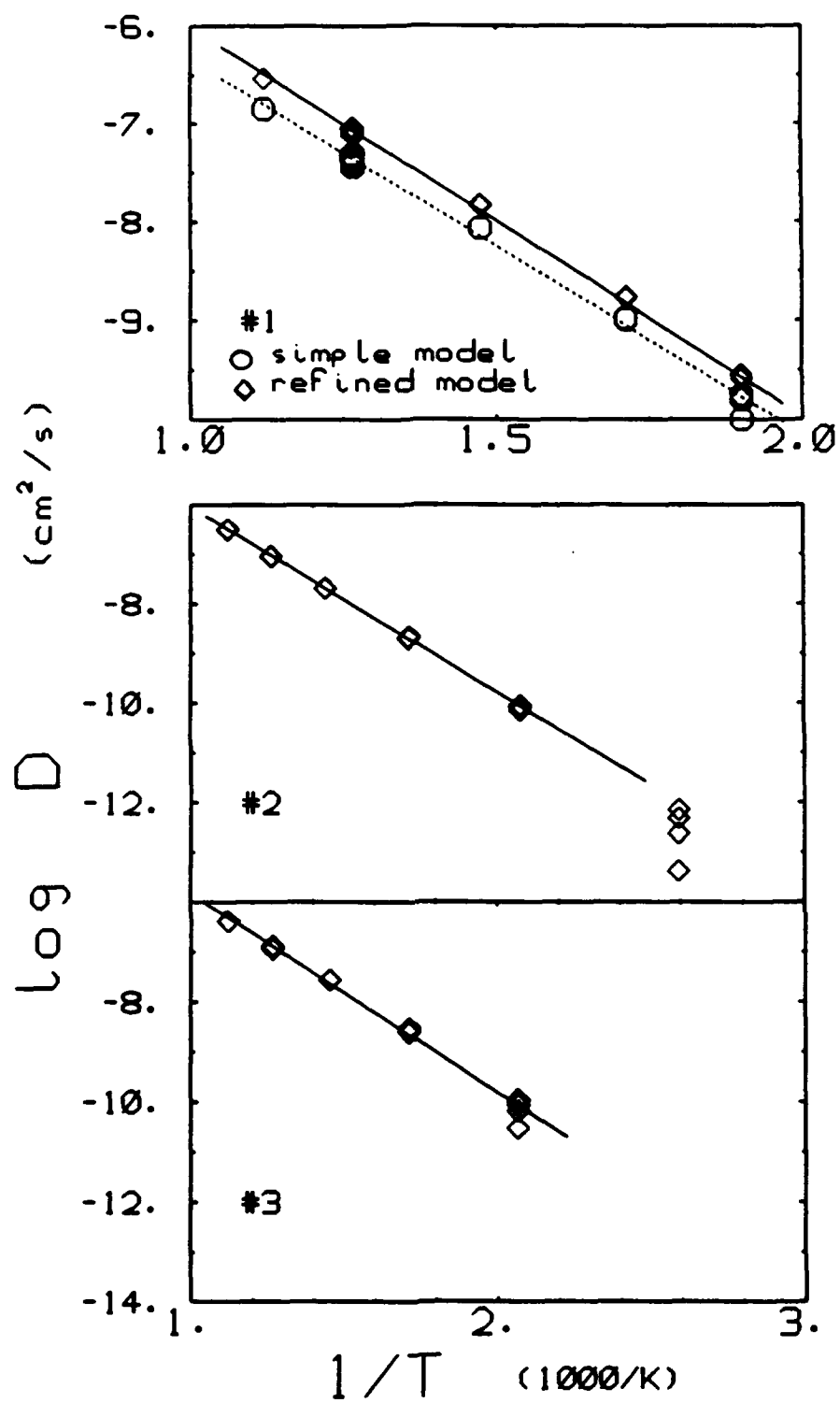
Figure 3.12 Arrhenius plots for Alv892-1a powder experiments #5
(75-106um) and #6 (38-53um). At top are diffusivities determined
using the equisized-spheres model (circles), which suggest non-
linear temperature dependence. Below are values corrected for
prior loss and size and shape variations using the refined model
discussed in the text (diamonds). In the bottom-left plot, a
comparison of the refined model with the spherical model using
prior loss adjusted data shows the improved linearity at high F
(brackets) provided by including shape and size variations in the
refine model.

Figure 3.12
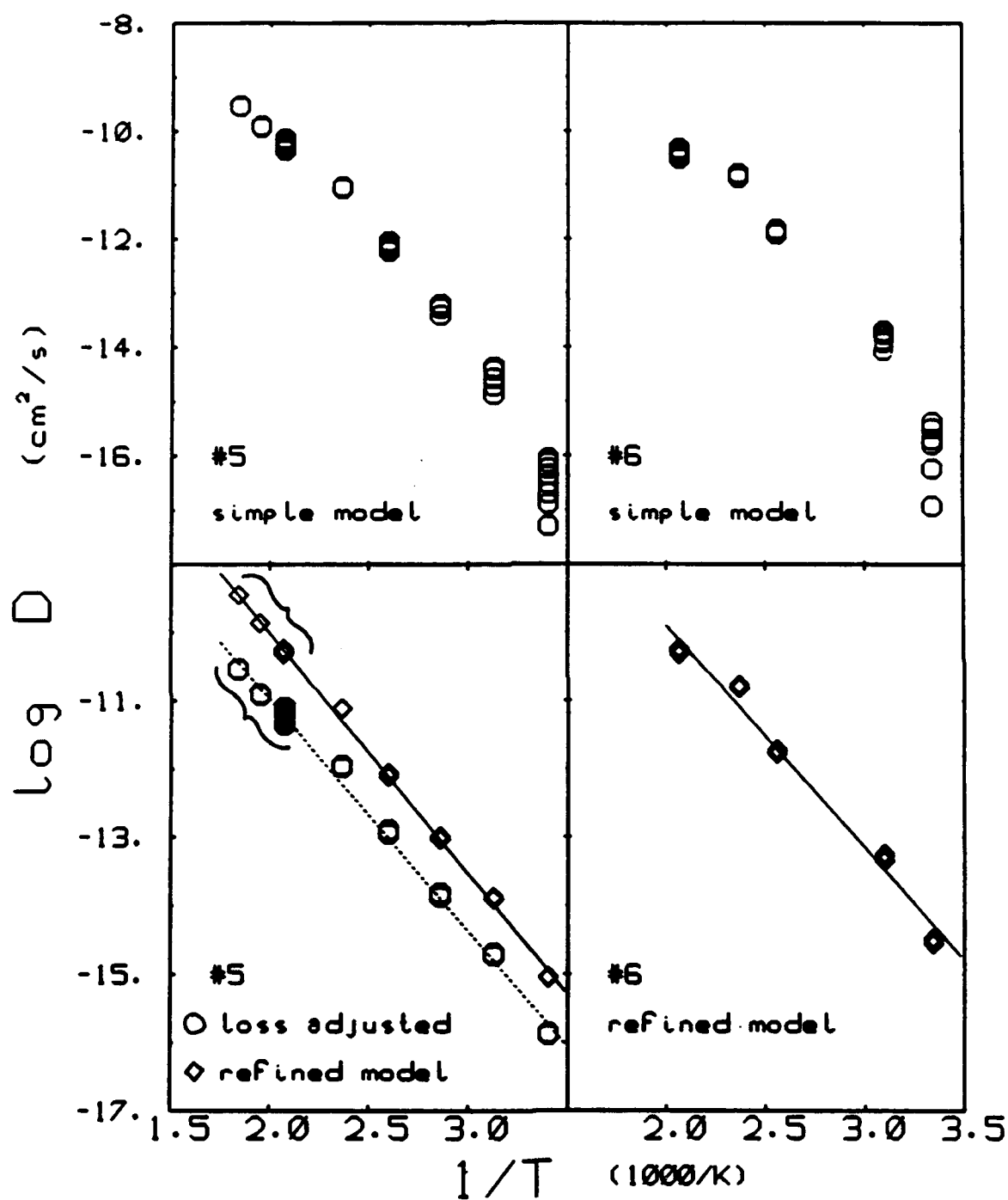
Figure 3.13 Refined-model Arrhenius plots for experiments with tholeiite Charco 98-11 (top), alkali basalt Aftermath D9 (middle), and for ^{*4}He diffusion in alkali basalt 1854B (bottom). Points outside the temperature ranges of the regression lines are affected by prior loss or exhibit constant temperature trends indicative of size description problems and were not used.

Figure 3.13
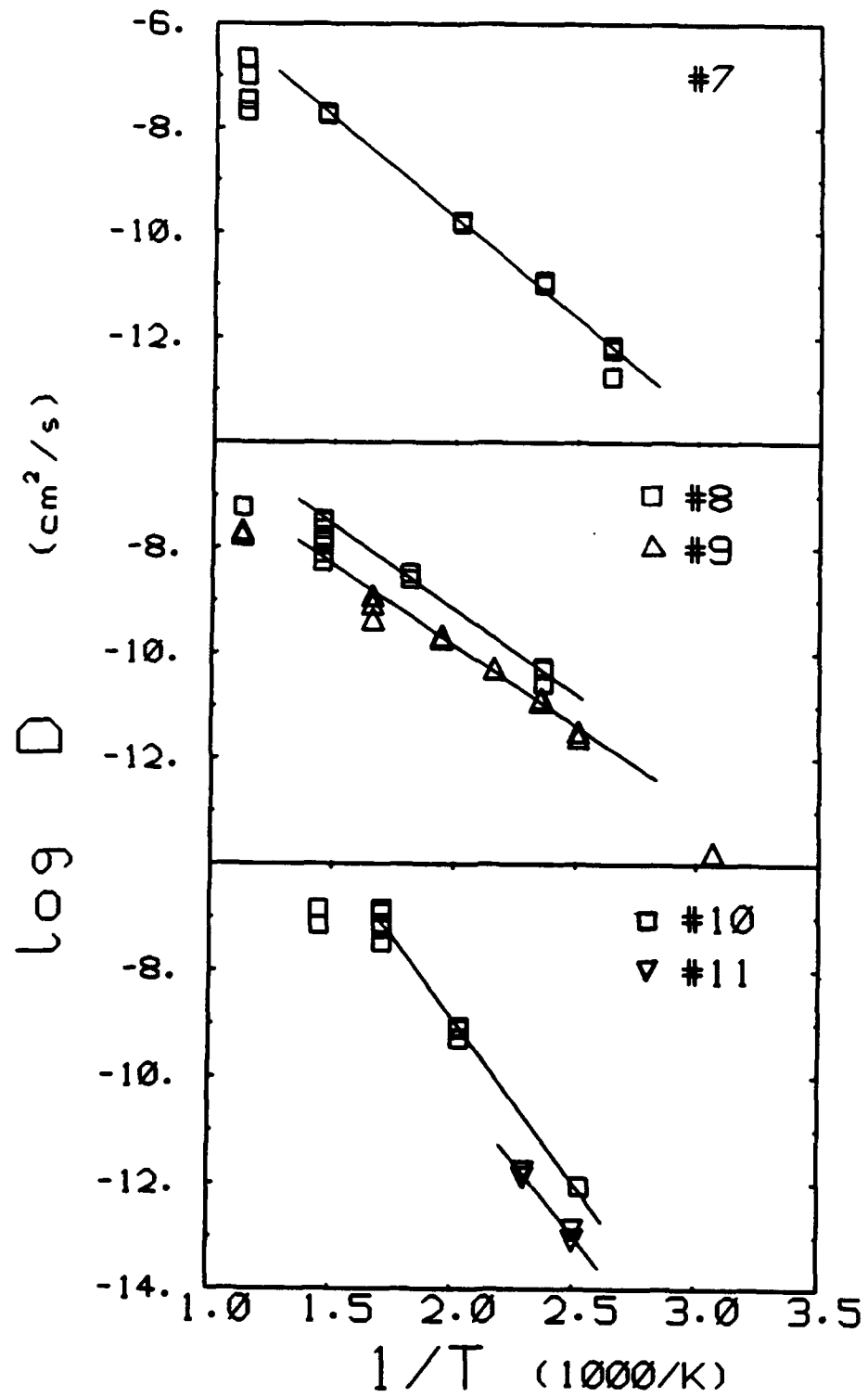
Figure 3.14 Comparison of Arrhenius slopes for all experiments.
The Alv892-1a tholeiite chip experiments (#1-3) are almost
coincident (subplot a, upper left) but the powder data (#5-6)
displays slightly less steep slopes (subplot a, lower right).
Subplot b reveals a similar Ea for the other tholeiite, Charco98-
11T (dashed line, expt. #7) to the mean of the Alv892-1a chip
slopes (solid line), but consistently lower temperature
dependence in the Aftermath D9 alkali basalt experiments (dotted
lines, #8,9). In contrast, thermal activation of ^{*4}He release in
alkali basalt 1854B is stronger than for inherited helium release
in the other samples (subplot c, dashed lines, #10,11; solid line
is mean of Alv892-1a chip values).

Figure 3.14
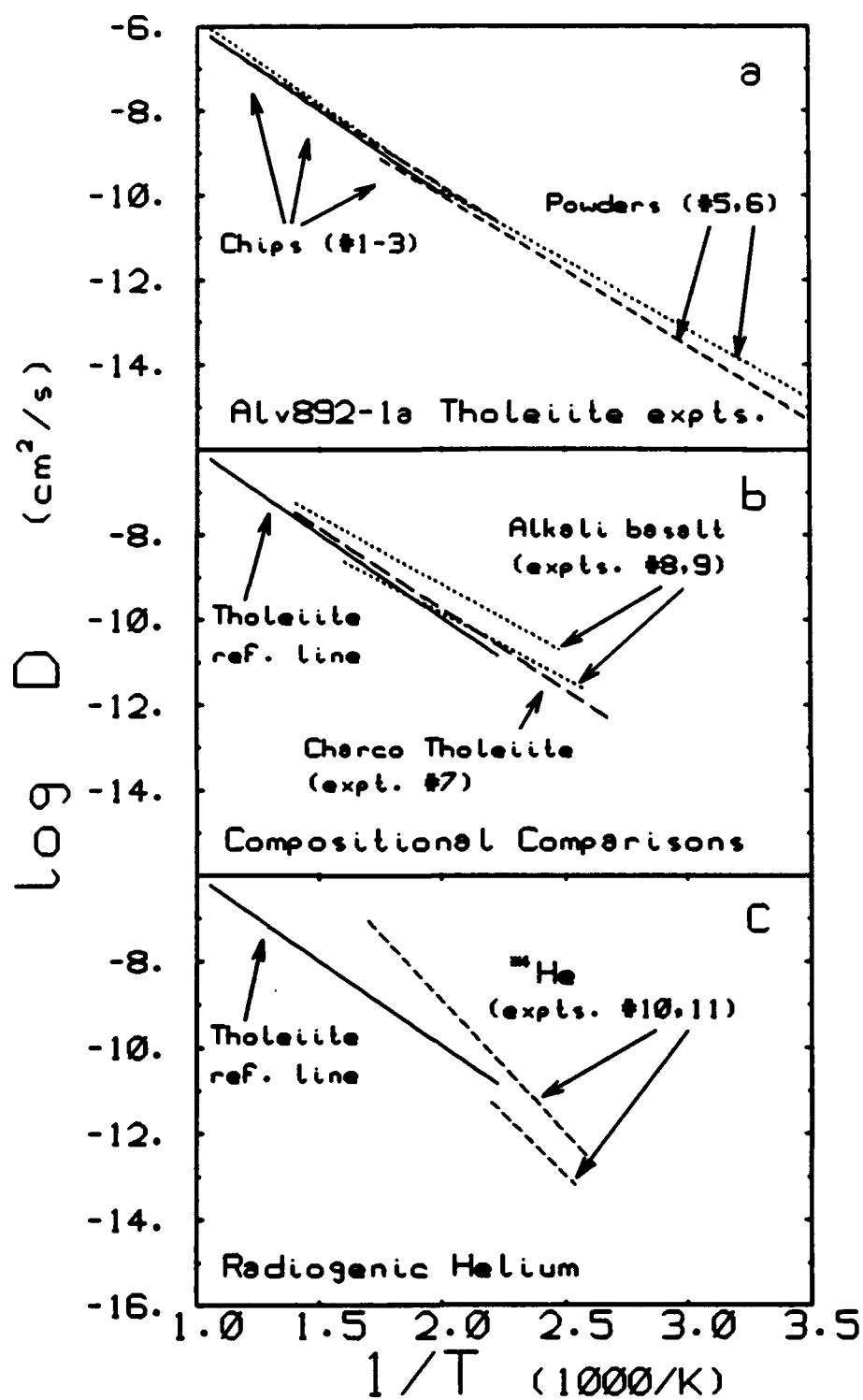
(figure 3.10). When prior loss corrections are made, the Ea values for the powder experiments (16.1 and 14.9 kcal/mole in expts. #5 and #6 at 20-200°C) are significantly less than for chips at higher temperature (table 3.4). In addition, the room temperature diffusivities (1-4 x 10^{-15} cm^2/s) are higher than values extrapolated from the chip experiments (3-9 x 10^{-16}). It is **important to note that these room temperature diffusivity values do not depend on the prior loss corrections.** The slopes of the room temperature F versus $t^{1/2}$ relations used in the prior loss corrections can also be used to determine D (and D^{3}He/D^{4}He) directly from the emanation data without correcting for prior loss. The approximation at low F (less than 10%, Inthoff and Zimen, 1956):

$$F = 2/\sqrt{\pi} \ \ x \ S/V \ x \ (Dt)^{1/2} \tag{3.3}$$

can be rewritten:

$$D = \pi/4 \ x \ (V/S)^2 \ x \ \{dF/d(t^{1/2})\} \tag{3.4}$$

where S/V is the surface to volume ratio for the collection of grains and the condition of low F must apply to the smallest grains and $dF/d(t)^{1/2}$ is the slope of the F versus $t^{1/2}$ plot. Values obtained this way, calculating S/V from the histograms, are indistinguishable from the refined model results. The advantage of making the prior loss estimate is that data obtained at higher F can then also be used to calculate correct diffusivities and activation energies.

Because one of the major goals of this study was to determine the helium diffusivity at seafloor temperatures, it is important to understand the differences between the powder and chip results and their implications for the temperature dependence of helium mobility. First of all, the higher diffusivities measured at room temperature are probably real. The error in measuring grain size of 10% gives them a precision of about 20%. In addition, the similar diffusivities obtained near 200°C for a wide range of grain sizes (experiments 1-7) suggest that the diffusion length scale corresponds to the physical grain size, and thus

that any effects of powder preparation, such as generation of internal cracks, are small. This is consistent with the optical and SEM appearance of the powder particles which showed no deep fracturing or particles finer than the sieve range, and with surface area measurements using the nitrogen condensation method (Brunnauer, Emmett and Teller, 1938) which gave values in good agreement with measured grain sizes (unpublished results). Therefore, the diffusivities are probably accurate as well, although differences between the powders throughout the 20-200°C range, as well as between all experiments in the vicinity of 200°C, allow variations of a factor of 2 to 3 (see figure 3.15). The powder activation energies rely on the prior loss corrections, but these are quite precise (table 3.4) and in accuracy are likely to err on the low side (because of the nature of the F vs. $t^{1/2}$ approximation) so that the activation energies are effectively maxima. This and the fact that both powder experiments have lower activation energies than the chip experiments suggests the difference in activation energies reflects the different temperature ranges of the experiments, powders below 200°C and chips above 200°C, rather than a dependence of helium mobility on grain size.

Synthetic glass studies have also found that helium diffusion activation energies increase slightly with temperature (Shelby and Keeton, 1974). These workers suggested this could result from the non-crystalline nature of glass structure, and showed that a Gaussian distribution of activation energies could account for the observed temperature-dependent activation according to:

$$D = D^o \, e^{(-u/RT)} \, e^{(s^2/4R^2T^2)} \qquad (3.5)$$

where s is the standard deviation of a normal distribution of activation energies with mean u. However, transition-state models assuming a single activation energy also allow for varying temperature dependence of the form:

$$D = D^o \, T^n \, e^{(-Ea/RT)} \qquad (3.6)$$

143

Depending on the assumptions made about solute atom motions in the transition state, n can take on the values of 1 (high frequency vibrations), 1/2 (translational motions), or 0 (low frequency vibrations) corresponding to the Arrhenius relation (e.g. Stearn and Eyring, 1940).

In an effort to investigate these different diffusion models, data from all the tholeiite experiments (#1-7) were combined (228 points after culling values affected by prior loss or size distribution problems) and examined for a best description of their temperature dependence by chi^2 minimization (Bevington, 1969). In terms of minimizing chi^2 values and producing temperature-independent scatter of residuals, none of the more complex expressions provided a better fit to the data than a simple Arrhenius exponential with Ea of 16.85$\pm$.13 and log D^O of -2.37$\pm$.06. However, this Arrhenius expression cannot incorporate the lower activation energies observed below 200°C in the powder experiments (less than 16 Kcal/mole). In this regard, the expressions with a non-zero T^n term also were unable to provide as large a variation in apparent Ea as observed in the experiments, and therefore offered no particular advantage over the Arrhenius relation. The function incorporating a distribution of activation energies could account for the increase of apparent activation energies (Arrhenius Ea values) from 15 to 16 Kcal at less than 200°C to 17 to 18 kcal above 200°C (table 3.4), provided the normal distribution was characterized by a mean (u) in the range of 20-21 Kcal/mole and a standard deviation (s) of 2.6 to 2.8 Kcal/mole. These expressions gave slightly higher chi^2 values in fitting the collected data than did the simple Arrhenius line. However, because the fitting errors are dominated by grain size errors, which affect the comparison of absolute diffusivities from different experiments to a far greater extent than they affect activation energies derived within single experiments, the ability to account for Ea values which vary with temperature is an important criterion in selecting a temperature-dependence equation. The distribution of activation energies model does the best job of incorporating this aspect of the data (a curve for u=20.5 and s=2.8 is shown along with the best Arrhenius fit in figure 3.15). However, it must be emphasized that

Figure 3.15 Temperature dependence of helium diffusion in
tholeiitic glass. Open circles- data combined from experiments
#1-7.; solid hourglass - storage results; solid circles - results
of Jambon, Weber and Begemann (1985). The dotted line shows the
Arrhenius temperature dependence ($E_a=19.9 \pm 1.0$ Kcal/mole)
determined by Kurz and Jenkins (1981). The solid line is a
least-square Arrhenius relation to the combined data from expts.
#1-7 and yields $E_a=16.85 \pm .13$ Kcal/mole. The dashed line is the
temperature dependence predicted for a Gaussian distribution of
activation energies with mean of 20.5 Kcal/mole and 2.8 Kcal/mole
standard deviation.

Figure 3.15
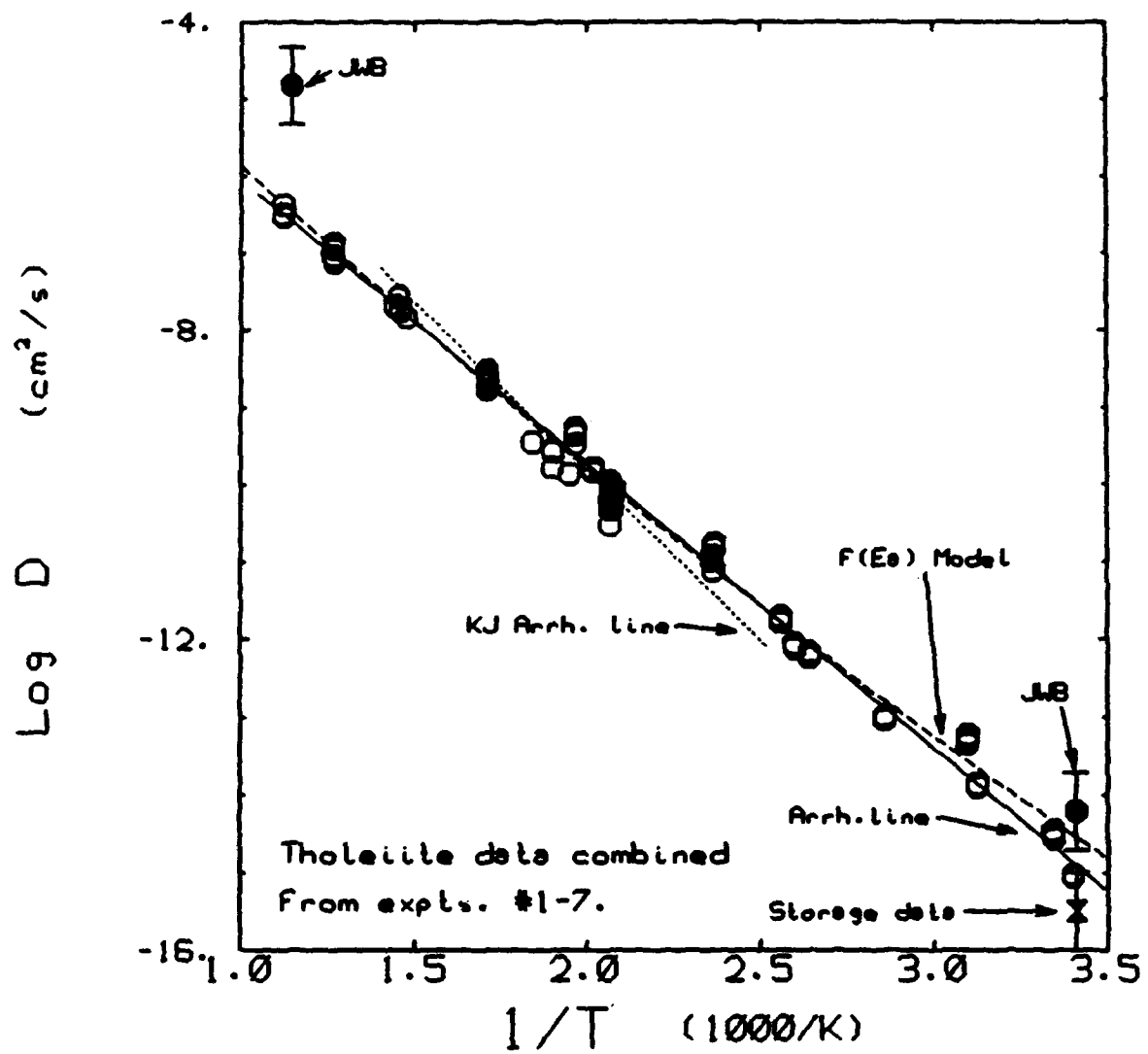
given the experimental errors it cannot be confidantly asserted that helium diffusion in basaltic glass must be characterized by a non-Arrhenius temperature dependence.

In principle, the distribution of activation energies model could be investigated further by measurements at higher temperature. It is also possible that the low temperature helium diffusivity departs from Arrhenius behavior for other reasons, such as contributions from more than one atomic mechanism for example extrinsic defects may be relatively important at low temperature but not at high temperature (e.g. Reynolds, 1960). In the discussion that follows, both the best-fit Arrhenius function and the distribution model are considered in extrapolating the measurements to different temperatures.

The results of experiments #5 and #6 represent the lowest temperatures, $21^{o}C$ and $26^{o}C$, for which helium emanation from basaltic glass has been measured. The diffusivities at these temperatures are $9.0_{+}.3 \times 10^{-16}$ and $21_{+}4 \times 10^{-16} cm^{2}/s$ respectively (Appendix A data tables #5 and #6). These values are in good agreement with the $20^{o}C$ diffusivities obtained by the overall Arrhenius fit to the 7 tholeiite experiments $(12_{+}2.5 \times 10^{-16} cm^{2}/s)$ and the distribution of activation energies model $(30_{+}10 \times 10^{-16} cm^{2}/s;$ table 3.5). In comparison to the "room temperature" storage results of Jambon, Weber and Begemann (1985), $60 \times 10^{-16} cm^{2}/s,$ the diffusivities obtained here are lower, but within the factor of 3 error bounds reported by those workers. The difference is consistent with the already discussed observation that storage results are likely to be biased toward high values because of experimental shortcomings.

The new diffusivity estimates are much higher than the value of $1.6 \times 10^{-16} cm^{2}/s$ at $20^{o}C$ implied by extrapolating the Arrhenius line obtained above 200 ^{o}C by Kurz and Jenkins (1981). In order to understand this difference, their data (published in Kurz, 1982) was re-examined. Evidence for prior loss was found in two of their 90 and 160um powder experiments which exhibited increasing apparent D values at constant temperature at low F. In addition, these workers combined D values from several experiments with different grain sizes to obtain an activation energy, a procedure which (as already discussed) introduces

grain size measurement errors into the E_a determination. Discounting
the prior loss compromised data and recalculating activation energies on
an individual experiment basis leads to a mean E_a of $17.8\pm.9$ Kcal/mole
(very similar to the results obtained for chips at elevated temperatures
here, table 3.4). It should also be pointed out that propagating the
reported error of 1 Kcal/mole in the original work to $20^{o}C$ leads to a
factor of 6 error in D, so that the apparently large difference between
D values reported by Kurz and Jenkins (1981) and Jambon, Weber and
Begemann (1985) was not as significant as initially suggested. To
summarize the new low temperature results and their relation to the
previous studies, it can be said that unconsidered errors in the
previous studies lead to diffusivity estimates which appeared to be
radically different but actually were not given the real errors
involved, and that the true low temperature helium diffusivity lies
between the previous results.

Extending the new results to seafloor temperatures ($0^{o}C$) suggests
values of a few times $10^{-16} cm^2/s$ for tholeitic glass, with the precise
value depending on the temperature relation chosen. Extrapolating the
powder Arrhenius fits (epxts. 5 and 6) suggests a one sigma range of 1-
8×10^{-16}, the overall Arrhenius fit to experiments 1-7 suggests
$1.4\pm.3 \times 10^{-16}$, and the distribution of activation energies model implies
$5\pm2 \times 10^{-16}$ (table 3.5). These variations can be taken as representative
of the errors in characterizing the temperature dependence of helium
diffusion. Note that all values are an order of magnitude higher than
the value ($1 \times 10^{-17} cm^2/s$) suggested by Kurz and Jenkins (1981). The
results can also be extrapolated to magmatic temperatures. The results
for a single chip at $200-600^{o}C$ (expt. #1) extrapolate to $1.2 \times 10^{-5} cm^2/s$
at $1100^{o}C$, the overall Arrhenius relation (expts. #1-7) yields
$9.2\pm.5 \times 10^{-6}$ at $1100^{o}C$ and $2.4\pm.6 \times 10^{-5} cm^2/s$ at $1350^{o}C$. These values are
very similar to the diffusivity of $5 \times 10^{-5} cm^2/s$ measured for tholeiitic
melt at $1350^{o}C$ by Lux (1987). In contrast, the distribution of
activation energies model suggests a diffusivity at this temperature of
a few times $10^{-2} cm^2/s$, implying that this model can not hold at higher
temperatures (above the glass transition).

Table 3.5 Helium diffusivity estimates for basaltic glass.

Experiment	log Do (cm^2/s)	Ea (Kcal/mole)	$D(20^oC)$ $(10^{-16}$	$D(0^oC)$ $cm^2/s)$
Tholeiitic basalt:				
Emanation experiments at 20-600°C (#1-7):				
Overall Arrhenius line	-2.37+.06	16.85+.13	12+2.5	1.4+.3
Ea Distribution model (mean u, stand. deviation s)	-1.5 +.15	u=20.5 +.5 s= 2.8 +.3	30+10	5+2
Diffusivities measured by emanation at room temperature: (21°C, expt. 5) (26°C, expt. 6)			8-9 23-35	
Diffusivities measured by storage at room temperature: Uncorrected Corrected for crushing losses			10-100 1-10	
Alkali basalt (200-600°C)	-3.24+.20	14.4+.5	150(x2)[a]	20(x2)
Radiogenic helium in alkali basalt (200-600°C)	+2.4 +1.0	27+2	.03(x5)	.003(x10)
Kurz and Jenkins (1981)	-1.2(.3)	19.9(1.0)	1.6(x6)	0.1(x7)

Tholeiitic basalt emanation data at 150-600°C. The low temperature diffusivities are imprecise because of the large temperature extrapolation. Errors associated with prior loss explain may explain the relatively high Ea (see text).

Jambon, Weber and Begemann (1985)	[+0.1(.8)]	19.2 [(1)]	60(x3)	[5(x14)]

Tholeiitic basalt room temperature storage data and a single loss estimate at 600°C. Values in square brackets estimated from data in original work. Initial losses related to crushing may account for the relatively high diffusivity at room temperature (see text).

3.3.7 Compositional effects on helium mobility

Relative to tholeiitic glass, alkali basalt (Aftermath D9) appears to have significantly lower activation energy (14-15 Kcal/mole vs. 17-18 Kcal/mole at 200-600°C), although both experiments with this sample exhibited scatter in their Arrhenius plots (figure 13b) and have correspondingly imprecise activation energies (table 3.4). However, the good agreement between the two experiments suggests the difference is indeed real. The alkali basalt results imply considerably higher diffusivities than for tholeiitic basalt glass when extrapolated to room and seafloor temperatures (table 3.5). Understanding which components of basaltic glass contribute to this difference is important to extending the results obtained here to other samples, for example, andesitic glasses in island arc environments (chapter 6).

Large compositional effects on noble gas mobility in synthetic silicate glasses are well recognized (e.g Doremus, 1973). Studies with several binary systems have shown that helium diffusivities generally increase (and activation energies decrease) with increasing mole percent silica (Shelby, 1973). These and other results have been interpreted as the relative effect of network formation by silica (which increases the partial molar volume of the glass, thereby providing passageways for interstitial diffusion), and network modification by other species which depolymerize the structure, thereby increasing glass density and blocking diffusive channels. This model can explain the much lower helium diffusivity in basaltic than synthetic glasses as the result of their lower silica content (Jambon and Shelby 1980, Kurz and Jenkins, 1981; Jambon, Weber and Braun, 1986).

However, the differences determined here can not be explained by silica content alone. The alkali basalt, with lower weight percent silica (and mole fraction SiO_2, 3.2b and 3.2c) has a lower Ea than the tholeiites, the opposite relation to that expected. In addition, the difference is larger than predicted from the small silica variation, for a silica difference of 3% the synthetic glass results suggest an activation energy difference of less than 1 Kcal/mole (Shelby and Eagan, 1976; Jambon and Shelby, 1980). This suggests, rather unsurprisingly,

that other components than silica are important in determining glass structure and helium mobility in basalts. To extend the network former/modifier model to multicomponent systems, TiO_2, P_2O_5 and some portion of Al_2O_3 (which can exhibit both properties) should be considered as polymeric components in addition to SiO_2 (e.g. Hess, 1980). For basalts, which have low Al/cation molar ratios (see table 3.2c), essentially all the Al is charge balanced and will act as a network former in this simple model, although the true structural behaviour of alumina is more complex (e.g. Mysen, Virgo and Scarfe, 1980). Titania contents vary enough in basalts to warrant their inclusion in the model, but phosphorous contents are too low to be of significance (table 3.2b). The role of other cations involves both their ability to depolymerize the network by complexing bridging oxygen atoms and the extent to which they "fill" the structure. Ionization energies correlate roughly with the proclivity for oxygen bond formation (Hess, 1980) and this data suggests that Ca plays a much larger role than Fe or Mg in depolymerization. Ionic radii indicate blocking ability, so that singly charged species such as alkalis may be particularly effective in filling internal spaces. These arguments suggest that helium diffusion in basalts will be enhanced by increased Si, Ti, and Al contents and decreased by Ca and alkali contents for a given total cation content.

Unfortunately, it is not possible to evaluate the individual importance of different glass components in limiting helium diffusion using the present data set, so two integrative properties, density and total network-former content were considered as possible indices for the compositional dependence of helium mobility. Helium solubilities in natural melts are known to decrease with melt density (Lux, 1987) and helium diffusivities increase with increasing solubility in many synthetic glasses (Doremus, 1973) so that increasing glass density may be an indicator of decreasing diffusivity. However, densities calculated for the glasses studied here do not differ sufficiently to be of use in predicting helium diffusion (table 3.2c). Including TiO_2 and Al_2O_3 as well as SiO_2 as network formers does suggest that helium will be more mobile in alkali basalt than in tholeiite, as observed (table 3.2c), and thus total-network-formers may be a useful index for helium

diffusivities. However, the 3 KcaL/mole difference in Ea remains large in comparison to synthetic results, where silica contents must increase by 10 mole percent to yield a similar change, and small changes in Al/cation ratios or TiO_2 contents result in Ea variations of 1 kcal/mole or less (Shelby and Eagan, 1976; Shelby, 1973). Therefore, other oxide components (e.g. Ca variations) may also be important, and extrapolations using total-network-former contents must be cautious.

The role of glass water contents in influencing helium diffusion is uncertain. Water is known to have large effects on synthetic glass properties, including lowering viscosities drastically, and increasing electrical conductivity and the diffusivity of sodium ions (Doremus, 1973 and references therein). Water may also diffuse relatively rapidly in glasses; estimates at $1000^{o}C$ range from 10^{-9} cm^2/s to 10^{-6} cm^2/s for synthetic glasses and obsidians (Doremus, 1973; Karsten, Holloway and Delaney, 1982). Extrapolating to the basalts and temperatures used here suggests water mobilities ranging from .001 to 1 times that for helium. Thus, water could affect helium diffusion by altering glass structure and perhaps also by sweeping helium through the glass structure if its mobility is high. However, direct measurements have not confirmed a role for water in controlling helium diffusion. Shelby (1972) found no difference for He diffusion between anhydrous glasses and those with up to .1 weight percent water, suggesting limited structural effects of water at low concentrations. However, the water content of alkali basalt D9 is higher than this (about 1% as opposed to only .1% for the tholeiites; D. Graham, personal communication), and without specific measurements at these higher water contents, the structural effect of water should be considered an unkown, but possibly important, control on He diffusion. The diffusivity of water in basalts has not been measured, but given the 1000-fold faster diffusivity of helium than water in obsidian (Jambon and Shelby, 1980; Friedman and Long, 1976), dynamic effects of water diffusion on helium mobility in basaltic glass seem unlikely.

3.3.8 Diffusion of Radiogenic Helium

The two experiments (#10 and #11) measuring loss of ^{*4}He from alkali basalt sample 1854B displayed higher diffusivities than inherited helium at temperatures of 200-400°C, and much greater temperature dependence (figure 3.14). The activation energy for ^{*4}He release (26-28 Kcal/mole, table 3) is larger than for inherited He release from the tholeiites (17-18 Kcal/mole) or the other alkali basalt (14-15 Kcal/mole; table 3.4). It is not likely that this difference is compositional, because network former contents predict that helium release from 1854B would have a lower, not higher, activation energy (table 3.2c).

The high thermal activation required for ^{*4}He release may represent the effect of trapping by site characteristics produced by the decay. That is, alpha-particle damage may actually reduce He mobility at low temperature instead of enhancing it! This seems counterintuitive, but similar effects have been observed for heavier noble gases. Diffusivities of neutron-irradiation produced argon decrease with increasing radiation dose, in both simple ionic crystals (e.g. Felix and Muller, 1976; Spindler and Lindner, 1966) and in lunar silicate minerals (Horn et al, 1975). Similar results were found for neon and helium release from basaltic glass, including an increase in activation energy with irradiation dose (Stettler and Bochsler, 1979). The mechanism responsible for reduced mobility probably involves increased trapping of the helium atoms in vacancies generated by the radiogenic decays (Kalbitzer, Kiko and Zahringer, 1969; Reed, 1977). This explanation implicitly recognizes that helium atoms in interstitial sites generate significant lattice strain, and that when vacancies are available, helium atoms will tend to reside in them. This is borne out by studies in pure metals which have documented that lattice strain energies for interstitial helium atoms (1.5 to 4.5 eV (35-100 Kcal/mole)) restrict the transfer of helium from lower energy vacancy sites (strain energy of about 1 eV) to the interstitial positions (e.g. Reed, 1977).

153

The activation energy observed for ^{*4}He suggests that diffusive loss at seafloor temperatures will be very slow (D=3×10^{-19}cm^2/s at 0°C; table 3.5), and much lower than for inherited helium (D greater than 10^{-16}cm^2/s). Therefore, the U/^{*4}He geochronology methodology developed for seamount basalt glasses by Graham et al (1987) should not be hampered by diffusive ^{*4}He loss. However, this result should be applied with caution because data was not obtained at low temperature, where it is possible that another diffusion mechanism comes into play, and because the relationship between extent of radiogenic decay and diffusion rate is unknown.

3.3.9 Isotopic fractionation during diffusion

Enhanced mobility of ^{3}He is evident in all the emanation experiments. In general, early releases have higher ^{3}He/^{4}He ratios than the bulk glasses, and the ^{3}He/^{4}He ratios of subsequent fractions decrease, often to below the bulk value at high F. This trend is well developed in both the Alv892-1a chip and powder experiments (figures 3.16 and 3.17). There are small differences between the experiments, however, including the exact F values at which the curves of decreasing ^{3}He/^{4}He ratios cross the bulk values of ^{3}He/^{4}He, and the extent of offset between the ^{3}He/^{4}He of initial releases and the bulk value. In addition, experiments #1 and #3 initially released helium of approximately bulk composition, before displaying a compositional trend similar to the other Alv892-1a experiments. The origin of this behavior is not clear, but the extents of release are too large for a surface origin, and the bulk release rates are not unusual, so that a decrepitation process is unlikely. The other tholeiite (Charco 98-11T) and the alkali basalt (D9) displayed similar trends to the Alv892-1a experiments (figure 3.18), although experiment #8 showed a return to bulk values at high F, after initial ^{3}He/^{4}He decrease. This could reflect either release of helium remaining in a large grain (for which the individual F is small) or activation of helium release from a vesicle at high temperature. Overall, it appears that diffusion is responsible for the preferential release of ^{3}He rather than a surface

Figure 3.16 Isotopic compositions of sequential releases in the Alv892-1a glass chip experiments. Asterisks indicate temperature ramp steps. Horizontal lines mark the bulk ^{3}He/^{4}He ratio summed from all steps. The curves in subplot #1 model release from a prismatic grain similar to the real chip shape for D^{3}He/D^{4}He of 1.152 (dotted) and 1.08 (solid). Grain size histograms as in figure 3.7.

Figure 3.16
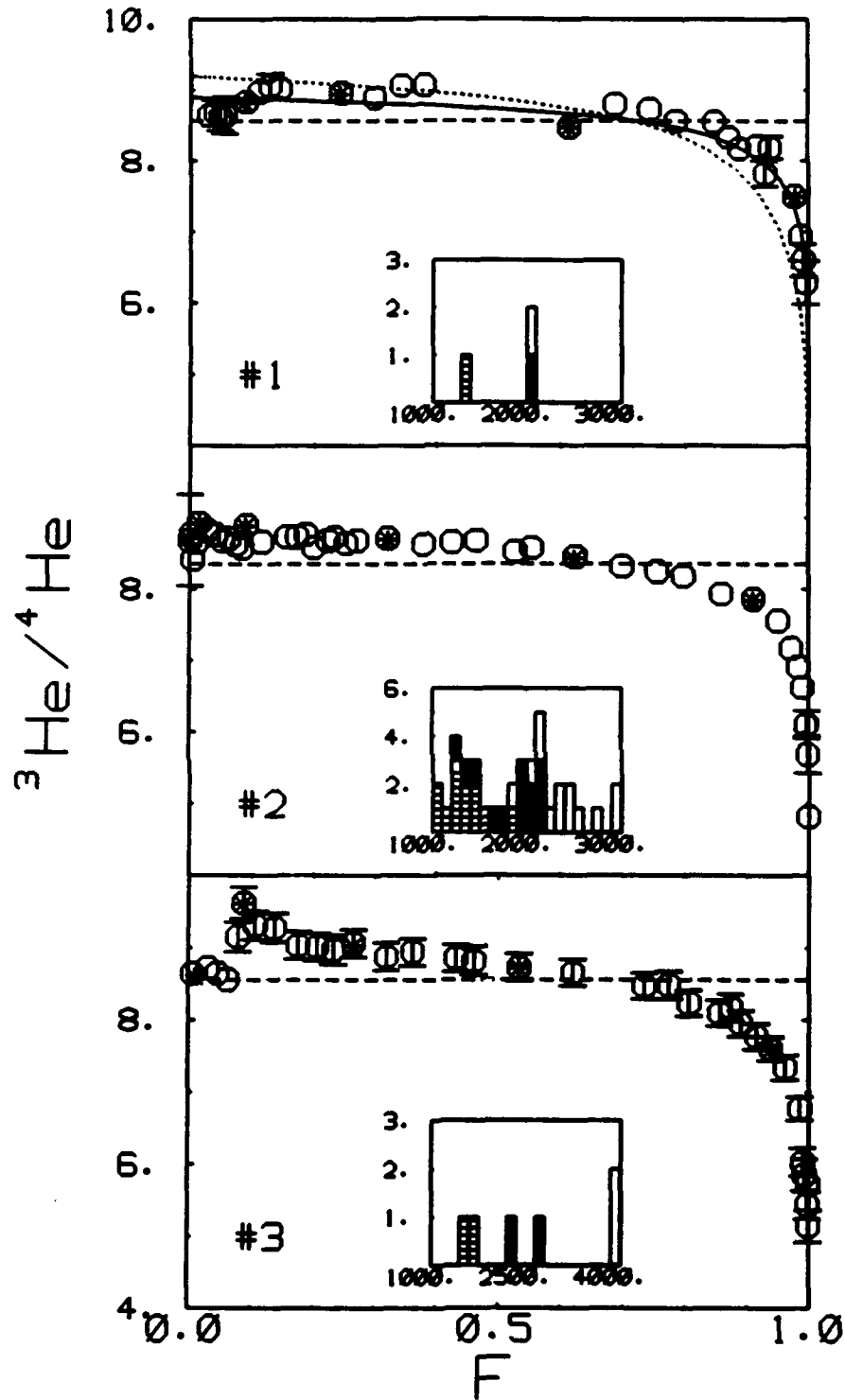
Figure 3.17 ^{3}He/^{4}He ratios versus extent of release for the Alv892-1a powder experiments. Symbols as in figure 3.16. The box in subplot #5 encloses aliquots for which ^{3}He releases were larger than the instrumentally calibrated range and may be slightly underestimated.

Figure 3.17
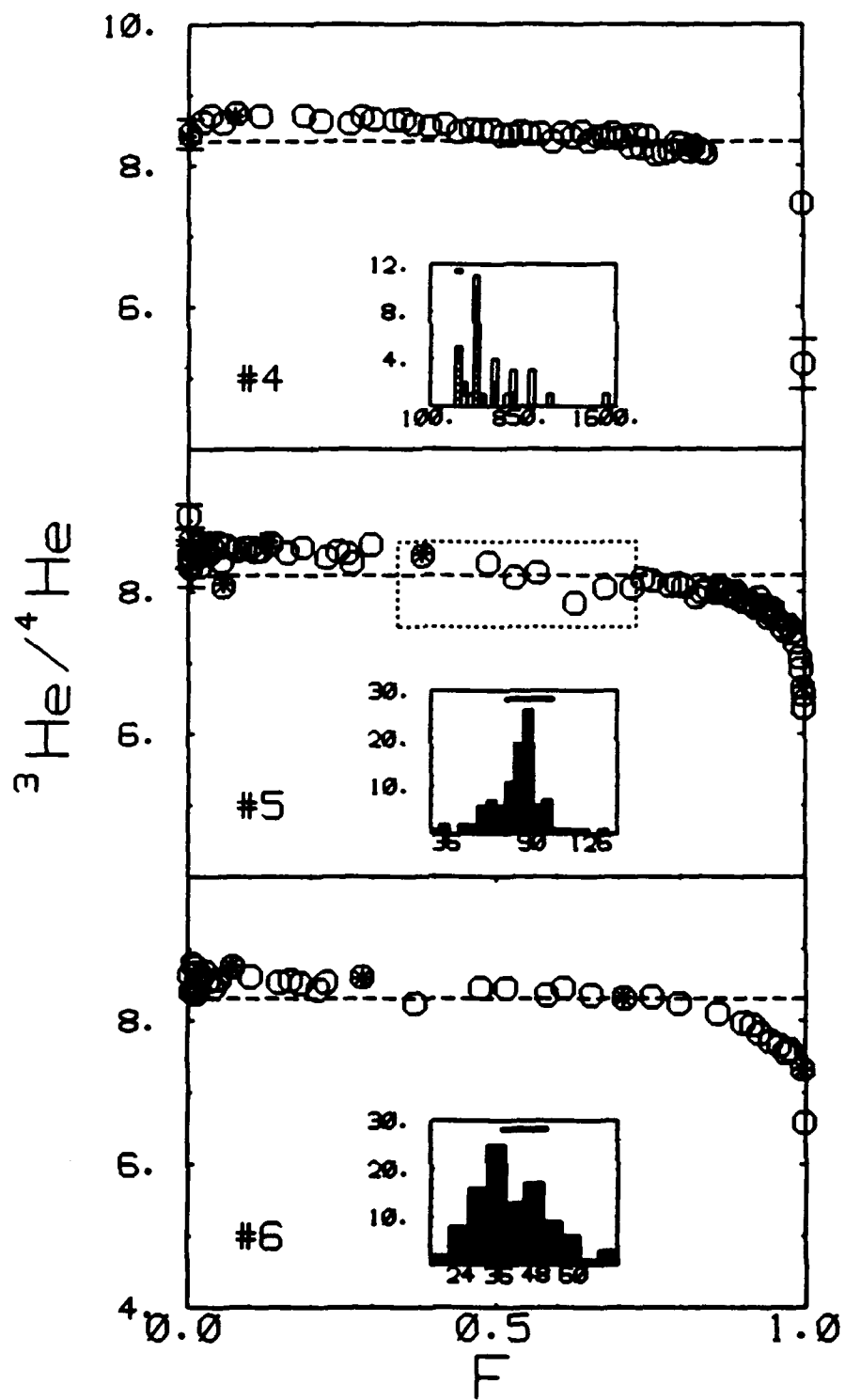
Figure 3.18 ^{3}He/^{4}He ratios for tholeiite sample Charco98-11T
(top) and alkali basalt Aftermath D9 (middle and bottom). Symbols
as in figure 3.16.

Figure 3.18
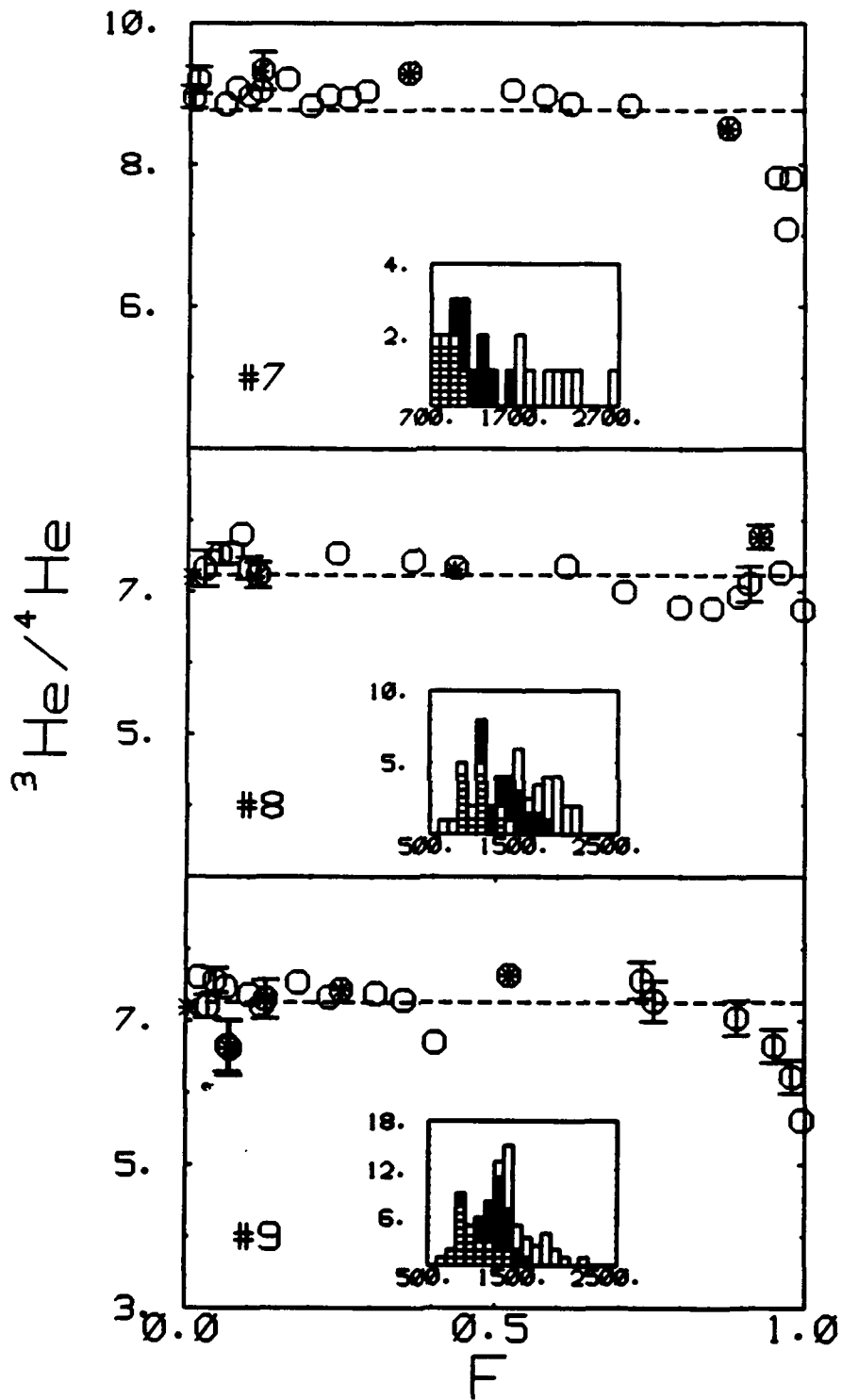
effect, because the decreasing trends continue to high F, and similar trends were observed for a wide range of particle sizes.

For each experiment the isotopic diffusivity ratio, D^3He/D^4He can be estimated in three related ways. The trends of ratio versus extent of release plots (figures 3.16-3.18) can be compared to model release curves calculated for different D^3He/D^4He values. This approach provides an estimate of the effective D^3He/D^4He ratio throughout the experiment and thus cannot be used to constrain any temperature dependence for D^3He/D^4He. Nonetheless, it immediately reveals that D^3He/D^4He may be less than 1.15, the value expected for inverse proportionality to the square root of mass (e.g. expt#1 in figure 3.16). Precise determination of D^3He/D^4He by this method must account for grain size distribution. Size distribution keeps the $^3He/^4He$ ratios of sequential aliquots relatively high to large F, yielding underestimated D^3He/D^4He ratios. Differing shapes are a much smaller effect, and are below the analytical resolution of these experiments (model calculations of the effect of size and shape variations on D^3He/D^4He values are presented in chapter 2).

The second way to determine the isotopic diffusivity ratio is to compare the $^3He/^4He$ ratios at low F to the bulk ratio. The initial releases will have $^3He/^4He$ ratios enhanced by a factor of $(D^3He/D^4He)^{1/2}$, as is readily seen from the approximation equations for D at low F (see section above). For the Alv892-1a experiments this suggests isotopic diffusivity ratios of 1.05 to 1.1, centered on 1.08, and in the powder experiments, where linear relations between F and $t^{1/2}$ were established at room temperature (figure 3.6), D^3He/D^4He is 1.06±.01. This method has the advantage of being relatively unaffected by grain size or shape variations, but again does not account for temperature variations when applied to step-heated experiments.

The most informative approach is to calculate the diffusivites of ^3He and ^4He independently using the refined model, and then take their ratio for each aliquot. This allows the investigation of variations during the experiment. Figures 3.19-3.21 show D^3He/D^4He values calculated this way. The one sigma uncertainties in these figures are relatively large, and reflect errors in measuring $^3He/^4He$ ratios of

Figure 3.19   Isotopic diffusivity ratios for the Alv892-1a chip
experiments as a function of release, calculated from the refined
model.

Figure 3.19
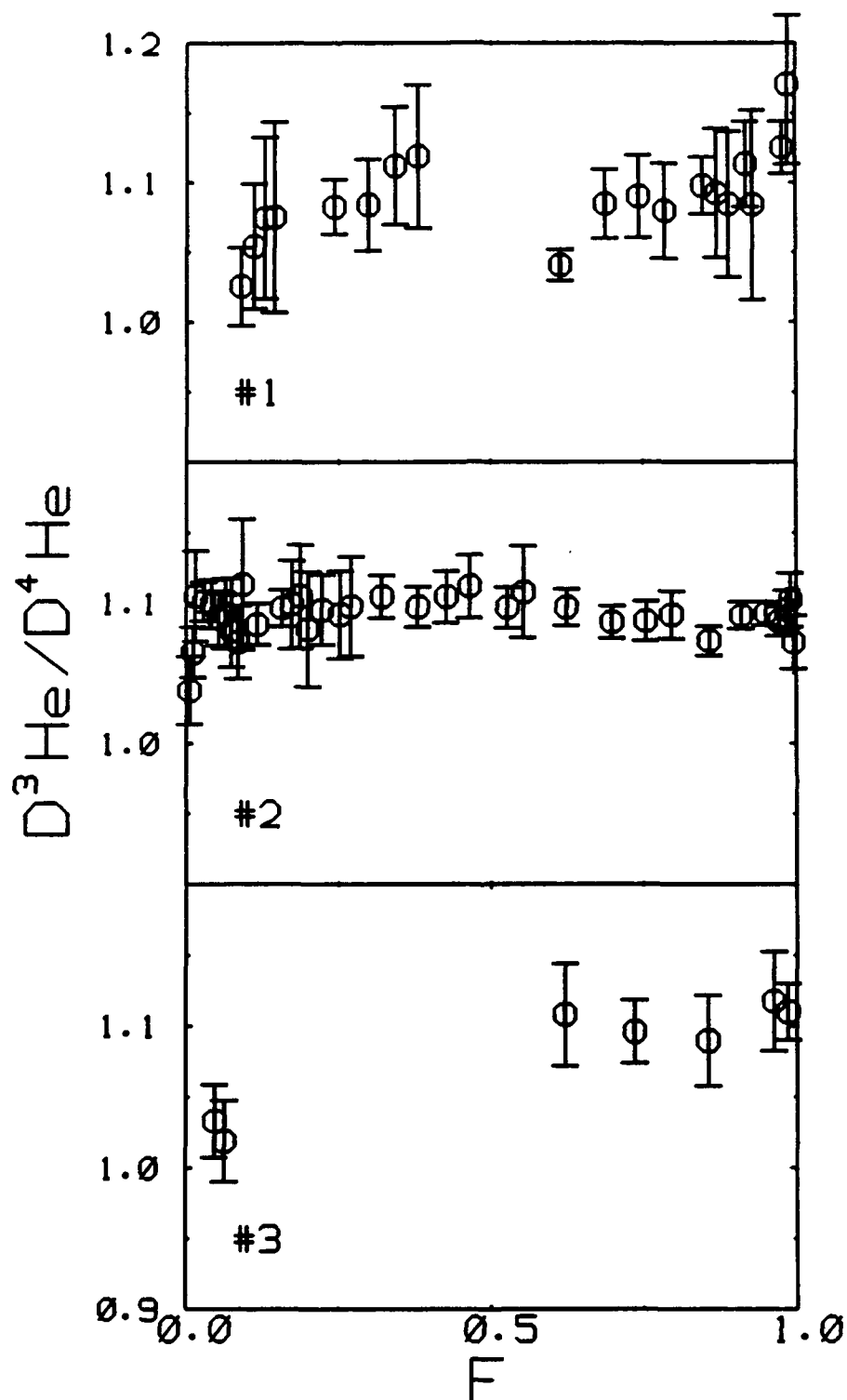
Figure 3.20 Isotopic diffusivity ratios for the Alv892-1a powder experiments as a function of release, calculated from the refined model.

Figure 3.20
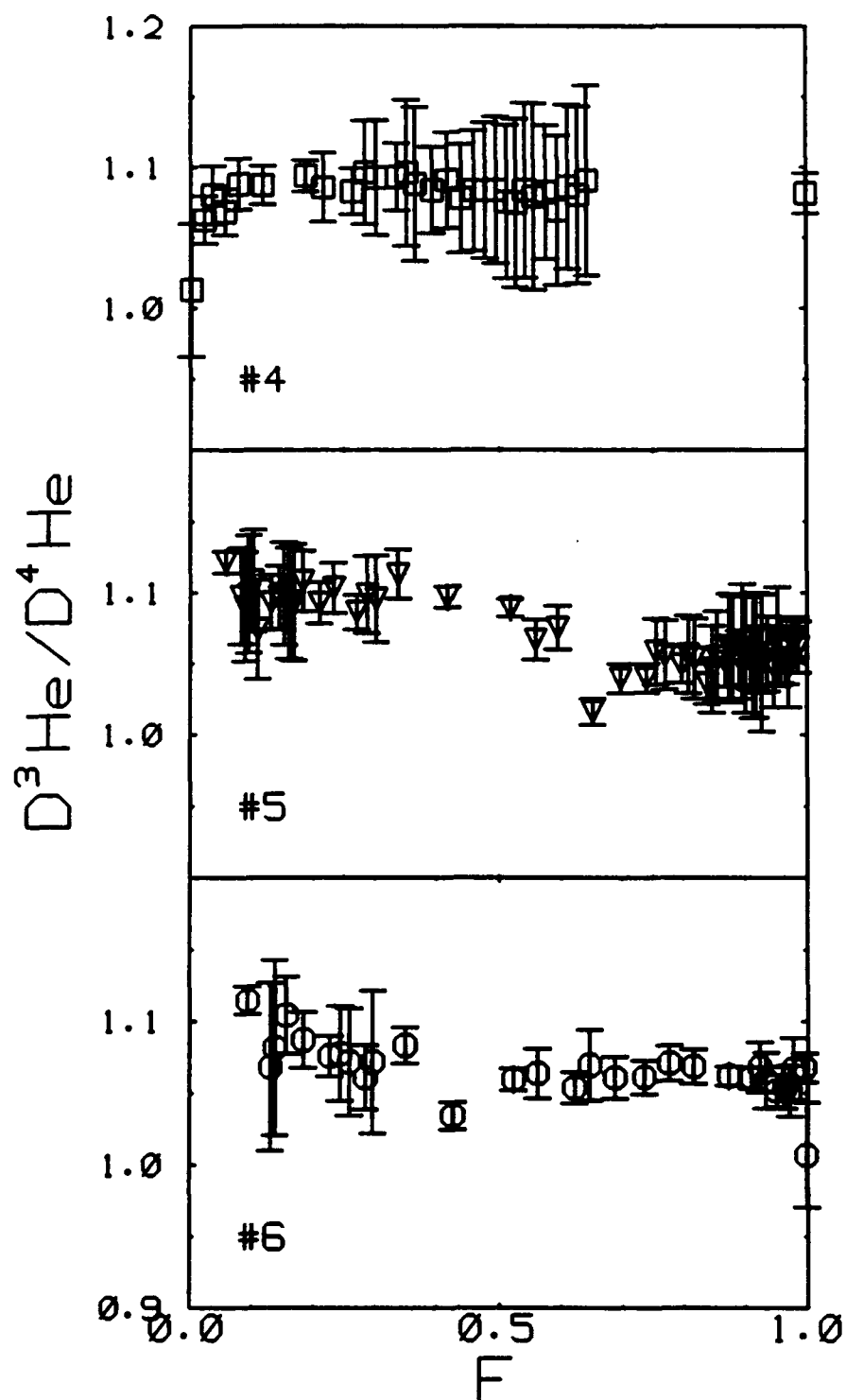
Figure 3.21 Isotopic diffusivity ratios for the other tholeiite, Charco98-11T (#7), and for the alkali basalt, Aftermath D9 (#8 and #9), calculated from the refined model.

Figure 3.21
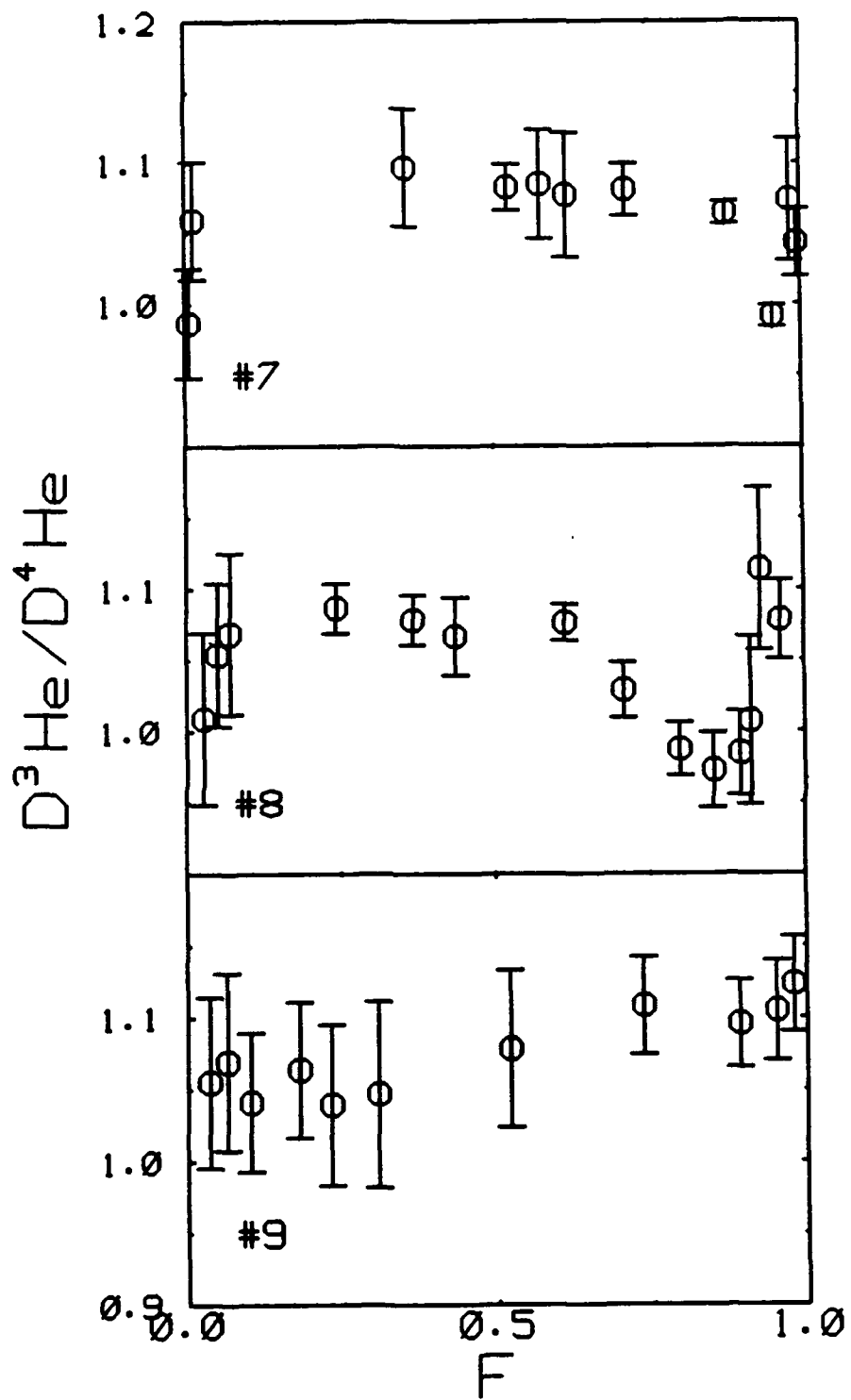
small helium quantities. However, it is clear that D^3He/D^4He is similar in all experiments, averaging about 1.08. Variations with F are small, with the exception of trends that reflect $^3He/^4He$ ratio variations in particular aliquots, such as the low D^3He/D^4He values at low F in experiments #1 and #3 and the apparent dip in D^3He/D^4He at high F in expt. #8. As with absolute diffusivities, misfits between the model and physical reality induce errors, but the effects are smaller because both isotopes are affected similarly. Given the 10% errors in measuring grain sizes, D^3He/D^4He can be underestimated by up to two percent or so at F >.9 and prior loss leads to small (.5% or less) overestimates (see model calculation in chapter 2). These effects may obscure small variations in D^3He/D^4He between or within experiments, but they do not alter the conclusion that the isotopic difusivity ratio is much less than 1.15.

To obtain an estimate of the mean isotopic difusivity ratio and examine any temperature dependence, D^3He/D^4He values obtained at F < .85 and with one sigma errors less than 2% were combined from all the tholeiite experiments (except #5, which had additional instrumental uncertainties) . These D^3He/D^4He values are confined between 1.0 and 1.15 and average 1.08+.02, as shown in figure 3.22 (bottom plot). A slight increase with temperature of the preferential mobility of ^3He is implied by an error-weighted fit of D^3He/D^4He versus 1/T (top plot in figure 3.22). This relation yields a 60+20 cal/mole difference in activation energies and suggests an isotopic diffusivity ratio of 1.13+.02 at infinite temperature (table 3.6). As shown in figure 3.22, helium diffusion in vitreous silica exhibits similar isotopic diffusivity ratios, but with a somewhat stronger temperature dependence of 130+20 cal/mole (Shelby, 1971).

While the temperature dependence of the isotopic diffusivity ratio in the basaltic glass experiments is difficult to resolve, it has important ramifications for helium isotopic fractionation in nature. Extrapolating the temperature dependence to 0^oC yields D^3He/D^4He of 1.02+.03, suggesting very little isotopic fractionation will accompany helium loss from seafloor basalts. This result is reinforced by the mean isotopic diffusivity ratio of 1.06+.01 obtained at room temperature

Figure 3.22 Examination of the temperature dependence of the isotopic diffusivity ratio, D^3He/D^4He for tholeiitic basalt glass. The data are 137 determinations combined from experiments #1-4,and #6-7, with one sigma errors of less than 2%. Error-weighted regression lines are shown to the data (solid line) and for results on vitreous silica (dotted line; Shelby, 1971). The slight temperature dependence suggests the activation energy for ^3He is 60 ± 20 cal/mole higher than for ^4He in basalt, and 130 ± 20 cal/mole higher in silica.

Figure 3.22
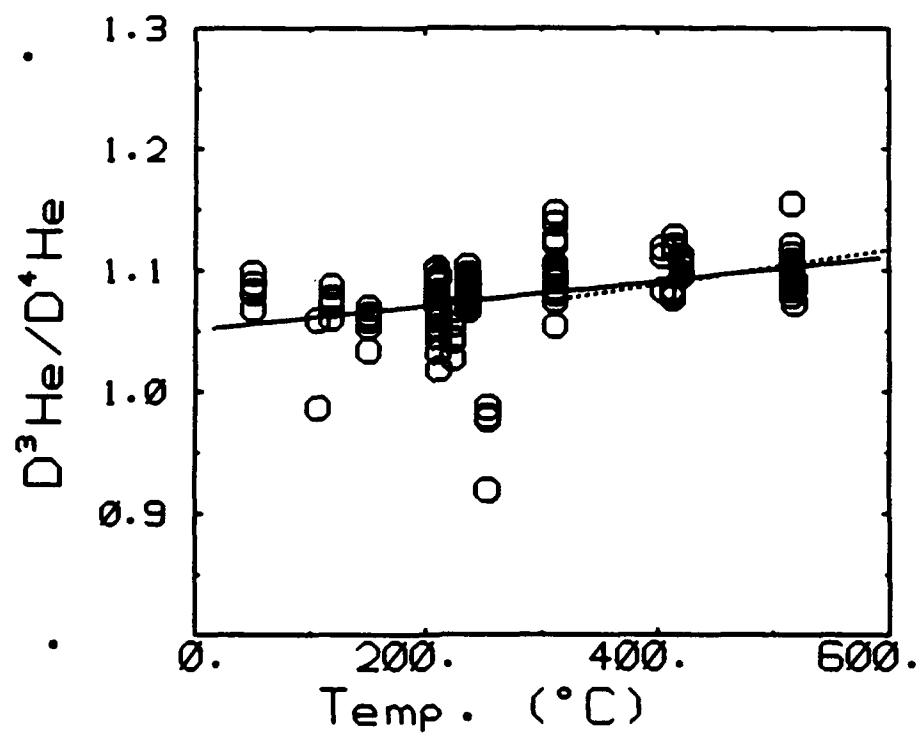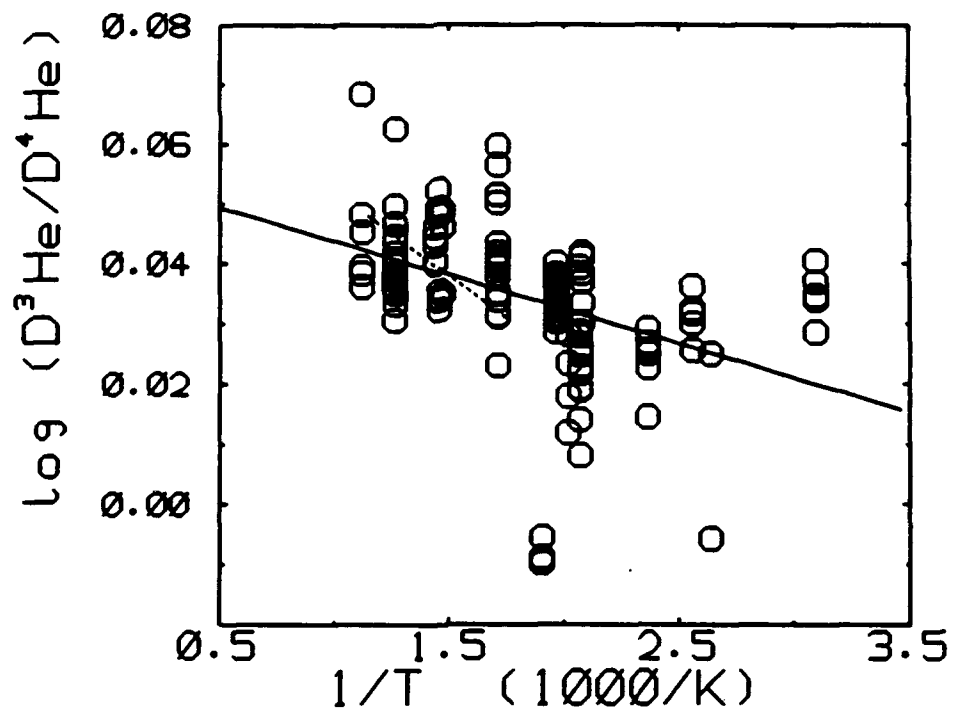
Table 3.6 The Isotopic Diffusivity Ratio of Helium
in Tholeiitic Glass.

Arrhenius equation for the temperature dependence of the isotopic diffusivity ratio:

$$D^3He/D^4He = D_o{}^3He/D_o{}^4He \times \exp\{-(E_a{}^3He - E_a{}^4He)/RT\}$$

	$D_o{}^3He/D_o{}^4He$	$(E_a{}^3He - E_a{}^4He)$
Basaltic glass results	1.13+.02	60+20 cal/mole
Vitreous silica (Shelby,1971)	1.20+.01	130+30
Classical prediction	1.152	0
Quantum theory prediction	1.23+2	125+25

171

in the powder experiments (as discussed above). In contrast, diffusive fractionation at magmatic temperatures will be higher, the extrapolated isotopic diffusivity ratio at $1100^{o}C$ is $1.12\underline{+}.02$.

Both the magnitude of the mean isotopic diffusivity ratio and the temperature effect are departures from the simple relation often quoted in the geochemical literature (e.g. Craig and Lupton, 1976; Hart, 1984; Kaneoka, 1980; Sarda, 1989):

$$D^{a}/D^{b} = (m^{b}/m^{a})^{1/2} = 1.154 \text{ for He} \qquad (3.7)$$

In addition, the idea that isotopic fractionation increases at higher temperature may seem counterintuitive. For these reasons, solid-state diffusion theory is briefly reviewed with the additional goal of evaluating the experimental results and understanding to what degree they can be extended to other geologic materials. The general expression for diffusion in isotropic, three-dimensional space is (Einstein, 1905; LeClaire, 1970):

$$D = \langle R^{2} \rangle / 6t \qquad (3.8)$$

where $\langle R^{2} \rangle$ is the mean square atomic displacement in time t. This can be expressed as a vector sum of N individual displacements:

$$\langle R^{2} \rangle = \langle (\ r_{i})^{2} \qquad (3.9)$$

$$= N \langle r_{1}^{2} \rangle + 2N \ \{ \langle r_{i} \cdot r_{i+1} \rangle + \langle r_{i} \cdot r_{i+2} \rangle + ... \}$$

$$= N \ \{ \langle r_{1}^{2} \rangle + 2 \langle r_{i} \rangle^{2} (\langle \cos w_{1} \rangle + \langle \cos w_{2} \rangle + ...) \}$$

where the $\langle \cos w_{i} \rangle$ are the mean values of the cosines of the angles between successive displacements.

Solid-state diffusion theory usually adapts this general expression by assuming that the r_{i} are approximately equal and correspond to atomic

spacings of lattice atoms in a crystal, leading to (adapted from LeClaire, 1970, Manning, 1971; Wolf, 1981):

$$D = fa^2N/6t \qquad (3.10)$$

where: $f = 1 + 2\sum_i \langle \cos w_i \rangle$ is called the correlation factor, and a is the atomic spacing. N/t is related to the availability of sites for the diffusing atom to move to and the rate at which the solute atom moves, often described as the jump rate, v_i. If lattice atom spacing and site availability is considered to be independent of the mass of the diffusing atom, the isotopic diffusivity ratio (written here for helium) can be expressed as a function of only correlation factors and solute atom jump rates:

$$D^3/D^4 = v_3 f^3/v_4 f^4 = (f^3/f^4)(v_3/v_4) \qquad (3.11)$$

Determining the mass dependence of the isotopic diffusivity ratio thus depends on evaluating f and v and their mass dependence.

Diffusion in solids is often divided into different "mechanisms", based on the type of sites the diffusing atom occupies. In interstitial diffusion the solute atom moves between spaces in the crystalline lattice which are not occupied by host atoms. If all these spaces are equally accessible and isotropically distributed the successive jumps of the solute atom will be random and f will equal 1 for all isotopes. In this case, the mass dependence of diffusivities depends only on the jump rates. Other mechanism classes include vacancy diffusion, in which the diffusing atom moves between lattice sites which are empty because of crystal imperfection; and interstitialcy, in which the diffusing atom moves between interstitial and lattice sites, displacing a host atom to an interstitial site in the process. Because these mechanisms involve the migration of lattice atoms or vacancies, which generally have different jump rates than the diffusing atom, successive solute atom jumps are correlated and f differs from 1. For example, a diffusing atom may exchange many times with an adjacent vacancy before moving to another vacancy which is opened up by slower host atom movements. Thus,

in these mechanisms the total population of vacancies, and thus crystal purity, also influences the extent of correlation.

Formulation of correlation factors in terms of host and solute atom jump rates has been done for several simple crystals (e.g. Lidiard, 1955) and reveals that for most vacancy diffusion mechanisms f values will range from 0 to 1 (Schoen, 1958) as shown by a general form proposed for f by LeClaire (1970):

$$f^i = u/(v_i + u) \qquad\qquad (3.12)$$

where u depends only on host atom jump rates. Combining this expression, written for each isotope, with the previous equation leads to:

$$(D^3/D^4) - 1 = f^3((v_3/v_4) - 1). \qquad\qquad (3.13)$$

This equation explicitly states that correlation effects reduce diffusive isotopic fractionation. It implicitly recognizes that when correlation occurs there will be an isotopic effect on the extent of correlation, i.e. f^3/f^4 in the previous expression for D^3/D^4 can only equal 1 if no correlation occurs (f=1). The exact relation between f^3/f^4 and extent of correlation depends on the solid structure and specific atomic movements, but its general form is a slow decrease in f^3/f^4 as correlation increases, as shown by the curve in figure 2.23 (calculated from theoretical results for cubic lattices Tharmalingan and Lidiard, 1959). An intuitive understanding of the role of correlation in limiting diffusive fractionation can be had by considering it as the temporal equivalent of a "reduced mass" effect. Because f values calculated for simple crystals are in the range of .6 to .8, where the isotopic effect on f is small, the superscript on f in the relation between diffusivities and jump frequencies is often dropped (LeClaire, 1966, 1970).

Evaluating the helium diffusion mechanism in basaltic glasses is one way to set limits on the role of correlation in reducing the isotopic diffusivity ratio. There are several experimental observations

Figure 3.23 Theoretical relation for the isotopic effect on
correlation in vacancy diffusion (Tharmalingan and Lidiard, 1959)
calculated for helium isotopes. The correlation factors f^3 and
f^4 are only equal at when no correlation occurs ($f=1$). However,
their values remain within 10% of each other for a large range in
f.

Figure 3.23

Isotopic effect on correlation for helium vacancy diffusion.
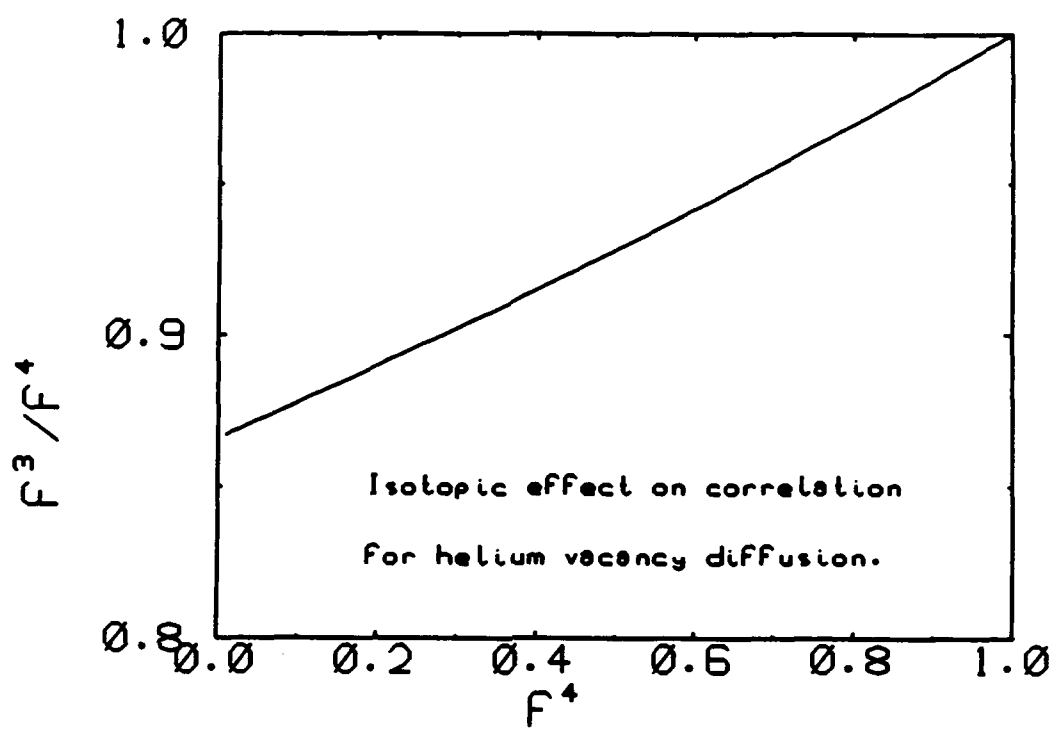
which are most easily explained if helium diffuses in silicate glasses by an interstitial mechanism. (In glasses, which do not have highly ordered lattice sites, interstitial may be taken to mean that passage of the helium atom does not involve displacements of the glass atoms which are large in comparison to vibrational excursions or which are not reversed). An interstitial mechanism can explain the 2-3 orders of magnitude higher diffusivities of helium in comparison to cations in synthetic glasses, obsidians and basalts (see Doremus, 1973; Jambon and Shelby, 1980; this work). The necessity of a fundamentally different mechanism is emphasized by considering the relative size of the helium atom and common cations. Helium atoms are larger than most cations, (Keevil, 1940; figure 3.24), yet diffuse more rapidly. In addition, helium diffusivities vary greatly between obsidian and basalt while many cation diffusivities are relatively unchanged (figure 3.25). This suggests the rates of glass host atom motions limit cation diffusion but not helium diffusion, consistent with interstitial helium diffusion and a vacancy mechanism for cations. In addition, the isotopic diffusivity ratio for neon (^{20}Ne/^{22}Ne) in silicate glasses appears to equal the inverse square-root of the isotopic masses (Frank, Swets, and Lee, 1961; Rama and Hart, 1965), suggesting no correlation effects, and thus an interstitial mechanism. Helium and neon have similar atomic sizes in crystals (figure 3.24) and exhibit similar diffusivities in synthetic glasses (Doremus, 1973) and basaltic melts (Lux, 1987) suggesting an identical mechanism and thus that correlation effects are not important for helium either.

The isotopic dependence of jump rates is difficult to determine. A model for the displacement must be constructed and then examined for mass dependence. Most previous studies have adapted transition-state theory developed for molecular reactions to describe a critical "saddle point" or "barrier" in the displacement of the diffusing atom (e.g. Stearn and Eyring, 1940; Wert and Zener, 1949; Vineyard, 1957). Notable exception to this approach is the work of Stoneham and Flynn (1971), who considered the probability of displacement to be governed by the total crystal configurational energies (Hamiltonians) for the initial and final (eigen)states, and made no assumptions about the transition. In

Figure 3.24 Comparison of effective atomic radii for helium,
other noble gases and common ions in crystals (Keevil, 1940).
The ionic radii were determined by x-ray diffraction measurements
in simple crystals, and the noble gas radii obtained by
interpolation between ions of different charges which share the
same electronic configuration as the noble gas. This data
suggests the atomic radius of helium is about 1.2 Angstrom, and
is very similar to the radius for Neon.

Figure 3.24

179.
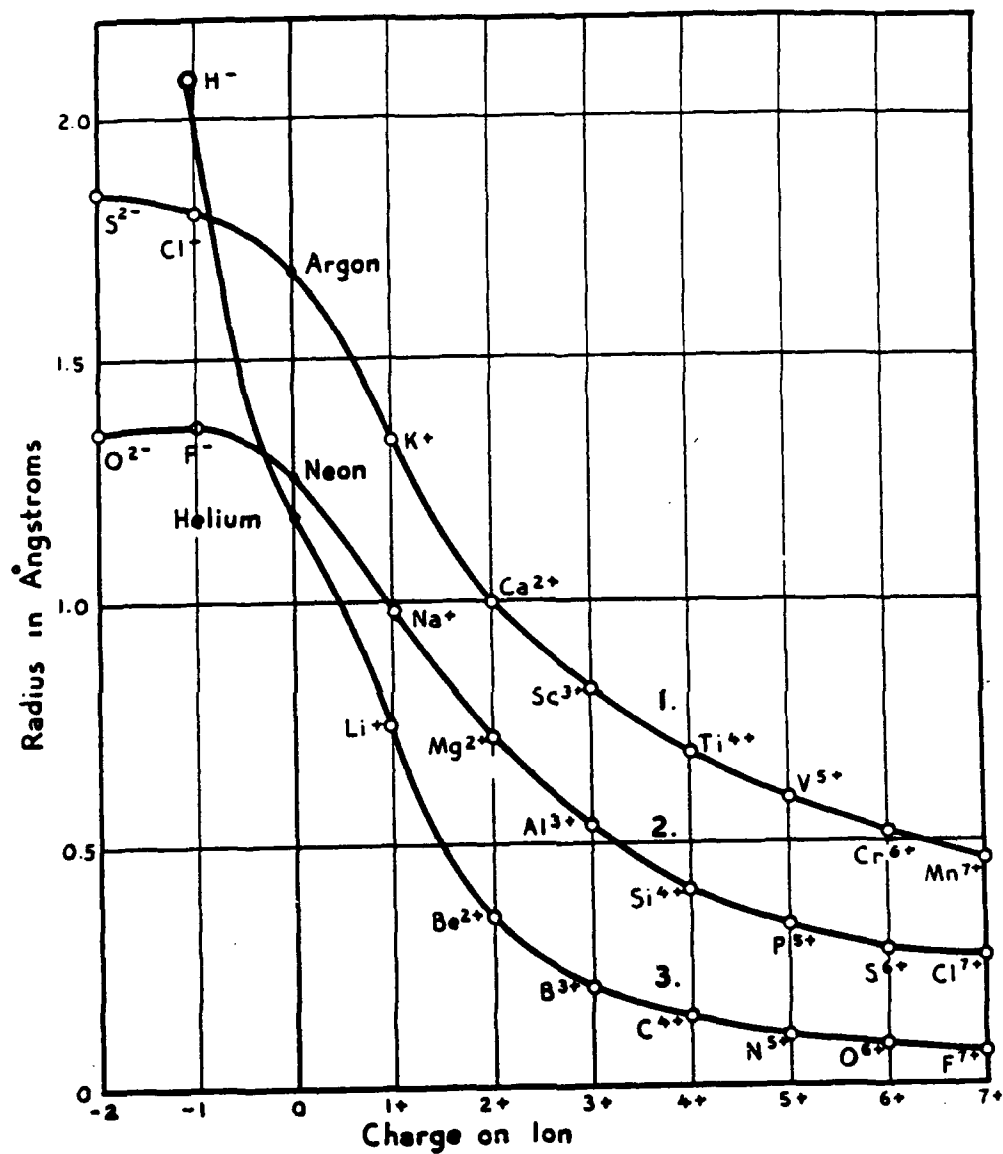
Figure 3.25 Comparison of diffusivities for common ions in basaltic glass and obsidian (Hoffman, 1980) with helium diffusivities in basalt glass (this study) and obsidian (Jambon and Shelby, 1980). Many of the ions show little difference between the two glasses, while helium diffusion changes by a factor of 100.

Figure 3.25

181
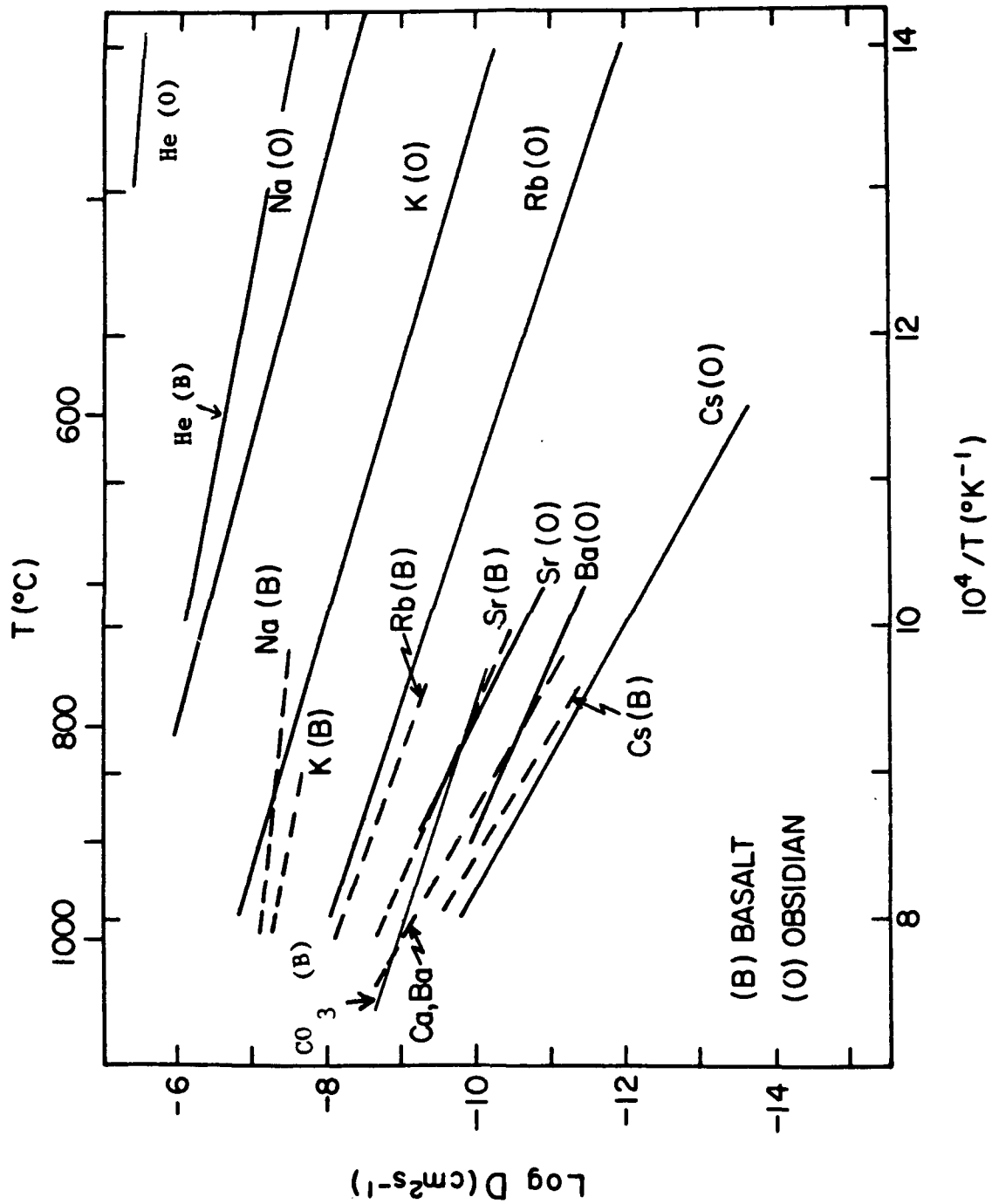
principle this method should better describe solute interactions, but in practice it has not been sufficiently developed to allow a quantitative evaluation of isotopic effects. In the transition state approach the barrier can be associated with an activation energy, and the ability of an diffusing atom to surmount it treated using Boltzman thermal distributions and appropriate partition functions. Vineyard (1957) has developed the most general expression of the classical transition-state theory, by taking the energy barrier to correspond to be a saddle-point on an N-1 dimensonal potential energy surface, P, where N is the number of atoms in the crystal. This allows the jump rate, v, of the diffusing atom to be expressed in terms of partition functions at the saddle-point, s, and initial atom site, a, and the potential energy difference between the sites. Assuming classical vibrational partition functions based in the harmonic approximation yields:

$$v = \prod_1^{3N+3} w_i \; / \; \prod_2^{3N+3} w_i' \quad e^{-(P(s)-P(a))/kT} \tag{3.14}$$

Here w and w' denote the normal frequencies of the entire atomic assembly of N atoms at the initial site and the N-1 frequencies of the system constrained to the surface at the saddle-point respectively. Translational and rotational frequencies need not be considered since we are concerned with single atom motions <u>within</u> the crystal.

As pointed out by Vineyard (1957) and Ebisuzaki, Kass, and O'Keefe (1967) this expression can be rewritten to obtain the familiar form of a frequency times a fraction of transition complexes, as encountered in rate process theory:

$$v = w^* \left(\prod_2^{3N+3} w_i \; / \; \prod_2^{3N+3} w_i' \right) e^{-(P(s)-P(a))/kT} \tag{3.15}$$

$$= w^* \cdot \left(z^*/z \right) \cdot e^{-(P(s)-P(a))/kT} \tag{3.16}$$

This is the form obtained directly from models which consider only one-dimensional solute atom motion, or which allow only the solute atom to vibrate, while keeping the crystal atoms fixed. However, it must be

pointed out that w^* has only imaginary significance, because the potential surface at the saddle-point must have negative curvature, and thus can not be equated with vibration of the diffusing atom (Ebisuzaki, Kass, and O'Keefe, 1967). Determining the mass effect on jump rate thus depends on evaluating the mass effect on the products of normal mode frequencies at both the initial configuration and constrained at the saddle point. Before summarizing those results, it is worth noting that the ratio Z^*/Z can be equated with the entropy change (S), and the potential difference, $P(s)-P(a)$, with the activation enthalpy (H) in the semi-empirical diffusion theory presented earlier by Wert and Zener (1949).

The mass dependence of the frequency product in the initial state is readily obtained from the <u>harmonic approximation:</u>

$$\mathcal{V} = 1/2\pi (k/\mu)^{1/2} \tag{3.17}$$

where k is the force constant for oscillation, and μ the reduced mass $m_1 m_2 / m_1 + m_2$ and the Redlich-Teller product rule (e.g. Vinyard, 1957), to obtain:

$$\prod_1^N w_i = (m_i)^{-3/2} \tag{3.18}$$

The dependence on mass in the surface-constrained transition state is more difficult to determine, but can be shown to depend on the product of $(m_i)^{-3/2}$ and the square-root of the "effective mass", m_i^*, associated with the imaginary N^{th} normal mode, w^* (Vineyard, 1957). Thus, v_i is proportional to $(m_i^*)^{-1/2}$. Therefore the isotope effect for helium atomic jump rates is proportional to $(m_4^*/m_3^*)^{1/2}$. The m^*, which can be thought of in a rough sense as reduced masses, are constrained to lie between the solute and crystal atom masses (Vineyard, 1957), so that the isotopic effect is predicted to vary between a maximum of $(m_4/m_3)^{1/2}$ and a minimum of zero. Mullen (1961) and LeClaire (1966) have extended and clarified this concept to identify m^* with the

183

fraction of kinetic energy possessed by the solute atom in the
vibrational mode which leads to a transition (ΔK), and thus obtained:

$$(w_3/w_4)-1 = \Delta K ((m_4/m_3)^{1/2} -1) \tag{3.19}$$

This can be combined with the previously obtained relation between
diffusivities and jump rates (equation 12) to yield:

$$(D^3/D^4)-1 = f \Delta K ((m_4/m_3)^{1/2} -1) \tag{3.20}$$

However, as might be expected, correlation factors and ΔK are related so
that this expression is only rigorously true when either f or ΔK equals
1 (LeClaire, 1966).

Equation 3.20 shows that the helium isotopic diffusivity ratio
observed in basaltic glasses may be smaller than the rule-of-thumb of
1.15 because more than one atom moves along the reaction coordinate
during the transition. However, this appears to be an unsatisfactory
explanation given the already discussed results for neon and helium
isotopes in synthetic glasses. First, it seems unreasonable that neon
isotopes would not also experience a "reduced mass" effect if helium
movements involve considerable coupling with glass atom motions and
secondly, given the drastic difference in helium diffusivities and
atomic compositions between vitreous silica and basaltic glass, how is
it that the helium isotopic diffusivity ratio, and thus the reduced mass
effect is so similar? This suggests that properties of the helium atoms
rather than the solids are responsible for the mass dependence.

In calculating the mass dependence of the jump rates above,
classical partition functions were used. However, this may not be
appropriate for light helium atoms. Substitution of quantum vibrational
partition functions is one way to estimate the effect of quantized
vibrational energies on diffusion. LeClair (1966) expanded the crystal
quantum vibrational partition function:

$$q_v = e^{-hv/2kT}/(1-e^{-hv/kt}) = kT/hv (1-1/24(hv/kT)^2+..) \tag{3.21}$$

and estimated quantum effects by retaining the first two terms in the series. This yields:

$$(D^3/D^4 - 1) = ((m_4/m_3)^{1/2} - 1) [1 - \{.207(hn/kT)^2((n'/n)^2 - 3/2)\}] \quad (3.22)$$

The second term on the right contains the quantum corrections to the classical relation. This equation implicitly assumes that both f and K are 1, as in interstitial diffusion, and that the atomic jump is reasonably characterized by oscillations of the diffusing atom alone in the initial state, n, and the transition state, n'. Examining the quantum correction term shows that the isotopic diffusivity ratio may be larger or smaller than $(m_4/m_3)^{1/2}$ depending on the size of n'/n. It also predicts that as the quantum effect diminishes with increasing temperature (hn/kT becomes small) the isotopic fractionation will approach the classical inverse-square-root-of-mass value.

Thus, quantized vibration is capable of explaining both the low helium isotopic diffusivity ratio and its increase with temperature in silicate glasses, provided quantum effects actually occur for helium at these temperatures. One way to assess this possibility is to estimate hn/k, which can reasonably be assumed to be at least as large as the vibrational temperature of the glass atoms, T_v. A simple approximation for T_v in crystals is the Debye temperature, which is generally about .7 times the melting point in metals (LeClaire, 1966). Extending this approximation to glass suggests that T_v and thus hn/k will be on the order of $800^{\circ}C$, so that quantum effects may reasonably be expected for the laboratory temperatures used ($20-600^{\circ}C$). Another way to assess the vibrational temperatures of basaltic glasses is through heat capacity data. In simple solids, constant volume heat capacities will increase to a high temperature limit of about 6 cal/mole-$^{\circ}K$ (3 times the gas constant R) as vibrational energy-level spacing becomes small in comparison to thermal energies (e.g. Nash, 1974). In more complex solids, heat capacities can exceed this value, but values less than 3R at a given temperature still suggest that vibrational energy gaps are large in comparison to thermal energies. Measured heat capacities of many simple silicate glasses as well as a glass of diopside composition

are less than 3R until temperatures exceed $800^{\circ}C$ (Stebbins, Carmichael and Monet, 1984). Thus, quantum effects for helium diffusion can reasonably expected in basaltic glasses up to $800^{\circ}C$ or so. For comparison, vibrational temperatures for hydrogen in metals are on the order of $1000^{\circ}C$ (Ebisuzaki, Kass and O'Keeffe, 1967).

What other ways are there to test the quantum explanation of helium isotopic diffusivity ratios in basaltic glasses? It is not possible to estimate n'/n directly. However, the quantum theory predicts a proportionality between the size of the isotopic diffusivity ratio's departure from the classical value and the steepness of its temperature dependence which can be compared with the experimental results (LeClaire, 1966), . Expressing the temperature dependence as the difference in activation energies for the two isotopes, this can be written (Shelby, 1971):

$$(E_a{}^3He - E_a{}^4He) = 2RT \{1-(D^3He/D^4He) / (m^4He/m^3He)^{1/2}\} \qquad (3.23)$$

Ea differences calculated from this equation are in excellent agreement with the measured values for synthetic glasses (Shelby, 1971). For the basalts, an activation energy difference of 60 ± 20 cal/mole was observed, somewhat less that the predicted value of 125 ± 25 cal/mole, but within the two sigma error bounds (table 3.6).

Overall, the quantum model is a reasonable interpretation of the experimental results, which has important implications. First of all, the model reinforces the experimental observation that helium isotopic diffusivity ratio is temperature dependent and at low temperature is likely to be very close to 1, and thus suggests that little fractionation will accompany gas loss on the seafloor. Secondly, the quantum model suggests that this behavior will apply to helium in many other geologic materials which have similar or higher melting points; especially if heat capacities (Cv) in the solids of interest are small (<3 R). This has been confirmed for olivine and pyroxene crystals, which appear to have D^3He/D^4He ratios of 1.08 to 1.10 at magmatic temperatures (close to their approximate Debye temperature of .7 times the melting point, chapter 4). However, because all diffusion models

make simplifying assumptions, extending the quantum model for He should be done with caution.

In summary, a brief review of solid-state diffusion theory revealed three major factors which affect isotopic fractionations: correlation (f), energy distribution during the atomic displacement (K), and quantization of vibrational energies. Correlation reduces isotopic fractionations and is most important in diffusion mechanisms involving host atom displacements. K effects can occur for any mechanism, but, as with correlation, are likely to be most important when solute and host atoms have similar masses or vibrational energies. Quantum effects are probably only important for light atoms above room temperature, but can either reduce or enhance isotopic effects. Quantum effects can explain the isotopic diffusivity ratios observed for helium in basaltic glass. In other solids the heat capacity may provide a rough guide to the likliehood of quantum effects. Overall, the transition-state theory suggests the $(m)^{1/2}$ approximation (equation 3.7) will often be an upper limit for isotopic effects. However, it must be emphasized that diffusion theories make many assumptions, and that larger isotope effects have been observed in some systems (e.g. Vinyard, 1957).

3.4 DISCUSSION

The measured helium diffusivities can be used to estimate timescales for helium loss. Model loss curves calculated for spheres with homogeneous initial concentrations and zero surface concentration, suggest 50% helium loss can occur about 1 million years for mid-ocean-ridge tholeiites, given the diffusivity of $5 \times 10^{-16} cm^2/s$ at $0^o C$ (table 3.5), and asssuming 1cm as a characteristic pillow lava glass fragment size (figure 3.26). In contrast, the higher helium diffusivity in alkali basalt glass yields approximately 100,000 years. Initial $^3He/^4He$ ratios would be changed very little by 50% gas loss, less than 2% given the D^3He/D^4He ratio of $1.02 \pm .03$ suggested for $0^o C$ by the temperature dependence of the isotopic diffusivity ratio (table 3.6). Even the mean value D^3He/D^4He value of 1.08 suggests 80% gas loss must occur to lower the initial $^3He/^4He$ ratio by 10% and this would require

Figure 3.26   Timescales for He loss or exchange for basaltic glasses. The model curves are calculated for spheres of radius a and zero surface concentration. For example, an alkali basalt glass with natural grain size of 1 cm and diffusion coefficient of 2×10^{-15} cm^2/s at $0^{\circ}C$ has log D/a^2 = -14.1 and can lose 50% of its initial helium in about 100,000 years.

Figure 3.26
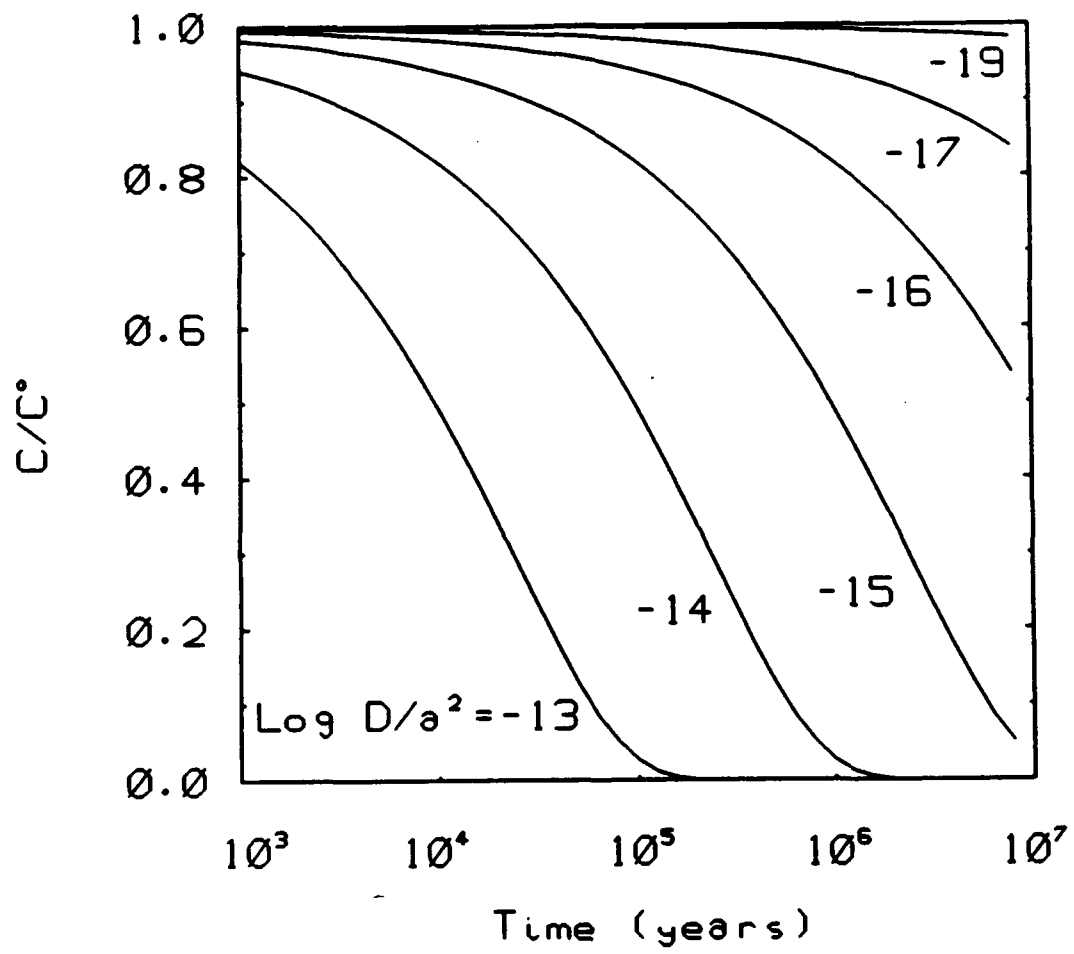
more than 5 times as long a loss period. (Model curves for the change in initial ratio as a function of loss are given in figure 4.8 for different values of the isotopic diffusivity ratio.) Thus, it is very unlikely that a significant fraction of the range of $^3He/^4He$ ratios observed in MORB (7-9 R_a) is produced by preferential loss of ^3He after eruption. This result is also clear from the lack of correspondence between helium concentration and isotopic composition in MORB (Kurz and Jenkins, 1981). The suggestion by Craig and Lupton (1976) that preferential helium loss accounted for isotopic systematics in their samples was based on high D and D^3He/D^4He estimates from synthetic glasses, and is not tenable given the results presented here.

Helium exchange with seawater will be a larger problem than preferential ^3He loss, because of the greater isotopic effect. The model curves of figure 3.26 can be used to evaluate this problem, considering that the y-axis (C/C_o) represents:

$$(C_t-C_o)/(C_f-C_o) \qquad (3.24)$$

where the subscripts t, o, and f refer to the concentrations at time t, initially, and after equilibrium has been reached, respectively. For diffusive equilibrium with seawater, C_f, is given by Henry's law and the partial pressure of each isotope in seawater (table 3.1). Denoting this value by C_s and the quotient in equation 3.24 by F, and equating F for each isotope (which assumes their Henry's law coefficients are identical) gives:

$$(R_tC_t - R_oC_o)/(R_sC_s - R_oC_o) = F \qquad (3.25)$$

where R refers to the respective $^3He/^4He$ ratios. This can be rewritten to obtain an expression for the fractional change in the initial ratio of the sample in terms of F:

$$R_t/R_o = \{F ([R_sC_s/R_oC_o) - 1] + 1\} / \{F ([C_s/C_o) - 1] + 1\} \qquad (3.26)$$

which shows that the fractional change depends on both the concentration and isotopic ratios between the glass and seawater, as expected.

Following the example of 50% loss for diffusion above, and considering $R_o/R_s = 8$, and $C_o/C_s = 100$ yields $R_t/R_o = .991$. Thus, exchange of helium with seawater is similarly ineffective to preferential ^{3}He loss in altering isotopic compositions of helium rich mid-ocean-ridge basalts. However, for samples with low helium contents it becomes very important, for example, if C_o equal to the seawater equilibrium value ($2-3 \times 10^{-9}$ ccSTP/g; see introduction), the initial ratio will be lowered by 44% for an F value of .5. Thus, glasses from island arc regions which have helium contents in this range, and relatively high diffusivities because of their more silicic compositions, can exhibit significantly altered isotopic compositions after relatively short residence on the seafloor (e.g. for a 2mm glass rind, F is about .5 after 10,000 years, considering $D = 2 \times 10^{-15}$ cm^2/s). This prediction is supported by the observation that Woodlark Basin andesites helium contents at or below the seawater equilibrium value exhibit atmospheric isotopic compositions (chapter 6). Curves showing the change in initial ratio as a function of F (equation 3.26) are given for several glass helium concentrations in figure 3.27.

The model curves and calculations presented above apply in a rough sense to radiogenic ^{4}He loss, given the appropriate D and a values. However, the solution for F in the case of simultaneous production and diffusion is developed in chapter 5 and provides more precise estimates of radiogenic helium loss rates. Discussion of the relative diffusivities of helium and other cations at high temperatures is presented in chapter 4.

Figure 3.27 Fractional change in the initial ^{3}He/^{4}He ratio (Ro) with extent of glass-seawater helium exchange (F). The solid curves are for different glass (C) to glass in equilibrium with seawater (Cs) helium concentration ratios, with an initial glass ratio of 8 Ra. The dotted line is for a concentration ratio of 10, but initial ratio of 4 Ra.

Figure 3.27

Helium Exchange with Seawater
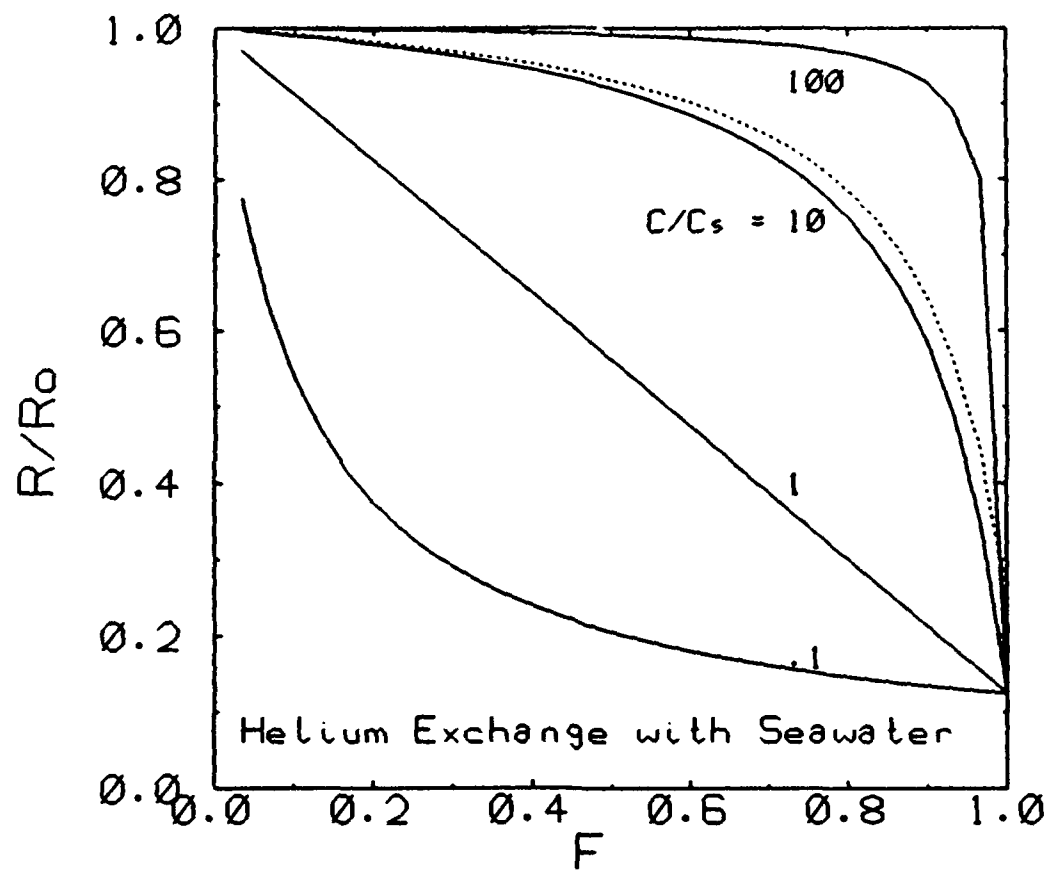
REFERENCES

ABE M., RAUCH B. and BRANDT W.W. (1971) Nonisothermal diffusion measurements on granular solids: Noble gas diffusion in fused silica. Zeitschrift Naturforsch. 26, 997-1004.

BENDER M.L. (1970) Helium-uranium dating of corals. Columbia University, Ph.D. (Pure Science), 149p.

BEVINGTON, P.R. (1969) Data Reduction and Error Analysis for the Physical Sciences. McGraw-Hill, New York, 336 p.

BOUGAULT H. and TREUIL M. (1981) Mid-Atlantic ridge: zero-age geochemical variations between Azores and $22^{o}N$. Nature 286, 209-212.

BRUNNAUER S., EMMETT P.H. and TELLER E. (1938) Adsorption of gasses in multimolecular layers. J. Am. Chem. Soc. 60, 309-319.

BYERLY G., MELSON W. and VOGT P. (1976) Rhyodacites, andesites, ferrobasalts and ocean tholeiites from the Galapagos Spreading Center. Earth Plan. Sci. Let. 30, 215-221.

CRAIG H. and LUPTON J.E. (1976) Primordial neon, helium, and hydrogen in oceanic basalts. Earth Plan. Sci. Let. 31, 369-385.

CRANK J. (1975) The Mathematics of Diffusion, 2nd edition, Oxford Press.

DOREMUS R.H. (1973) Glass Science John Wiley and Sons, New York, p349.

EBISUZAKI Y., KASS W.J. and O'KEEFFE M. (1967) Isotope effects on the diffusion and solubility of hydrogen in nickel. J. Chem. Physics 46(4), 1373-1378.

EINSTEIN A. (1905) Ann. Physik 17, 549.

FANALE F.P. (1964) Helium in magnetite. Columbia University Ph.D., (Geology), 135 p.

FECHTIG H. and KALBITZER S. (1966) Diffusion of argon in potassium bearing solids. In: Potassium-Argon Dating (ed. O. SCHAEFFER) p68-106

FELIX F.W. and MULLER M. (1976) Radioactive rare gas atoms as a probe for lattice defects in ionic crystals. Indian J. Pure and Appl. Physics 14, 247-252.

FISHER D.E. (1971) Incorporation of Ar in east Pacific basalts. Earth
    Plan. Sci. Let. 12, 321-324.

FLEISCHER R. L. (1988) Alpha-recoil damage: relation to isotopic
    disequilibrium and leaching of radionuclides. Geochim. Cosmo.
    Acta 52, 1459-1466.

FLEISCHER R.L. and RAABE O.G. (1978) Recoiling alpha-emitting nuclei:
    mechanisms for uranium-series disequilibrium. Geochim. Cosmo.
    Acta 42(7), 973-978.

FRANK R.C., SWETS D.E. and LEE R.W. (1961) Diffusion of neon isotopes
    in fused quartz. J. Chem. Physics 35(4), 1451-1459.

FRIEDMAN I. and LONG W. (1976) Hydration rate of obsidian. Science
    191, 347-352.

GALLAGHER K.J. (1965) The effect of particle size distribution on the
    kinetics of diffusion reactions in powders. In Reactivity of
    Solids. 5th International Symposium on the reactivity of solids.
    Munich, August 2-8, 1964. (ed. G.M. SCHWAB), Elsevier, New York,
    192-203.

GILETTI B.J. and KULP J.L. (1955) Radon leakage from radioactive
    minerals. Am. Mineralogist 40, 481-496.

GRAHAM D. V. (1987) Helium and lead isotope geochemistry of oceanic
    volcanic rocks from the East Pacific and South Atlantic. WHOI/MIT
    Ph.D., 252 p.

GRAHAM D.V., JENKINS W.J., KURZ M.D. and BATIZA R. (1987) Helium
    isotope disequilibrium and geochronology of glassy submarine
    basalts. Nature 326(6111), 384-386.

GRAHAM D.V., ZINDLER A., KURZ M.D., JENKINS W.J., BATIZA R. and
    STAUDIGEL H. (1988) Helium, lead, strontium and neodymium
    isotope constraints on magma genesis and mantle heterogeneity
    beneath young Pacific seamounts. In press.

HART S.R. (1984) He diffusion in olivine. Earth Plan. Sci. Let. 70,
    297-302.HESS P.C. (1980) Polymerization model for silicate melts.
    In Physics of Magmatic Processes (ed. R.B. HARGRAVES) pp.3-44.
    Princeton Univ. Press, Princeton, N.J.

195

HOFMANN, A.W. (1980) Diffusion in natural silicate melts: a critical review, in Physics of Magmatic Processes (ed. R.B. HARGRAVES) pp.3-44. Princeton Univ. Press, Princeton, N.J.

HORN P., JESSBERGER T., KIRSTEN T. and RICHTER H. (1975) ^{39}Ar-^{40}Ar dating of lunar rocks: Effects of grain size and neutron irradiation, Proc. Lunar Sci. Conf. 6 p 1563-1591.

HUNEKE J.C., NYQUIST L.E., FUNK H., KOPPEL V. and SIGNER p. (1969) The thermal release of rare gases from separated minerals of the Mocs meteorite. In Meteorite Research (ed. MILLMAN) pp 901-921. D. Reidel, Dordrecht, Holland.

HURLEY P.M. (1954) The helium age method and the distribution and migration of helium in rocks. In Nuclear Geology (ed. H. FAUL) pp. 301-329. J. Wiley and Sons, New York.

INTHOFF W. and ZIMEN K.E. (1956) Kinetik der Diffusion radioaktiver Edelgase aus festen Stoffen nach Bestrahlung (Edelgasdiffusion in Festkorpern 2). Trans. Chalmers. Univ. Techn. (Goteborg) 176, 16p.

JAMBON A. and SHELBY J.E. (1980) Helium diffusion and solubility in obsidians and basaltic glass in the range 200-300°C. Earth Plan. Sci. Let. 51, 206-214.

JAMBON A., WEBER H.W. AND BEGEMANN F. (1985) Helium and Argon from an Atlantic MORB glass: concentration, distribution and isotopic composition. Earth Plan. Sci. Let. 73 255-267.

JAMBON A., WEBER H. and BRAUN O. (1986) Solubility of He, Ne, Ar, Kr and Xe in a basalt melt in the range 1250-1600°C. Geochemical implications. Geochim. Cosmo. Acta 50, 401-408.

JENKINS W.J., EDMOND J.M. and CORLISS J.B. (1978) Excess ^{3}He and ^{4}He in Galapagos submarine hydrothermal waters. Nature 272, 156-158.

KALBITZER S., KIKO J. and ZAHRINGER J. (1969) The diffusion of ^{3}He and ^{4}He in LiF. Zeitschrift. Naturforsch. 24a, 1996-2000.

KANEOKA I. (1980) Rare gas isotopes and mass fractionation: an indicator of gas transport into or from a magma. Earth Plan. Sci. Let. 48, 284-292.

KARSTEN J., HOLLOWAY J.R. and DELANEY J.R. (1982) Ion microprobe
    studies of water in silicate melts: temperature-dependent water
    diffusion in obsidian. Earth Plan. Sci. Let. 59, 420-428.

KEEVIL N.B. (1940) Interatomic forces and helium in rocks. Proc. Amer.
    Acad. Arts and Sci. 73, 311-359.

KURZ M.D. and JENKINS W.J. (1981) The distribution of helium in
    oceanic basalt glasses. Earth Plan. Sci. Let. 53, 41-54.

KURZ M. D., JENKINS W. J., SCHILLING J. G. and HART S. R. (1982)
    Helium isotopic variations in the mantle beneath the central
    North Atlantic Ocean. Earth Plan. Sci. Let. 58, 1-14.

LE CLAIRE A.D. (1966) Some comments on the mass effect in diffusion.
    Phil. Mag. 14, 1271-1284.

LE CLAIRE A. D. (1970) Isotope effects in self-diffusion. In
    Diffusion Processes (ed. J.N. SHERWOOD, A.V. CHADWICK, W.M. MUIR
    and F.L. SWINTON) pp. 153-171. Gordon and Breach Sci. Pub., New
    York.

LEVENTHAL J.S. (1975) An evaluation of the U-Th-He method for dating
    young basalts. J. Geophys. Res. 80, 1911-1914.

LIDIARD A.B. (1955) Phil. Mag. 46, 1218.

LUPTON J.E. and CRAIG H. (1975) Excess ^{3}He in oceanic basalts:
    evidence for terrestrial primordial helium. Earth Plan. Sci. Let.
    26, 133-139.

LUX G (1987) The behavior of noble gases in silicate liquids:
    solution, diffusion, and surface effects, with applications to
    natural samples. Geochim. Cosmo. Acta 51, 1549-1560.

MANNING J.R. (1968) Diffusion kinetics for atoms in crystals. p. 115,
    D. van Nostrand, Princeton.

MULLEN J.G. (1961) Phys. Rev. 121, 1649.

MYSEN B.O., VIRGO D. and SCARFE C.M. (1980) Relations between the
    anionic structure and viscosity of silicate melts - a Raman
    spectroscopic study. Am. Mineralogist 65, 690-710.

NASH L.K. (1974) Elements of Statistical Thermodynamics. Addison-
    Wesley Pub. Co., Inc., Reading, MA, 138 p.

PRIGOGINE I. and BAK T.A. (1959) Diffusion and chemical reaction in a one-dimensional condensed system. Jour. Chem. Physics 31(5), 1368-1370.

RAMA S.N.I. and HART S.R. (1965) Neon isotope fractionation during transient permeation. Science 147, 737-738.

RAMA and MOORE, W.S. (1984) Mechanism of transport of U-Th series radioisotopes from solids into ground water. Geochim. Cosmo. Acta 48, 395-399.

REED D.J. (1977) A review of recent theoretical devlopments in the understanding of the migration of helium in metals and its interaction with lattice defects. Radiation Effects 31, 129-147.

REYNOLDS J.H. (1960) Rare gases in tektites. Geochim. Cosmo. Acta 20, 101-114.

RISON, W. and CRAIG, H. (1983) Helium isotopes and mantle volatiles in Loihi seamount and Hawaiian Island basalts and xenoliths. Earth Plan. Sci. Let. 66, 407-426.

SARDA P., STAUDACHER T. and ALLGRE C.J. (1989) Neon isotopes in basalts. In press.

SCHOEN, A.H. (1958) Correlation and the isotope effect for diffusion in crystalline solids. Phys. Rev. Let. 1(4), 138-140.

SHAKED H. (1965) Simple theory for the release of fission gas from powders. J. Nucl. Materials 17, 136-141.

SHELBY J.E. (1971) Diffusion of helium isotopes in vitreous silica. Physical Review B 4(8), 2681-2686.

SHELBY J.E. (1972) Helium migration in natural and synthetic vitreous silica. J. Am. Ceram. Soc. 55(2), 61-64.

SHELBY J.E. (1973) Effect of phase separation on helium migration in sodium silcate glasses. J. Am. Ceram. Soc. 56(5), 263-266.

SHELBY J.E. (1973) Neon Migration in TiO_2-SiO_2 glasses. J. Am. Cer. Soc. 56(6), 340-341.

SHELBY J.E. and KEETON S.C. (1974) Temperature dependence of gas diffusion in glass. J. App. Physics 45(3), 1458-1460.

SHELBY J.E. and EAGAN R.J. (1976) Helium migration in sodium aluminosilicate glasses. J. Am. Cer. Soc. 59(9-10), 420-425.

SPINDLER P. and LINDNER R. (1966) Diffusion of xenon-133 in UO_2 single crystals. Zeitschrift Naturforsch. 21, 1723-1725.

STEARN A.E. and EYRING H. (1940) Absolute rates of solid reactions: diffusion. J. Phys. Chem. 44, 955-980.

STEBBINS J.F., CARMICHAEL I.S.E. and MORET L.K. (1984) Heat capacities and entropies of silicate liquids and glasses. Contrib. Mineral Petrol. 86, 131-148.

STETTLER A. and BOCHSLER P. (1979) He, Ne and Ar composition in a neutron activated sea-floor basalt glass. Geochim. Cosmo. Acta 43, 157-169.

STOLPER E. (1982) The speciation of water in silicate melts. Geochim. Cosmo. Acta 46, 2609-2620.

STONEHAM A.M. and FLYNN C.P. (1971) Quantum theory of interstitial diffusion. In Atomic Transport in Solids and Liquids (eds. A. LODDING and T. LAGERWALL) pp.365-376. Verlag der Zeitschrift fur Naturforschung, Tubingen.

THARMALINGAM K. and LIDIARD A.B. (1959) Isotope effect in vacancy diffusion. Phil. Mag. Series 8, 899-906.

TRULL T.W., PERFIT M. R. and KURZ M.D. (1988) Helium and strontium isotopic constraints on the origin of island arc magmas in the Woodlark Basin. In press.

VINYARD, G.H. (1957) Frequency factors and isotope effects in solid state rate processes. J. Phys. Chem. Solids 3, 121-127.

WEISS R.F. (1971) The solubility of helium and neon in water and seawater. J. Chem. Eng. 16, 235.

WERT C. and ZENER C. (1949) Interstitial atomic diffusion coefficients. Phys. Rev. 76, 1169-1175.

WOLF D. (1981) Theory of correlation effects in diffusion. In Mass Transport in Solids (eds. F. BENIERE and C.R.A. CATLOW) pp. 149-168. Plenum Press, New York.

Chapter 4.

Diffusivity of ^{3}He and ^{4}He in olivine and clinopyroxene
at magmatic and mantle temperatures.

4.1 INTRODUCTION

Helium measurements in crystalline phases have many applications in igneous geochemistry, including U+Th/He geochronology, the identification of mantle components in ultramafic xenoliths, and the characterization of magmatic volatile sources via measurements on phenocrysts in volcanic rocks. Many of these studies require estimates of the extent of equilibration of helium between different phases within the source region, the magma, or the rocks after eruption. For example, if the helium isotopic composition of xenolith minerals is to be considered a signature of the mantle source region it must be clear that the host magma has not exchanged helium with the xenolith. Similarly, the relation between helium isotopic compositions and the source of other magma components is unclear if it is possible that helium is transported rapidly in the mantle. Another example is the significance of helium isotopic disequilibrium between fluid inclusions and helium dissolved in crystal lattices (e.g. data in chapter 6; Polve and Kurz, 1989). Other studies of helium isotopic variations as indicators of magma sources rely on assumptions of minimal gas loss or that loss has not affected helium isotopic compositions. Zindler and Hart (1986) have pointed out that this may not be true for the sources of certain oceanic island basalts or magma chambers in general, both because helium loss leads to accelerated change of the residual ^{3}He/^{4}He ratio by radioactive decay and because ^{3}He may be preferentially lost.

In general, the degree to which helium isotopic compositions of crystalline phases (or glasses) have exchanged or lost helium depends on the helium transport rate in comparison to the rates of the important geologic processes in the system, such as magma migration rates, degassing rates, and cooling rates. Little is known about helium mobility in crystalline phases at high temperature. Gramlich and Naughton (1972) measured single estimates of helium diffusion coefficients for olivine and pyroxene at about 1100°C, but did not investigate the temperature dependence. Hart (1984) measured the helium diffusivity in olivine at three temperatures and obtained a rough

Arrhenius relation, which suggested He diffusion was strongly temperature dependent and several orders of magnitude higher than for many cations of geologic importance. No measurements of the relative diffusivity of ^{3}He and ^{4}He in basaltic minerals have been made. Because of the small amount of previous work, and the importance of helium isotopic studies to basaltic petrogenesis studies, this chapter focuses on the measurement of ^{3}He and ^{4}He diffusion in two common igneous minerals (olivine and clinopyroxene) at magmatic and mantle temperatures, with the goal of defining rates of isotopic equilibration between basaltic magmas and minerals, and setting limits on the extent of isotopic fractionation accompanying helium loss from these minerals as magma chambers age and lavas cool.

4.2 METHODS

Diffusivities were estimated for olivine and pyroxene by measuring ^{3}He and ^{4}He degassed from mineral separates <u>in vacuo</u> in a high temperature furnace at 700-1400°C. After obtaining several sequential release aliquots over a period of hours to days, the samples were melted to determine their total helium contents, allowing the calculation of fractional release rates. The experiments were done primarily at constant temperature, but in two cases (expts. 4 and 8) the temperature was increased during the experiment and more aliquots were collected at higher temperature before melting. Diffusion coefficients for each release aliquot were then calculated using model equations which assume equisized, spherical grains with initially homogeneous helium concentrations. The furnace, helium mass spectrometry, and diffusivity calculations are described in detail in chapter 2, and are discussed below as neccesary in interpreting the experimental results.

The mineral separate samples were loaded as loose grains into a sample holder mounted above the furnace crucible and maintained at room temperature. This device, "the 4-shooter", is pictured in figure 2.1 (chapter 2), and allowed the furnace crucible to be baked out (1600°C), equilibrated at the run temperature, and a blank analyzed before introducing the sample. In addition, each experiment used a new

tantalum crucible insert cup to avoid the potential problem of reaction with previously melted samples. The furnace blanks were identical to typical processing line blanks of $4-5 \times 10^{-15}$ ccSTP He, with atmospheric isotopic composition. However, some diffusion experiments extended to nearly 30 hours between aliquots, so high temperature long-time "closeups" were also analyzed. The mean leak rate was 1.5×10^{-16} cc ^{4}He/s with a high of 2.8×10^{-16} cc/s and a low of $.45 \times 10^{-16}$ cc/s, or always less than 3×10^{-11} cc/day. For all experiments this leak contributed less than 2% of the helium in any aliquot, and for most aliquots significantly less. The leak was corrected for, assuming an atmospheric isotopic composition. Less than 4 parts per thousand of any release aliquot was lost during sample processing, as verified by analyzing the helium left after melting a sample, and by analyzing an air standard expanded into the furnace volume. Combined with frequent calibration by comparison to air standards (see chapter 2), the low blanks and losses allowed the fractional releases (F values) to be calculated with high precision (1 sigma error of .2 to .3%) and accuracy (1 sigma error <.5%).

Furnace temperatures were measured using an optical pyrometer (Micro-optical model, Pyro. Instr. Co.). The pyrometer was focused through the sapphire viewing port and onto the smooth floor of the tantalum crucible insert, i.e. the surface on which the mineral grains rest. The measured pyrometric temperatures were corrected for the emissivity of this surface (using data for polished Ta metal provided by the instrument manufacturer) and for transmission losses through the sapphire window, which reduced apparent temperatures by 20 to 40°C over the range of 800 to 1700°C (as measured by focusing the pyrometer on the source filament of a thermal ionization mass spectrometer, with and without the window in the line of sight). Succesful use of the pyrometer required considerable care, because small variations in the azimuth angle to the window produced deviations of up to 20°C, and different observers percieved temperatures differing by 10°C or so. However, repeated measurements by a single observer with constant pyrometer allignment were reproducible within $5-8^{\circ}$C, and established

that the furnace maintained constant temperature at constant power for long periods (up to several days).

Using a freshly cleaned window and empty crucible, a pyrometric temperature versus power calibration curve was determined (J symbols in figure 4.1a). This figure also shows that in some experiments, particularly those of long duration, progressive coating of the sapphire window reduced apparent pyrometric temperatures by as much as 200°C. Fortunately, this effect was made obvious by temporal decreases in apparent temperatures at constant furnace power. In these experiments, the power-pyrometric temperature calibration curve was used to obtain sample temperatures. Figure 4.1b shows that throughout the experiments (using 2 crucibles and 9 inserts over the course of 5 months) the power-current relation was essentially constant: the maximum power difference for a given currrent is 20 watts which corresponds to less than 10°C. This suggests that the furnace resistance element did not oxidize or otherwise age during the experiments, and lends credence to relying on constant power as an indicator of constant temperature when the window becamed coated.

Unfortunately, the pyrometric temperature measured for different crucible inserts during the experiments did not always agree with the pyrometric temperature versus power calibration curve, even when the window remained clean. For example, measurements in one experiment suggested temperatures up to 100°C above the calibration curve (V symbols in figure 4.1a). In order to better understand this variation, and to determine the accuracy of the pyrometric temperatures, the furnace power-temperature relation was also calibrated by melting pure metals (Ag, Au, Mn, Ni, Pd; less than 1 ppm impurities; Johnson-Matthey Inc.). In general, the metals were observed to melt at a sharp temperature to form a small pool of liquid. An exception was nickel, which appeared to melt over a large temperature range and was not used in the calibration. The currents at which silver and manganese melted were reproducible to within about 5 amps (equivalent to 15°C for Ag and 10°C for Mn; figure 4.2). Reproducibility for palladium was poorer, about 15 amps (45°C), in part reflecting the difficulting in stepping the furnace temperature by small amounts (less than 5 amps) at high

Figure 4.1 Apparent pyrometric temperature (uncorrected
for emissivity) as a function of furnace power (a, at top). The
low values (e.g. H and D symbols) are the result of coating of
the sapphire window. Symbols correspond to different emanation
experiments and calibrations (J). The reproducible current power
relation for the furnace during all the experiments is shown at
the bottom (b).

Figure 4.1
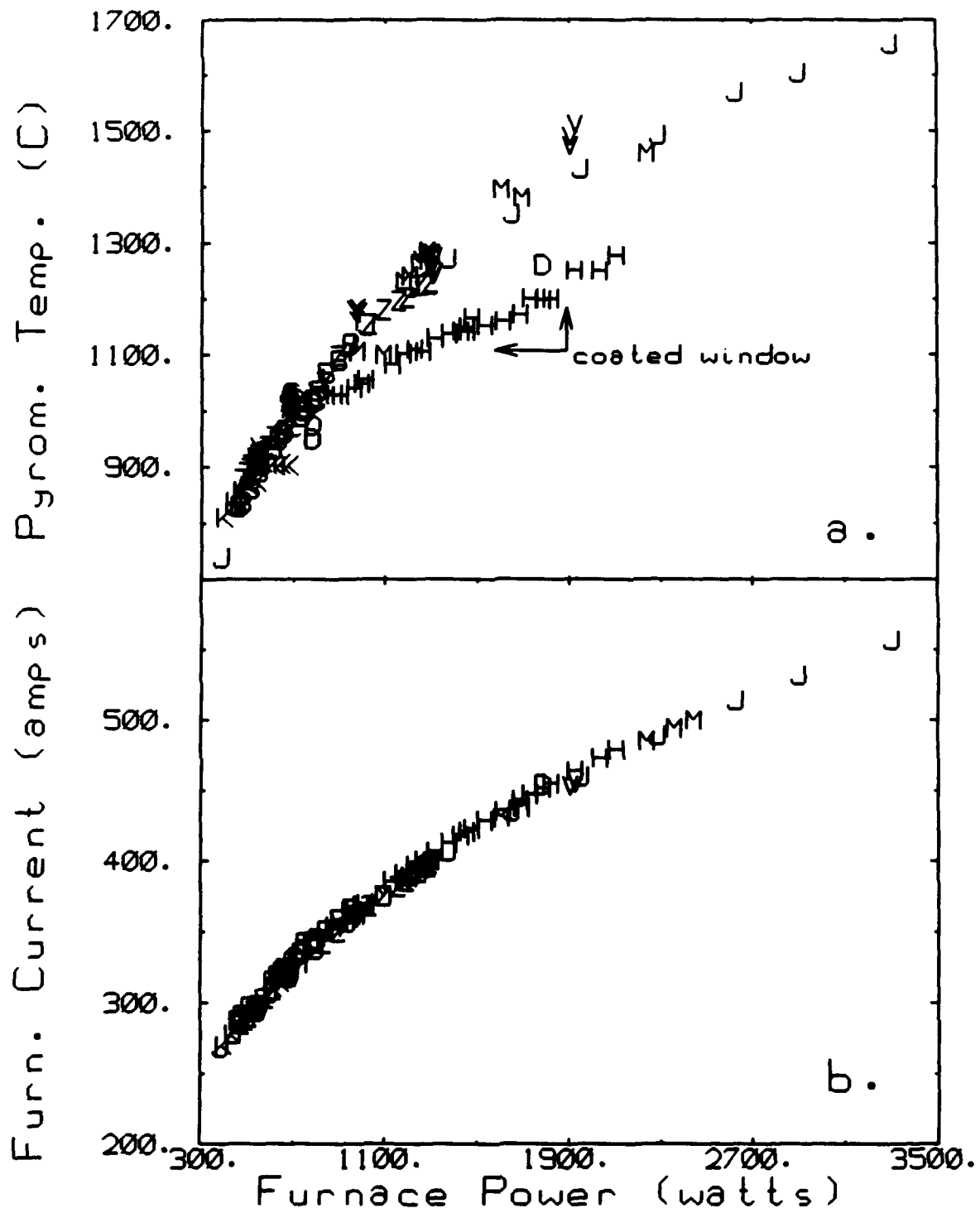
Figure 4.2 Comparison of pyrometric temperature calibration (curves) with fusion data for pure metals placed directly in the crucibles and for one gold sample in a tantalum foil boat. Two gold calibrations were performed in a different crucible than was used for most of the experiments (solid dots). The raw pyrometric temperature data has uncertainties of 5-8° C, and the melting point current uncertainties are about 10 amps. The corrected pyrometric curve accounts for emissivity changes for Ta with temperature and for the measured attenuation of the sapphire window. The metal fusion data suggests corrected pyrometric temperatures are overestimated above 1200° C.

Figure 4.2
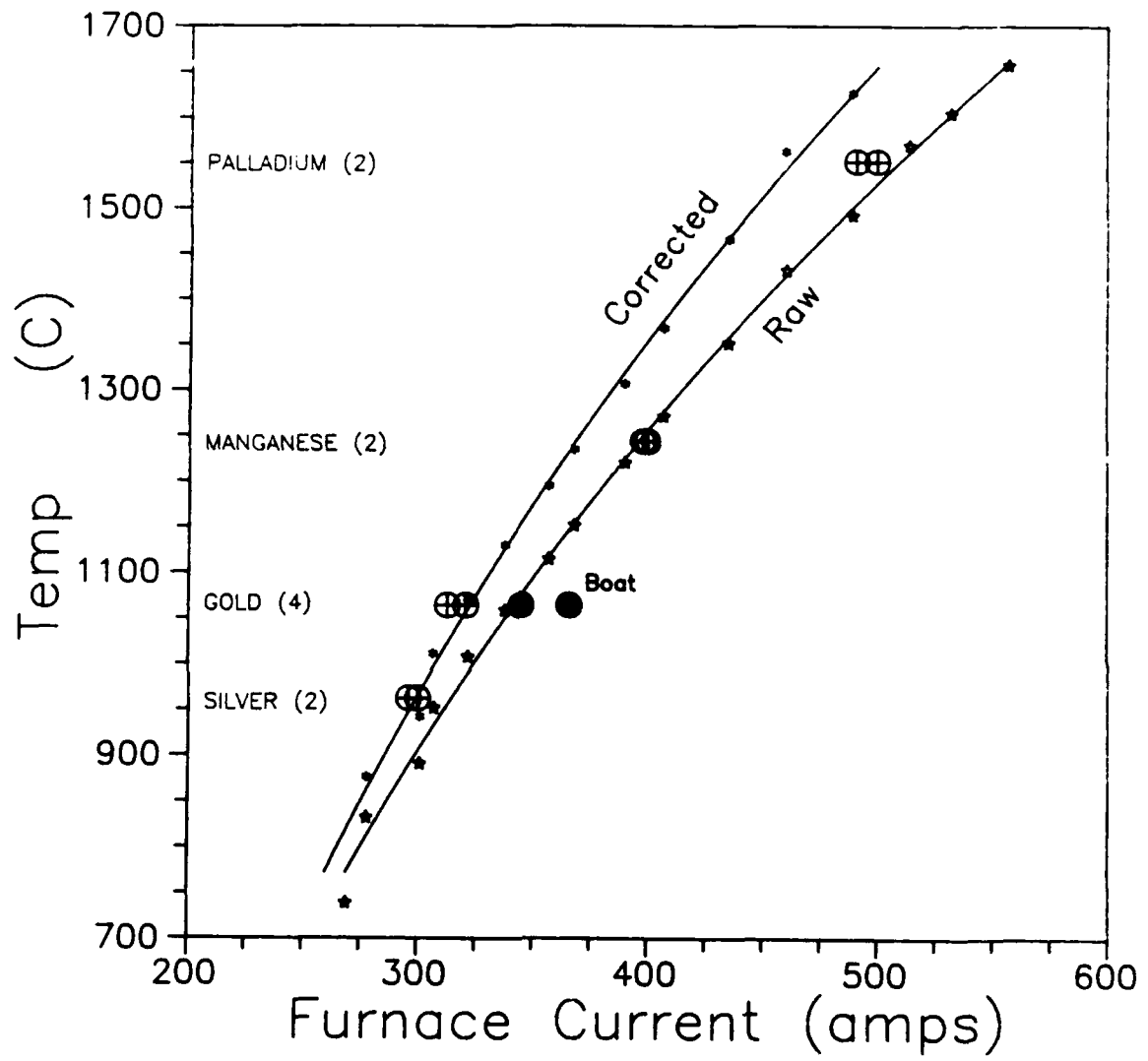
power. The current required to melt gold varied by 15 amps (50°C) for two calibration runs with different inserts within the same crucible. However, an even larger difference was observed for different outer crucibles. Gold melted at a greater current (equivalent to almost 100°C higher temperature) in the first crucible used (C6) for experiments #4 and #8, than in the second crucible (C8) used for all the other (isothermal) experiments. In addition, melting a gold sample loaded in a small tantalum boat (crucible C6) required a higher current than any of the loose samples.

The variations in the furnace currents required to melt the standard metals may be best explained as a combination of different placements of the two outer crucibles with respect to the heating element and variations in the heat shielding effect of the loose-fitting crucible inserts (and tantalum boat). This explanation also accounts for the fact that the observed pyrometric temperature tended to increase with the amount of current required to melt a standard, as follows. The pyrometer, in some sense, integrates the light emitted by the crucible insert bottom and the light emitted from the gap between the insert and crucible wall, which appeared to be at higher temperature, by up to 40°C. Thus, when the insert is a relatively poor fit the inner cup temperature is relatively cool and more power is required to melt a standard metal, but the "temperature" measured by pyrometry appears higher, because more high temperature radiation is emitted from the insert-crucible gap then when the insert fits well. The currents at which the metal standards melted agreed reasonably well with the corrected pyrometric temperatures at low temperature (Ag and Au), but at higher temperatures (Mn and Pd) the metal melting data suggests the furnace is approximately 100°C cooler than the corrected pyrometry data (figure 4.2). This suggests the emissivity correction may be overestimated at higher temperatures.

Because of the uncertainties in calibrating the power-temperature relation and in using the pyrometer most of the diffusion experiments were performed isothermally at furnace currents very close to the melting points of the metals. Temperatures and associated uncertainties (which range from 10 to 30°C, see data tables, Appendix C) for these

experiments were then obtained by comparing both the current and pyrometric temperature for the experiment with the closest fusion calibrations in the same crucible, to correct for both differences in furnace power and differing extents of heat shielding by the inserts. The shape of the pyrometric curve obtained in the same crucible (and where possible, the same insert) was used to extrapolate from the melting calibration current to the diffusion experiment current. In some cases, e.g. experiments 1 and 5, the current and pyrometry for the experiment and for melting the nearest standard (Ag) were in excellent agreement and these temperatures are reasonably certain (within $10^{o}C$) . For other experiments, the agreement was poorer, and the uncertainty therefore larger (up to $30^{o}C$).

4.3 SAMPLES

Diffusion measurements were made on clinopyroxene and olivine mineral separates from Hawaiian mafic xenoliths. These samples were chosen because of the ease of preparation of pure phase separates, and their relatively high helium contents. The mineral separates were prepared by Dr. Mire Polve using previously described methods (Polve and Kurz, 1989).

The olivine mineral separate was prepared from a dunite xenolith (USNM 113987-107) from the 1801 alkali basalt flow of Hualalai Volcano, Hawaii. The grains used in the experiments (500-710um) are intermediate in the size spectrum present in the porphyroclastic rock (.1-2mm). As observed previously, (Kurz et al, 1983), the grains contain abundant arrays of small (approximately 5 microns in diameter) fluid inclusions, and only rare larger inclusions in this grain size. Comparing the relative release of helium by in vacuo crushing and by melting the grains suggests that most (90% or more) of the helium is contained in these inclusions (table 4.1). The isotopic compositions of helium released by these methods are indistinguishable. The grains handpicked for the diffusion measurements were roughly spherical, completely devoid of adhering matrix or other phases, and showed no signs of internal cracking or crystal domains in thin-section.

The clinopyroxene sample was prepared from a spinel-lherzolite nodule (69SAL219) from Salt Lake Crater, Oahu, which has been extensively studied for the distribution and isotopic composition of helium (Polve and Kurz, 1989). Approximately 50% of the helium in these crystals is released by crushing, the remainder is presumably dissolved in the crystal lattice, rather than trapped in fluid inclusions. These two components have identical helium isotopic compositions (table 4.1). In thin section, the pyroxene grains were not zoned, and were generally free from internal cracks. Fifteen separated pyroxene grains were examined by back-scattered electron imaging and no evidence of extensive pyroxene exsolution was found at the resolution of this technique (a micron or so). However, exsolved, lamellar chrome spinel inclusion on the order of 5-15 by 1-5 microns were found in abundances ranging up to 10 or slightly more per 500-1000um grain. In addition, in 3 of the 15 grains some evidence of slight compositional variability (Wollastonite 46-48) was found in diffuse zones on the order of 100um in size. In general, the appearance of the grains did not suggest the presence of any features which might make the diffusive length scale differ greatly from the physical grain size.

The 500-710um sieve fraction used in all but one experiment was composed primarily of broken grains from the porphyroclastic whole rock. The larger grain separate (.5-1mm, expt. #8) was more representative of the original grain sizes. Both size fractions had small (1% or less by volume) amounts of adhering neoblasts of olivine and orthopyroxene. These phases contribute an even smaller fraction of the total helium because of their low helium contents (Polve and Kurz, 1989). In contrast to all the other samples, the larger grain size separate also had small amounts (2% by volume) of adhering basaltic matrix. (The experiment with this separate, designated #8 here, was performed first as a trial.) All the mineral separates were cleaned by ultrasonic agitation in distilled water, acetone, and methanol prior to analysis.

Table 4.1 Sample compositions and bulk helium contents.

MINERAL	Olivine	Diopside
COMPOSITION	Forsterite 89.2	$Ca_{.46}Mg_{.49}Fe_{.05}$
SAMPLE NAME	USNM 113987-107	69 SAL 219
PROVENANCE	Dunite xenolith from 1801 alkali basalt flow of Hualalai Volcano, Hawaii	Spinel lherzolite xenolith from Salt Lake Crater, Oahu, Hawaii

Helium Contents:

	[He] $10^{-7}cc/g$	$^3He/^4He$ x Ra	[He] $10^{-7}cc/g$	$^3He/^4He$ x Ra
A	2.9 +.1	9.0 +.2	4.0 +.2	8.8 +.2
B	2 to 5	8.8 to 8.9	3 to 7	8.6 to 8.8

A. Helium released by crushing large (1-2mm) crystals, data for olivine from Kurz et al (1983), and for diopside from Polve and Kurz (1988).
B. The range of results for helium released in several step-heating experiments with .5 to 1mm grains that culminated in fusion.

4.4 RESULTS

For both olivine and diopside, three isothermal multiple-release experiments were performed in the temperature range 960 - 1260°C, using 500-710 um grains. These experiments (designated #1-3 for olivine and #5-7 for diopside) allowed the nature of the helium release mechanism to be considered from the time dependence of sequential releases and provided a three point temperature trend. In addition, for both phases, experiments were run in which the temperature was increased after partial release, to obtain an estimate of the temperature dependence from a single sample, which minimizes grain size effects (experiments 4 and 8). These experiments also extended the temperature range to 750 to 1400°C. Figure 4.3 shows that for low extents of fractional release (F less than .4 or so) the time dependence of helium release varied linearly with the square root of time, as is consistent with volume diffusion. In contrast, loss by leaks along cracks from a large internal reservoir such as a fluid inclusion would be expected to display a linear F versus time relation at low to medium F, and this was not observed (figure 4.3). (A more complete discussion of helium release systematics and their relation to release mechanisms appears in chapter 3, section 3.3.3) The general smoothness of the releases also argues against a loss process involving disruption of fluid inclusions or crystal fracture. This is consistent with the visual examination (80x) of pyroxene grains after heating at 770°C in experiment #8, which revealed no changes, and with the unchanging appearance of the grains as observed in the crucible through the sapphire window. In summary, it appears helium release from both olivine and pyroxene was controlled by diffusion during the experiments.

Diffusion coefficients calculated using the spherical model (designated Dsm in the data tables, Appendix C) are generally constant for constant temperature, as shown in figure 4.4. However, there are several exceptions, including trends of increasing D values at low F in experiments 2 and 4 with olivine, and decreasing D values for pyroxene at both low and high F in experiment 8. Understanding the cause of these trends is important to obtaining best estimates for the

Figure 4.3 Fractional release of He versus time and versus the square root of time. The top plots are for Olivine (O expt. 1, □ expt. 2, △ epxt. 3, ◊ expt. 4) and the bottom plots for pyroxene (O expt. 5, □ expt. 6, △ epxt. 7, ◊ expt. 8). Filled symbols designate Load,Ramp, or Cool steps. The time dependence of helium release is more consistent with volume diffusion (linear in $t^{1/2}$ at low F) than with leaks from fluid inclusions (expected to be linear in t, perhaps with excursions).

Figure 4.3
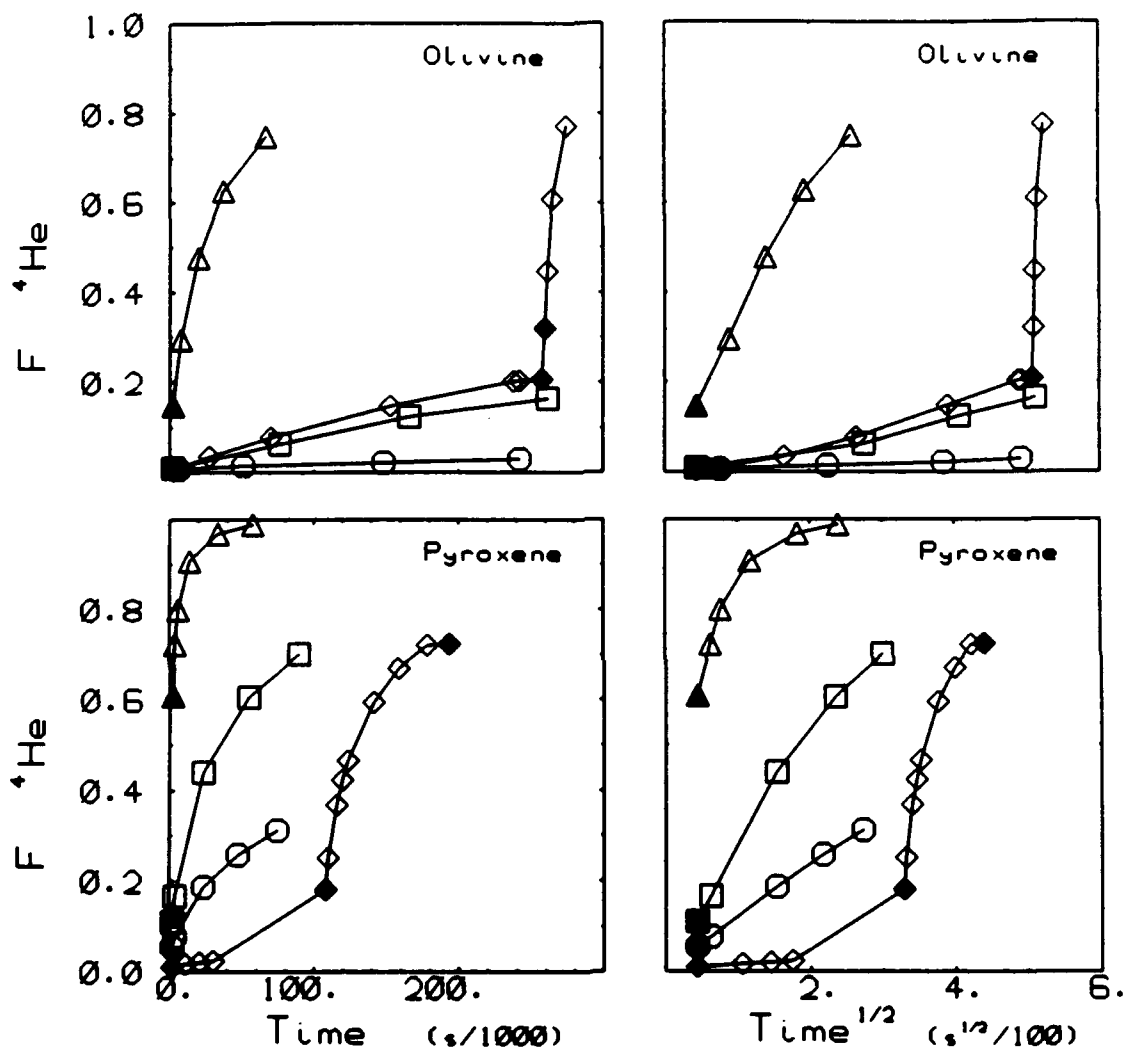
Figure 4.4 Helium diffusion coefficients as a function of
fractional release, F, for each experiment (symbols as in figure
3). The lines connect releases at constant temperature; ramp
steps are not shown. One sigma error bars are smaller than the
symbols, unless shown. The apparent increase in D at constant
temperature for two olivine experiments (squares and diamonds at
low F) suggests these samples lost helium by diffusion prior to
analysis. The decrease in D at high F for one pyroxene
experiment (triangles, expt. 7) reflects the distribution of
grain sizes and shapes within the sample, which is not accounted
for by the diffusion model. Adhering basaltic matrix in one
grain separate produced an initially rapid He release (high D),
but with relatively radiogenic isotopic composition.

Figure 4.4
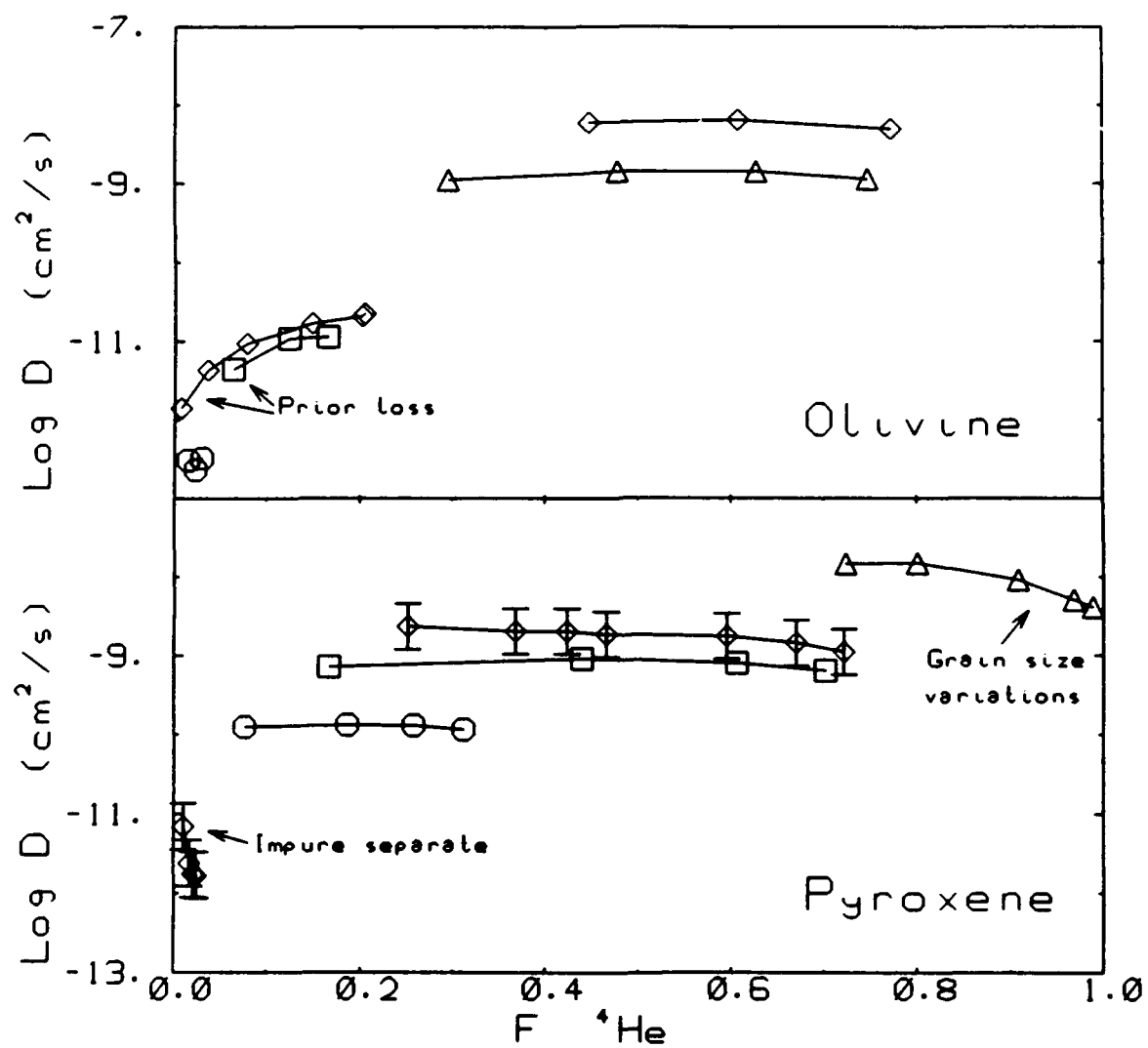
diffusivity of helium in these minerals. These trends are not the result of temperature variations, because pyrometric temperatures and furnace currents were constant (within $10^{\circ}C$) during the experiments and the long emanation times (hours to days) suggest thermal equilibrium. Instead, the explanation lies in the nature of the helium distribution in the samples, as becomes apparent on examining the assumptions of the spherical loss model and the isotopic data for these experiments.

In addition to the assumption of volume diffusion, calculation of diffusion coefficients from the spherical model assumes complete release of helium, an initially homogeneous distribution of helium within the crystals, and the approximation of equisized grains of idealized shape. Complete release was verified by melting the samples at the end of the experiment, and is not a potential problem. Homogeneous distribution is clearly an approximation, because much of the helium resides in fluid inclusions, particularly in the olivine grains (table 4.1). The inclusions are small in comparison to the grain size (1% or less), but tend to be aligned in planar arrays within ₁ne grains, ratₗer than being smoothly distributed. The approₓᵢmaₜion may nonetheless be reasonable because the arrays occur at varying angles within single grains, and many (50-100) grains were used in eaₒh experiₘent. If helium escape occurred primarily along the arrays, rather than radially through the crystal volumes, the measured diffusivities would be upper limits.

There are two ways by which heterogeneouₛ initial distribution of helium could explain the strong increases in D observed at low F in experiments 2 and 4. One explanation is that the initial releases are low until a diffusive profile is established between the inclusions, which contain most of the helium, and the surrounding crystal volume. If this "transient permeation" occured, the best D estimate would be the asymptotic value approached at higher F. Note that this explanation does not require or deny any barrier to transport at the fluid inclusion - crystal interface, but just reflects departures between the model and true initial distributions. However, this mechanism would predict that release rates increase over the F ranges in question (0 to 20%, figure 4.4), and they do not. Instead, the release rates drop by about a factor of 2. (Increasing D values still result because the spherical

model predicts release rates should drop by a factor of 8 over this F range.) A better explanation is that the grains have already established diffusive profiles from helium loss prior to analysis, as could have occurred during transport in the host magma or in the cooling lava flow (Hart, 1984; discussion below). As discussed in chapters 2 and 3, this condition leads to underestimated D values that increase assymptotically with F to true diffusivities (e.g. figure 2.6). This behavior is consistent with the D versus F trends observed, assuming prior losses of 8 to 10%, and suggests the best diffusivity estimates in these experiments are the highest values.

It is also worth noting that, in principle, apparent diffusivity variations related to transient permeation may be distinguished from prior loss problems by differing isotopic effects. Transient permeation from the fluid inclusions to the crystal surfaces would significantly increase preferential release of ^{3}He in comparison to loss from a solid with homogeneous distribution. This effect was demonstrated for neon isotopes in synthetic glass, and discussed theoretically, by Rama and Hart (1965). The extent of isotopic fractionation depends only on the ratio of release rate during the transient to the rate at steady state, for a given isotopic diffusivity ratio. In contrast, prior loss slightly reduces the ^{3}He/^{4}He ratios measured in later releases, because some preferential ^{3}He loss has already occured. Unfortunately, the helium isotopic ratios in these experiments could not be determined precisely enough to distinguish these possibilities, as is discussed further below.

Violation of the single grain size assumption is almost certainly responsible for the decrease in D values at high F (>.8) for pyroxene in experiment 7. The apparent D values decrease because smaller grains have released all their helium, as shown in model calculations in chapter 2 and for real distributions of glass particle sizes in chapter 3. The values of D obtained at lower F are most reliable, because they are least affected by the misfit between the model assumptions and the true helium distribution among the different grains. Finally, the decrease in D values at <u>low</u> F (770°C) in experiment 8 reflects early enhanced helium loss from adhering basaltic matrix (present in this

experiment only). This is apparent from the low ^{3}He/^{4}He ratios of the first releases (data table 8, Appendix C). Thus, the lower D values obtained at higher F at this temperature are most reliable for diffusion in the pyroxene itself.

In summary, many of the D variations can be understood in light of the model assumptions, and this understanding allows best estimates to be made for the diffusivities. While a refined grain size model could be applied (as in chapter 3), the extra effort is not warranted given other uncertainties, such as the internal helium distribution and temperature control. It is important to recognize that calculated diffusivities have inherent uncertainties, and potentially systematic inaccuracies, that derive from model simplifications, in addition to analytical uncertainties. In these experiments, potential errors from model misfits are estimated to be a factor of 2 or so based on experience with the refined model of chapter 3, and possibly more in experiment 8 which used a larger range of grain sizes.

The temperature dependence of helium diffusion displays simple exponential (Arrhenius) relations for both olivine and diopside (figure 4.5). The lines ($\log D = \log D^O - E_a/RT$) in this figure were estimated considering the already discussed systematics within individual experiments and, as is readily apparent, are not best fits to all the data. Considering the Arrhenius slopes reasonably accomodated by the data, the activation energies are distinctly different for the two phases, 100$\pm$5 Kcal/mole in olivine and 70$\pm$10 Kcal/mole in diopside (table 4.2). The diffusivities and activation energy determined for olivine are in good agreement with measurements by Hart (1984), but are somewhat higher than the results determined by Gramlich and Naughton (1972; see figure 4.6). Gramlich and Naughton also found a lower diffusivity for pyroxene than measured here (Gramlich and Naughton, 1972), although this could reflect the mix of orthopyroxene and clinopyroxene used in their experiment, if the orthopyroxene contained a significant fraction of the helium and had a lower helium diffusivity. In contrast, extrapolating lower temperature results for radiogenic ^{4}He diffusion in augite (Lippolt and Weigel, 1988) suggests much higher diffusivities than observed here (figure 4.6). The difference may

Figure 4.5 Arrhenius diagrams for helium diffusion in olivine and pyroxene. Symbols identify individual experiments as in figure 3. The error symbol, lower left, denotes the upper range of 1 sigma errors. Lines are best estimates based on diffusivity systematics within and between individual experiments and are not regressions to all the data. The highest D values obtained in experiments affected by prior loss or size distribution at high F were judged most reliable, and the lowest D values in one experiment with an impure mineral separate (see text). Note that the temperature trends determined in the step-heating experiments (diamonds) are similar to the isothermal results (all other points).

Figure 4.5
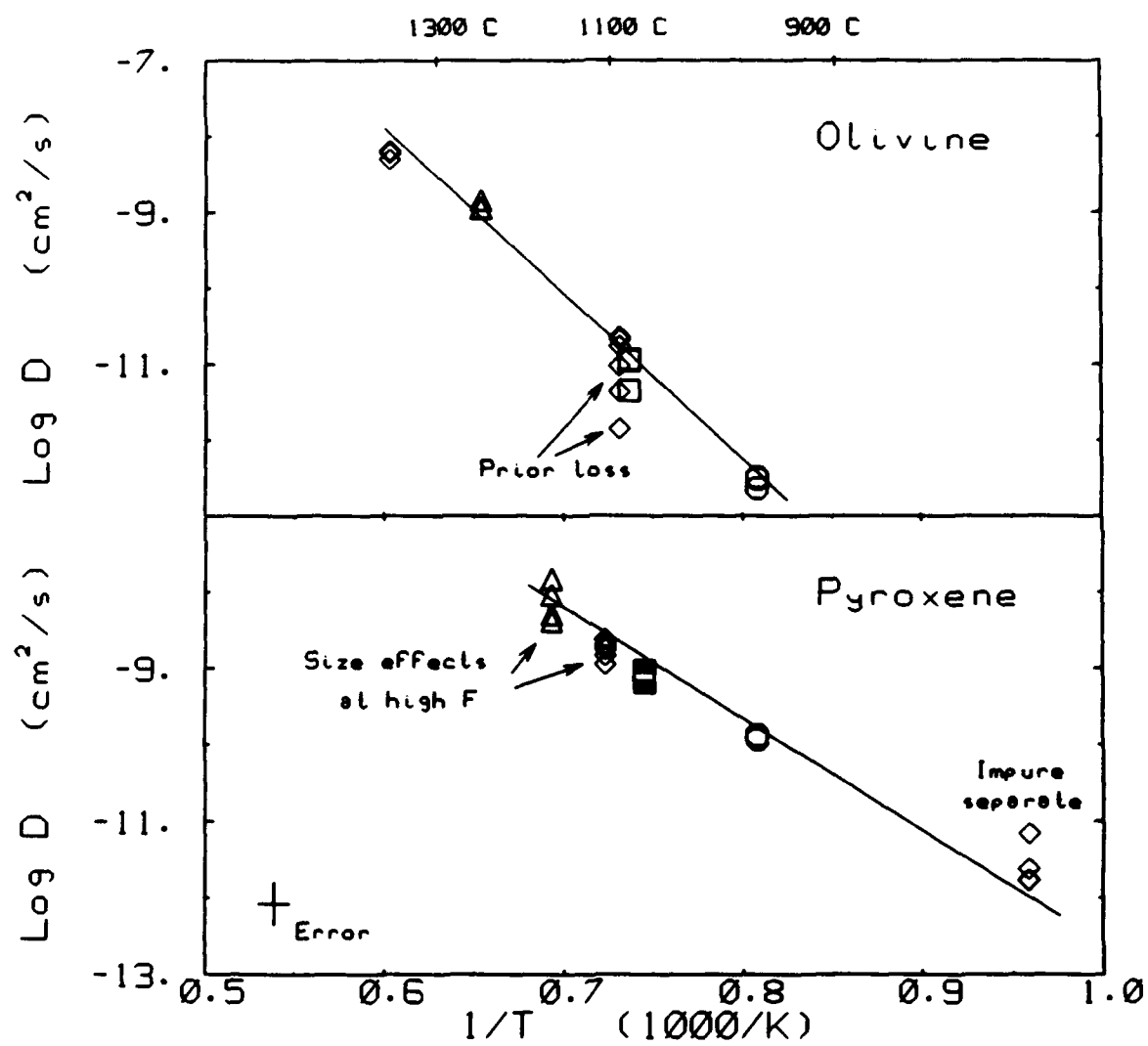
Table 4.2 Helium Diffusivity Results

Mineral	Temp. Range (^oC)	E_a (kcal)	$\log D^o$ (cm^2/s)	D at 1100 ^oC (cm^2/s)
Olivine	965–1385	100±5	$^+5.1±.7$	2×10^{-11}
Diopside	770–1170	70±10	$^+2.1±1.2$	1×10^{-9}

a. Approximate 1 sigma errors estimated as described in the text are given for E_a and D^o values.
b. D estimates at 1100 ^oC have 1 sigma errors of a factor of 2, as estimated from data scatter, temperature uncertainty, and particle size range.

Figure 4.6 Comparison of diffusivity results for pyroxene and olivine. Also shown are literature values, dotted line and anvil symbols for olivine (Hart, 1985); cross for olivine and triangle for a mix of clino- and ortho- pyroxene grains (Gramlich and Naughton, 1972). The dotted line at the upper right is an extrapolation of radiogenic helium diffusivities obtained below 800°C in augite (Lippolt and Weigel, 1988). The higher diffusivity in their study may reflect differences between inherited and radiogenic helium, or perhaps compositional effects, and is a cautionary note in the application of the results presented here to other rock types.

Figure 4.6
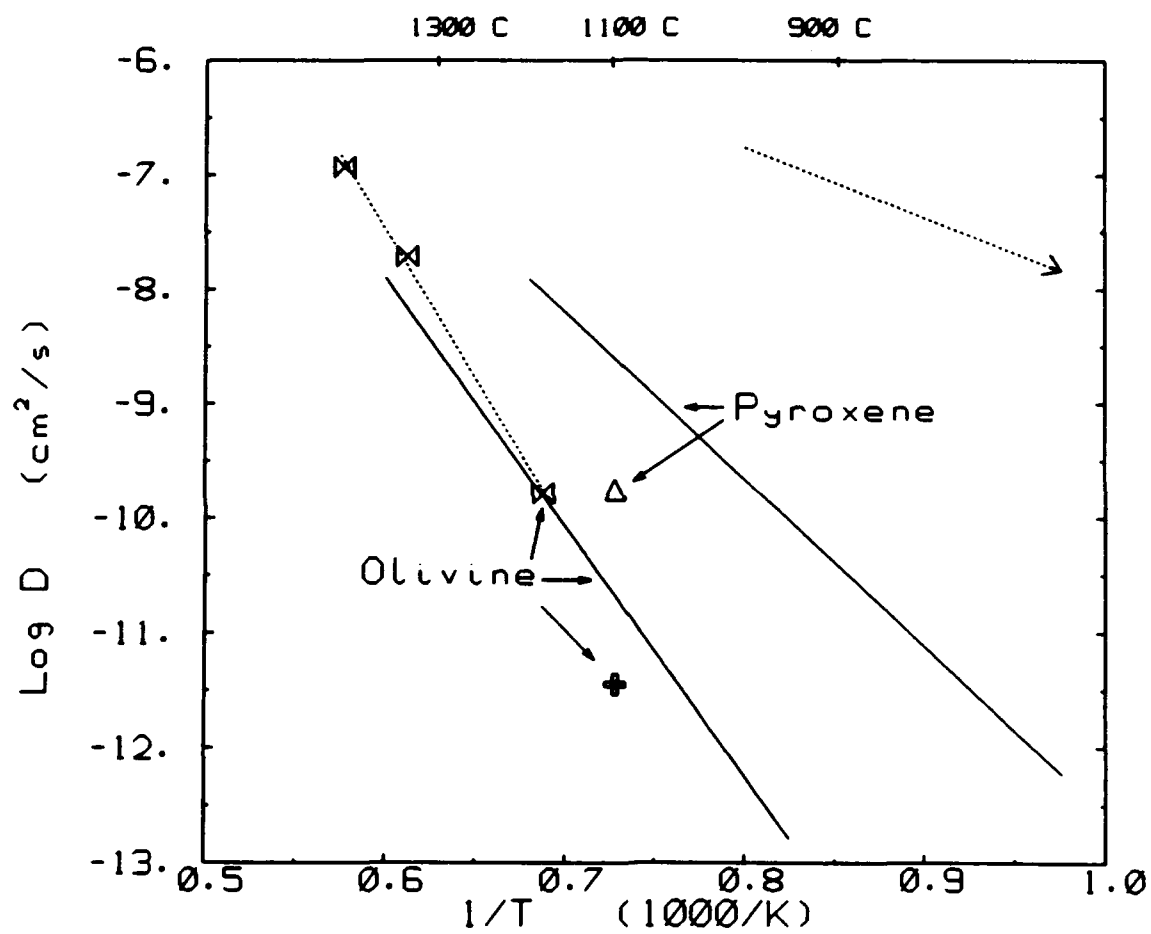
reflect decay-enhanced release, compositional effects, or the possibility that the physical grain size in this experiments is larger than the effective diffusive length scale.

While the activation energy difference between pyroxene and olivine is undoubtedly real, the relative helium diffusivities in these phases are less certain. It is possible that the diffusive length scale differs from the physical grain size in either or both minerals, and thus that the D estimates could be offset from the true values. The best way to examine this problem is to determine diffusivities using a wide range of grain sizes, which has not been done. However, at present it seems reasonable that the physical grain size corresponds to the diffusive length scale because the results of Hart (1984) for olivine are similar to those presented here, despite a factor of two difference in mean grain size; and because the pyroxene experiment with .5-1mm grains yielded the same D values as obtained with .5-.7mm grains. However, the uncertainties in measured D values could accomodate this relatively small range in grain sizes, so this question remains a problem for determining the true relative diffusivites of helium in pyroxene and olivine. Comfortingly, other researchers (Gramlich and Naughton, 1972; Hunecke et al, 1969) have also found higher helium diffusivities in pyroxene than olivine. However, no systematic examination of variations with grain size has been conducted, and it is possible these workers are making similar errors. In this regard, cation diffusivities in pyroxene are generally much lower than in olivine (e.g. Sneeringer, Hart and Shimizu, 1984; Hart, 1981), casting some doubt on the the opposite relation found here for helium, although helium and cations may well diffuse by different mechanisms. Sneeringer, Hart and Shimizu (1984) found that cation diffusivities in annealed synthetic pyroxenes were much lower than in natural samples (and varied with crystallographic direction). This may reflect a difference between physical and diffusive grain sizes in the natural samples, or perhaps enhanced mobility in response to higher defect populations. To summarize, until the relation between physical and diffusive length scales in the laboratory is better understood (and the role of defects in governing diffusion is documented), the suggestion

that helium diffuses more rapidly in pyroxene than olivine (and more rapidly than cations) must be viewed with caution. Given this caveat, in the discussion that follows the helium diffusivities are taken at face value.

The isotopic compositions of sequential releases in the emanation experiments are consistent with a small preferential loss of ^{3}He, although the analytical uncertainties are large (figure 4.7). These trends of ^{3}He/^{4}He versus extent of release (F) and the isotopic diffusivity ratios calculated for individual aliquots (experimental data tables 1-8, Appendix C) suggest a D^3He/D^4He value between 1.0 and 1.15, with the possibility of a lower value in pyroxene (1.04 $\pm$ .04) than in olivine (1.08 $\pm$ .04). Both phases suggest values somewhat lower than 1.15, corresponding to the inverse square-root of the ratio of the masses, $(m_4/m_3)^{1/2}$. As discussed in detail in chapter 3, there are several reasons for departures from this relationship, including diffusion mechanisms which involve correlation of successive atomic jumps, coupled motions of the diffusing atom and host crystal atoms, and vibrational energy quantization for light atoms like helium. The quantum explanation was found to best account for the low isotopic diffusivity ratio in basaltic glasses and is probably also tenable for the crystals studied here at higher temperature (see chapter 3) The small isotopic diffusivity ratio, D^3He/D^4He, implies large amounts of helium loss must occur to significantly affect the residual ^{3}He/^{4}He ratio (figure 4.8).

In summary, helium release from olivine and diopside mineral separates in laboratory heating experiments appears to be dominated by volume diffusion at magmatic and mantle temperatures. The temperature dependence of helium mobility is different for the two phases with loss from pyroxene occuring about 50 times faster than in olivine at 1100°C but with similar loss rates at higher temperatures, near 1550°C. The measured helium diffusivities are higher than most cation mobilities in pyroxenes and olivine. Figure 4.9 shows the helium results in comparison to a compilation of pyroxene diffusivities (Sneeringer, Hart and Shimizu, 1984). He is more mobile than all cations at 1100°C, except Pb, and has a similar diffusivity to argon. In olivine, helium

Figure 4.7 Helium isotopic data for emanation experiments. The average ^{3}He/^{4}He obtained by summing the incremental losses are shown for each phase by solid lines, along with the expected fractionation trends for isotopic diffusivity ratios of 1.15 (dotted) and 1.04 (dashed), assuming spherical geometry. Overall, the data suggest a somewhat lower isotopic diffusivity ratio for pyroxene (1.04 + .0 $\cdot$) than for olivine (1.09 + .04).

Figure 4.7
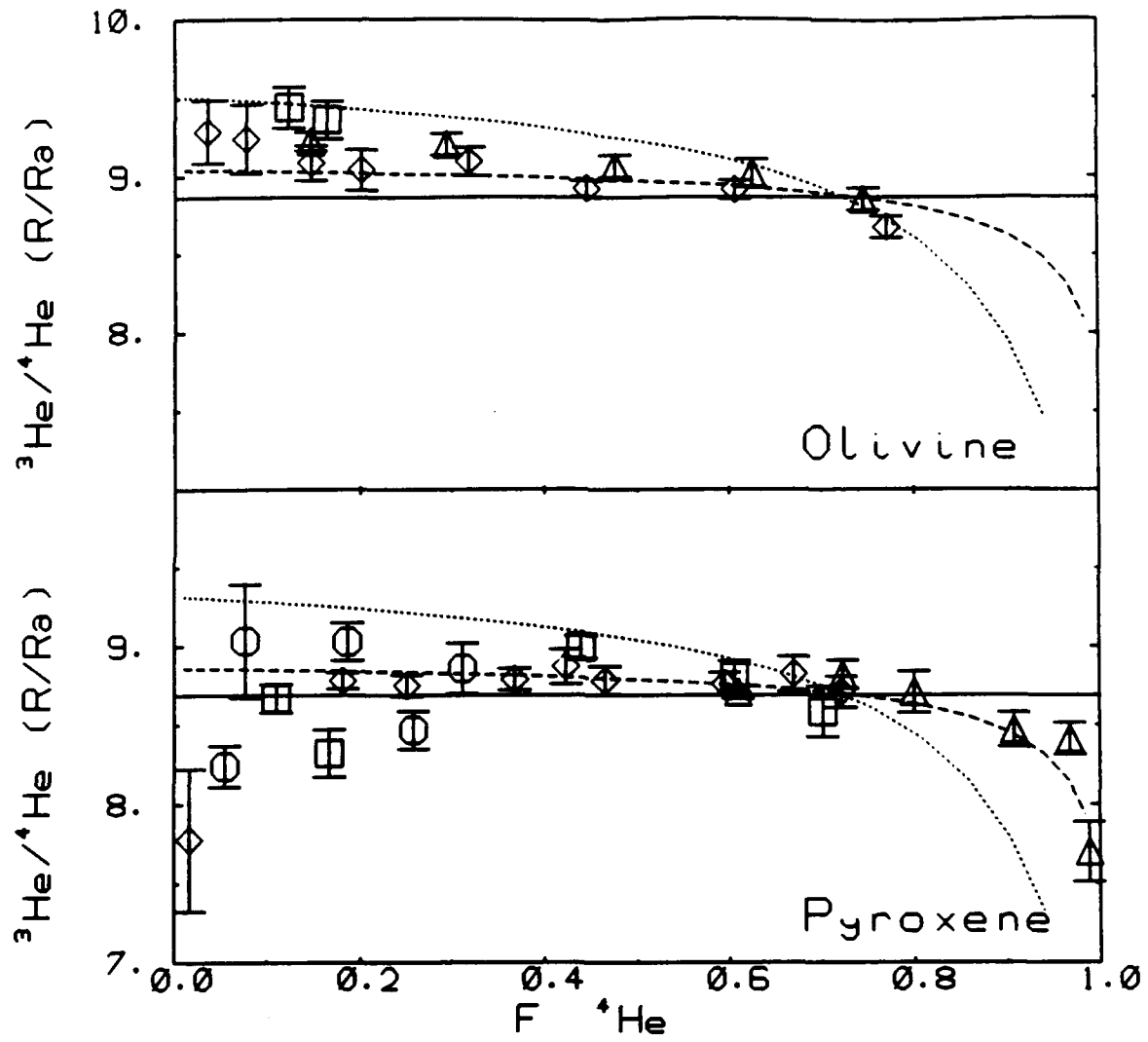
Figure 4.8 Reduction in initial ^{3}He/^{4}He ratio as a function of fractional helium loss for several values of the isotopic diffusivity ratio.

Figure 4.8
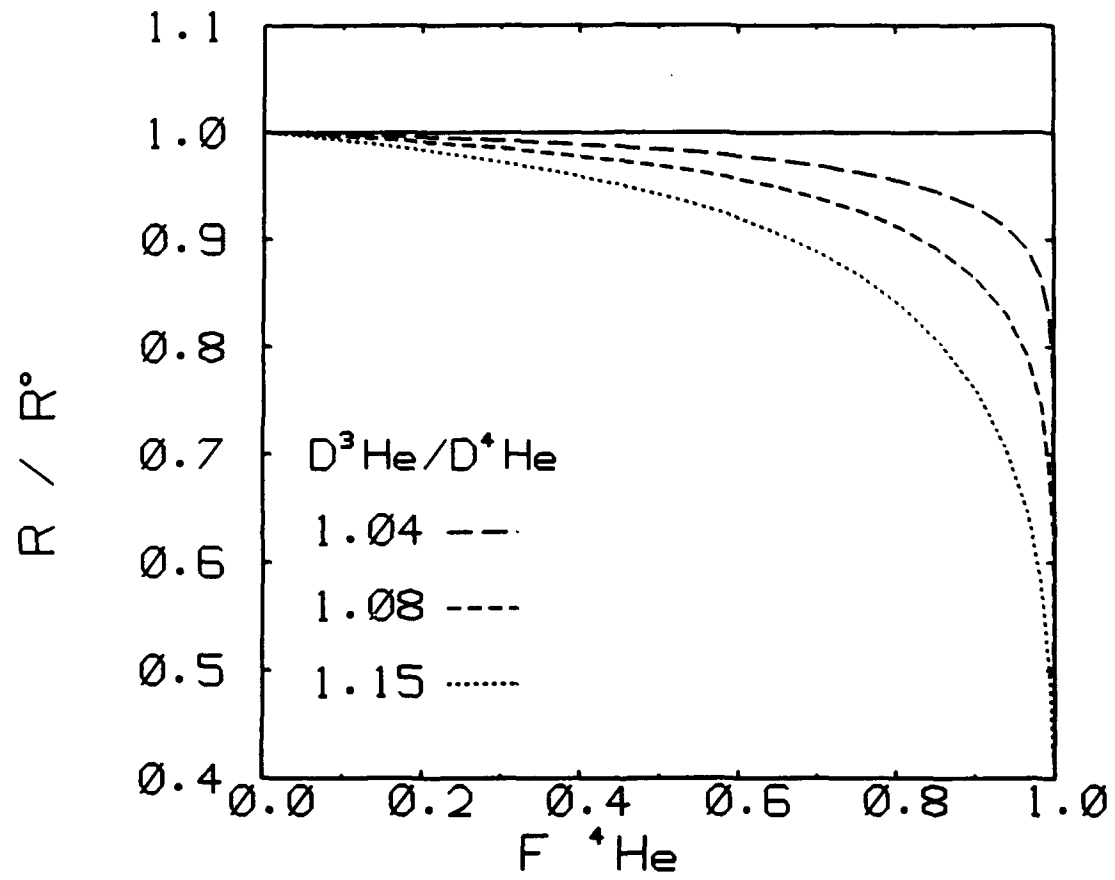
Figure 4.9 Comparison of the helium diffusivity in diopside and olivine with argon and common cation diffusion coefficients in various pyroxenes (compilation from Sneeringer, Hart and Shimizu, 1984).

Figure 4.9
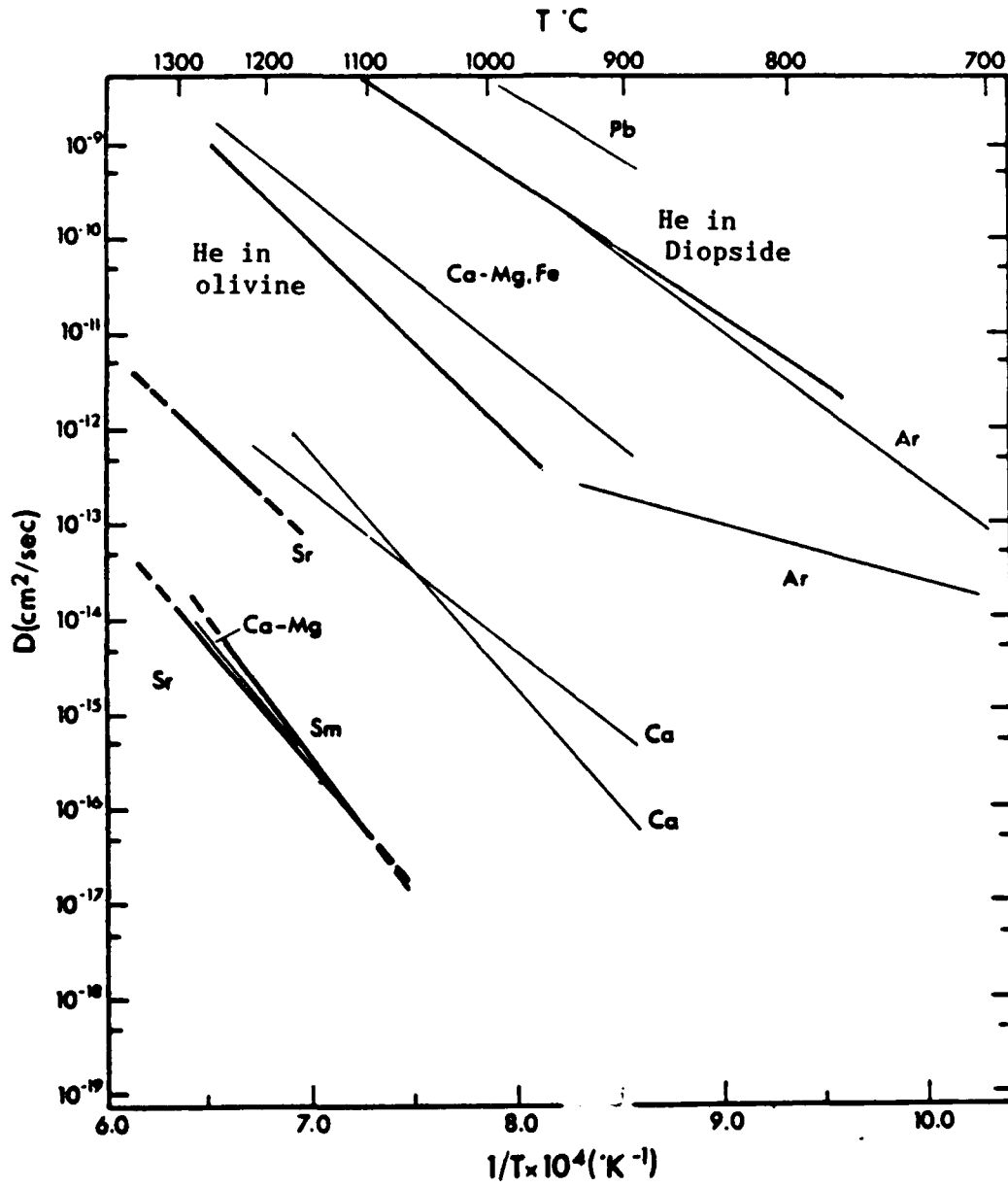
Figure 4.10 Diagram comparing the helium diffusivity and activation energy in olivine to a compensation trend for cations in olivine and other orthosilicates (Hart, 1981). He has a relatively high D_o value for its activation energy, suggesting it may diffuse by a different mechanism. Note that oxygen anions also depart from the compensation line, but in tne direction of lower mobility.

Figure 4.10
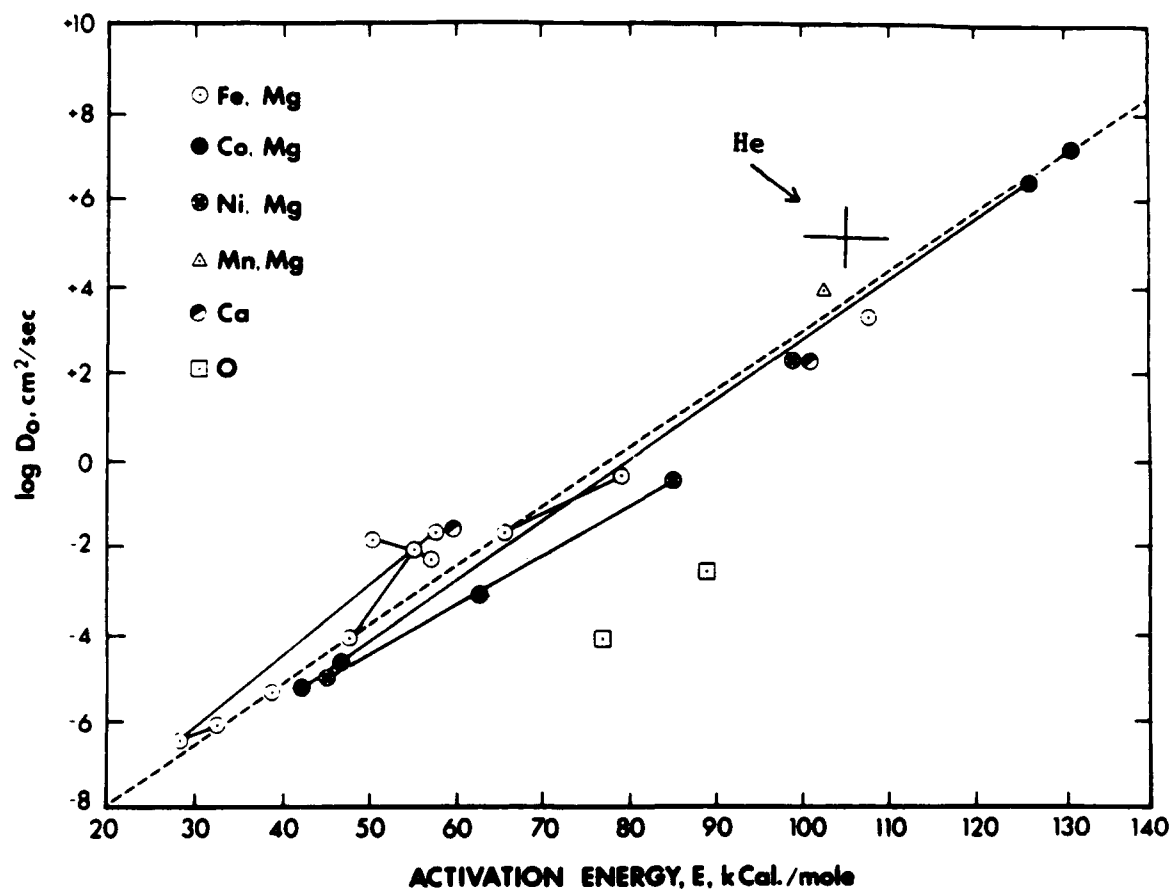
diffusion is also enhanced over cations, and along with oxygen anions departs from the compensation trend observed for many elements (figure 4.10; Hart, 1981). These differences are reasonably explained by an interstitial mechanism for helium and argon diffusion, in contrast to vacancy diffusion for the cations and larger, close-packed oxygen ions. It was not possible to establish the extent of isotopic fractionation accompanying diffusion with high precision, but the results suggest that this effect is not large, $1 < D^3He/D^4He < 1.15$, although greater preferential ^3He loss may occur in olivine than pyroxene.

4.5 DISCUSSION

Helium diffusion coefficients can be used to assess time and spatial scales for helium transport. The goals of this section are to compare these timescales to those involved in igneous petrogenesis, to determine whether helium's relatively high mobility leads to fundamentally different behavior than for other isotopic tracers, and to consider the timescales over which diffusion and/or radiogenic ^4He production can alter the $^3He/^4He$ ratio of igneous materials. A useful concept in this assessment is the "characteristic diffusive length", defined by:

$$X = (Dt)^{1/2} \qquad\qquad (4.1)$$

This relation is plotted for a range of diffusivities applicable to high temperature transport in olivine, pyroxene, and tholeiitic melt in figure 4.11. The meaning of the characteristic length is clarified by considering that 99% of diffusive loss, gain or exchange of helium will occur for a spherical volume of diameter X in time t, and that 50% transfer occurs in about 1/5 this time, as shown by the curves (scaled to phenocryst sizes) given in figure 4.12.

Proceeding sequentially from the mantle source region to melt generation, magma transport, chamber storage, and eruption; the effect of diffusive helium transport on natural variations in helium isotopic compositions is considered. Two general principles are worth noting.

Figure 4.11 Characteristic diffusive length scales ($x^2 = Dt$) for helium diffusion in olivine (dashed lines) and diopside (solid lines) at magnetic and mantle temperatures. The dotted line is for $D = 5 \times 10^{-5}$ cm^2/s in tholeitic melt at $1350^\circ C$ (Lux, 1987).

Figure 4.11
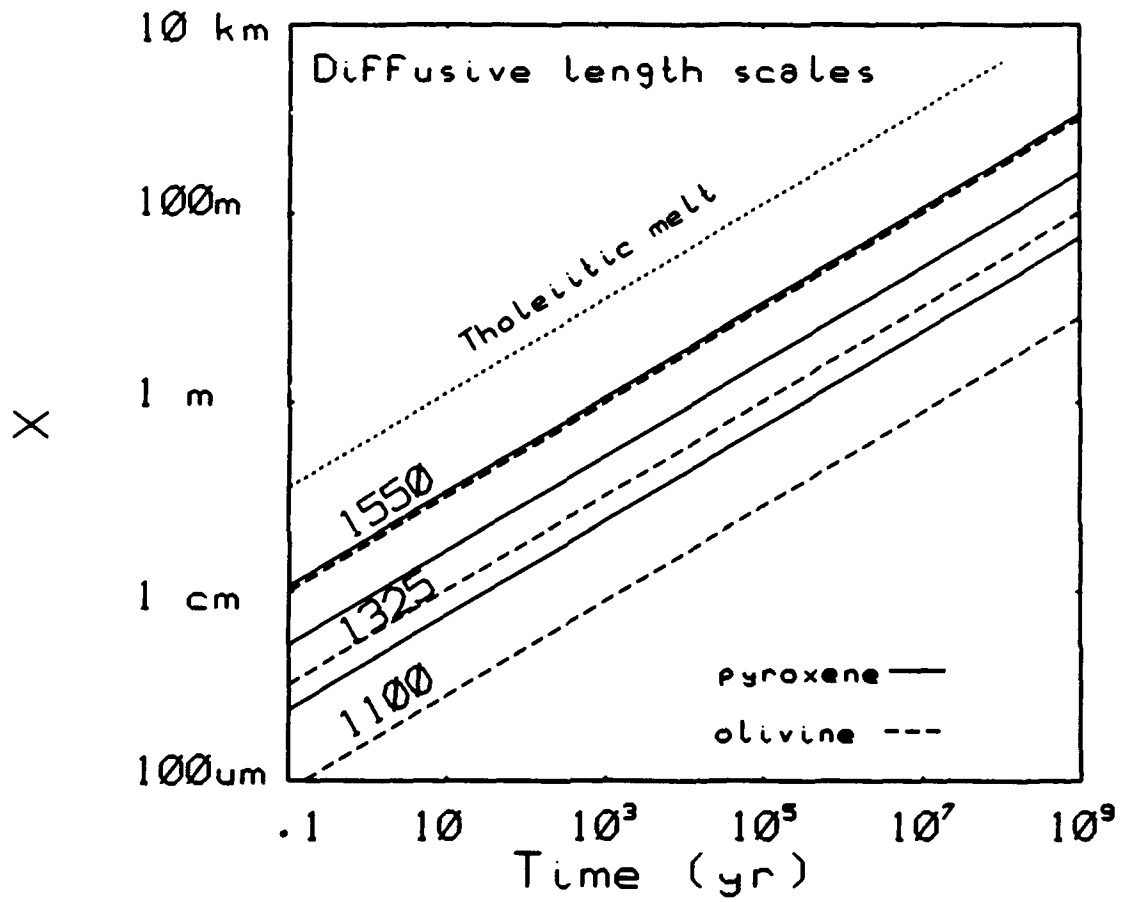
Figure 4.12 Fractional loss or equilibration curves for helium
diffusion from a sphere for several values of the diffusion
coefficient and grain radius (a). For example, 2mm diameter
diopside grains with a diffusivity of $1 \times 10^{-9} cm^2/s$ at $1100^\circ C$ have
a log D/a^2 value of -7 and will lose 60% of their initial helium
in a few days, provided the surrounding magma or rock contains no
helium. These curves also apply to the timescales required to
exchange helium with the surrounding medium.

Figure 4.12
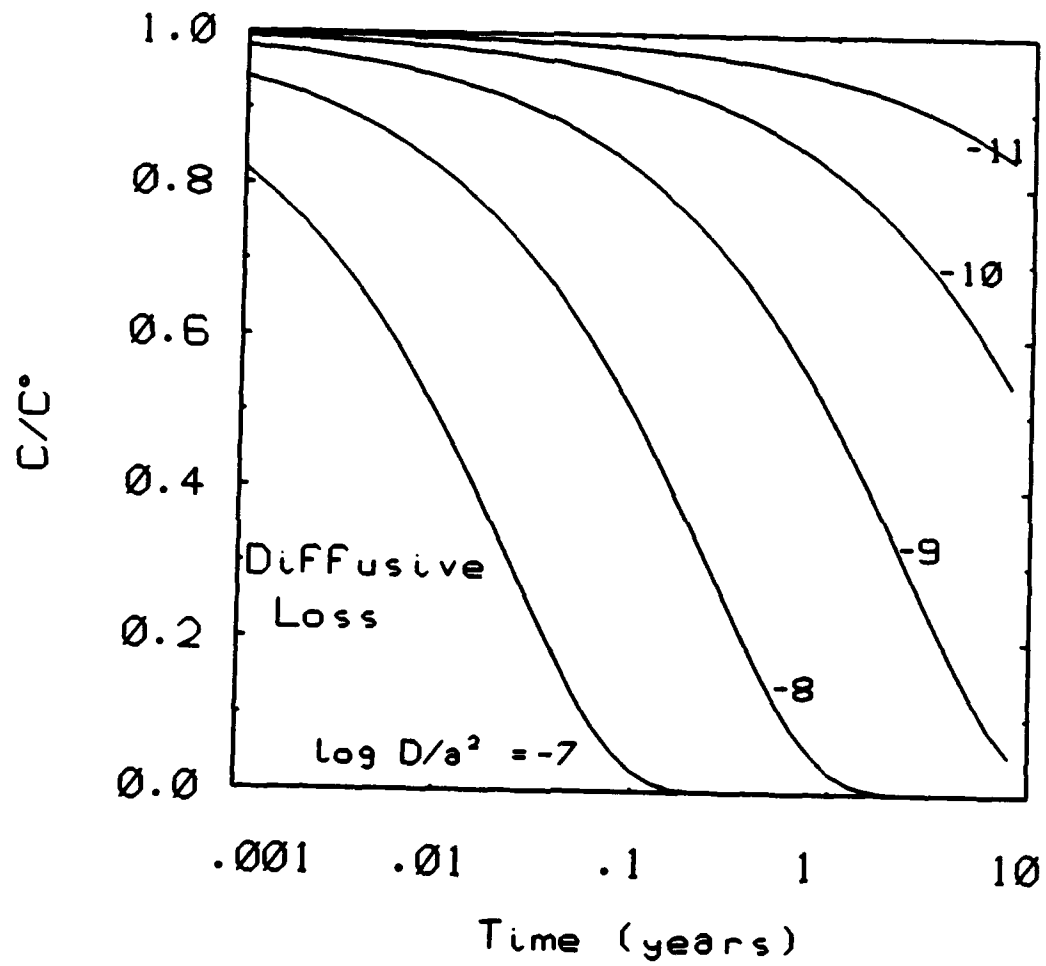
Figure 4.11 emphasizes that helium diffusion in the solid state proceeds very slowly in comparison to transport in magmas, where the helium diffusivity is about 5×10^{-5} cm^2/s (Lux, 1987). This is also true for isotopic tracers such as Pb, Sr and Pb and cations in general which have melt diffusivities on the order of 10^{-6} to 10^{-7} cm^2/s (e.g. Hoffman, 1980 and figure 3.25, chapter 3). Thus, when melt is present it will dominate diffusive mass transport. Secondly, conductive heat transport occurs far more rapidly than diffusive elemental migration (thermal diffusivities are on the order of 10^{-2} cm^2/s; e.g. Spera, 1980), suggesting cooling may limit diffusive transport in igneous systems which are not maintained at high temperature by insulating boundaries or heat inputs. In this regard, heat flow is a good analogy for diffusive mass transport, because it emphasizes the dependence on both the diffusivity (conductivity), and the difference in chemical potential (temperature) between the exchanging reservoirs. For example, a high helium diffusivity will i.t lead to gas loss from a phenocryst if the surrounding magma or cooling lava is helium rich.

Diffusion is not an effective means of transporting helium in the mantle on a large scale. At 1550°C, the characteristic diffusive length scale is only 1 km after 1 billion years (figure 4.11). The presence of melt enhances transport, but not greatly, X is about 13 km considering the diffusivity in magma of about 5×10^{-5} cm^2/s to apply to the mantle. The presence of a carbon-oxygen-hydrogen fluid in the mantle is likely to lead to a similar estimate, because helium diffusion in water is similar to the melt value (Jahne, Heinz and Dietrich, 1987). Grain boundary diffusion may enhance helium transport, but will occur more slowly than tranport in a melt or fluid phase (e.g. Hoffman and Hart, 1978). Pressure effects may alter these length scales to some degree, but not greatly given the less than an order of magnitude variations in diffusivities (factor of 3 in X) observed in experiments up to 10's of kilobars (e.g. Watson, 1981; Shimizu and Kushiro, 1984; Sneeringer, Hart and Shimizu, 1984).

Therefore, helium can not "permeate" the mantle, and large scale helium transport must occur by convection, as it does for other elements. This means that the relatively narrow range of $^3He/^4He$ ratios

of mid-ocean-ridge basalts (e.g. Kurz, 1982; Mamyrin and Tolstikhin, 1984) is related to mantle mixing processes, rather than properties of helium transport. In addition, different regions of the mantle can build up varying helium contents and isotopic compositions by radioactive decay, depending on their uranium and thorium contents. This process may explain the low ^{3}He/^{4}He region of the Mid-Atlantic-ridge adjacent to the Azores which was suggested to derive from uranium enriched, subducted lithosphere by Kurz et al (1982).

On a mineral scale diffusion becomes important as a control on helium isotopic compositions and the separation of helium from other elements. Mineral grains will equilibrate rapidly with a melt or other crystals. For example, for 2mm grains the characteristic timescale is 63 years for olivine and 1.3 yr for pyroxene at 1100^oC (figure 4.11). Therefore, equilibrium will govern helium separation during most melt generation and fractional crystallization events. This means that helium isotopic zoning in crystals is not to be expected, a contrast with some other cationic tracers. In addition, the generation of different ^{3}He/^{4}He ratios in minerals with varying U/He ratios will tend to be homogenized by diffusion within the mantle and lower lithosphere. The conclusion that the mantle is isotopically homogeneous on a mineral scale and melts to yield isotopic compositions characteristic of the bulk source region, have been previously championed by Hofmann and Hart (1978) who considered more detailed inter-mineral exchange constraints, and the lower diffusivities of Sr and other cations. However, the possibility of dramatically different grain sizes and defect populations (and thus effective diffusivities) in the mantle than in laboratory experiments makes this conclusion less than absolute, as pointed out in the more recent discussion by Sneeringer, Hart and Shimizu (1984).

Interaction of migrating melts with mantle solids or lithospheric and crustal wall rocks may be enhanced for helium in comparison to other trace elements, because of its higher mobility. The specific extents of exchange depend on the magma migration rate, flow geometry (e.g. conduit or porous flow), temperature, and partitioning of helium between the solids and the melt (e.g. Navon and Stolper, 1987). Kurz et al, 1987 have suggested that this process could explain the fact that temporal

helium isotopic changes in Hawaiian basalts are more pronounced than for strontium isotopes. It is difficult to quantify models of this type and as pointed out by these workers, differing partition coefficients and degrees of melting also produce elemental abundance variations, which affect the degree to which wall-rock interaction alters isotopic compositions. However, enhanced exchange for helium will clearly be more important in the lithosphere than at crustal depths where magma transport is likely to occur in larger conduits driven by crustal fracture (Spera, 1980).

Diffusive transport of helium in magma is slow enough that stratified magma chambers derived from sequential episodes of injection, assimilation and fractional crystallization can maintain different ^{3}He/^{4}He ratios for long times. For example, over a million years is required to homogenize a 1 km magma body, considering the diffusivity in tholeiitic melt (figure 4.11). In order for diffusive degassing to change initial magmatic ^{3}He/^{4}He ratios by preferential ^{3}He transport large gas losses must occur. For example, a 10% lowering of the initial ratio requires 65% gas loss for an isotopic diffusivity ratio of 1.15 (figure 4.8), which would require several hundred thousand years for the example of a 1 km sphere. Maintaining the magma volume above the solidus for this long would require a thermal contrast between magma and wall rock of less than 10°C (e.g. Hart and Zindler, 1987). Many aspects of magma degassing in real volcanos make these conductive and diffusive timescales heuristic at best. However, given the much greater diffusivity of heat than helium, it seems likely that magma bodies, whatever their geometry or rate of convection will tend to cool before significant helium loss occurs, unless they are deep-seated and thermally insulated.

Another way in which magmatic helium isotopic compositions can be lowered during chamber residence is by radiogenic ingrowth of ^{4}He. Zindler and Hart (1986) have suggested that exhalative helium degassing accompanying saturation of carbon dioxide may increase the U/He ratio of a magma, leading to decreases in its ^{3}He/^{4}He ratio over times ranging 10^5 to 10^6 years. These workers find suggestive evidence for this process in a correlation of increasing U/He ratios with decreasing Mg

number (an index of increased fractional crystallization). However, it is not clear that the lower helium contents in the more evolved rocks derive from earlier magma chamber degassing rather than processes associated with eruption. As pointed out by Zindler and Hart (1986), if this process is responsible for significant lowering of mantle $^3He/^4He$ ratios, for example as observed at Hawaiian volcanos over time (Kurz et al, 1987), magma chambers must remain at high temperature for long periods at relatively shallow depths where CO_2 degassing can occur. This requires periodic chamber replenishment, and leads to a rapid decrease in $^3He/^4He$ ratios after a long period without much change (Zindler and Hart, 1986). This pattern of $^3He/^4He$ change is similar to that for preferential diffusive loss of ^3He (figure 4.8), and both processes would tend to produce large differences in $^3He/^4He$ ratios of magma batches which had undergone only small differences in degassing and cooling histories.

To date, temporal studies of individual volcanos have neither documented nor excluded this process. However, helium isotopic variations in Hawaiian volcanos are generally slow and smooth and are reasonably described by changes in source compositions related to tectonic plate motions (Kurz et al, 1987). Further study of the role of shallow degassing in altering $^3He/^4He$ ratios is warranted, and may provide a way to study magma chamber residence times. Coupling helium measurements with carbon isotopic determinations may prove useful, because phase separation of CO_2 leads to decreases in $^{13}C/^{12}C$ ratios (e.g. Javoy, Pineau and Delorme, 1986) which should correlate with helium changes. However, helium diffusion in phenocrysts is too rapid for zoned phenocrysts to record magmatic $^3He/^4He$ changes.

The high diffusivities of helium in olivine and pyroxene also constrain the origins of ultramafic xenoliths. Rapid helium exchange between xenoliths and host magmas is predicted by the characteristic time scales in figure 4.11. However, several studies have found that xenoliths and magmas have different helium isotopic compositions (e.g. Kurz et al, 1983; Polve and Kurz, 1989), an observation made for other isotopic systems as well (e.g. Hofmann and Hart, 1978). This means that xenoliths must spend very short times in magmas (weeks at most for 1mm

grains, figure 4.12). For a depth of origin of 30 km this suggests ascent rates are on the order of .05 meters per second. Similar velocities have been suggested from phase equilibrium constraints and transport kinematics (e.g. Spera, 1984). In addition to helium isotopic disequilibrium between magmas and xenoliths, small isotopic differences have been observed between different minerals in Hawaiian ultramafic xenoliths (Polve and Kurz, 1989). One means for producing the differences would be preferential ^{4}He production in the phases with low ^{3}He/^{4}He ratios. Given the 500,000 year timescale required to produce the observed differences (op. cit.) the diffusivity of helium must be less than $6 \times 10^{-16} cm^2/s$ to avoid homogenization. This suggests the xenoliths must come from lithospheric depths where the temperature is on the order of 550 to 750°C, given the Arrhenius relations for pyroxene and olivine, respectively.

Finally, consider helium loss from phenocrysts erupted in lavas, as are often used for helium isotopic studies of basaltic petrogenesis. As pointed out by Hart (1984) the combination of high diffusivities and observable helium contents in these samples suggests that they do not lose all their helium during eruption because the magma has a high helium fugacity (chemical potential). As pointed out for olivine (op. cit.), the closure temperatures (Dodson, 1973) for helium in pyroxene are below the solidus for basalts, except for very high cooling rates. For example, a 1mm pyroxene has a closure temperature of about 800°C for a cooling rate of 10^7 °C/million years, a typical rate for the interior of a thick basalt flow (Hart, 1984). Thus, some helium loss may occur as the basalt fugacity drops during cooling after eruption. However, this is unlikely to be important for most extrusive rocks, because they cool too quickly, but will become important in studying intrusive rocks.

The large differences in helium diffusivities between pyroxene and olivine place strong contraints on the importance of preferential ^{3}He loss in altering the isotopic composition of phenocrysts. Because He will be lost much faster from pyroxene, its ^{3}He/^{4}He ratio will be significantly lower than cogenetic olivine whenever diffusion has contributed to significant gas loss. As an example, lowering the ratio of 1mm spherical olivine grains from 8.4 to 6.9 R_a in this manner would

yield a ratio of less than 5 Ra in pyroxene grains of similar size, for an isotopic diffusivity ratio of 1.08 and 100-fold faster diffusion in pyroxene at 1000°C. This difference will be larger at lower temperatures. Similarly, crystals of different sizes would be expected to be differentially depleted in ^{3}He. When disequilibrium of this nature is observed (i.e between cogenetic minerals), it also provides an indication of the integrated thermal history (for rocks of known ages) or rough ages for defined cooling rates by backtracking diffusive loss to helium isotopic equilibrium at emplacement (as demonstrated earlier by Gramlich and Naughton, 1972). Helium will be separated from other volatile elements if diffusion does occur, so that elemental abundances in phenocrysts (or basaltic glasses) may differ from those of the primary system.

In conclusion, diffusion is an important mechanism for equilibrating the helium isotopic compositions of minerals and melts, but not on mantle scales. Diffusion is slow in comparison to many volcanic cooling and transport rates so that measurements on glasses and phenocrysts can be used to characterize magmas, however caution must be exercised in systems which remain at high temperature for longer times. Finally, diffusive separation of helium from other elements may be important in processes such as melt percolation, and wall-rock interaction. The importance of diffusion in altering isotopic compositions may be examined by comparing cogenetic olivine and pyroxene crystals, because these minerals have dramatically different helium diffusivities.

REFERENCES

DODSON M.H. (1973) Closure temperature in cooling geochronological and petrological systems. Contrib. Mineral. and Petrol. 40, 259–274.

GRAMLICH J.W. and NAUGHTON J.J. (1972) Nature of source material for ultramafic minerals from Salt Lake Crater, Hawaii, from measurment of helium and argon diffusion. J. Geophys. Res. 77-17, 3032–3042.

HART S.R. (1981) Diffusion compensation in natural silicates. Geochim. Cosmo. Acta 45, 279–291.

HART S.R. (1984) He diffusion in olivine. Earth Plan. Sci. Let.70, 297–302.

HART S.R. and ZINDLER A., Constraints on the nature and development of chemical heterogeneities in the mantle, in Mantle Convection R. Peltier, ed. in press.

HOFMANN A.W. (1980) Diffusion in natural silicate melts: a critical review, in Physics of Magmatic Processes (ed. R.B. HARGRAVES) pp.3–44. Princeton Univ. Press, Princeton, N.J.

HOFMANN A.W. and HART S.R. (1978) An assessment of local and regional isotopic equilibrium in the mantle. Earth Plan. Sci.Let. 38, 44–62.

HUNECKE J.C., NYQUIST L.E., FUNK H., KOPPEL V. AND P. SIGNER (1969) The thermal release of rare gases from separated minerals of the Mocs meteorite, in: Meteorite Research, Reidel, Dordrecht, p901.

JAHNE B., HEINZ G. and DIETRICH W. (1987) Measurement of the diffusion coefficients of sparingly soluble gases in water JGR 92, 10767–10776.

JAVOY M., PINEAU F. AND H. DELORME, (1986) Carbon and nitrogen isotopes in the mantle, Chemical Geology 57 p41-62.

KURZ M.D. (1982) Helium isotope geochemistry of oceanic volcanic rocks: implications for mantle heterogeneity and degassing. PhD. Diss., MIT/WHOI.

KURZ M. D., JENKINS W. J., SCHILLING J. G. and HART S. R. (1982) Helium isotopic variations in the mantle beneath the central North Atlantic Ocean. Earth Plan. Sci. Let. 58, 1-14.

KURZ M.D., JENKINS W.J., HART S.R. and CLAGUE D. (1983) Helium isotopic variations in volcanic rocks from Loihi Seamount and the Island of Hawaii. Earth Plan. Sci. Let. 66, 388-406.

KURZ M.D., GARCIA M.O., FREY F.A. and O'BRIAN P.A. (1987) Temporal helium isotopic variations within Hawaiian volcanoes: basalts from Mauna Loa and Haleakala. Geochim Cosmo. Acta 51, 2905-2914.

LIPPOLT H.J. and WEIGEL E. (1988) ^{4}He diffusion in ^{40}Ar-retentive minerals. Geochim. Cosmo. Acta 52, 1449-1458.

LUX G (1987) The behavior of noble gases in silicate liquids: solution, diffusion, and surface effects, with applications to natural samples. Geochim. Cosmo. Acta 51, 1549-1560.

MAMYRIN B.A. and TOLSTIKHIN I.N. (1984) Helium Isotopes in Nature. Elsevier, Amsterdam.

NAVON O. and STOLPER E. (1987) Geochemical consequences of melt percolation: the upper mantle as a chromatographic column. J. Geol. 95, 285-307

POLVE M. and KURZ M. (1989) ^{3}He/^{4}He systematics in spinel-lherzolite nodules. In press.

RAMA S.N.I. and HART S.R. (1965) Neon isotope fractionation during transient permeation. Science 147, 737-738.

SHIMIZU N. and I. KUSHIRO (1984) Diffusivity of oxygen in jadeite and diopside melts at high pressures, Geochim. Cosmochim. Acta 48 p1295-1303.

SNEERINGER M., HART S.R. and SHIMIZU N. (1984) Strontium and samarium diffusion in diopside. Geochim. Cosmo. Acta 48, 1589-1608.

SPERA F.J. (1980) Aspects of magma transport. In: Physics of Magmatic Processes (ed. R.B. HARGRAVES) pp.265-323. Princeton Univ. Press, Princeton, N.J.

SPERA F.J. (1984) Carbon dioxide in petrogenesis III: role of
      volatiles in the ascent of alkaline magma with special reference
      to xenolith-bearing mafic lavas. Contrib. Mineral. Petrol. 88,
      217-232.

WATSON E.B.(1984) Diffusion in magmas at depth in the earth: the
      effects of pressure and dissolved H_2O. Earth Plan. Sci. Let. 52,
      291-301.

ZINDLER A. and HART S. (1986) Helium: problematic primordial signals.
      Earth Plan. Sci. Let. 79, 1-8.

Chapter 5.

Diffusion
of cosmogenic ^{3}He
in olivine and quartz:

Implications for surface exposure dating.

5.1 INTRODUCTION

The recently identified production of ^{3}He in Hawaiian basalts by
in-situ interaction with cosmic rays offers great promise for studies of
surface exposure ages, erosion rates, and ancient cosmic ray fluxes
(Kurz et al, 1985; Kurz, 1986a,b; Craig and Poreda, 1986; Marti and
Craig, 1987). Before this discovery can be widely applied as a
geochemical tool several fundamental aspects of the behavior of
cosmogenic helium (^{3}He$_c$) must be better understood, including its
production rate, the extent to which it is retained in rocks, and how it
can be distinguished from inherited or radiogenic helium. This chapter
focuses on quantifying losses related to the formation mechanism of
^{3}He$_c$ or which occur by diffusion. To this end, the diffusivity of ^{3}He$_c$
was measured in two minerals important to present and future cosmogenic
helium studies, olivine and quartz. The measurements also suggest ways
by which inherited and cosmogenic helium can be separated.

Several nuclear reactions contribute to ^{3}He$_c$ production in surface
rocks. Most important is spallation of major element target atoms by
high energy neutrons which are produced as secondary particles in the
atmosphere when the primary cosmic rays (predominantly protons, but
containing some neutrons and multi-nucleonic particles) collide with
atmospheric atoms (Lal and Peters, 1967; Kurz, 1986b; Lal, 1987). These
endothermic reactions produce ^{3}H, ^{3}He and ^{4}He, leading to an overall
^{3}He/^{4}He production ratio of about .1 (Kurz, 1986a). The great
difference between this ratio and that of unexposed terrestrial rocks
(10^{-8} to 10^{-5}; e.g. Mamyrin and Tolstikhin, 1984) is essential to the
detection of ^{3}He$_c$. Because the energy spectrum of cosmic rays falls off
very steeply with increasing energy, most of these reactions occur at or
near the threshold interaction energies for the target elements, which
are in the range of 10-50 MeV (Lal and Peters, 1967; Lal, 1987). As
discussed further below, these energies may contribute to ^{3}He$_c$ mobility.
The attenuation half-length for the cosmic neutron flux, and thus
spallation production of ^{3}He$_c$, is approximately 160 g/cm^2, or about 60
cm in dense rock (Kurz, 1986b and references therein).

Another production reaction is the interaction of thermalized cosmogenic secondary neutrons with ^{6}Li to yield equal amounts of ^{3}He and ^{4}He. For rocks with lithium contents of a few parts per million this mechanism is only about 1% as effective as spallation, but it becomes roughly equivalent in importance for Li contents of about 100 ppm (Kurz, 1986b; Simmons, 1986). This exothermic reaction releases similar energies to uranium and thorium series decays, about 5 MeV (Lal, 1987). Its depth dependence is essentially the same as for spallation, because the thermal neutron population derives from the fast neutrons. An exception occurs at the atmosphere-rock density boundary, where thermal neutron production can be enhanced several times by thermalization of atmospheric fast neutrons (e.g. Kurz, 1986a). It is also worth pointing out that the ^{6}Li reaction is responsible for some production of ^{3}He even in the absence of cosmic irradiation, from neutrons supplied predominantly by X(alpha,n)Y reactions on major rock elements instigated by radiodecay of ^{238}U and ^{232}Th (Morrison and Pine, 1955). Because only a small fraction of these alpha particles produce neutrons, the ^{3}He/^{4}He radiogenic production ratio is very low in most unexposed rocks, on the order of 10^{-7} to 10^{-9} depending on lithium content (op. cit.; Andrews, 1985), and thus is readily distinguished from cosmogenic helium.

A third mechanism produces much less ^{3}He$_c$ and only becomes relatively important at depths below where the secondary neutrons have been largely absorbed (a meter or more). This is the interaction of cosmogenic muons with major element nuclei to produce neutrons which then interact with ^{6}Li by the low-energy reaction already described, yielding a ^{3}He/^{4}He production ratio of 1 (Lal and Peters, 1967; Kurz, 1986b; Lal, 1987). The half-depth for ^{3}He$_c$ production is basalt by this process is on the order of 1000 g/cm^2 (Kurz, 1986b).

It is important to keep these production mechanisms and their associated energies in mind when assessing helium mobility. Elevated losses of alpha-decay produced nuclides are known to occur, particularly in weathering processes, but also from rock interiors (e.g. Giletti and Kulp, 1955; Rama and Moore, 1984; Fleischer, 1988). For this reason, it may not be appropriate to apply diffusivities determined for inherited

helium to cosmogenic helium problems. However, it should be noted that even in ancient rocks the low cosmogenic neutron flux (order 10^{-4}/g/s ; Kurz, 1986a) and $^3\text{He}_c$ production rate (order 100 atoms/g/yr; Kurz, 1986b) will lead to much lower radiation doses than experienced by irradiated basalts (circa 10^{18}neutrons/g) or alpha-decay damaged metamict zircons (circa 10^{13}decays/g) which display elevated noble gas mobilities (Stettler and Bochsler, 1979; Damon and Kulp, 1957). To preface the results, $^3\text{He}_c$ diffusivities in quartz and olivine were found to be compatible with both these observations, in that release was enhanced over inherited helium, but was still much slower than from damaged crystals or glasses (analogous to the metamict state).

Finally, it should be pointed out that the in-situ $^3\text{He}_c$ production rate and its possible variation are not yet well known. To date, the production rate has only been measured in Hawaiian basalts (using olivine phenocrysts and calibrating to ^{14}C ages; Kurz, 1986b; Kurz et al, 1989). It is about 125 ($\pm$25) atoms/g/yr at sea-level at that geomagnetic lattitude. This rate is expected to very significantly with altitude (e.g. 2-fold increase at 1000m) and lattitude (2 to 3-fold increase from the equator to the poles depending on altitude) because cosmic rays are deflected by Earth's magnetic field and attenuated by the atmosphere (for a recent review see Lal, 1988). Theoretical estimates of the dependence of production rates on these factors, as well as with depth in the rock, are available (e.g. Lal and Peters, 1967; Lal, 1987, 1988; Yokoyama, Reyss, and Guichard, 1977). However, the theory does not fully explain variations in apparent production rate of 25% or so observed at Hawaii (Kurz et al, 1989), and thus may only be applied in an approximate way in extending the Hawaiian results to other locations. Measurements of the compositional dependence of ^{3}He production in meteorites (Bogard and Cressy, 1973) and theoretical estimates (Lal, 1987) do agree in suggesting this effect will be small (5 to 10% for most silicate rocks). More measurements from other locales and improved theory are both required, if $^3\text{He}_c$ exposure geochronology is to become a precise and widely applicable method.

5.2 METHODS AND SAMPLES

Diffusivities were estimated for olivine and quartz by measuring ^{3}He and ^{4}He degassed from mineral separates <u>in vacuo</u> during incremental heating in a specially designed vessel (figure 2.2). The samples were then melted in a furnace to obtain total helium contents, allowing the calculation of fractional release rates. Diffusion coefficients were calculated for each sequential release using model equations which assume equisized, spherical grains with initially homogeneous helium concentrations. The diffusion vessel, furnace, analytical methods and model equations are described in detail in chapter 2, and are discussed below as neccesary in interpreting the experimental results.

Basaltic olivine crystals were chosen for study because of their importance in determining the production rate for ^{3}He$_c$ in Hawaiian rocks (Kurz et al, 1988). The olivine mineral separate was prepared from sample HA6 of the Kula formation ankaramite flow (approximately 500-800,000 years old McDougall, 1964; Naughton et al, 1980) which forms White Hill near the summit of Haleakala Volcano, Maui. This extremely fresh, porphyritic rock has been previously described and contains abundant cosmogenic helium predominantly produced by spallation, rather than by reaction with ^{6}Li (Kurz, 1986a). The rock was crushed in a stainless steel mortar and large (1-2mm) olivine grains were handpicked to be free of adhering basalt matrix, alteration, or other mineral phases, although grains with a few small spinel inclusions were accepted. These grains were then crushed and sieved (in methanol to disrupt aggregates and remove fines), dried in air and handpicked again to provide the 212-250um particles used in the diffusion experiment.

Crushing removed most of the helium contained in fluid inclusions, as revealed by comparing the total ^{4}He contents of the sieved separates (1.7×10^{-10}cc/g on fusion) with the contents of whole olivine grains (1.3×10^{-8}cc/g as measured in a 1-2mm olivine separate from the same rock by Kurz, 1986b). In addition to removing magmatic helium, crushing the phenocrysts should produce subgrains with relatively homogeneous ^{3}He$_c$ distributions, which is an assumption of the diffusion model. Microscopic examination of these particles revealed no pervasive

internal cracking, suggesting that using particle size as the effective
length scale in calculating diffusivities was also valid. Electron
microprobe analysis of 10 olivine grains yielded identical chemical
compositions (Forsterite-78) within analytical errors (table 5.1).

Quartz was chosen for study for several reasons. It is a common
mineral in glacial terrains in the Dry Valleys of the Transantarctic
Mountains, an area for which efforts are underway in this laboratory to
obtain ^3He_c exposure ages, in order to constrain the history of the
Antarctic ice cap. The issue of helium retention on several thousand to
several million year timescales is important to this research. In
addition, quartz is an ideal phase for the measurement of another
cosmogenic nuclide, $^{26}Al_c$, because of its low natural Al background (Lal
and Arnold, 1985; Nishiizumi et al, 1986). Combined measurement of
$^{26}Al_c$, with a half-life of 705,000 years and stable ^3He_c offers promise
for determining prior surface exposures of rocks that are now buried, if
both nuclides are effectively retained. Finally, quartz is a ubiquitous
mineral and understanding ^3He_c mobility in it will be valuable to future
cosmogenic helium studies in other environments.

The quartz separate was prepared by crumbling a friable ortho-
quartzite rock (BW84-105) recovered from high altitude (1300 meters) in
Arena Valley in the Transantartic Mountains (provided by G. Denton,
Univ. of Maine). This rock is from the Taylor IVb moraine, which is
estimated to be 2-4 Myr old based on field relations with K-Ar dated
lava flows (personal communication from G. Denton to M. Kurz). As in
the olivine sample, spallation dominates (>90%) the ^3He_C production in
this rock, because lithium contents are relatively low (about 10 ppm, D.
Colodner, unpublished results). The quartz grains were sieved,
handpicked to avoid discolored grains and adhering iron hydroxide
phases, and cleaned by ultrasonic agitation in distilled water, acetone
and methanol. The grains used in the diffusion experiment (500-710um
sieve fraction) are typical of the size in the rock, and thus may have
inhomogeneous internal helium distributions if diffusive loss has
already occurred. Several grains were examined by electron microprobe.
They were almost exclusively silica, but a few (1-5 per grain) 5 to 15
micron in size inclusions were found and were tentatively identified

Table 5.1 HA6 Olivine Composition

Oxide	Weight %
MgO	41.7
Al_2O_3	0.1
SiO_2	38.8
CaO	0.2
TiO_2	0.1
Cr_2O_3	0.1
MnO	0.3
FeO	20.3
NiO	0.1
TOTAL	101.7

Ca/Mg/Fe	0.003/0.784/0.213
Mg/(Mg+Fe)	0.786

a) Average of 10 microprobe
   determinations.
b) Ca/Mg/Fe normalized to 1.0

(from energy-dispersive x-ray spectra) as iron oxides (hematite?), phosphate minerals (apatite and fluoroapatite, some of which contained elevated rare earth or actinide element contents), zircon, barite, and sulfide minerals (pyrite and chalcopyrite). The zircons and phosphate inclusions may contain significant fractions of the U and Th, which could be important for radiogenic helium production, but this could not be measured. No phases enriched in lithium (above the detection limit of about 30 ppm) were found. More work is needed to determine typical abundances and compositions of these inclusions.

5.3 RESULTS

5.3.1 Olivine

A single step-heating experiment was performed for olivine over the temperature range of 200-600 ^{o}C (table 5.2). Only $^{3}He_c$ could be measured in the released aliquots as ^{4}He release was two small to be distinguished above background, except on fusion. The calculated diffusivities define a linear trend in an Arrhenius diagram (figure 5.1) as is often observed for volume diffusion governed by a single activation energy, here found to be 25$\pm$4 Kcal/mole (log D^o = -3.7$\pm$.8 cm^2/s). This result must be considered preliminary until it is reproduced because of the narrow temperature range. However, the data demonstrate that $^{3}He_c$ release is greatly enhanced in comparison to inherited helium in dunitic olivine (figure 5.2). The activation energy is greatly different than for inherited helium diffusion in olivine (100 Kcal/mole, chapter 4), and may reflect a different mechanism for $^{3}He_c$ release, perhaps involving increased vacancy populations associated with the cosmic neutron flux.

Extrapolating the $^{3}He_c$ diffusivity results to 40°C, as a reasonable upper limit to the mean annual temperature of a Hawaiian lava flow, suggests a $^{3}He_c$ difffusivity of 7 x 10^{-22} cm^2/s with an upper limit of 1.5 x 10^{-17}cm^2/s based on two-sigma uncertainty of the Arrhenius least-squares line. Equivalent values at 20°C are 5 x 10^{-23} and 1 x 10^{-18}cm^2/s respectively. Errors in these values from the model assumption of equisized spherical grains should not be larger than a

Table 5.2. Step-heated Release of Cosmogenic ^{3}He from Olivine.

Sample: HA 6 Olivine, 212-250um sieve fraction.
44.9mg,   model grain radius = 116$\pm$19 um.

#	Temp. (^{o}C)	Time (hr)	^{3}He (10^{-16}cc)	1s	F (fraction)	1s	D (cm^2/s	1s	E x 10^E)
1	Ramp	---	2.1	1.1	.0020	.0010	---	---	---
2	209.	7.01	.7	1.0	.0027	.0013	1.5	3.3	E-15
3	Ramp	1.62	2.6	1.1	.0051	.0017	3.7	3.5	E-15
4	Tmp?	37.39	221.	13.	.2093	.0110	4.3	0.5	E-12
5	465.	25.88	73.	2.	.2767	.0111	5.1	1.0	E-12
6	Ramp	1.08	14.	21.	.2893	.0168	2.8	3.8	E-11
7	541.	16.18	202.	3.	.4758	.0132	4.3	0.4	E-11
8	541.	12.94	75.	3.	.5453	.0121	3.1	0.6	E-11
9	Ramp	0.54	20.	6.	.5638	.0116	2.3	1.5	E-10
10	623.	6.47	137.	7.	.6908	.0085	1.8	0.2	E-10
11	623.	10.24	92.	3.	.7758	.0065	1.1	0.1	E-10
12	Left	1.62	.8	1.0	.7765	.0064	---	---	
13	Melt	---	242.	4.	1.0				

Total ^{3}He$_c$ = 1.08x10^{-13}cc (2.41x10^{-13}cc/g)

a. Step 4 varied between 300 and 450°C because of instrumental difficulties.
b. The amount of ^{3}He released was within one sigma of the detection limit in aliquots 2,6 and 12. The diffusivities for these steps are within error of zero. This data is included because these releases affect the determination of F values for other steps, and because the low releases set upper limits on diffusivities within these steps.

258

Figure 5.1. Arrhenius relation for the release of cosmogenic ^{3}He$_c$ from olivine crystals. One sigma errors are close to the symbol size, except for the point near 200°C which released so little helium that only an upper bound could be obtained. The best fit line is not significantly changed if this point is not included.

Figure 5.1
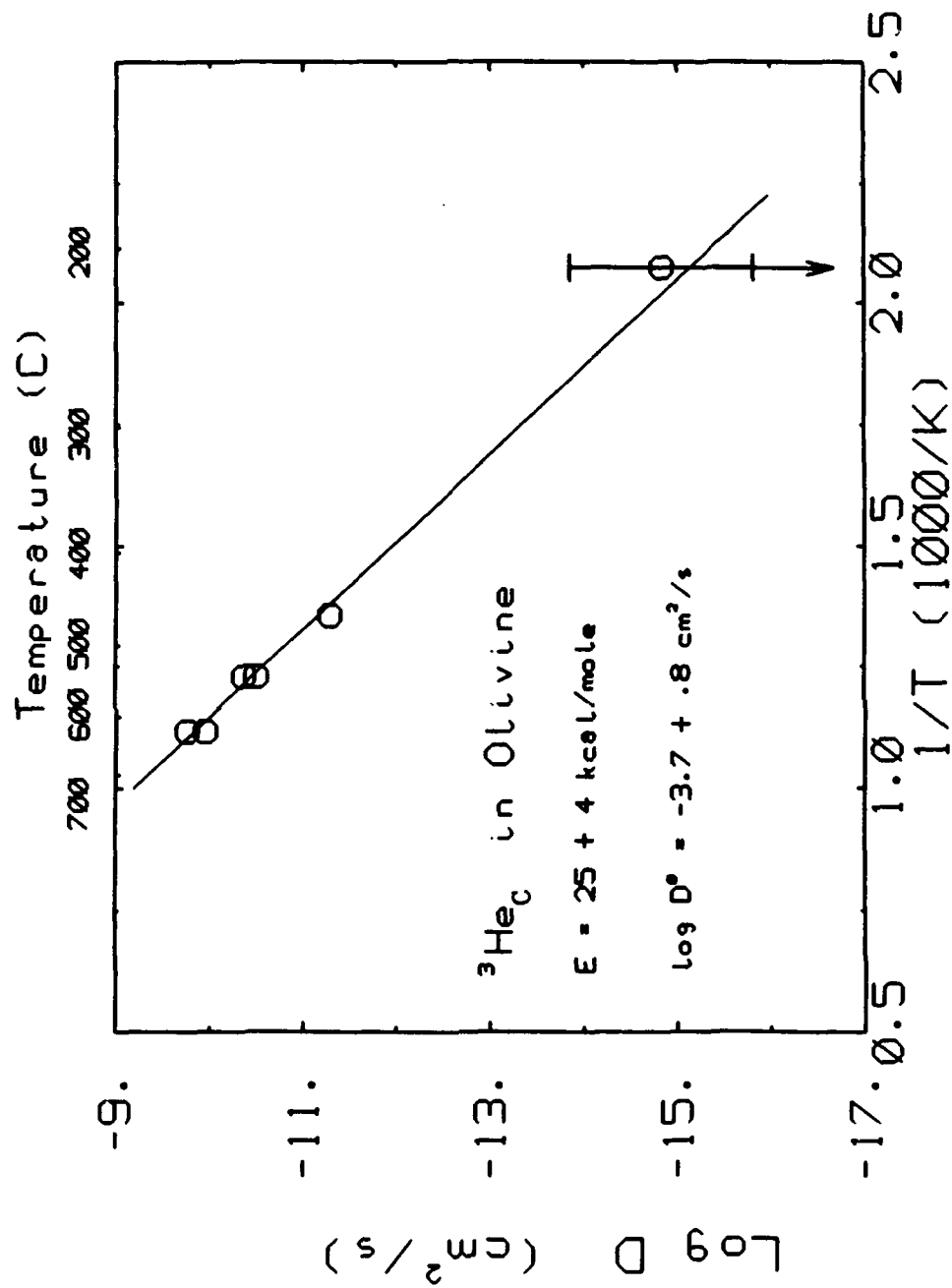
Figure 5.2. Diffusive release of cosmogenic ^3He_c appears to be both considerably enhanced and less thermally activated that the release of inherited ^3He from olivine. However, because the results were obtained on different samples over different temperature ranges, these conclusions must be viewed with caution. Arrhenius line for inherited ^3He from chapter 4.

Figure 5.2
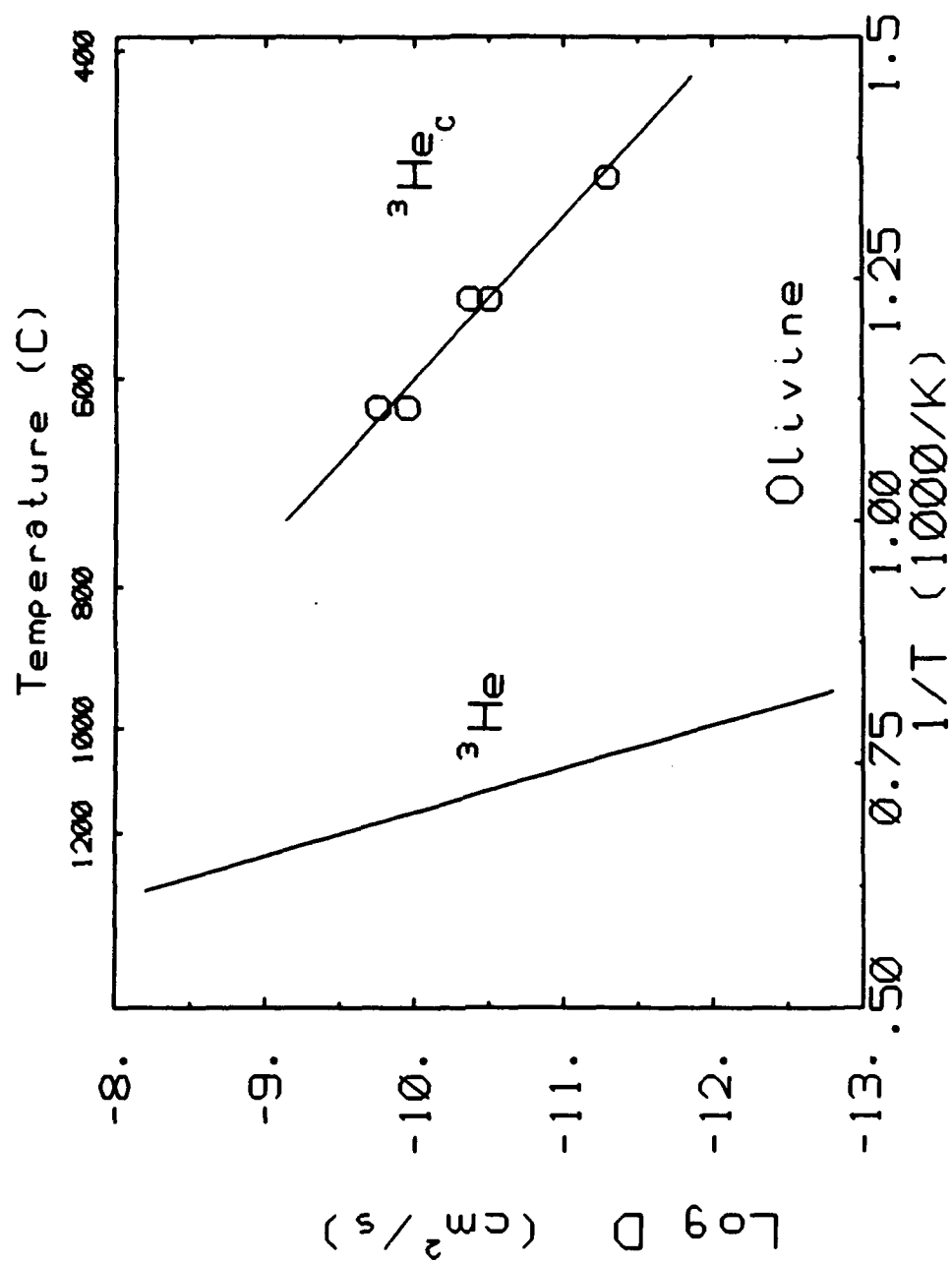
factor of two given the narrow particle size range used, provided that the ^3He_c content does not vary strongly with size in this range. This is a safe assumption because the grains were prepared by crushing larger grains, thereby homogenising any initial variability. The greatest uncertainty in determining a low temperature diffusivity is the extent of extrapolation required, because it is possible the temperature dependence of ^3He_c changes at lower temperature. Lower temperature emanation experiments with larger samples of smaller particles could reduce this problem somewhat, although not a lot because the strong decrease in diffusivity with temperature would make it difficult to obtain release rates much above typical atmospheric ^3He leak rates into the vessel and mass spectrometer. Measurement of helium remaining after storage of a powder separate may be a more appropriate way to refine these preliminary results.

5.3.2 Quartz

It was possible to measure both ^3He and ^4He in the quartz diffusion experiment, which extended from 150 to 600 $^\circ C$ and involved more than forty steps before melting the grains (table 5.3). ^3He was released far more rapidly and at lower temperature than ^4He (figure 5.3). The smooth character of these releases suggest a volume diffusion process rather than disruption of vesicles or the grains themselves. Examination of the grains under a binocular microscope at 80x before and after heating revealed no changes, also implying a diffusive mechanism. The early dominant release of ^3He is reflected in the isotopic compositions of the aliquots (figure 5.4). With the exception of a few heating steps which released very little helium, the early releases had greatly elevated $^3He/^4He$ ratios, near 120 R_a, in comparison to the bulk helium composition of 11.3 R_a (table 5.3). These ratios steadily decreased to values of .01 to .02 R_a, at which point approximately 70% of the total ^4He still remained, although more than 99% of the ^3He had been released. This strong separation suggests that essentially all the ^4He is radiogenic, and all the ^3He of cosmogenic origin. Thus, the ^3He release rates can be used to obtain diffusivities for cosmogenic ^3He_c without any correction for inherited helium. In addition, this means

Table 5.3 Step-heated Release of Cosmogenic 3He and Radiogenic 4He from Quartz.

Sample: BW84-105 Quartz, 300-355um sieve fraction, 115.6mg, model radius = 164±28 um.
The values shown for step 39 were estimated from those for adjacent steps.

#	Temp. C	Time hr	4He cc.E-10	1s	3He cc.E-14	1s	3He/4He R/Ra	1s	F(4He)	F(3He)	D(4He) cm2/s	1s	D(3He) cm2/s	1s
1	Ramp	0.53	.162	.005	.02	.01	9.	5.	.0002	.0002	5.5 E-16	.3	3. E-16	4.
2	146.	1.62	.279	.006	.25	.03	64.	6.	.0006	.0022	1.16 E-15	.05	2.0 E-14	.5
3	147.	9.74	.776	.010	1.10	.03	102.	2.	.0016	.0115	1.49 E-15	.03	8.6 E-14	.5
4	148.	9.33	.475	.004	.72	.02	109.	2.	.0022	.0176	1.67 E-15	.05	1.2 E-13	.1
5	Ramp	0.54	.281	.003	.38	.03	99.	5.	.0026	.0208	2.1 E-14	.1	1.5 E-12	.2
6	210.	1.63	1.25	.004	1.92	.03	111.	1.	.0042	.0371	4.52 E-14	.06	3.8 E-12	.1
7	210.	1.62	.930	.004	1.57	.02	122.	2.	.0055	.0503	4.77 E-14	.09	4.8 E-12	.2
8	210.	1.62	.800	.003	1.35	.03	123.	3.	.0065	.0618	5.1 E-14	.1	5.4 E-12	.3
9	Ramp	0.54	.693	.003	1.14	.02	119.	2.	.0074	.0714	1.53 E-13	.04	1.6 E-11	.1
10	235.	0.54	1.10	.003	1.80	.02	118.	1.	.0089	.0866	2.85 E-13	.05	3.1 E-11	.1
11	235.	1.08	2.22	.004	3.66	.04	119.	2.	.0118	.1176	3.64 E-13	.03	4.2 E-11	.2
12	235.	1.08	1.84	.004	2.92	.04	115.	2.	.0142	.1423	3.79 E-13	.04	4.3 E-11	.2
13	235.	1.08	1.58	.004	2.59	.03	119.	2.	.0163	.1642	3.81 E-13	.05	4.6 E-11	.2
14	235.	1.08	1.40	.003	2.26	.03	117.	2.	.0181	.1833	3.83 E-13	.06	4.7 E-11	.2
15	235.	1.08	1.33	.004	1.97	.02	107.	1.	.0199	.2000	4.01 E-13	.07	4.6 E-11	.3
16	235.	1.62	1.57	.005	2.33	.04	107.	2.	.0220	.2197	3.47 E-13	.06	4.0 E-11	.2
17	Ramp	0.54	1.49	.03	1.96	.03	95.	2.	.0239	.2363	1.09 E-12	.02	1.11 E-10	.07
18	280.	0.54	2.34	.04	3.14	.04	97.	1.	.0270	.2628	1.89 E-12	.02	2.00 E-10	.08
19	280.	0.54	2.18	.003	2.81	.03	93.	1.	.0299	.2866	1.97 E-12	.03	2.02 E-10	.09
20	280.	1.08	4.25	.005	5.12	.06	87.	1.	.0355	.3299	2.20 E-12	.02	2.14 E-10	.06
21	280.	1.08	3.71	.005	4.27	.04	83.	1.	.0403	.3660	2.30 E-12	.02	2.11 E-10	.07
22	280.	1.08	3.29	.005	3.66	.04	81.	1.	.0447	.3969	2.29 E-12	.03	2.07 E-10	.08
23	280.	1.08	2.85	.009	3.12	.04	79.	1.	.0484	.4233	2.18 E-12	.03	2.0 E-10	.1
24	279.	0.54	1.23	.005	1.38	.04	81.	2.	.0500	.4349	1.99 E-12	.07	1.8 E-10	.2
25	Ramp	0.54	5.33	.01	5.18	.07	71.	1.	.0570	.4788	9.43 E-12	.09	7.8 E-10	.2
26	342.	1.08	11.7	.03	9.69	.09	60.	.6	.0724	.5607	1.26 E-11	.01	9.1 E-10	.2
27	342.	0.54	17.4	.04	12.7	.1	53.	.5	.0953	.6684	4.94 E-11	.03	3.37 E-09	.05
28	Ramp	0.54	27.1	.07	15.8	.1	42.3	.3	.1309	.8020	1.07 E-10	.01	6.82 E-09	.07
29	413.	0.54	25.3	.06	11.0	.1	31.5	.3	.1642	.8951	1.34 E-10	.01	8.9 E-09	.1
30	413.	0.54	14.2	.04	4.94	.06	25.2	.2	.1828	.9369	9.1 E-11	.1	7.1 E-09	.1
31	413.	1.08	16.0	.04	4.20	.06	19.0	.3	.2039	.9724	5.79 E-11	.07	5.8 E-09	.1
32	Ramp	1.08	44.2	.1	2.98	.03	4.89	.05	.2619	.9976	2.01 E-10	.01	1.7 E-08	.1
33	515.	0.54	23.5	.06	.13	.02	.40	.06	.2928	.9987	2.66 E-10	.03	8. E-09	4.
34	515.	0.54	14.9	.04	.05	.01	.24	.05	.3124	.9991	1.89 E-10	.04	5. E-09	5.
35	515.	0.54	11.2	.03	.01	.01	.09	.06	.3272	.9992	1.53 E-10	.04	2. E-09	6.
36	515.	1.08	17.3	.06	.01	.02	.04	.07	.3500	.9993	1.28 E-10	.02	.7 E-09	--
37	Ramp	0.54	63.9	.2	.02	.01	.02	.01	.4340	.9994	1.17 E-10	.01	3. E-09	8.
38	622.	1.08	75.7	.2	.02	.01	.02	.01	.5336	.9996	9.75 E-10	.06	3. E-09	6.
39	Lost	3.25	(85.)	--	(.02)	--	(.02)	--	.6453	.9998	5.32 E-10	.02	2. E-09	--
40	622.	7.59	73.0	.2	--	--	--	--	.7412	--	2.89 E-10	.02	--	--
41	622.	1.08	5.47	.01	--	--	--	--	.7484	--	1.9 E-10	.2	--	--
42	622.	3.25	14.3	.01	--	--	--	--	.7673	--	1.74 E-10	.06	--	--
43	622.	3.79	8.92	.006	--	--	--	--	.7790	--	10.0 E-11	.6	--	--
44	Cool	8.67	.941	.003	--	--	--	--	.7802	--	4.8 E-12	2.	--	--
45	Melt	6.90	167.	.6	.03	.01	.011	.004	1.0	1.0	--	--	--	--
Total			760.		118.		11.27	.03						

Figure 5.3. Comparison of ^{3}He and ^{4}He release from quartz grains during the step-heating experiment. ^{3}He was released more rapidly (top) and at lower temperature (bottom) than ^{4}He. The ^{4}He remaining after 75 hours was released by melting the sample. Temperature ramp steps are not shown in the lower plot.

Figure 5.3
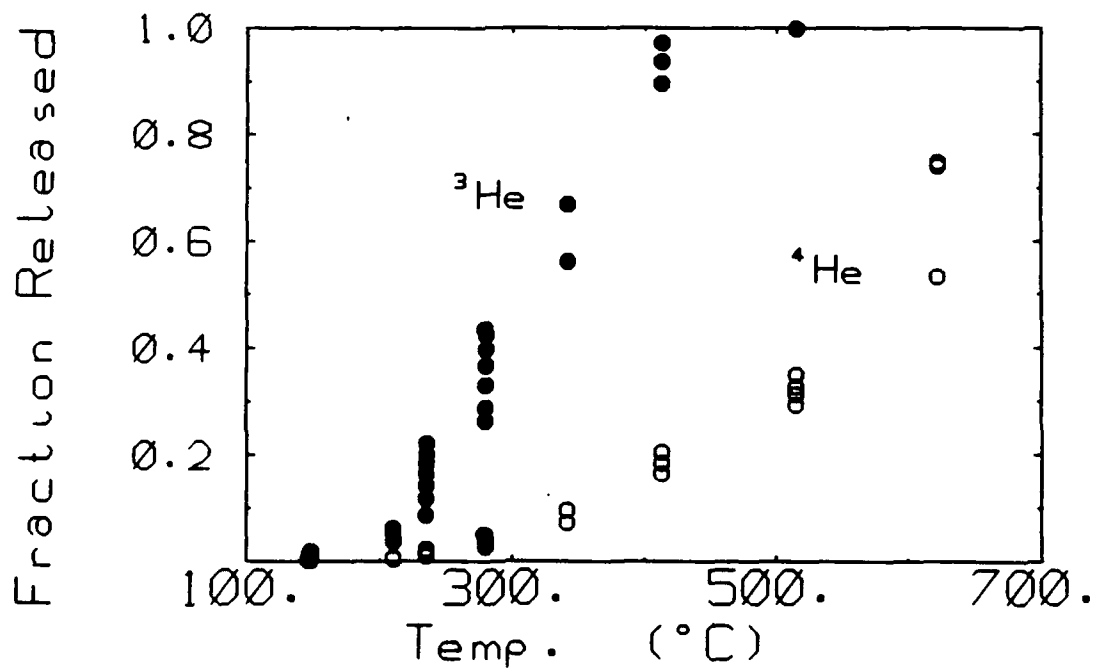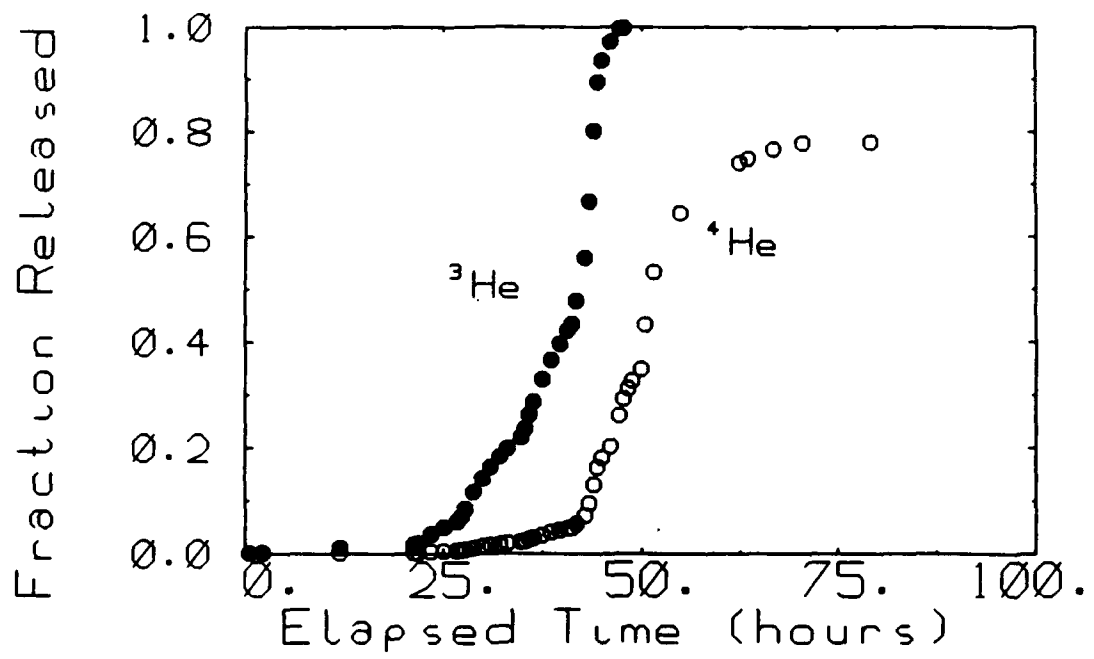
Figure 5.4   Isotopic compositions of sequential releases from
BW84-105 quartz grains (500-710 um). The overall pattern is
highly preferential release of ^3He_c, in comparison to the total
$^3He/^4He$ ratio in the sample (dotted lines). The few initial
aliquots with relatively low $^3He/^4He$ ratios contained very little
helium (0.2% cf ^4He) and probably reflect loss of ^4He from
surface sites. After 30% release of ^4He, no measurable ^3He
remained (x-axis, top plot) and the isotopic composition of the
remaining helium approached the radiogenic production ratio (.01
Ra).

Figure 5.4
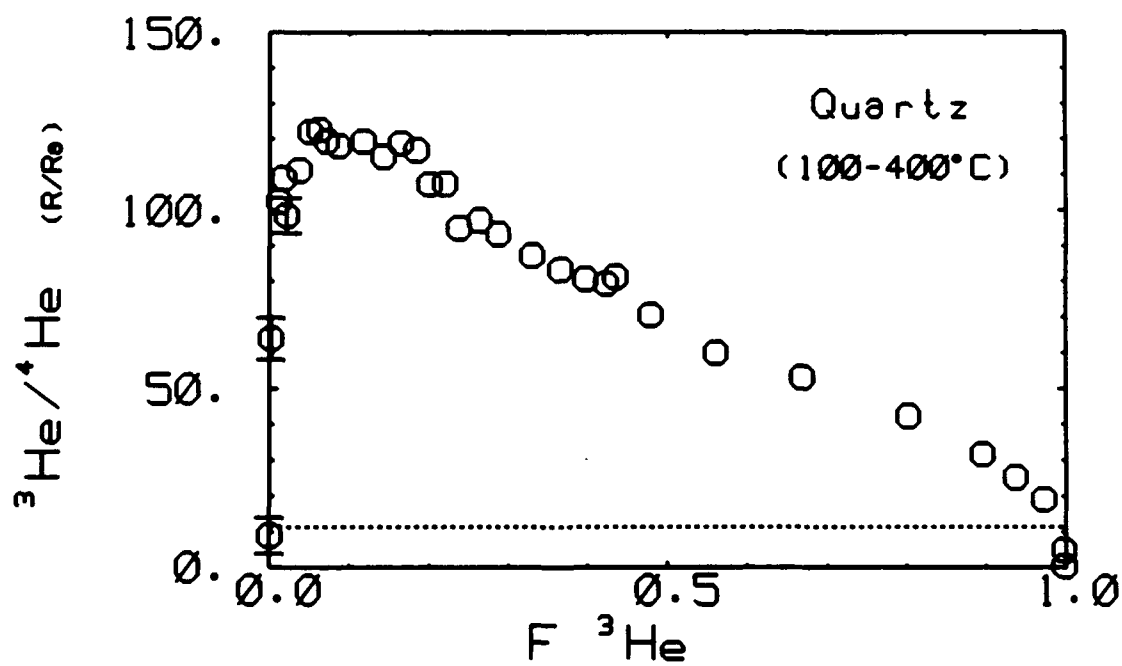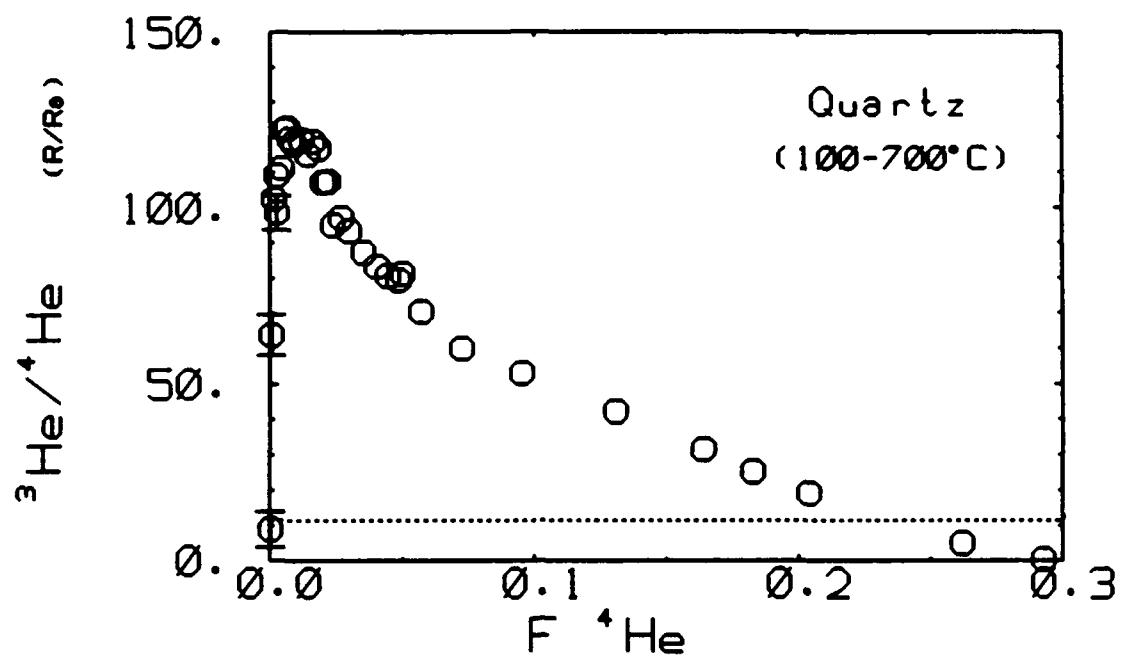
that the bulk ^{3}He/^{4}He ratio reflects the integrated production of cosmogenic and radiogenic helium since formation and exposure respectively, rather than characterizing a source component.

The ^{3}He/^{4}He ratio of the helium released by fusion, after driving off all the ^{3}He$_c$, was .011$\pm$.004 R$_a$ (table 5.3). This represents the radiogenic production ratio, R$_p$, in the quartz grains in the absence of cosmogenic effects. The small amount of radiogenic ^{3}He is produced from the reaction ^{6}Li(n,α)T ^{3}He, with the neutrons supplied by X(α,n)Y reactions on major elements (X), which are caused by uranium and thorium radio-decay (Morrison and Pine, 1955). In common silicate rocks, R$_p$ is about .01 to .02 R$_a$, but its exact value depends on Li contents, and to a lesser extent on the major element composition of the rock. For quartz, the observed ratio of .011$\pm$.004 R$_a$ corresponds to a Li content of 10 to 25 ppm (Andrews, 1985), in good agreement with preliminary measurements of Li in the sample (10 ppm, D. Colodner unpublished data).

Calculated helium diffusivities for each isotope are shown as a funtion of release in figure 5.5. Multiple steps at constant temperature exhibited constant diffusivities for most of the ^{3}He$_c$ releases, consistent with the volume diffusion model . In contrast, ^{*4}He release exhibited this behavior in the early low temperature releases (most easily seen from table 5.3) but at temperatures above 400°C, diffusivities tended to decrease within constant temperature plateaus (figure 5.5). This behavior was encountered in the basaltic glass diffusion experiments described in chapter 3, and was demonstrated to derive from the presence of a range of grain sizes in those samples. However, this explanation is not reasonable here because of the wide range of F (^{4}He) values over which it occurs (.15-.8) and because similar behavior was not observed in the ^{3}He$_c$ releases over this F (^{3}He$_c$) range.

In general, changes in slope in Arrhenius temperature-dependence plots are attributable to three classes of phenomena: a change in diffusion mechanism of a single specie, a change in the specie that is diffusing, or a change in the solid through which diffusion is occuring. If more than one diffusion mechanism applies, the one with higher activation energy will dominate at higher temperature. Thus, this is

Figure 5.5. Examination of ^3He_c and ^4He diffusivities in quartz. Solid dots are heating steps between temperature plateaus (^oC). ^3He release is characterized by generally constant D values at constant temperature, except at very low F (perhaps because of prior loss) and at very high F (where the calculation model is poor). In contrast, ^4He exhibits decreasing D values within several temperature plateaus. Most of these releases occurred after all ^3He was released (shown by hatched box in lower figure) and at higher temperature. This behavior may reflect a phase change in the mineral grains - see text. One aliquot was lost to valve failure, and the release shown is an estimate. Uncertainty in this estimate is insignificant for ^3He diffusivities, but contributes 10% error to the ^4He diffusivities.

Figure 5.5
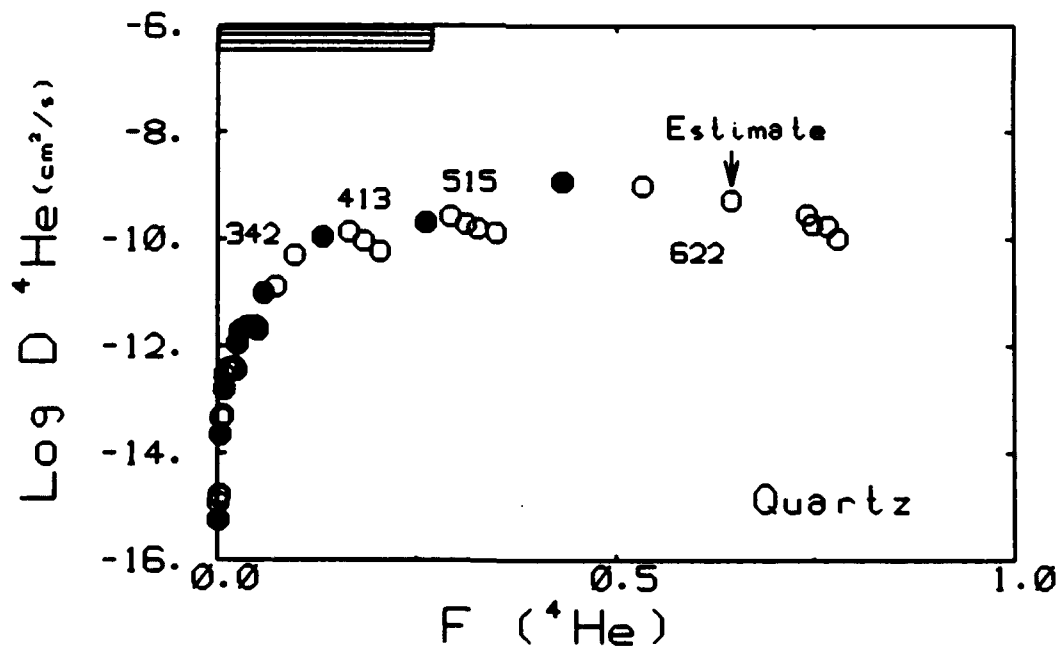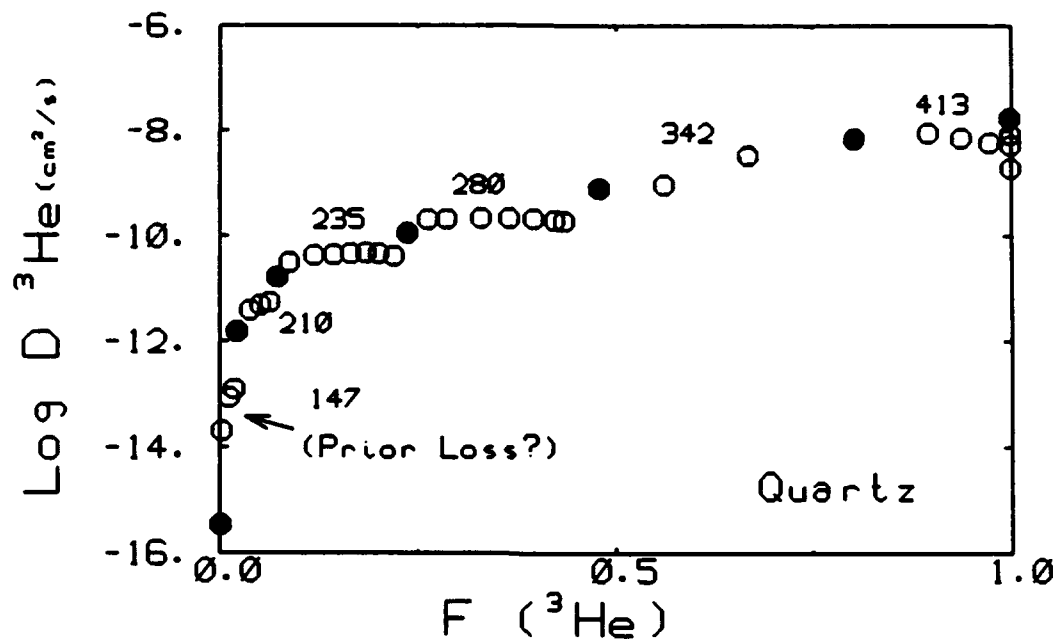
Table 5.4   Total Helium contents of BW84-105 Quartz grains.

Sample and Method	Grain Size	^3He_c (atoms/g)	$^{*4}He$ (atoms/g)
1. Step-heating and fusion, this study.	500-710um	2.74×10^8	1.76×10^{13}
2. 3 heating steps and fusion.	500-1000um	4.80×10^8	1.60×10^{13}
3. Crushing,	500-1000um	1.88×10^8	0.24×10^{13}
followed by fusion.		4.06×10^8	3.82×10^{13}
Total:		5.94×10^8	4.06×10^{13}

a. Analyses 2 and 3 are unpublished results provided by Dr. M.D. Kurz.
b. 1-sigma precisions are ~1% for ^3He_c and ~.3% for $^{*4}He$.

Table 5.5   Diffusion parameters for cosmogenic ^3He and radiogenic ^4He in olivine and quartz.

	Log Do (cm^2/s)	Ea (kcal/mole)
Olivine		
^3He_c	$-3.7 \pm .8$	25 ± 4
Quartz		
^3He_c	$+.2 \pm .4$	$25.2 \pm .9$
$^{*4}He$	$-2.1 \pm .3$	$24.4 \pm .6$

not a possible explanation for the ^{*4}He behavior which involves a decrease in temperature dependence at higher temperature. Similarly, it is unlikely that the change in slope represents a difference between the release of inherited ^{4}He residing in fluid inclusions and in-situ generated ^{*4}He, because 1) crushing the sample released only 6% of the total ^{4}He (table 5.4), and the change in release behavior occurs at F of about 20% and 2), if two components of ^{4}He were involved and governed by separate activation energies, the change in Arrhenius slope would be towards higher temperature dependence at higher temperature, as with a change in mechanisms.

The preferred explanation is that the change in ^{*4}He release reflects a change in the quartz matrix. A phase change occurs in quartz near 570°C for conversion of the low temperature stable form, trigonal alpha-quartz, to a more ordered hexagonal form, hexagonal beta-quartz (Deer, Howie, and Zussman, 1966). However, this conversion occurs quite sharply (over 2-3°C), and it is unlikely to affect diffusion at temperatures below 500°C. In contrast, rapid annealing of defects in quartz occurs in the temperature range of 300-400 °C, as shown by studies of electron spin resonance associated with Schottkey-Frenkel defects generated by alpha-decay (e.g. Odom and Rink, 1988). This process is the likely source of the decrease in ^{*4}He release rate, which occurs in this temperature range (figure 5.6). Helium diffusion in a well-annealed hexagonal silica polymorph, tridymite, exhibits a similarly low activation energy to the ^{*4}He results obtained at annealing temperatures here (figure 5.7), although caution must be used in comparing the release of trace quantities of natural helium with these results, which were obtained by experimentally equilibrating heated grains with large amounts of helium (Barrer and Vaughan, 1967). The annealing explanation could be verified by reproducing the break in Arrhenius slope, while simultaneously measuring electron spin resonance changes. In general, understanding the role of lattice-damage and its annealing rate will be important to the use of ^{*4}He, ^{3}He$_c$, or electron spin resonance (Odom and Rink, 1988) as quartz geochronometers, because diffusivities and annealing rates may depend on radiation doses. In the

present work, it appears both ^{*4}He and ^{3}He$_c$ releases were governed by Arrhenius behavior at the low temperatures of interest.

Below 400°C, cosmogenic ^{3}He$_c$ diffusion proceeds almost 100 times as fast as radiogenic ^{*4}He diffusion, but the two species are governed by indistinguishable activation energies, 25.2+.9 and 24.4+.6 kcal/mole respectively (log D^o values are +.2+.4 and -2.1+.3; figure 5.6). This suggests that thermal activation is controlled by properties of the quartz matrix (e.g. lattice vibrational moments and the extent of thermal expansion), and that the rapid ^{3}He$_c$ release may reflect greater access to spallation related lattice damage that enhances loss. Further experiments with different grain sizes of different exposure ages may help to establish the extent to which lattice damage controls ^{3}He$_c$ and ^{*4}He release.

Because the activation energies for ^{*4}He and ^{3}He$_c$ release are large, the diffusivity for a natural sample may vary considerably seasonally, for example D is 45 times higher at 25°C than at 0°C. The long-term effective diffusivity is thus the mean value associated with the time integral of the temperature-dependent diffusivity (see equation 2.4, chapter 2). Because of the strong increase in D with temperature this effective diffusivity will generally be higher than the diffusivity implied by the mean annual temperature. Extrapolating the temperature trends in figure 5.6 to 0°C implies very low diffusivities for both isotopes, 2 x 10^{-20} cm^2/s for ^{3}He$_c$ and 1 x 10^{-22} cm^2/s for ^{*4}He with 1-sigma errors of a factor of two (figure 5.7). As elaborated below, these low diffusivities suggest helium loss will not greatly impede surface exposure dating in the Antartic Dry Valleys, where mean annual temperatures are close to -20°C and rarely much above freezing (C. Hendy, personal experience). As always in experiments of this type, temperature extrapolations assume that the diffusion mechanisms which dominate in the laboratory also control release at lower temperature, and that the temperature dependence is indeed a simple exponential. However, there is no evidence to suggest this is a bad assumption and the results are in reasonable agreement with the value of 10^{-20} cm^2/s suggested by Tolstikhin et al (1974) to explain the presence of internal isotopic disequilibrium in geologically old quartz grains.

Figure 5.6 Arrhenius relations for cosmogenic ^{3}He and radiogenic ^{4}He diffusion in BW84-105 quartz grains have identical activation energies (24.4 $\pm$ .6 and 25.2 $\pm$ .9 kcal per mole, respectively) but ^{3}He$_c$ diffusivities are 200 times higher (Log D^o values = -2.1 $\pm$.3 and +.2 $\pm$.4). 1 sigma errors are similar or smaller than the symbol size. The departure from linearity for ^{4}He at high temperature may reflect annealing of defects within the quartz grains (see text).

Figure 5.6
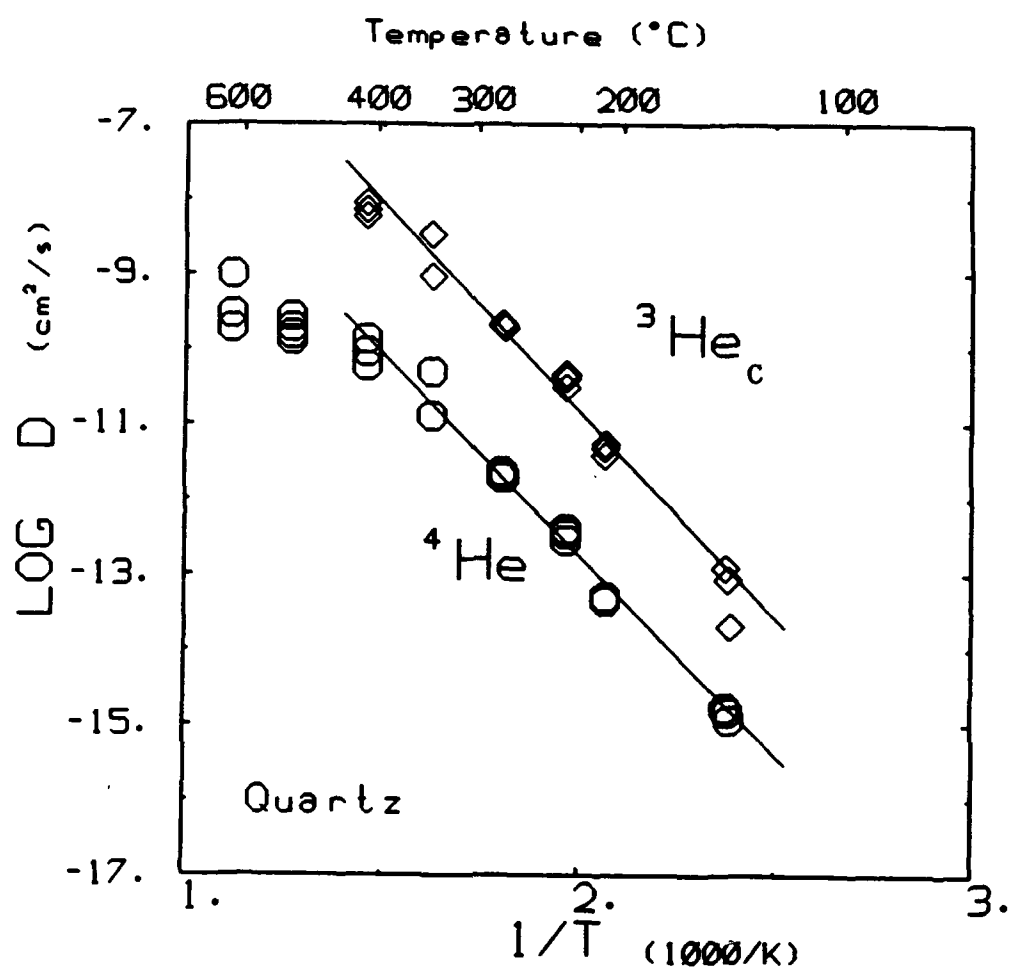
Figure 5.7 Comparison of Arrhenius relations for $^3\text{He}_c$ and $^{*4}\text{He}$ in quartz with release of ^4He from tridymite (Barrer and Vaughan, 1967). The dashes extrapolate the experimental results to low temperature, suggesting $D = 2 \times 10^{-20}$ and 1×10^{-22} $^3\text{He}_c$ and ^4He at 0°C. The break in slope in $^{*4}\text{He}$ diffusion above 400°C may reflect annealing of defects in the quartz sample. The activation energy (slope) above 400°C is similar to the value determined in an annealed quartz polymorph, tridymite, at lower temperature by Barrer and Vaughan, 1967).

Figure 5.7
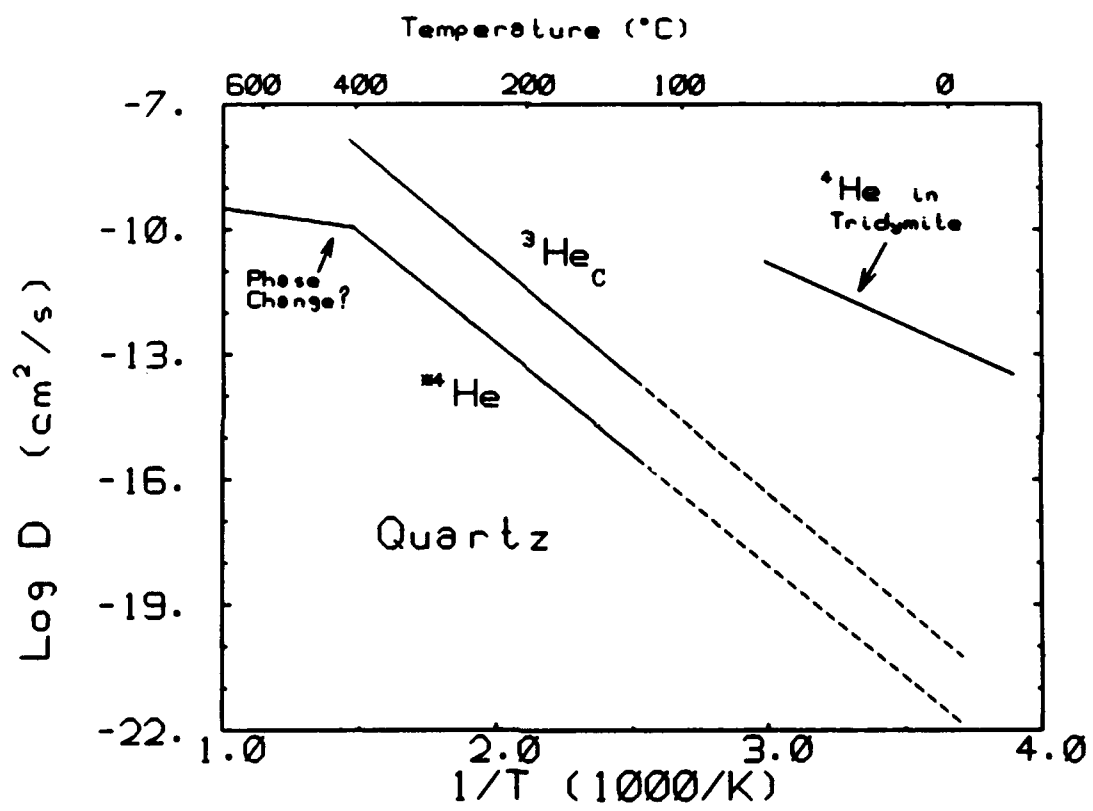
For those who feel that a low mass neutral atom like helium must be more mobile than this, it is worth repeating the words of Keevil (1940) – "Statements are sometimes made that helium should be able to diffuse through certain kinds of crystals because of their open structure, but these appear to be guesses without any quantitative picture of the situation". Keevil went on to discuss the interatomic potentials governing lattice spacings in silicate crystals including quartz, and concluded that helium atomic dimensions were relatively large (effective radius of .95 to 1.3 Angstrom) in comparison to any "holes", so that its mobility was likely to be low, and would require local distortions, coupled vibrations, and the crossing of significant energy barriers. Refining the estimates obtained here through experimentation at lower temperatures will face the same difficulties as for olivine, although somewhat alleviated by the roughly 5-fold higher $^{3}He_{c}$ contents in the quartz sample. An alternative method of assessing ^{3}He mobility at low temperature would be to compare the cosmogenic helium content of a wide range of natural grain sizes from a sample of known age.

5.4 DISCUSSION

The measured diffusivities can be used to place limits on helium loss problems in surface exposure dating. For a mineral grain undergoing both diffusive loss and constant production by cosmic ray spallation the helium concentration is governed by:

$$dC/dt = D \nabla^2 C + P \tag{5.1}$$

where P is the production rate (per unit volume). This equation assumes that the helium diffusion coefficient, D, is independent of concentration, which is probably true for typical trace helium contents, but may not hold in crystals which have undergone extreme bombardment, e.g. lunar materials. The fraction of produced helium which remains at time t can then be written:

$$F_t = C/Pt = \{ Pt - \int_0^t (dC/dt)dt \} / Pt \tag{5.2}$$

This fraction represents the underestimation of an exposure age produced by diffusive loss. For example, if F_t is .2, the model age

$$t' = C/P \qquad\qquad (5.3)$$

will be underestimated by a factor of five.

F_t values calculated numerically for spherical grains (see Appendix D) are plotted for several diffusivities in figure 5.8. Compared with diffusive loss in the absence of production, the fractional loss of cosmogenic helium is slower, but both scale with the ratio D/a^2, where D is the diffusion coefficient and a the spherical grain radius. (The infinite-series solution used to calculate the curves for diffusion alone is given in chapter 2.) Similarly, radial concentration profiles for the two solutions have generally similar shapes, but the profile for production and diffusion evolves more slowly and reaches a steady state quadratic profile (figure 5.9). Both the effect of loss on apparent ages and the approach to steady state are very clear in figure 5.10, which shows the relationship between apparent (C/P) and true ages for different D/a^2 values. For example, at a D/a^2 value of $1\times10^{-15}\text{cm}^2/s$ model ages will begin to underestimate true ages at about 1 million years, and will become meaningless in rocks over 10 million years once the helium content has reached steady-state. These curves provide a way to correct model ages using measured grain sizes and diffusivities. For this purpose, an expanded plot is given, which, while drawn for the time interval of .1 to 1 million years, can be used for any order of magnitude age range by scaling the diffusivities (figure 5.11).

For olivine, diffusive loss of cosmogenic helium will not significantly affect surface exposuring dating except in the smallest grain sizes. Given the extrapolated diffusivity of $7\times10^{-22}\text{cm}^2/s$ at 40°C (as an upper limit for Hawaiian lavas), log D/a^2 values are less than -17 for grains greater than .25mm in diameter. Thus, exposure dates will not be in error for ages less than 100 million years (figure 5.10)! This result is apparent from the diffusive length scale ($x^2 = Dt$) of 1um for this D value (22um is the 2-sigma upper limit at 40°C). This low predicted mobility of $^3\text{He}_c$ in olivine is consistent with the

observation that inherited helium released from fluid inclusions by crushing Hawaiian olivine phenocrysts is never contaminated by ^{3}He$_c$ produced in the crystal matrices, at least for rocks less than 1 million years old (Kurz, 1986a,b). Therefore, cosmogenic dating of basaltic rocks using olivine mineral separates is more likely to be limited by geologic problems such as shielding and erosion than by helium loss problems.

Diffusive effects on exposure ages are somewhat greater in quartz than olivine, but are still relatively small. For the Antarctic sample studied here, the grain size of .5mm and the approximation of the 0^oC diffusivity for the seasonal average, $D/a^2 = 3.2 \times 10^{-17}$, so that apparent exposure ages begin to be significantly underestimated (factor of 2) for samples older than about 10 million years (figure 5.10). The ^{3}He$_c$ content of Bw84-105 quartz ($3-6 \times 10^8$ atoms/g; table 5.4) suggests an age of 800,000 to 1.7 million years, given a production rate of 360 atoms/g/yr. (The production rate has not been measured directly and was estimated from a Hawaiian sea-level rate of 100 atoms/g/yr (Kurz, 1986b) adjusting for lattitude (factor of 1.4) and altitude (factor of 2.55 at 1300m); the error should be less than a factor of 2). Correcting these model ages for diffusive loss suggests the corresponding true ages are 850,000 and 2.1 million years (figure 5.11), i.e a 5-20% correction. At present, this is well within other uncertainties such as the precise production rate, and the origin of the factor of two variability in ^{3}He$_c$ contents of replicate analyses (table 5.4). However, diffusive effects will be more important at higher temperatures, for example at an environmental temperature of 30^oC, the quartz ^{3}He$_c$ diffusivity is about 140 times higher than at 0^oC, so that model ages for .5mm grains will err by a factor of two at ages of about 100,000 years (figure 5.10).

The F_t curves can also be used to consider diffusive loss problems for U+Th/He geochronology, since ^{*4}He production is essentially constant for ages much less the mean life of its radioactive parents (billions of years). The measured ^{*4}He diffusivities in quartz are 100-fold smaller than ^{3}He$_c$ values, so that radiogenic helium is likely to be quantitatively retained for ages less than 100 million years even in

Figure 5.8. Comparison of diffusive helium loss with and without helium production. The model curves are for spherical grains with constant isotropic helium production and homogeneous initial helium distribution, respectively. The y-axis represents the remaining fraction of helium produced (F_t) or initially present (C/C^o). Fractional loss occurs more rapidly in the absence of production, but both loss problems scale with the ratio of the diffusion coefficient (D) to the square of the grain radius, a.

Figure 5.8
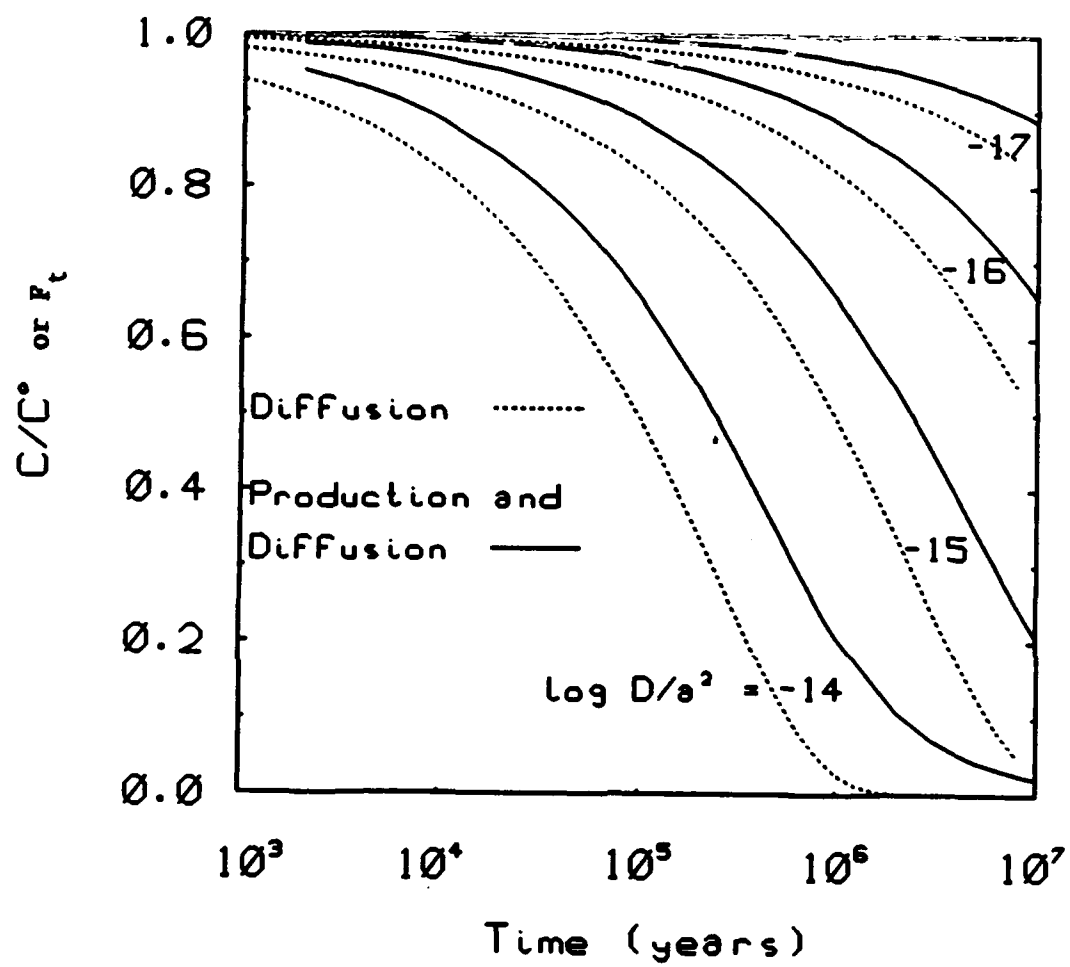
Figure 5.9. Comparison of diffusive profiles with and without production. Production profiles are steeper at a given time (non-dimensional) than for diffusion alone, and evolve to a quadratic curve as production and diffusive loss reach steady-state. All curves are normalized to the concentration at the center of the grain, C(o). Fractional helium contents (F) are also shown for each profile and time.

Figure 5.9
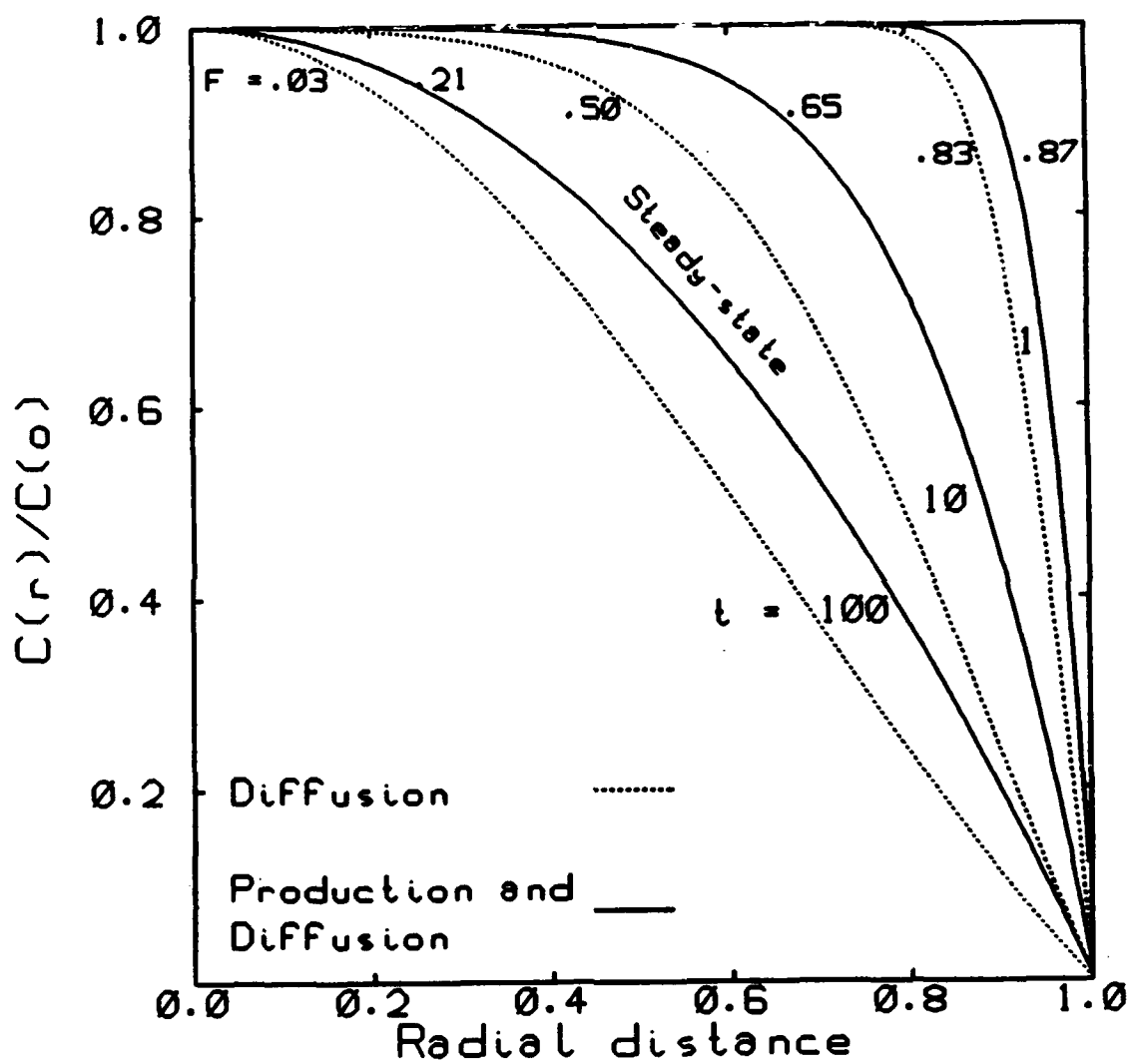
Figure 5.10. Effect of diffusive loss on cosmogenic helium model ages (C/P) for several values of D/a^2. Models ages progressively underestimate true ages, and eventually reach maximum values (minimum true ages) as production and loss approach steady-state (at this point the curves are horizontal). Model age errors increase with higher diffusivities, D, and smaller grain radii, a. The curves can be used to estimate feasible age ranges for exposure dating from D measurements in different materials, and to correct model ages for diffusive loss when both D and a are known.

Figure 5.10

Production and diffusion
for a sphere

Log D/a^2 = -14

-17

-16

-15

C/P or "Time" (years)

Time (years)
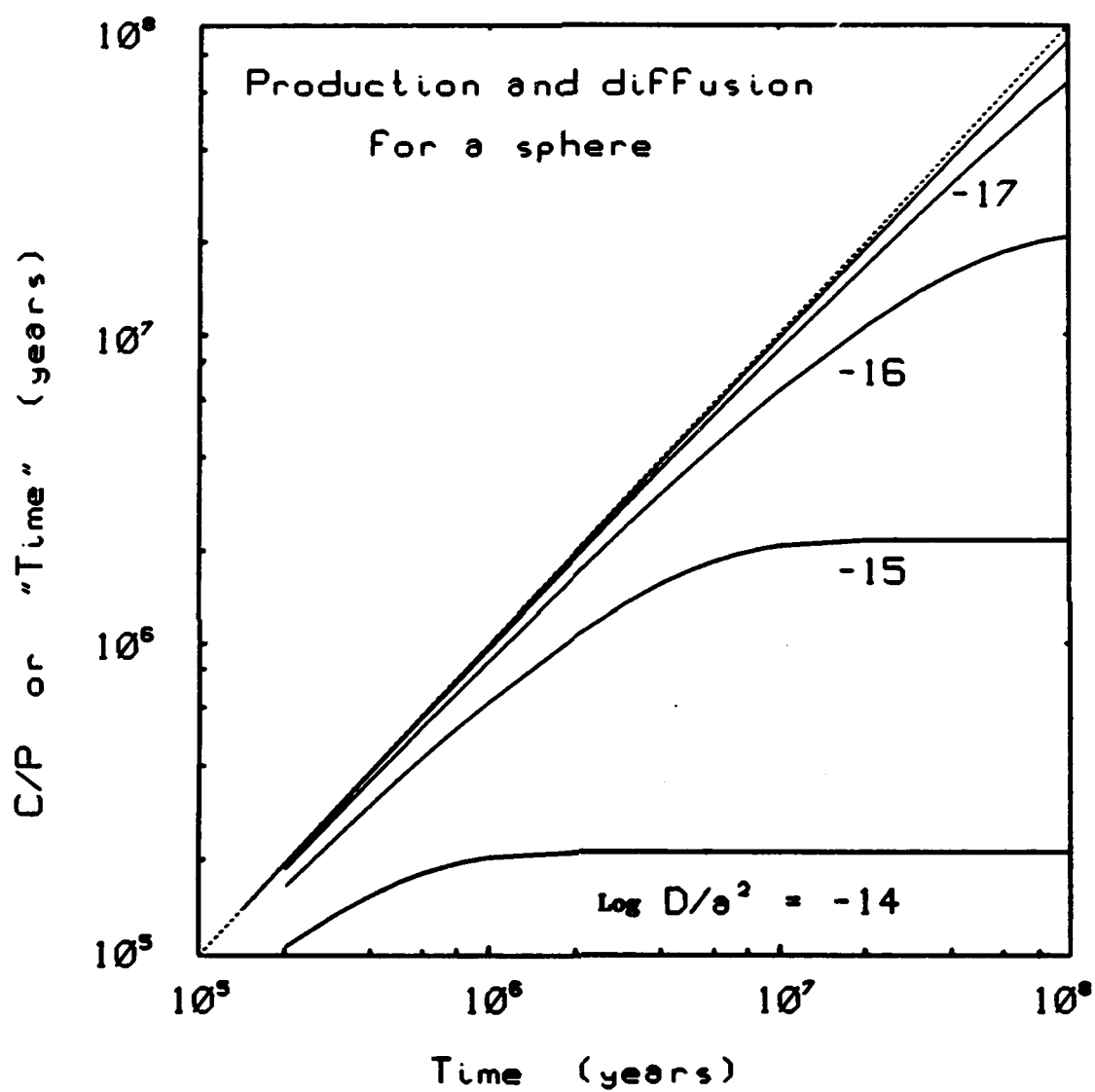
Figure 5.11. Expanded scale plot for correcting model ages for diffusive loss, drawn for an age range of .1 to 1 million years. The figure can be used for any order of magnitude age range by scaling the diffusivities, e.g. for 1 to 10 million years, add 1 to each log D/a^2 value.

Figure 5.11
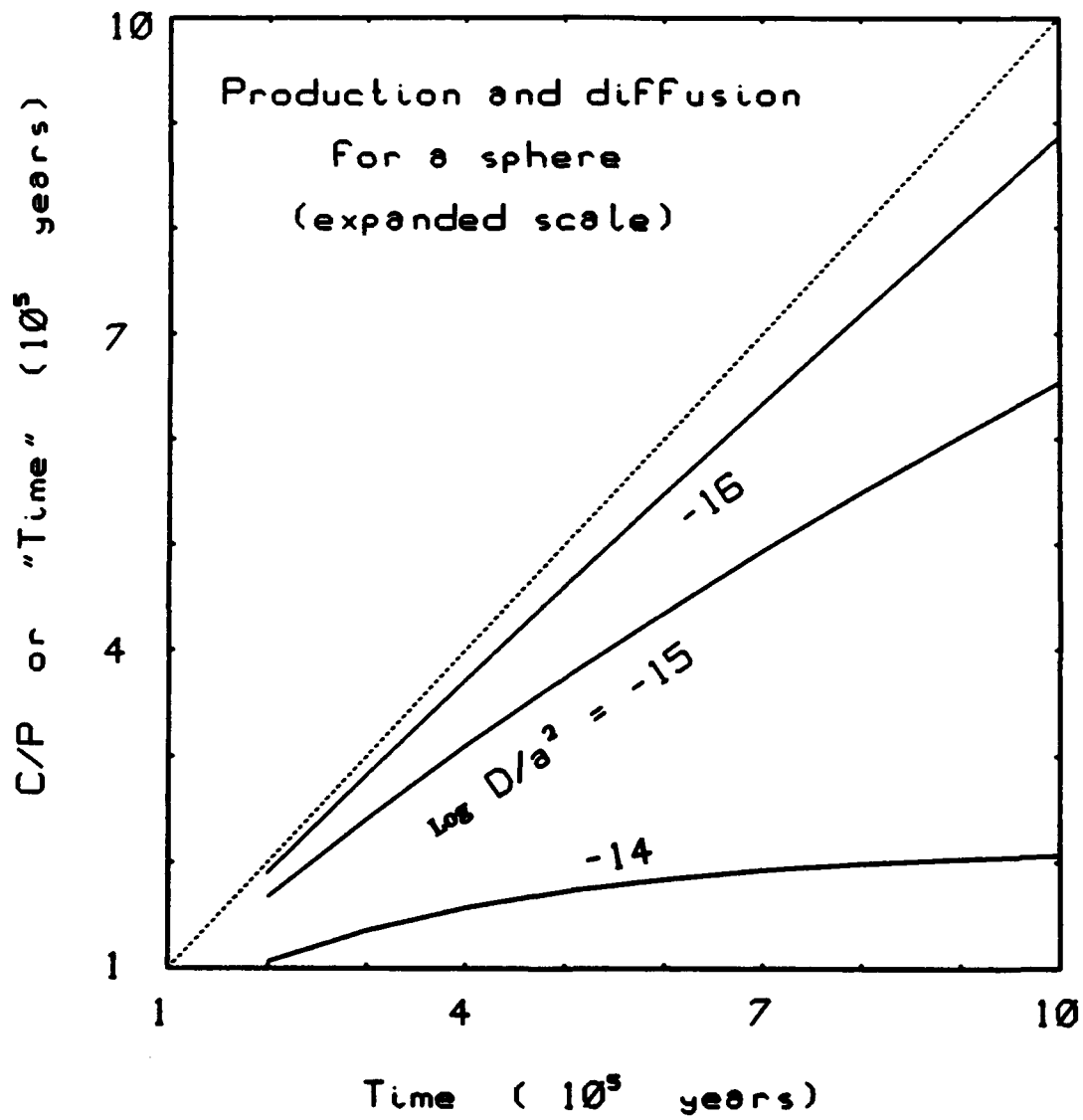
.1mm diameter grains. Given the ^{*4}He content of BW84-105 quartz (2-4x10^{13}atoms/gr; table 5.4), a very rough U content estimate of less than 10 ppb (based on a microprobe K estimate of less than .01%, and K/U of about 2x10^4 in orthoquartzites, Murray and Adams, 1958), and a Th/U ratio of 3-4 (op.cit.), the age for this sample is on the order of 200 to 600 million years. This age is in the range of the postulated Triassic to Devonian geologic ages for the likely quartz source rocks (e.g. Barrett, 1972). Uranium measurements will allow the possibility of a ^{*4}He geochronometer for quartz to be further evaluated. Overall, the low ^{*4}He diffusivities measured offer promise for the application of U+Th/He geochronology to quartz samples. The great difference between ^{4}He and ^{3}He$_c$ diffusivities in quartz is also important because it allows cosmogenic and inherited helium components to be separated. This is particularly valuable, because crushing of quartz grains appears to release both species (table 5.4) in contrast to the good separation obtained this way for olivine and pyroxene (Kurz, 1986b).

Diffusive losses from olivine and quartz have been shown to be small, but what about losses related to the formation of ^{3}He$_c$ and ^{*4}He? Both production mechanisms, spallation and alpha-decay respectively, involve energetic nuclear reactions capable of imparting significant recoil ranges in their products. Before estimating these ranges, it is worth pointing out that recoil in itself will not produce losses, unless either the production rate or recoil range varies significantly within the rock. For example, spallation induced ejection of ^{3}He$_c$ from olivine crystals will be be balanced by injection of cosmogenic helium produced in the surrounding basaltic matrix, because spallation rates are only slightly composition dependent (less than 20% variation in common silicate rocks; Bogard and Cressy, 1973; Lal, 1987) and charged-ion stopping power is similarly constant because it is dominated by interactions with oxygen and silica (e.g. Friedlander et al, 1981). This balance will even hold for rocks with significant porosity, because stopping power is roughly proportional to density (op. cit.) so that particles ejected from grains will tend to cross pore spaces and enter other grains. For example, the range of alpha-particles in air is several centimeters (Friedlander et al, 1981). However, production of

^{*4}He and the component of ^{3}He$_c$ formed by neutron reactions on ^{6}Li may vary within rocks because of heterogeneous distribution of U, Th or Li. Thus, in basalts more radiogenic helium will be injected into olivine and other phenocrysts than is ejected because U and Th, as incompatible elements, are relatively enriched in the ground mass. A similar situation may hold for ^{6}Li produced ^{3}He$_c$.

The fraction of helium injected or ejected from any location within a spherical grain can be calculated from the fraction of particles whose recoil paths reach the grain boundary. Making the approximations of a constant stopping range (r*) and that the distribution of recoil directions is isotropic, the loss can be integrated over the spherical volume for a homogeneous spatial distribution of production to give:

$$F = 3/4 \ (r^*/r_o) - 1/16 \ (r^*/r_o)^3 \qquad\qquad (5.4)$$

where r$_o$ is the grain radius (Flugge and Zimens, 1939; Giletti and Kulp, 1955). This formula assumes r* is less than 2r$_o$. The stopping range of alpha-particles (^{*4}He) in basalt and quartz can be calculated from experimental data for major element targets. For the 3-6 Mev alpha-decay energies of the U and Th series, the mean stopping distance is 25um (range 20-45um) in basalt and somewhat less in quartz (Graham, 1987). For this range, the ^{*4}He fraction lost or added to a 1mm diameter grain is only 4% (8% for .5mm) of the production in the grain or surrounding matrix, respectively. This loss would be insignificant for U+Th/He geochronology studies in minerals, but the injection could be important to mineral separate helium isotopic studies of petrogenesis in uranium rich, older rocks. The injection of ^{*4}He also has a small, indirect effect on the determination of phenocryst ^{3}He$_c$ contents, because the ^{4}He content of the crystals is used to correct for inherited (magmatic) ^{3}He (Kurz, 1986a,b). Injection of ^{*4}He produced in the surrounding, relatively U and Th rich matrix will lead to overcorrection and thus low ^{3}He$_c$ ages. However, this error will generally be insignificant in comparison to other uncertainties, e.g. less than 4% in the approximately 500,000 yr old Kula basalt samples studied by Kurz (op. cit.). The small component of ^{3}He$_c$ produced by the reaction of

thermalized neutrons with ^{6}Li will also have a short recoil range (about 30um), because the energy of this reaction is less than 5 MeV (Lal, 1987), so that injection and ejection processes for this component are insignificant.

In contrast to alpha-particles and ^{6}Li produced ^{3}He, the recoil range of spallation produced helium is not well known. The track lengths of spallation produced alpha-particles in film emulsions exposed to cosmic rays at high altitude range from 50-250um (Rossi, 1952). However, most spallations in surface rocks will occur at lower energies than these events. Cosmic-ray neutrons are responsible for the vast majority of spallation events in surface rocks (e.g. Lal and Peters, 1967; Kurz, 1986b). Because the energy spectrum for these particles at sea level drops off extremely rapidly with increasing energy (e.g. Wolfendale, 1973) and spallation cross-sections for the important target elements are relatively invariant with energy above a threshold value (10-50 MeV), essentially all ^{3}He$_c$ production will occur at energies close to the thresholds (Lal and Peters, 1967). A maximum energy for a spalled nuclide can be estimated from the threshold energies by considering the reaction to be a two-body collision (between the neutron, n, and a target atom, X) which yields only two products (a daughter nuclide, d, and the spalled nuclide, s). Conserving momentum, kinetic energy, and <u>mass</u> in this reaction gives the approximation:

$$E_s = E_n \cdot m_x(m_x - m_s) / (m_n + m_x)^2 \qquad\qquad (5.5)$$

Which can be written, for $m_x \gg m_s$, as:

$$E_s = E_n \ (1 - m_s/m_x) \qquad\qquad (5.6)$$

which shows that the energy of the spalled particle approaches that of the incoming cosmic neutron as the target mass increases. This large energy transfer occurs because the products must equipartition the initial momentum of the cosmic neutron (in the center-of-mass coordinate system), so that the velocity and therefore the energy share of the small spallation nuclide is relatively large. For target elements of

mass 16 (O) to 28 (Si), the approximate energy of a spalled ^{3}He will be 70 to 85% of the incoming neutron energy.

This estimate is a maximum for two reasons. First, the approximation ignores the conversion of kinetic energy into nuclear binding energy, that is, mass is not actually conserved. Considering the curve for binding enerfy per nucleon as a function of nuclear mass shows that 10-20 MeV of the incoming energy will be lost to increased mass of the products (s and d), for typical target masses of less than 50 amu. Secondly, more than two products are generally produced in spallation reactions. Three to five or more particles are common (Rossi, 1952; Lal, 1988 figure 2).- The partitioning of energy between these particles depends on their masses, binding energies and directions of recoil and can not be readily calculated, but in a rough sense the total energy will be equipartitioned because the spectrum of particle masses produced in low energy spallation reactions is very narrow and centered on low mass particles (Friedlander et al, 1981) which have similar binding energy deficits in comparison to target atoms. This suggests that many spallation reactions will produce ^{3}He$_c$ particles with quite low energies. For example, 10 MeV of the incoming energy (say 50 MeV) may be lost to mass increase in each of three products, and the remaining 20 MeV of kinetic energy split among them to give an average energy of 6-7 MeV.

The stopping range for these energies can be estimated by comparison with empirical results for alpha-particles in aluminum (an element with similar stopping power to Si, and less power than oxygen). At 6-7 MeV, a range of 20 to 30um is predicted (Friedlander et al, 1981). However, it must be emphasized that individual ^{3}He$_c$ atoms may have higher energies, and that the stopping range has never been measured for geologic materials. As a note of caution - the predicted stopping range at 50 MeV is approximately 600um. If the stopping range estimate of 20-30 um is correct, ejection will clearly be an insignificant problem in most surface exposue dating efforts. For larger stopping distances this will still tend to be true, because of the general balance between injection and ejection. Therefore, it appears ^{3}He$_c$ retention is unlikely to limit ^{3}He$_c$ geochronology.

5.5 SUMMARY

Measured diffusivities for cosmogenic ^{3}He in quartz and olivine were enhanced by several orders of magnitude over those for inherited helium, but were still very low. Extrapolating the approximately 25 Kcal/mole Arrhenius temperature relations, observed at 150-400°C in both minerals, suggests 20°C diffusivities of less than 10^{-18} and 10^{-22} cm^2/s for quartz and olivine, respectively. Comparing these low mobilities to model calculations for production and diffusive loss suggests surface exposure dating using ^{3}He$_c$ will not be limited by losses for timescales up to 10 million years in quartz and 100 million years in olivine (for 1mm grains). However, this conclusion depends strongly on the mineral grain sizes used, for smaller grains (e.g. 250um) sample ages will begin to be underestimated at 100,000 to 1 million years. When significant loss occurs, the model curves can be used to correct the apparent ages, whenever the ^{3}He$_c$ diffusion coefficient and grain size are known or measured.

Consideration of ^{3}He$_c$ formation processes also suggests that ^{3}He$_c$ is likely to be highly retained. Recoil energy estimates and thus stopping ranges are relatively low (20-30um, similar to radiogenic alpha-particles). Moreover, in most rocks any ejection losses are likely to be balanced by injection. Combined with the low diffusivities, this suggests helium losses will not hamper most ^{3}He$_c$ studies, at least in olivine and quartz. In addition, it appears cosmogenic helium can be operationally distinguished from inherited helium in these sample types, because crushing olivine releases only magmatic helium, and incremental heating of quartz releases ^{3}He$_c$ more rapidly and at lower temperatures than inherited or radiogenic helium. U+Th/He geochronology may be possible in quartz because of this low ^{*4}He diffusivity, as well. In summary, the measurements presented here suggest the potential problems of accounting for inherited helium and helium loss in ^{3}He$_c$ studies are readily surmountable, which is good news for future applications of cosmogenic helium geochronology.

REFERENCES

ANDREWS J.N. (1885) The isotopic composition of radiogenic helium and
     its use to study groundwater movement in confined aquifers. Chem.
     Geol. 49, 339-351.

BARRER R.M. and VAUGHAN D. E. W. (1967) Solution and diffusion of
     helium and neon in tridymite and cristobalite .Trans. Farad. Soc.
     63, 2225-2290.

BARRETT P.J. (1972) Stratigrapgy and petrology of the mainly
     fluviatile Permian and Triassic part of the Beacon Supergroup,
     Beardsmore Glacier area. In: Antarctic Geology and Geophysics
     (ed. R.J. ADIE), Scandinavian University Books.

BOGARD D.D. and CRESSY P.J. (1973) Spallation production of ^{3}He, ^{21}Ne,
     and ^{38}Ar from target elements in the Bruderheim chondrite.
     Geochim. Cosmo. Acta 37, 527-546.

CRAIG H. and POREDA R.J. (1986) Cosmogenic ^{3}He in terrestrial rocks:
     the summit lavas of Maui. Proc. Natl. Acad. Sci. 83, 1970-1974.

DAMON P.E. and KULP J.L. (1957) Determination of radiogenic helium in
     zircon by stable isotope dilution technique. Trans. Am. Geophys.
     Union 38, 945-953.

DEER, HOWIE and ZUSSMAN (1966) Rock Forming Minerals. Longmens,
     London, 528 pp..

FLEISCHER R. L. (1988) Alpha-recoil damage: relation to isotopic
     disequilibrium and leaching of radionuclides. Geochim. Cosmo.
     Acta 52, 1459-1466.

FLUGGE S. and ZIMENS K.E. (1939) Die Bestimmung von Korngrossen und
     von Diffusionkonstanten aus dem Emaniervermogen. Z. Physik.
     Chem.42, 179-220.

FRIEDLANDER G., KENNEDY J.W., MACIAS E.S. and MILLER J.M. (1981)
     Nuclear and Radiochemistry. John Wiley and Sons, Inc., New York.

GILETTI B.J. and KULP J.L. (1955) Radon leakage from radioactive
     minerals. Am. Mineralogist 40, 481-496.

GRAHAM D. V. (1987) Helium and lead isotope geochemistry of oceanic
     volcanic rocks from the East Pacific and South Atlantic. WHOI/MIT
     Ph.D., 252 p.

INTHOFF W. and ZIMEN K.E. (1956) Kinetik der Diffusion radioaktiver Edelgase aus festen Stoffen nach Bestrahlung (Edelgasdiffusion in Festkorpern 2). Trans. Chalmers. Univ. Techn. (Goteborg)176, 16p.

KEEVIL N.B. (1940) Interatomic forces and helium in rocks. Proc. Amer. Acad. Arts and Sci. 73, 311-359.

KURZ M.D., O'BRIAN P., GARCIA M. and FREY F.A. (1985) Isotopic evolution of Haleakala volcano: Primordial, radiogenic, and cosmogenic helium. EOS 66, 1120.

KURZ M.D. (1986a) Cosmogenic helium in a terrestrial igneous rock. Nature 320, 435-439.

KURZ M.D. (1986b) In situ production of terrestrial cosmogenic helium and some applications to geochronology. Geochim. Cosmo. Acta 50, 2855-2862.

KURZ M.D., COLODNER D., TRULL T.W., SAMPSON D., MOORE R.B. and O'BRIAN K. (1989, in revision) Exposure-age dating with cosmogenic ^{3}He.

LAL D. and PETERS B. (1967) Cosmic-ray-produced radioactivity on the earth. In: Handbuch der Physik XLVI/2 (ed. S. FLUGGE), pp. 551-612. Springer-Verlag, Berlin.

LAL D. and ARNOLD J.R. (1985) Tracing quartz through the environment. Proc. Indian Acad. Sci. (Earth Planet. Sci.) 94, 1-5.

LAL D. (1987) Production of ^{3}He in terrestrial rocks. Chemical Geology (Isotope Geoscience Section) 66, 89-98.

LAL D. (1988) In situ-produced cosmogenic isotopes in terrestrial rocks. Ann. Rev. Earth Planet. Sci. 16, 355-388.

MAMYRIN B.A. and TOLSTIKHIN I.N. (1984) Helium Isotopes in Nature. Elsevier, Amsterdam.

MARTI K. and CRAIG H. (1987) Cosmic-ray-produced neon and helium in the summit lavas of Maui. Nature 325, 335-337.

MCDOUGALL I. (1964) GSA 75, 107-128.

MORRISON P. and PINE J. (1955) Radiogenic origin of the helium isotopes in rock. Ann. N.Y. Acad. Sci. 62, 71-92.

MURRAY E.G. and ADAMS J.A.S. (1958) Thorium, uranium and potassium in some sandstones. Geochim. Cosmo. Acta 13, 260-269.

NAUGHTON J.J., MACDONALD G.A. and GREENBERG V.A. (1980) J. Volcan.
Geotherm. Res. 7, 335-339.

NISHIIZUMI K., LAL D, KLEIN J, MIDDLETON R and ARNOLD J.R. (1986)
Production of ^{10}Be and ^{26}Al by cosmic rays in terrestrial quartz
in situ and implications for erosion rates. Nature 319, 134-136.

ODOM A.L. and RINK, W.J. (1988) Natural accumulation of Schottkey-
Frenkel defects: Implications for a quartz geochronometer.
Geology 17, p55-58.

RAMA and MOORE, W.S. (1984) Mechanism of transport of U-Th series
radioisotopes from solids into ground water. Geochim. Cosmo. Acta
48, 395-399.

ROSSI B. (1952) High Energy Particles. Prentice-Hall, Inc., Englewood
Cliffs, N.J.

SIMMONS S.F. (1986) Physio-chemical nature of the mineralizing
solutions for the St. Nino Vein; results from fluid inclusion,
deuterium, oxygen and helium studies in the Fresnillo District,
Zacatecas, Mexico. University of Minnesota PhD., 192 pp.

STETTLER A. and BOCHSLER P. (1979) He, Ne and Ar composition in a
neutron activated sea-floor basalt glass. Geochim. Cosmo. Acta
43, 157-169.

TOLSTIKHIN I.N., PRASOLOV E.M., KHABARIN L.V. and AZBEL I.Y. (1974)
Estimation of the helium diffusion coefficient in crystalline
quartz. In: Geokhimiya radioactivnykh i radiogennykh isotopov
(eds. Y.A. SHUKOLYUKOV and E.K.GERLING), pp 19-90. Nauka,
Lenningrad.

WEED R. (1985) Chronology of chemical and biological weathering of
cold desert sandstones in the Dry Valleys, Antarctica. University
of Maine at Orono Master's Thesis, 138 pp.

WOLFENDALE A.W. (1973) Cosmic Rays At Ground Level. The Institute of
Physics, London.

YOKOYAMA Y., REYSS J. and GUICHARD F (1977) Production of
radionuclides by cosmic rays at mountain altitudes. Earth Plan.
Sci. Let. 36, 44-50.

CHAPTER 6

Helium and strontium isotopic constraints on the origin of
island arc magmas in the Woodlark Basin - Solomon Islands region.

T.W. Trull[1], M.R. Perfit[2], and M.D. Kurz[1]

1. Dept. of Chemistry
Woods Hole Oceanographic Institution
Woods Hole, MA 02543

2. Dept. of Geology
University of Florida
Gainesville, FL 32611

ABSTRACT

In an effort to better understand volatile sources and petrogenesis in island arcs, helium and strontium isotopes were measured in dredged volcanic rocks from the Woodlark Basin (western Pacific), the site of subduction of the Woodlark spreading center (WSC) beneath the Solomon Islands. Helium isotope ratios (^{3}He/^{4}He) range from 0.01 to 9 times the atmospheric ratio (R_a). However, low concentrations in whole rocks and some glasses, and helium isotopic disequilibrium observed by crushing and melting phenocrysts in vacuo, suggest that post-eruptive addition of radiogenic and seawater helium produces part of this variability. ^{3}He/^{4}He ratios in WSC tholeiites and NaTi basalts are indistinguishable from mid-ocean-ridge-basalt (MORB) values (8-9 R_a) despite the small size of the Woodlark Basin and extensive subduction in the surrounding area. Samples from Kavachi submarine volcano (Solomon Islands forearc), exhibit significantly lower magmatic ^{3}He/^{4}He ratios (6.9 $\pm$ .2 R_a), which may derive from the source region, or from degassing and ^{4}He ingrowth during long (>10,000 yr.) magma transport times.

Strontium isotope ratios (^{87}Sr/^{86}Sr) range from 0.7026 (typical of MORB) in tholeiites and NaTi basalts from the WSC and triple-junction region to a high of 0.7040 in a calcalkaline dacite in the forearc, with intermediate values in transitional rock types. Systematic increases in Sr contents and ^{87}Sr/^{86}Sr from the central Woodlark Basin toward the active arc suggest a mixing origin for the lower ^{3}He/^{4}He and higher ^{87}Sr/^{86}Sr ratios (approximately .7036) observed in Kavachi lavas. Contributions to the sub-arc mantle from Pacific lithosphere subducted during the Miocene may best explain these compositions, but fluids introduced by subduction do not appear to be directly involved in the current magmagenesis, because predominantly radiogenic ^{3}He/^{4}He ratios (1 R_a or less) were not observed.

6.1 INTRODUCTION

Isotopic and elemental compositions of island arc basalts (IAB) require a more complex petrogenesis than closed system melting of an upper mantle similar in composition to the source of mid-ocean-ridge-basalts (MORB),(e.g. Perfit et al,1980; Morris and Hart, 1983; Davidson, 1987). Geophysical models suggest that release of C-O-H fluids from hydrated minerals of the ocean crust, in response to increasing pressure and temperature during subduction, may play an important role in arc volcanism (e.g. Ringwood, 1974; Kay, 1980; Gill, 1981; Wyllie, 1982). These fluids appear capable of strong inter-element fractionation and may serve as a flux in melting the overlying mantle wedge (e.g. Kushiro, 1975; Flynn and Burnham, 1978). However, the location of fluid release, and therefore the role of this metasomatic process in controlling arc petrogenesis, is uncertain (e.g. Wyllie, 1984).

In this study helium and strontium isotopes were measured in island arc basalts and andesites, and nearby spreading center basalts, in an effort to examine the role of slab-derived fluids in arc petrogenesis. The He isotopic composition of subducted lithosphere beneath arcs depends essentially on its age and uranium and thorium contents. It is expected to have ^{3}He/^{4}He significantly lower than the ratio of 8.4 $\pm$ .3 R_a (Ra = atmospheric ratio) observed in normal MORB and thought to characterize the upper mantle (Kurz et al, 1982). As a noble gas, helium partitions strongly into fluids relative to crystals, glasses, and melts (Kurz and Jenkins, 1981; Kurz, 1982) and may therefore act as a tracer of fluids derived from subducted lithosphere. Thus, fluids released from subducted oceanic lithosphere may contribute radiogenic ^{4}He to magmas that erupt at convergent plate boundaries, thereby lowering their ^{3}He/^{4}He ratios. Similarly, Sr acts as an incompatible element during melting and may be concentrated in melts or fluids derived from subducted lithospere along with other large ion lithophile elements (LIL) that are characteristically enriched in IAB. Positive correlations between ^{87}Sr/^{86}Sr ratios and important geochemical parameters (e.g. Sr/Zr, La/Yb, and Ba/La) in MORB and IAB from western Melanesia (Perfit, McCulloch and Johnson, 1982; and Perfit, unpublished

data) indicate Sr isotopes are sensitive indicators of variations in source chemical compositions as well as of sample contamination on the seafloor. Combining He and Sr isotopic studies may improve our understanding of the behavior of Sr during dehydration of subducted lithosphere, allowing further discrimination of the components involved in arc petrogenesis.

Previous efforts to exploit He as a slab-derived-fluid tracer have focused on the measurement of volcanic gases and fluids (Craig, Lupton, and Horibe, 1978; Poreda, 1983; Sano and Wakita, 1985; Sano, Wakita, and Giggenbach, 1987). Hydrothermal fluid samples have $^3He/^4He$ ratios ranging from about 0.1 R_a to nearly 9 Ra. However, fumarole gases, especially those from volcanic summits, exhibit a narrower range, roughly 6 – 9 R_a, suggesting that radiogenic He from crustal rocks contributes to at least some gas samples. Direct measurement of helium isotopes in volcanic rocks may better characterize volatiles from magmatic source regions. The few rocks previously analysed exhibit a wide range in $^3He/^4He$ ratios; from extremely radiogenic ratios (approximately .06 R_a) to normal MORB ratios and higher (Poreda, 1983; 1985; Mamyrin and Tolstikhin, 1984 and references therein). Unfortunately, these samples were of uncertain age and part of the range in $^3He/^4He$ ratios may be produced by ingrowth of ^4He from the decay of U and Th after eruption. Because of the scarcity of helium data from arc rocks, and the unknown extent to which the helium isotopic composition of a sample reflects source characteristics, a major goal of this study is to understand how helium may be used as a tracer in arc environments.

6.1.1 Petrogenesis in the Woodlark Basin – Solomon Islands region.

The Solomon Island-Woodlark Basin region was chosen for study because fresh basaltic samples were available from both the overriding and downgoing plates, and many samples have glassy rims, which have been shown to trap magmatic gases (e.g Funkhouser, Fisher, and Bonatti, 1968). This area in the western Pacific can be divided into three tectonic regions: the Woodlark Spreading Center (WSC) which is a normal accretionary ridge in the middle of the Woodlark Basin, the forearc

slope of the Solomon Islands arc to the northeast (including the active Kavachi submarine volcano), and the complex triple junction region (encompassing Simbo and Ghizo ridges) where the WSC subducts into the trenches along the western edge of the Solomon Islands. Figure 6.1 shows the tectonic relations and dredge sites. An excellent overview of the tectonic history and regional geology of the arc was presented by Dunkley (1984), and the triple junction area has been described in detail (Taylor, 1987).

The rocks dredged from the Woodlark Basin and studied here are geochemically diverse (Johnson et al, 1987; Perfit et al, 1987; Staudigel et al, 1987) but can be grouped into three general petrologic associations: basalts with compositions similar to MORB, rocks ranging from basalt to dacite with typical island arc basalt (IAB) compositions, and a few basalts and basaltic andesites with chemical compositions that are transitional between the MORB and IAB compositions. These groupings correspond roughly to the three tectonic regions mentioned above.

Predominantly normal MORB were recovered from the WSC (dredges 26 and 29). Some basalts from dredge 29 have slight back-arc-basin-basalt (BABB) characteristics (e.g. increased Sr/Zr, La/Yb, and $^{87}Sr/^{86}Sr$). In addition, a unique basalt type with trace element and isotopic characteristics similar to MORB but exceptionally high Na_2O and TiO_2 was recovered at dredge site 32 where the WSC meets Simbo ridge. These NaTi basalts (samples 32-8,9,10) have depleted large ion lithophile and rare earth element abundances despite being nepheline normative (Perfit et al, 1987). The MORB from dredges 29 and 26 probably best represent the composition of the ocean floor that is subducted beneath the Solomon Islands.

Both medium- and high- K_2O island arc lavas were recovered in the forearc slope region (dredges 24 and 25). However, at the active submarine volcano, Kavachi, only low- K_2O island arc tholeiites were recovered (dredges 34,35). These rock types are very similar to those erupted on the New Georgia Islands and in the nearby New Hebrides and New Britain arcs (Johnson et al, 1985). They represent typical eruptive products of subduction zone magmagenesis.

Figure 6.1 Tectonic map for the Woodlark Basin and Solomon Islands region, modified from Taylor and Exon, 1984). The Woodlark spreading center (WSC) has been opening at 7 cm/year for about 5 Ma. This new seafloor is being subducted orthogonally into the New Britain (NBT) and San Cristobal (SCT) trenches at about 10 cm/yr. The trenches shoal from their typical depths of 4000m or more to less than 2000m near their intersection with the WSC. The complex triple-junction region encompasses Simbo ridge, thought to be an extinct ridge transform fault and Ghizo ridge, which may represent a deformed spreading segment. Dredge 33 marks the location of Kana Keoki seamount near the end of Simbo-Ghizo Ridge. Historical volcanism has occurred on most of the Western Islands – along the line between Guadalcanel (GC) and Vella Lavella (VL). Kavachi submarine volcano is presently active. Santa Isabel (SL) and the other Eastern Islands were volcanically active in the Miocene, when subduction occurred from the northeast, at the now extinct Vitiaz Trench (VT). The WSC is propagating westwards at approximately 12 cm/yr into the submarine extension of Papua New Guinea, as marked by the 2000 m rise contours. Dredge locations are numbered correspond to the sample numbers in Table 6.1

Figure 6.1
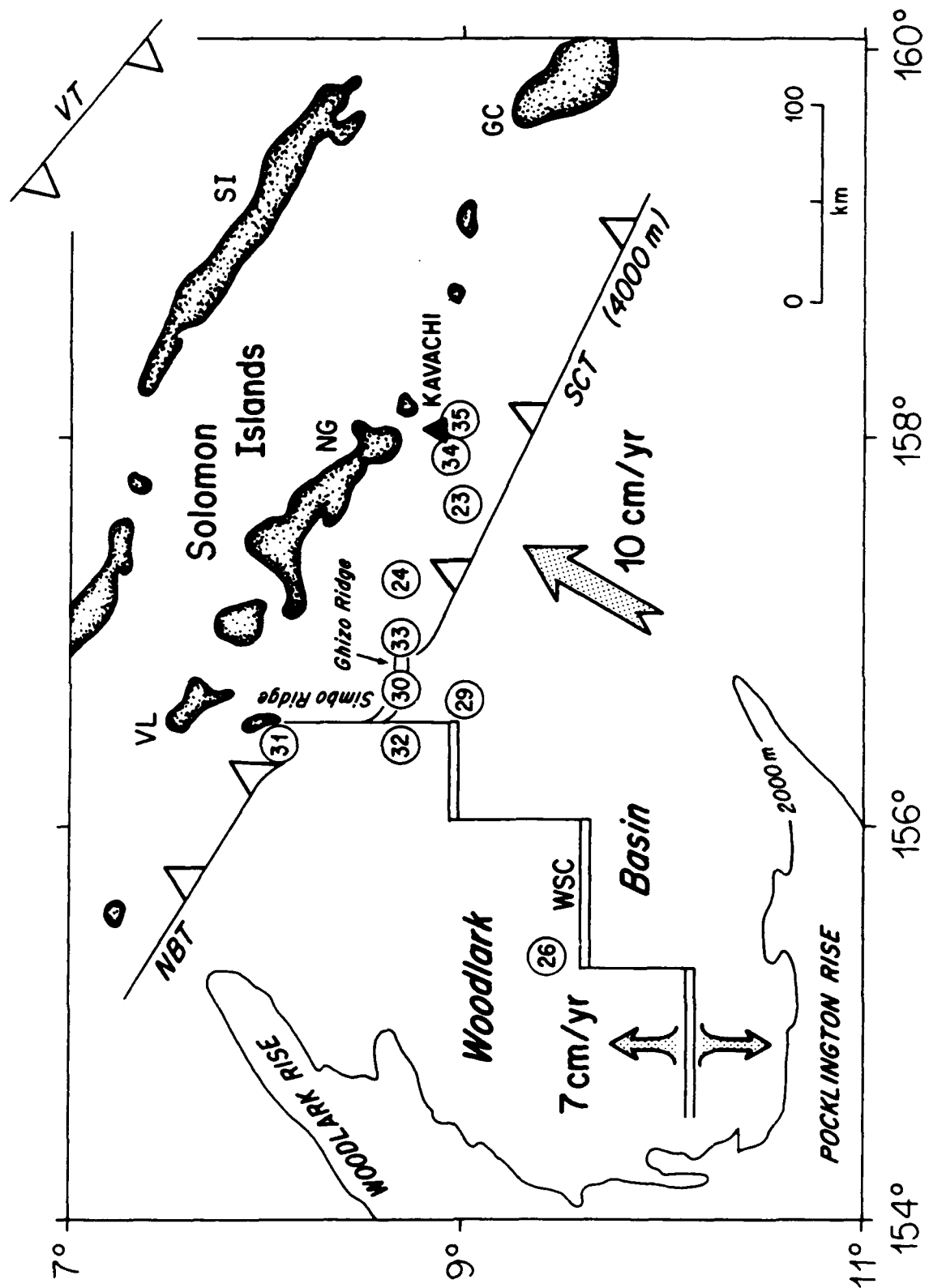
Rocks ranging in composition from high-Mg basalts ("boninites") to low K_2O tholeiites, to normal calcalkaline dacites and rhyolites were recovered from the complex triple junction region encompassing the Simbo and Ghizo ridges (dredges 30,31, and 32) and Kana Keoki Seamount (dredge 33). The more silicic rocks (dredge 33), including glassy dacites, are similar to highly fractionated arc rocks found in New Britain and Bougainville (Johnson et al, 1987). Perfit et al (1987) have shown that the tholeiitic basalts and basaltic andesites from dredges 30 and 32 are chemically transitional between the WSC MORB and the forearc IAB. Thus, these samples span the compositional range of rock types seen in island arcs, including extreme compositions.

Overall, the trace element and isotopic variability of the samples from the Woodlark Basin-Solomon Islands region is less extreme than the diversity of petrologic types. For example, both the unusual NaTi basalts and the more normal spreading-ridge environment basalts found along the WSC have rare earth element patterns and Sr isotopic compositions similar to MORB (Johnson et al, 1987; Perfit et al, 1987; this study). Moreover, Perfit et al (1987) and Staudigel et al (1987) have shown that isotopic compositions and trace element ratios that indicate relative source enrichments, vary smoothly spatially in the Woodlark Basin-Solomon Islands region.

These researchers have proposed that the observed variation represents an increase toward the arc in the petrogenetic involvement of upper mantle previously modified by subduction of lithosphere along the Vitiaz Trench (figure 6.1). This was the locus of convergence and volcanism until Miocene time (Dunkley, 1984 and references therein). In this view, subduction of the WSC acts as a "thermal trigger" to melt the modified mantle. The thermal anomaly associated with the WSC is reflected in the shoaling of both the bathymetric expression of the trench and the loci of subduction-related earthquakes by several kilometers near the triple junction (Cooper and Taylor, 1985), in the rapid uplift of the islands of the New Georgia Group on the overriding Pacific plate (Taylor, 1987), and in the unusually small gap between the trench and the volcanic front (e.g. just 30 km at Kavachi submarine volcano).

Alternatively, Abbot and Fisk (1986) have suggested that relict
Pacific lithosphere continues to release volatiles into the mantle
beneath the Woodlark Basin, and that this process is actively involved
in determining the compositions of erupted rocks. The extension of
ancient Pacific lithosphere under the Solomon Islands is suggested by
the spatial distribution of deep earthquakes in the region (Cooper and
Taylor, 1985). If this model is correct, correlation between source
composition indicators (such as isotopic and incompatible element
ratios) and the nature of petrogenesis (as reflected in rock type) would
be expected to be stronger than for tectonically controlled melting of a
previously modified and laterally variable mantle. For example, island
arc basalts (IAB) should have similar, radiogenic, helium and strontium
isotope compositions, whether erupted in the forearc or the triple-
junction region. In either case, one probable petrogenetic effect of
ridge subduction is the unusual exposure of voluminous mafic lavas,
including picrites in the New Georgia island group of the Solomon
Islands. These compositions appear to result from accumulation of mafic
phenocrysts and the lavas have trace element and isotopic signatures
similar to more typical arc basalts from elsewhere in the Solomon
Islands and other island arcs (Cox and Bell, 1972; Ramsay, Crawford and
Foden, 1984, Staudigel et al, 1987; Perfit et al, in preparation).
Unfortunately, we were unable to obtain samples of these rocks as part
of this study.

6.2 METHODS

6.2.1 Helium

In light of the diversity of rock types erupted at arcs, an
important aspect of this study was determining the best way to obtain
the magmatic helium isotopic composition from arc samples. Whole rocks,
mineral separates (olivine, pyroxenes, and plagioclase), and glass
fragments were analysed to determine which phases contained measurable
amounts of helium, and which were reliably free from air or seawater
contamination. In addition, the generally low He concentrations

observed and the indeterminate age of the dredge samples required developing analytical criteria to distinguish samples affected by post-eruptive radiogenic ^{4}He contamination. These criteria are discussed briefly here and in more detail below. Brief sample descriptions are given in Table 6.1, detailed petrographic descriptions of the whole rocks can be found in Johnson et al (1987) and Perfit et al (1987).

Glass samples analyzed were chips greater than 1mm in their largest dimension, free of visual alteration in reflected light under 40x magnification. For most samples, with the notable exception of those from dredge 30, this was much larger than the mean vesicle diameters. From 20 mg to 1 gram of clean glass was analyzed, depending on the sample's helium concentration. Some glass samples (see Table 6.1) were pretreated by ultrasonic cleaning in 8N nitric acid as a means of removing altered material. Optically clean fragments were then chosen from the leached material. Experiments on leached and unleached glass suggest that concentrations and isotopic compositions are not significantly affected by this process. However, this treatment was performed only on samples with slight alteration - visible as hazing or discoloration of surfaces.

Mineral separates were handpicked from the 1-2 mm size fraction (or smaller in some cases) of jaw-crushed samples and contained as little adhering matrix and/or other mineral phases as possible (less than 1%). Inclusions of devitrified melt were often present, particularly in clinopyroxene separates and many olivine samples contained small spinel inclusions. Fluid inclusions were often visible in these crystal types, both in thin section and by viewing the grains in transmitted light. Depending on helium concentrations, from ten to a few hundred milligrams of crystals were analyzed, generally consisting of 10 - 50 individual grains.

Groundmass samples were picked from the .8 - 1.0 mm size fraction to be free of obvious crystals, and were cleaned ultrasonically in H_2O for approximately an hour. These samples were dried in air overnight, at 40-80°C; this had no effect on helium concentrations or compositions, based on duplicate analyses.

In order to assess the contribution of radiogenic ^{4}He added after eruption to the observed isotopic compositions, samples were analyzed first by crushing the grains in vacuo and then by melting the resulting powder in the vacuum furnace. Because crushing selectively releases gases trapped in vesicles and inclusions, this helium should represent the isotopic composition of the magma at eruption. In contrast, helium released by melting includes radiogenic ^{4}He from U and Th series alpha-particle decay in the solid phases. These procedures and the instrumentation for helium extraction have been described recently (Kurz, Gurney, Jenkins and Lott, 1987). The mechanical efficiency of crushing varies according to sample type and weight, and concentrations of helium released by crushing are thus operationally defined. All powders analyzed by melting passed through a 100 um sieve, with the exception of a few mineral separate samples for which a 200 um separation was used in order to have enough material to analyze (see Table 6.1). Therefore, inclusions smaller than these dimensions contribute helium to the melt analysis. The degree to which this (and incomplete operational separation of inherited and ingrown helium, in general) affects the determination of the ^{3}He/^{4}He ratio of the magma at eruption is discussed in the results section below.

Glasses and groundmass were melted at 1300°C, and mineral separates at approximately 1500°C. The estimated uncertainty in these temperatures is 30°C. Powders were loaded in aluminum foil boats (approx. 20 mg) for melting in the furnace; melting of the samples was verified by examination of the silicate slag after heating, and by the absence of additional helium in procedural blanks following the analyses.

Procedural blanks for crushing and melting were identical and ranged from 3 to 6 x 10^{-11} ccSTP He. The isotopic ratio of the blank was always within 2 sigma of the atmospheric ratio. Blank corrections for the samples reported in Table 6.1 were generally much less than 1%, and rarely exceeded 10%. The detection limit for ^{3}He (2 sigma on the ^{3}He blank) was approximately 3 x 10^{-16} ccSTP. Samples with less ^{3}He than this are reported as having ^{3}He/^{4}He ratios less than or equal to

the ratio of the detection limit for ^{3}He to the observed ^{4}He concentration (see Table 6.1).

6.2.2 Strontium.

Strontium isotopes were measured using a VG Isomass 354 thermal ionization mass spectrometer at the University of Florida. Measurements of ^{87}Sr/^{86}Sr were made by simultaneous collection into three Faraday cups and normalized to ^{86}Sr/^{88}Sr = 0.1194. The value of NBS SRM 987 during the time period of these analyses averaged 0.710240 (12 %, 2 sigma). Total procedural blanks were 1 ng Sr. A few samples were spiked prior to dissolution and Sr and Rb were determined by isotope dilution.

Where possible fresh hand-picked glasses were selected for analysis. Even the optically freshest samples were ultrasonically cleaned in 1N HCl for 20 minutes and triple-distilled H_2O for up to an hour. Glasses and glassy samples with slightly oxidized or discolored surfaces were leached in 2N HCl for up to 12 hours before being washed in clean H_2O. Whole rocks were trimmed of macroscopic alteration prior to crushing and hand-picking. The freshest fragments containing both groundmass and crystals were leached in 2N HCl and washed in clean H_2O. All samples were dried under heat lamps for more than 12 hours before being powdered in a tungsten-carbide ball-mill (most glasses were dissolved without pulverization). Between 50 and 100mg of sample were dissolved in 3-5ml of 50% HF and 3 drops of 14N HNO_3. Samples were sealed in teflon reaction vessels and kept at 100^{0}C for 48 hours. They were converted to chloride form before using standard cation exchange columns to separate Rb, Sr, and the rare earth elements. Samples were loaded as a nitrate on oxidized Ta filaments.

A few experiments with the cleaning and leaching techniques showed that even the freshest looking samples may have minor amounts of alteration that contain radiogenic Sr from seawater. In most cases cleaning with 1N HCl was sufficient to remove this material, but in others, noteably the crystalline samples, leaching in 2N HCl was

Table 1. Helium Isotope Data

L O C A T I O N			S A M P L E D E S C R I P T I O N					*METHOD	H E L I U M A N A L Y S I S					
LATITUDE (South)	LONGITUDE (East)	DEPTH (meters)	DREDGE #	SAMPLE #	ROCK TYPE[a]	PHASE[b]	COMMENTS		WGT (mg)	3He/4He (R/Ra)[c]	1σ	[He] (10^-7 cc/g)	4He₁ (10^-10 cc/g)[d]	4He₂ (10^-10 cc/g)
9°29.94' 155°25.15' WSC axis, 180 km west of the trench.		3830-3460	26	11	MORB	glass	~ 3% vesicles	1	448	8.44	.05	87	310±80	310±80
						glass		2	115	7.84	.03	4.3		
9°05.44' 156°41.11' WSC axis, 80 km west of the trench.		3973-3570	29	5	MORB	glass		2	28	8.42	.05	3.0		
				A	MORB	glass	40' leach 50% HNO₃	1	35	8.43	.05	.85		
				B	MORB	glass		1	35	8.48	.05	4.6		
				C	MORB	glass		1	28	9.14	.04	6.1		
				D	MORB	glass		1	32	9.30	.05	3.9		
					MORB	glass		1	37	8.44	.05	1.7		
					MORB	glass		1	155	8.18	.03	21		
				H	BABB?	glass		3	113	8.95	.05	.75		
8°45.39' 156°27'13" West flank of southern end of Simbo Ridge, near its inter-section with Ghizo Ridge, in the triple-junction region.		2830-2050	32	8	NaTi Basalt	glass		3	129	8.96	.06	19		
						glass		2	335	9.2	.1	.027		
						glass		3	75	9.0	.1	.49		
				9	NaTi Basalt	glass	10% dulled surfaces	3	213	7.4	1.0	.009		
						glass	10% dulled surfaces	3	290	5.0	.4	.023		
						glass	40' Leach 8N HNO₃	1	135	7.8	.1	.17		
						glass	40' Leach 8N HNO₃	1	290	6.4	.4	.019		
						glass	>200um powder	2	429	5.7	.4	.011		
						glass	<200um powder	2	213	8.2	.1	.19		
						glass	step-heating sum	2	147	8.3	.1	.15		
				10	NaTi Basalt	glass		2	92	7.7	.7	.12		
						glass		1	170	8.73	.04	3.1		
				16	Basaltic andesite	glass		1	194	1.3	.6	.11		
						glass		2	174	1.0	.4	.015		
8°47'19" 156°43'15" South flank of Ghizo Ridge in the triple-junction region.		3830-3460	30	5	Basaltic andesite	altered glass	10% palagonite	3	280	.8	.2	.026		
						glass	10% of surfaces altered	1	303	.5	.2	.009		
						glass		2	168	1.1	.2	.16		
						glass	20' Leach 50% HNO₃	1	288	1.2	.1	.13		
						glass	40' Leach 50% HNO₃	2	144	1.6	.2	.10		
						glass	<100um powder	2	171	1.1	.2	.13		
						glass	>200um powder	2	95	2.1	.4	.015		
						glass		1	60	1.2	.6	.040		
8°12'43" 156°27'56" West flank of northern end of Simbo Ridge in the triple-junction region.		2065-1635	31	6	Basaltic andesite	glass		1	175	1.22	.08	.12		
				1	High-Mg andesite ("boninite")	glassy groundmass		1	114	1.3	.1	.076	40±10	560±50
						glassy groundmass		2	95	.35	.2	.058		
						bronzite (Mg₃Fe₁₄Ca₀₄)		1	167	5.4	.2	.028	11±2	10±1
						bronzite		2	143	5.07	.5	.011		
				10	High-Mg andesite ("boninite")	glassy groundmass		1	251	.6	.2	.024	240±30	270±30
						glassy groundmass		2	128	.06	.03	.27		
						bronzite	partial crush	1	260	2.7	.4	.012	9±2	13±1
						(Mg₃Fe₁₄Ca₀₄)	recrush	1	260	2.1	.4	.009		
						bronzite		1	220	.9	.3	.014		
						bronzite		3	221	2.0	.3	.02		
				13	High-SiO₂ andesite	augite (Mg₃Fe₁Ca₃ₛ)		1	230	.6	3	.002	5±2	6±1
						augite		2	191	1.5	.7	.007		
						hypersthene		1	170	2.2	.5	.008	9±3	9±1
						hypersthene		2	141	5.08	.04	.009		

* Method codes: 1 = crushing, 2 = melting of powder (less than 100μm unless otherwise indicated), 3 = melting of whole grains or shards.

a. Rock types are from Johnson et al (1987) and Perfit et al (1987).

b. Phenocryst identifications are based on microprobe analyses performed at MIT with the help of Steve Recca.

c. 1 sigma errors in the 3He/4He ratios are based on a single mass spectrometer analysis.

d. Errors for 4He contents are 1 sigma calculated from analytical errors in the 3He/4He ratios.

e. Maximum values of 3He/4He ratios are reported for samples with 4He contents below the detection limit.

Table 1. (cont.) Helium Isotope Data

LOCATION LATITUDE (South)	LONGITUDE (East)	DEPTH (meters)	DREDGE #	SAMPLE #	ROCK TYPE	PHASE COMMENTS	METHOD	WGT. (mg)	3He/4He (R/Ra)	1σ	[He] (10^-9 cc/g)	3He1 (10^-10 cc/g)	4He2 (cc/g)
8°48.5' 157°14'57" Lower forearc slope south of Rendova Island		3405-2800	24	4	Trachy-basalt	glass	1	148	1.5	.1	.048	410±40	430±40
						glass	2	96	.08	.02	.43		
						plagioclase (Ca85Na42K02)	1	84	8	1	.009	7±2	7±2
						plagioclase	2	75	2.4	.3	.010		
				12	Low-SiO2 Andesite	whole rock	2	275	1.9	.5	.048		
						augite melt inclusion poor (Mg50Fe12CA38)	1	252	4.2	1	.013		
						augite melt inclusion rich (Mg51Fe04CA45)	3	109	3.7		.025	5±1	5±1
						augite melt inclusion rich	2	342	4.0	.4	.007		
								301	.9	.1	.006		
8°59'54" 157°59'43" Southeast flank of Kavachi submarine volcano		925-870	34	1	Quartz tholeiite	diopside (Mg51Fe04CA45)	1	165	6.29	.09	.12		
						olivine	1	321	7.08	.09	.094		
				7	Quartz tholeiite	diopside	1	160	7.09	.06	.36		
						diopside	2	136	7.0	.1	.12		
						olivine	1	43	6.0	.4	.067	80±20	74±8
						olivine	2	33	5.01	.3	.076		
				9	Quartz tholeiite	glassy groundmass	1	386	3.0	.2	.015		
						diopside	1	235	6.98	.05	.14	3±1	12±5
						diopside	2	260	6.6	.1	.057		
						diopside	1	277	6.6	.2	.21		
						groundmass	1	222	4.8	.2	.021		
						groundmass	2	210	4.9	.5	.008		
9°00.08' 157°58'04" Southwest flank of Kavachi submarine volcano		410-380	35	2	Low-SiO2 Andesite	diopside (Mg49Fe05CA46)	2	285	6.6	.7	.083	2±1	4±1
						diopside	2	159	5.0	.6	.01		
						olivine	1	225	7.0	.2	.034		
						olivine	2	191	7		.005		
						augite (Mg44Fe14Ca42)	1	67	6	3	.004	18±7	21±2
						augite	2	57	1.4	.6	.024		
				6	Quartz tholeiite	diopside	1	158	6.4	.2	.075		
						diopside	2	137	5.5	.8	.009		
						olivine	1	208	6.9	.2	.042		
						olivine	2	173	6.9	.5	.009		
8°44'12" 157°03'48" Kana Keoki seamount, southwest of Rendova Island and west of the line of the trench.		1550-1250	33	8	Dacite	glassy rock (air contamination	1	432	1.0	.01	.32		
						glassy rock problem, see text)	3	358	.86	.2	.21		

* Method codes: 1 = crushing, 2 = melting of powder (less than 100um unless otherwise indicated), 3 = melting of whole grains or shards.
a. Rock types are from Johnson et al (1987) and Perfit et al (1987).
b. Phenocryst identifications are based on microprobe analyses performed at MIT with the help of Steve Recca.
c. 1 sigma errors in the 3He/4He ratios are based on a single mass spectrometer analysis.
d. Errors for 4He contents are 1 sigma calculated from analytical errors in the 3He/4He ratios.
e. Maximum values of 3He/4He ratios are reported for samples with 4He contents below the detection limit.

neccesary. Leaching in stronger acid (see Staudigel et al, 1987) did
not significantly improve the results.

6.3 RESULTS

6.3.1 Helium isotopic variabilty.

Samples from the Woodlark Basin - Solomon Islands region have
helium isotopic compositions spanning a broad range (Table 6.1), from
MORB values (1.1-1.2 $x10^{-5}$, or 8 - 9 R_a) to nearly as low as the $^3He/^4He$
production ratio ($2x10^{-8}$, or 0.01 R_a). Figure 6.2 reveals that this
diversity exists for helium released by both the crushing and melting
methods, and that there are strong correlations between tectonic regions
and the observed $^3He/^4He$ ratios.

The highest $^3He/^4He$ ratios are observed exclusively in dredged
samples erupted along the Woodlark Spreading Center. These glasses
generally exhibit ratios between 8 and 9 R_a; the few exceptions with
lower ratios (32-9 on crushing, and 32-16) have probably been
contaminated after eruption. Strikingly, this association of MORB
helium isotopic compositions with the Woodlark spreading center extends
to the unusual NaTi basalts recovered close to the triple junction.
Within the WSC basalts there is no difference in helium compositions
between samples with MORB chemical compositions and a sample from dredge
29 with trace element characteristics similar to back-arc-basin-basalts
(BABB, see Table 6.1).

Analyses of samples from the forearc region are primarily mineral
separates from Kavachi submarine volcano. Overall, samples from Kavachi
have $^3He/^4He$ ratios that range from 0.01 R_a to 7.1 R_a. However,
measurements on helium released by crushing mineral separates have
$^3He/^4He$ ratios between 6 and 7 R_a, and probably best represent the
magmatic helium isotopic composition, as discussed below. This places
Kavachi island arc basalts within the total range of MORB samples, but
significantly lower than both normal MORB samples (Kurz et al, 1982;
Kurz, 1982) and the nearby WSC samples. Other samples from the forearc

Figure 6.2 Histograms of ^{3}He/^{4}He compositions (normalized to the atmospheric ratio, R_a = 1.38 x 10^6) of gas released by powder melting (a) and crushing (b) of Woodlark Basin dredge samples. Symbols denote tectonic regions: WSC (squares), triple-junction region (circles), Kavachi submarine volcano (diamonds), forearc (triangles). Samples plotted in the first column at left have ^{3}He/^{4}He ratios less than 0.5 R_a. Duplicate analyses are not displayed.

Figure 6.2

a) $(^{3}He/^{4}He)_{by\ melting\ powder}$

b) $(^{3}He/^{4}He)_{by\ crushing}$

314
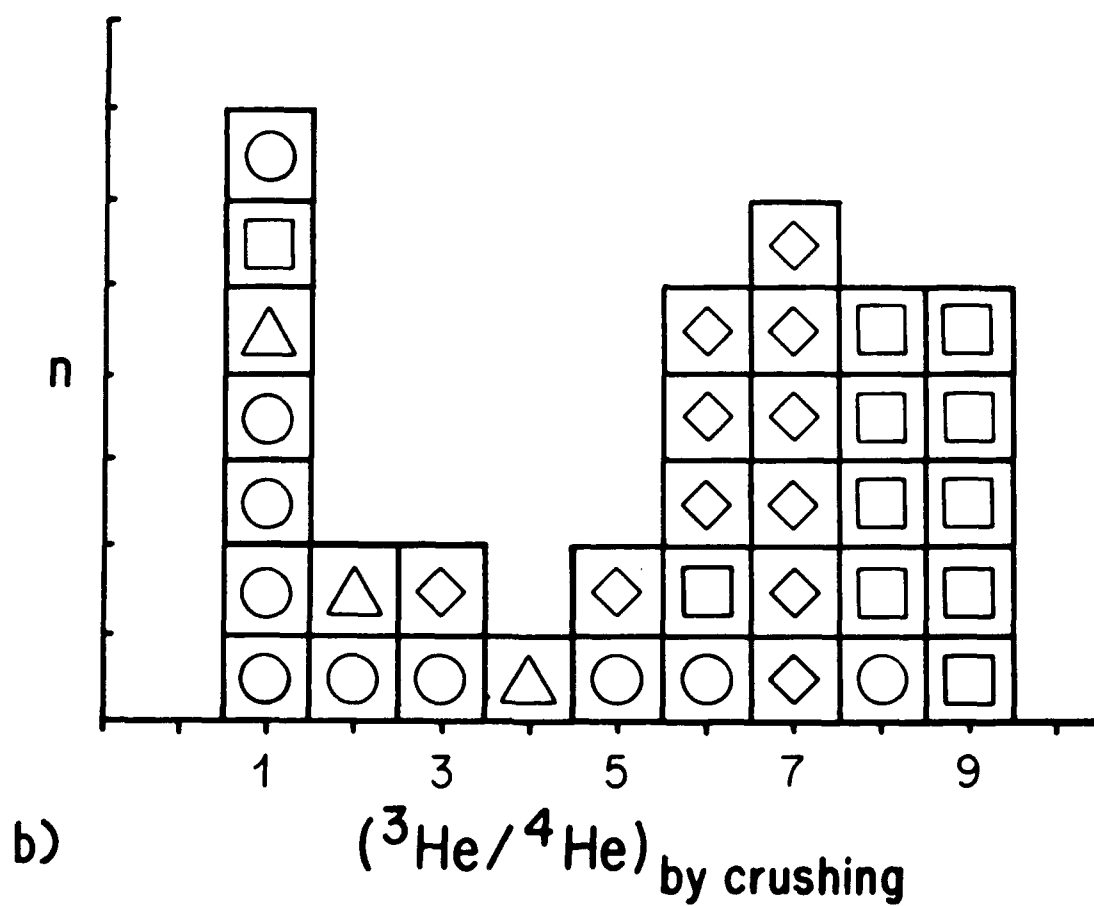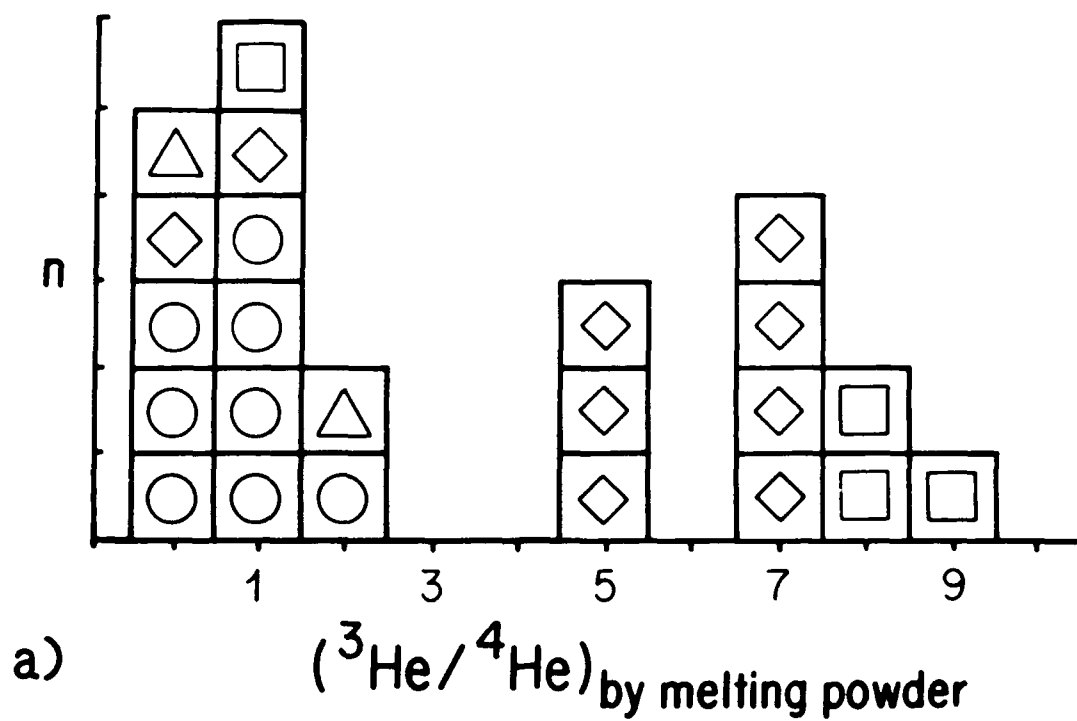
generally exhibit lower $^3He/^4He$ ratios than the Kavachi samples, extending to very radiogenic ratios lower than the atmospheric ratio.

Samples from the triple junction area generally have much lower $^3He/^4He$ ratios than rocks from either the spreading center or overriding plate, but also include values as high as $8R_a$. Among the low ratio samples are the high MgO andesites ("boninites") of dredge 31, a rock type thought to involve slab-derived hydrous fluids in its petrogenesis (e.g. Cameron, McCulloch, and Walker, 1983). Triple junction sample types included mineral separates, glasses, and groundmass (Table 6.1).

In summary, samples from the volcanic forearc and nearby triple junction area have distinctly lower $^3He/^4He$ ratios than do rocks from the Woodlark Spreading Center. However, in order to relate the regional helium isotopic variations to differences in source materials, or petrogenetic variables, it is neccesary to establish that the measured $^3He/^4He$ ratios on rocks, glasses, and mineral separates represent magmatic isotopic compositions.

a) Alteration of magmatic $^3He/^4He$ ratios after eruption.

Contamination of the helium isotopic compositions of rocks erupted on the seafloor may occur by either the exchange of helium with seawater or the addition of radiogenic ^4He within the sample. Both processes are time dependant and affect samples with low initial helium contents most severely.

High helium contents (10^{-7} ccSTP/g or more) are essentially limited to glasses from the WSC basalts from dredges 26 and 29. Addition of ^4He by either process will not have significantly altered the isotopic composition of helium released by crushing these samples, because of their high helium contents and geologically young ages (see discussion below). Consistent with this conclusion is the lack of any correlation between $^3He/^4He$ ratios and helium concentrations for these samples. The helium contents of these samples are approximately one tenth that of mid-Atlantic-ridge basalts, but are very similar to results from the Marianas and Lau back-arc basins (Kurz and Jenkins, 1981; Poreda, 1985). Helium concentrations in glasses from other rock types (NaTi basalts of dredge 32, basaltic andesites of dredge 30 in the

triple junction region, and the forearc andesite 24-4) are much lower (10^{-8} to 10^{-9} ccSTP/g). As shown below, some of these samples may have been contaminated by helium addition after eruption.

Low He concentrations (order 10^{-8} ccSTP He/g) were found in all mineral separate samples, similar to the amounts observed in phenocrysts from Hawaiian and other oceanic island basalts by Kurz, Jenkins, and Hart (1982), and Kurz et al (1983). Figure 6.3 shows that a large fraction (50-99%) of the helium is released by crushing. Clinopyroxenes contained the most He and released a larger percentage by crushing than olivines and orthopyroxenes. Samples with high gas contents in one phase tend to have elevated levels in other phases as well, although this is not a strong correlation. These results are in agreement with the qualitative abundances of melt and fluid inclusions in the crystals, and suggest that the He primarily resides in the inclusions. Similar helium distributions were found by Polve and Kurz (1988) for mineral separates from ultramafic xenoliths. Note that while mineral separate helium contents are lower than those of glasses, crystals are not necessarily more prone to contamination because they also have lower uranium and thorium contents and slower diffusive exchange for He (Polve, 1985; Trull, 1988).

Groundmass (holocrystalline) samples generally contain on the order of 10^{-9} ccSTP He/g. Such low concentrations, coupled with high uranium and thorium contents in comparison to mineral separates, and short paths for diffusive exchange (i.e. small grain size) make this sample type readily susceptible to contamination. In addition, groundmass samples may contain atmospheric helium. Analysis by crushing and melting of a glassy dacite sample, 33B, released 2 and 3 x 10^{-8} ccSTP He/g respectively, each time with atmospheric isotopic composition. This is probably helium from air trapped in microscopic intergranular spaces within the sample, which is also consistent with the elevated pre-extraction blanks observed for this sample. One percent pore space is required, in good agreement with the sample's appearance in thin section. This process may affect groundmass samples in general, yet it would go undetected for samples with more typical helium contents of 10^{-9} ccSTP/g. Based on this, and other information discussed below, we

Figure 6.3 Comparison of the quantity of helium released by crushing versus melting powdered mineral separates. Tielines connect observed values (open symbols) with points corrected for radiogenic helium ($^*He_1$ in table 6.1; filled symbols). Errors are about 1% and are smaller than the symbols.

Figure 6.3
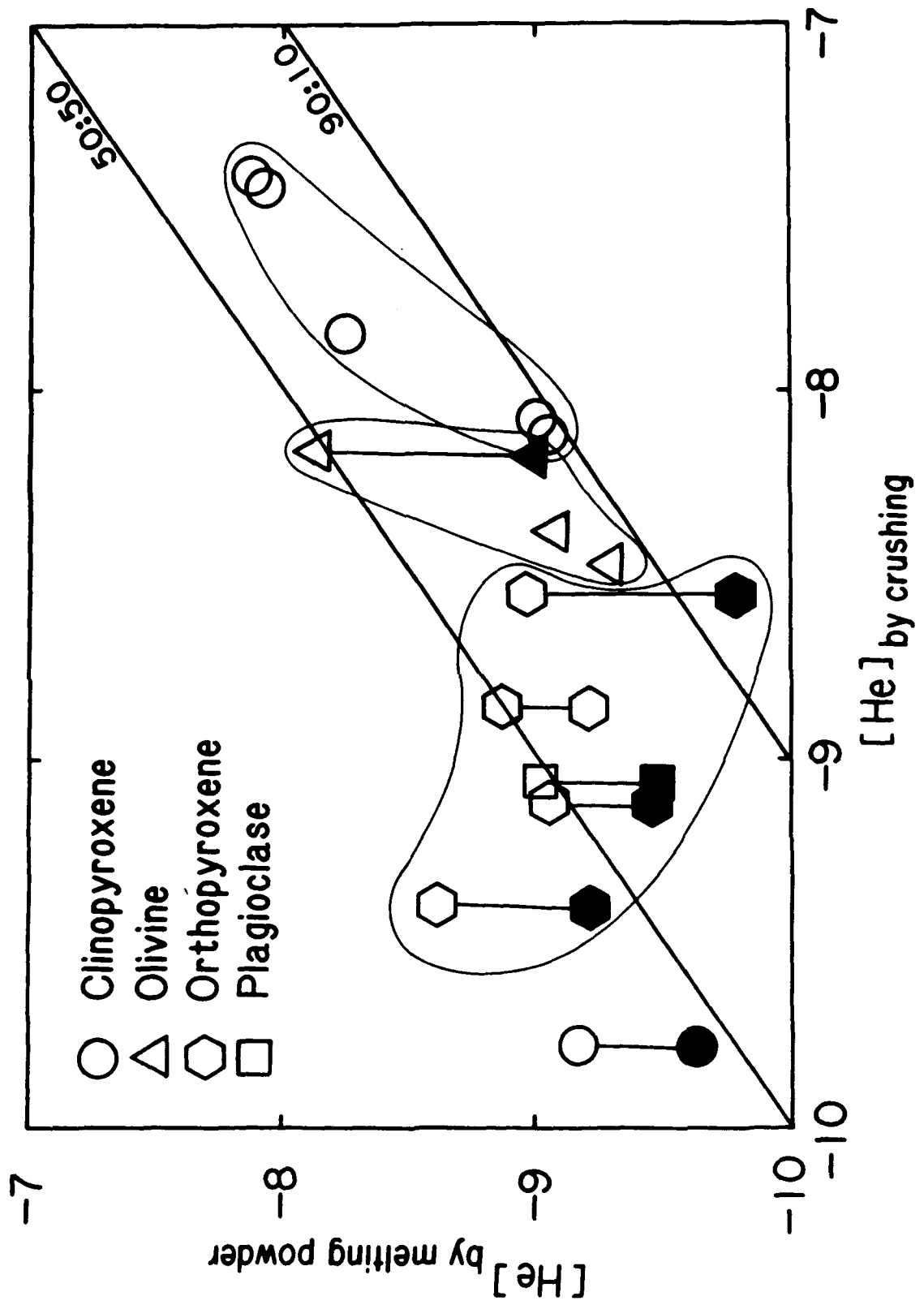
consider groundmass samples unreliable in determining magmatic helium isotopic compositions.

One way to assess the addition of radiogenic He to samples of uncertain age, such as these, is by comparison of the isotopic composition of helium released by crushing with that released by melting the crushed powder. Figure 6.4 reveals that many samples from the forearc region and triple junction exhibit significantly lower $^3He/^4He$ ratios when melted. In contrast, most samples from the WSC and from Kavachi Volcano lie along the line representing isotopic equilibrium in this figure. Lower $^3He/^4He$ ratios on melting are consistent with the post-eruptive addition of radiogenic ^4He in the solid phase. Note that significant disequilibrium is observed in both glasses and mineral separates. The only sample to exhibit a higher $^3He/^4He$ ratio on melting than crushing (32-9) was probably affected by helium from seawater (discussed below). It is possible that small amounts of basaltic matrix adhering to mineral separates contribute significantly to the observed disequilibrium because of their higher U and Th contents.

The possibility of radiogenic helium addition to these samples suggests that magmatic $^3He/^4He$ ratios of arc rocks cannot reliably be obtained by total fusion analysis, at least for samples of unknown age. However, combined crushing and melting analyses allow an estimate of the importance of radiogenic helium and may allow the determination of the magmatic $^3He/^4He$ ratio, even if disequilibrium is observed. The $^3He/^4He$ ratio obtained by crushing will not be disturbed unless the amount of radiogenic He generated in the solid phase is a significant fraction of the helium content released by crushing. The total amount of radiogenic ^4He is given by:

$$^*He = [He]_m \times [R_i - R_m] / [R_i - R_p]$$

(R = $^3He/^4He$ ratio, m = melted powder, i = inherited ratio at eruption, p = production ratio accompanying radiodecay.)

We can approximate R_i by R_c, the ratio obtained by crushing the sample, yielding a minimum estimate for $^*He$, since any transfer of radiogenic

Figure 6.4 Internal isotopic disequilibrium is shown in this plot of the ^{3}He/^{4}He ratios measured by crushing, versus melting the resultant powder. Samples below the equilibrium line have been affected by ingrowth of ^{4}He after eruption. WSC sample 32-9 is the only sample to plot significantly above the line and is discussed in the text. Error bars are 1 sigma. Symbols denote tectonic regions as in figure 6.2.

Figure 6.4
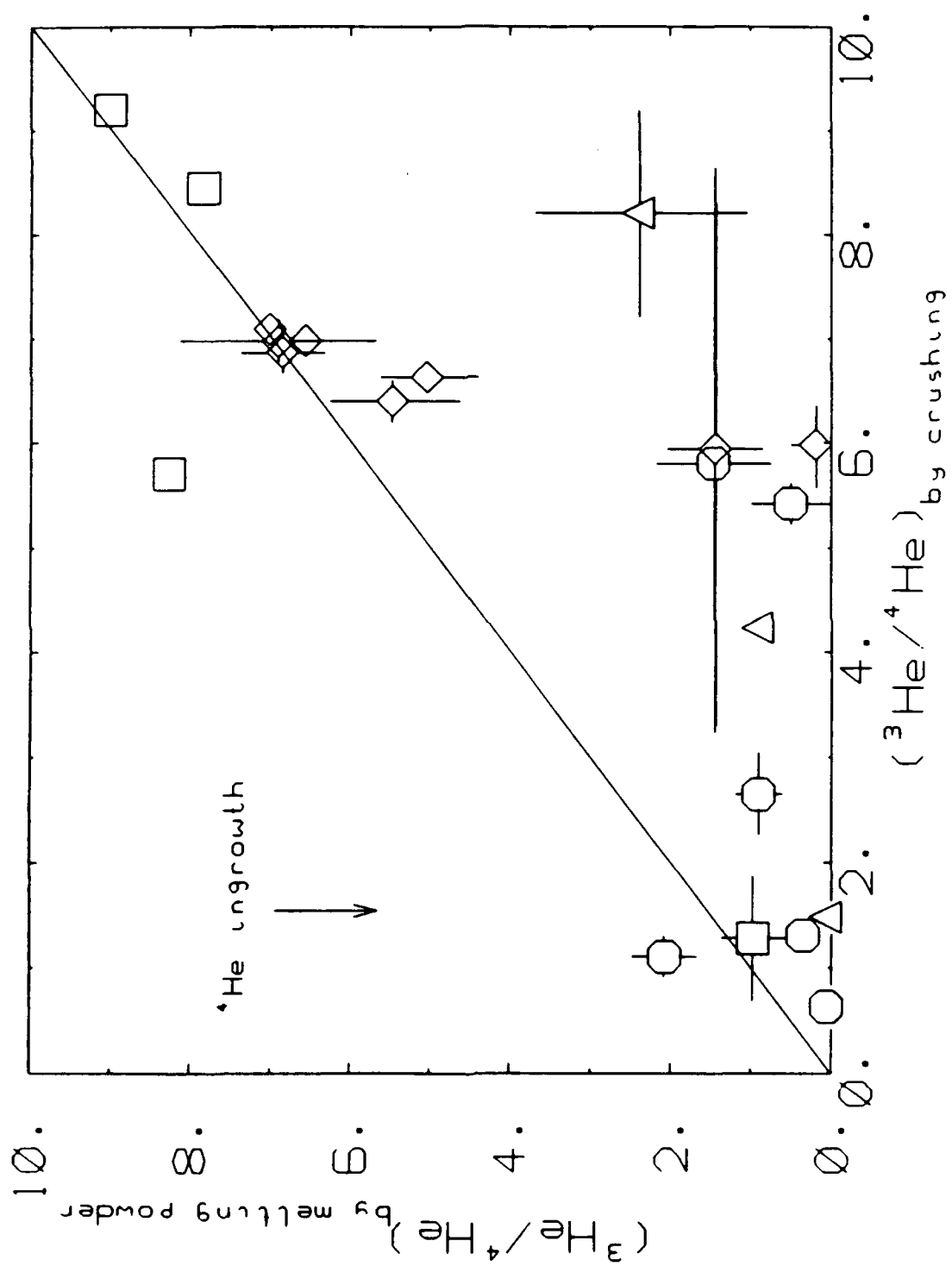
helium from the solid phase to the helium released by crushing will reduce the observed disequilibrium. This includes alpha-particle ejection, diffusive exchange on the seafloor, and any release of radiogenic He during crushing. Note that any retention of inherited He in the melted powder does not alter estimates of *He. Alternatively, *He can be estimated by assuming a value for R_i, for example the normal MORB value of 8.4 $\pm$ .3 R_a. The amounts of *He obtained by these two methods are listed in Table 6.1. For most samples they are not greatly different. Implicit in both calculations of *He is internal isotopic equilibrium at eruption. This has been well documented for MORB glasses (Kurz and Jenkins, 1981; Kurz et al, 1982) and appears reasonable for mineral separates (Kurz et al, 1983; this study).

Only a fraction of the radiogenic *He will be added to the gas-phase helium released by crushing because Th and U are in the solid phase. Thus, the ratio of *He to the amount of helium released by crushing, $[He]_c$, gives an indication of the likelihood of contamination by radiogenic helium. Figure 6.5 shows that some samples have very low *He/$[He]_c$ ratios and thus yield uncompromised estimates of the magmatic ^{3}He/^{4}He ratio (e.g. glass from WSC sample 26-11, clinopyroxene from Kavachi volcano sample 35-2). However, for many samples the calculated portion of *He is large in comparison to the quantity of helium released by crushing ($\log_{10} {}^*$He/$[He]_c$ order zero or greater). These samples may not yield reliable estimates of magmatic ^{3}He/^{4}He ratios, if any of the radiogenic helium has contaminated the reservoir of magmatic helium that is released by crushing. Many of these samples do exhibit low ^{3}He/^{4}He ratios on crushing (figure 6.5).

Proving that the low ^{3}He/^{4}He ratios observed on crushing are the result of actual transfer of radiogenic helium is difficult. Recent study of disequilibrium within alkali basalt glasses (Graham et al, 1987) suggests that transfer did not occur in these materials, because closely clustered ^{3}He/^{4}He ratios are found on crushing samples which contain large and widely varying amounts of radiogenic ^{4}He. Studies of in-situ cosmogenic ^{3}He generated in situ in phenocrysts by cosmic ray bombardment demonstrate that even with large quantities of cosmogenic ^{3}He present, none is released by crushing (Kurz, 1986a,b). Repeated

322

Figure 6.5 Comparison of the ^{3}He/^{4}He ratio measured by crushing versus the model quantity, $\log(^*\text{He}_1/[\text{He}]_{\text{Crushing}})$, for samples that exhibit significant isotopic disequilibrium. *He$_1$ represents the quantity of radiogenic ^{4}He required to produce the observed disequilibrium (in ccSTP/g see Table 6.1). Error bars are 1 sigma. Symbols denote tectonic regions as in figure 6.2. All samples are phenocrysts with the exceptions of glass from sample 26-11, which has the highest ^{3}He/^{4}He ratio plotted, and a glass and two glassy groundmass samples from the forearc and triple-junction respectively, which have the lowest ^{3}He/^{4}He ratios plotted.

Figure 6.5

Figure 6.5
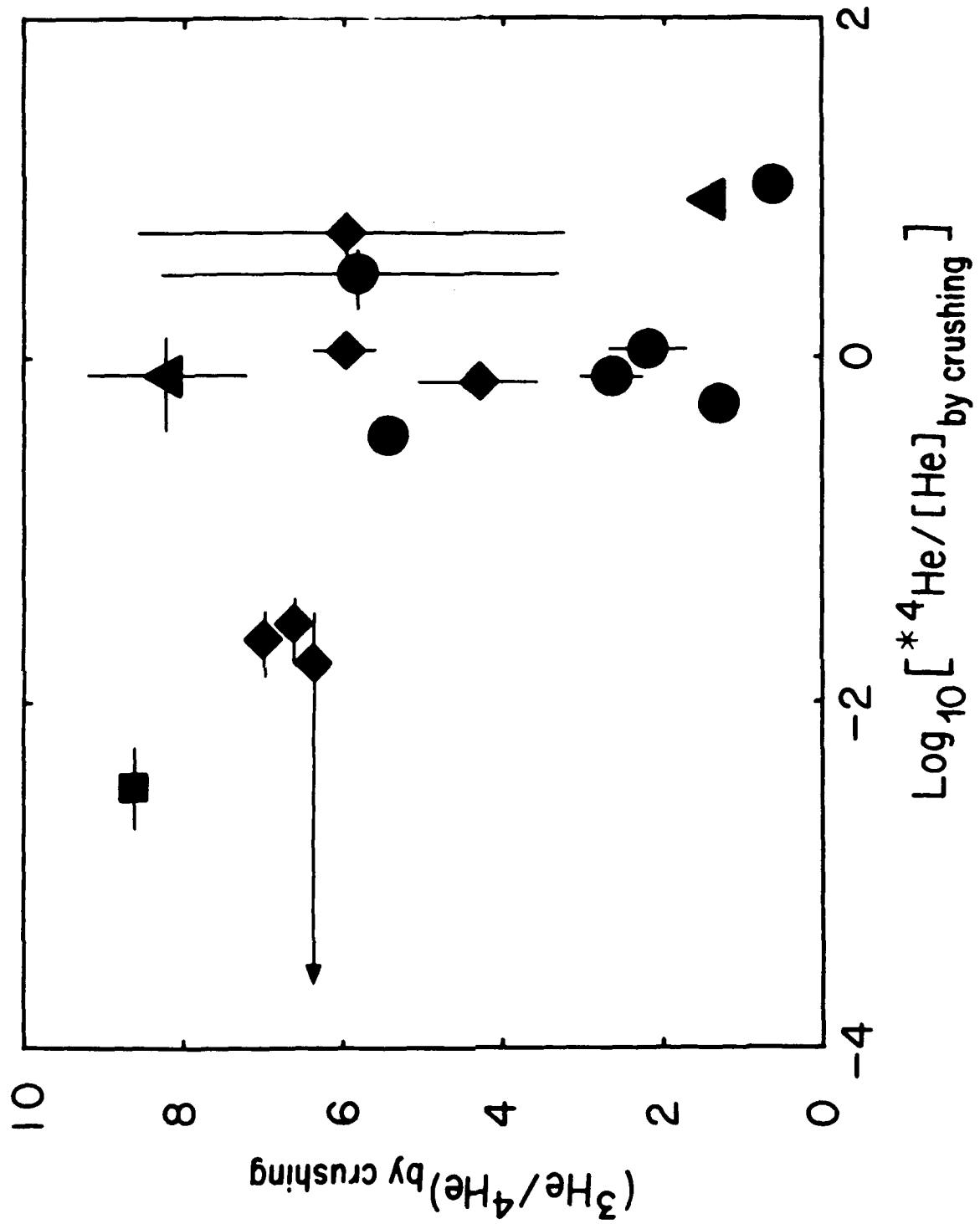
crushing of bronzite from sample 31-10 (Table 6.1) yielded indistinguishable isotopic compositions, suggesting limited release of radiogenic He during crushing (0 to at most 20%). The production of new surfaces by crushing can release at most 1-2% of any radiogenic helium present.

However, transfer of radiogenic helium may occur in mineral grains by alpha - particle ejection, because stopping ranges are tens of microns and uranium mainly resides in melt inclusions (Polve, 1985; and unpublished fission track maps of these samples) which are often closely associated with the helium containing fluid inclusions. For this reason, and the suggestive evidence in figure 6.5, we consider samples exhibiting high *He/[He]$_c$ ratios to be unreliable in determining magmatic helium isotopic compositions. This criterion also discredits any phenocryst samples which may have large amounts of radiogenic helium "shot in" from U and Th in the surrounding matrix.

In summary, radiogenic helium addition (revealed by internal isotopic disequilibrium) prevents the determination of magmatic ^{3}He/^{4}He ratios for many samples from the forearc and triple junction regions. In contrast, internal equilibrium for many Kavachi volcano samples (as well as identical helium isotope compositions obtained by crushing more than one mineral phase from the same sample, Table 6.1) strongly suggests that the observed helium isotopic compositions are those of Kavachi magmas at eruption. No single mineral phase emerged as most commonly free of contamination by radiogenic He. However, clinopyroxenes consistently release the most helium on crushing (figure 6.3), making them a good choice for analysis. Groundmass samples consistently exhibited lower ^{3}He/^{4}He when crushed (and larger radiogenic helium contents) than did mineral separates from the same sample, confirming their likely contamination (Table 6.1; samples 24-4, 31-1, and 31-10).

Comparison of calculated radiogenic helium contents with production rates by uranium and thorium decay suggests that samples from the triple-junction region, forearc, Kavachi submarine volcano, and the Woodlark Spreading Center are on the order of 10^4 to 10^5 years old (figure 6.6). These ages appear reasonable within the geologic setting,

Figure 6.6 The amount of He added by radiodecay is shown for different uranium contents (in ppm) as a function of time (solid lines), assuming a Th/U ratio of 3.0, and secular equilibrium. Samples are plotted based on their calculated radiogenic ^{4}He content (*He$_1$ in Table 6.1), and an estimate of their uranium content. The age estimate error bar corresponds to 1 sigma in the *He content, but does not include the error in estimating uranium contents. The uranium estimates were derived from whole rock U analyses for the sample or a similar rock (Johnson et al, 1987) and, for the phenocrysts, a bulk partitioning coefficient derived from examination of induced-fission-track maps of uranium distributions made from thin-sections of the sample or a similar rock. This estimate is very uncertain because the track studies were performed on whole rocks rather than on splits of the mineral separates used for helium analyses. However, the track maps did uniformly suggest that phenocryst contents of uranium are fairly high, and derive from included melt fractions of generally a few percent (Trull, unpublished results; see also Polve, 1985). Another complication in deriving an age estimate from the amount of radiogenic helium observed in a sample is the injection of *He from the surrounding rock matrix. For a spherical phenocryst .5mm in diameter this injection contributes *He equivalent to an internal uranium concentration of 10% of that of the whole rock (for a 1mm crystal the contribution drops to a little less than 5%). Similarly, even small amounts of adhering basaltic matrix will increase the apparent disequilibium, and therefore the age estimate. These effects were considered in estimating the rather high effective uranium contents used to plot the points in the figure. For example, the Kavachi sample with the greatest *He content (olivine from 34-7) is plotted at relatively high U contents because it was composed of small crystals with some adhering basalt matrix. Because of the uncertainties in both uranium contents and the calculation of *He the ages should be considered only as an order of magnitude estimate. Symbols: WSC glass sample (square), forearc minerals (triangles), triple junction minerals (octagon), Kavachi submarine volcano minerals (diamonds).

Figure 6.6
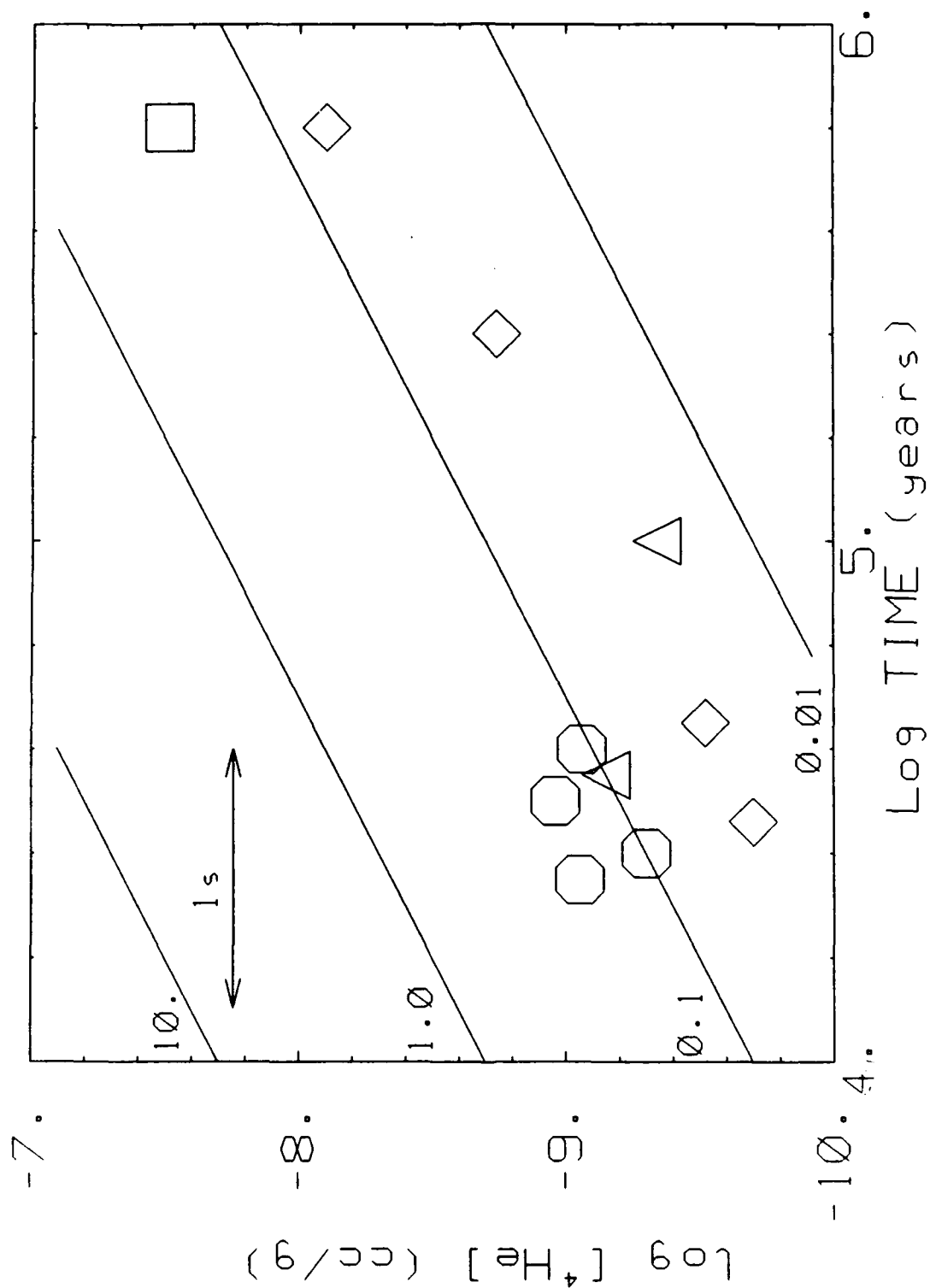
given the large uncertainties. The apparent ages of different samples from Kavachi overlap and are probably not distinguishable. However, they do suggest that these dredged rocks are at least tens of thousands of years old, despite their unaltered appearance and the recent eruptive activity of Kavachi. Further refinement of these age estimates, and the use of internal helium isotopic disequilibrium in minerals as a geochronometer in general, is difficult and would require careful documentation of crystal grain sizes and the internal distributions of uranium contents.

Another potential contamination problem is diffusion of atmospheric He into vesicles and glass of submarine basalts (Diffusion into mineral separates proceeds so slowly that radiogenic contamination is a greater problem). We evaluated this problem by comparison of a sample's helium content with that predicted by equilibrium with helium in seawater (figure 6.7). Samples with helium concentrations similar or smaller than the equilibrium model were considered potentially contaminated and unreliable in determining the magmatic isotopic ratio. Samples with concentrations greater than the equilibrium model are susceptible only to helium loss or isotopic exchange. Gas loss may also alter the erupted isotopic ratio if one isotope is lost preferentially. However, large fractional gas loss is required, and timescales are much longer than for He addition because the diffusive fractionation (W ^{3}He/^{4}He Z 1.08) is much smaller than the isotopic effect of adding helium with atmospheric composition (W ^{3}He/^{4}He Z 6-8). All glasses judged potentially contaminated by the seawater equilibrium model do exhibit low ^{3}He/^{4}He ratios, very near atmospheric compositions for analyses by crushing, and atmospheric or lower for fusion analyses. Furthermore, all samples judged uncontaminated by this model have ^{3}He/^{4}He ratios much different than seawater (most are 8.4 R_a or greater). Thus, the model appears to be a good indicator of the likelihood of diffusive contamination of helium isotopic compositions in submarine glasses, but we emphasize that it does not represent a definitive test.

Diffusive contamination may also explain the unusual isotopic composition of NaTi basalt glass sample 32-9. This was the only sample to exhibit a higher ratio when the powder was melted than on crushing

Figure 6.7 Comparison of observed helium concentrations with expected values for equilibrium with seawater. The curves model concentration equilibrium of helium dissolved in seawater with helium in basaltic glass (G-SW, at left) and vesicles (G-V, at right). The model assumes that helium behaves ideally in the vesicle gas, and that the Henry's law coefficients for glass - vesicle partitioning during eruption (Kurz and Jenkins, 1981) and seawater - atmosphere equilibration apply during diffusive reequilibration on the seafloor. Samples are plotted according to their measured helium concentrations by crushing and powder melting. Symbol shapes denote tectonic regions or rock types: WSC (squares), triple-junction region (octagons), Kavachi submarine volcano (diamonds), forearc (triangles), NaTi basalt glasses (crosses). Filled symbols are samples with ^{3}He/^{4}He ratios significantly greater than 1 R_a, open symbols are samples with ratios near 1 R_a or less, the half-filled symbol (sample 32-9) may be partially contaminated, see text.

Figure 6.7
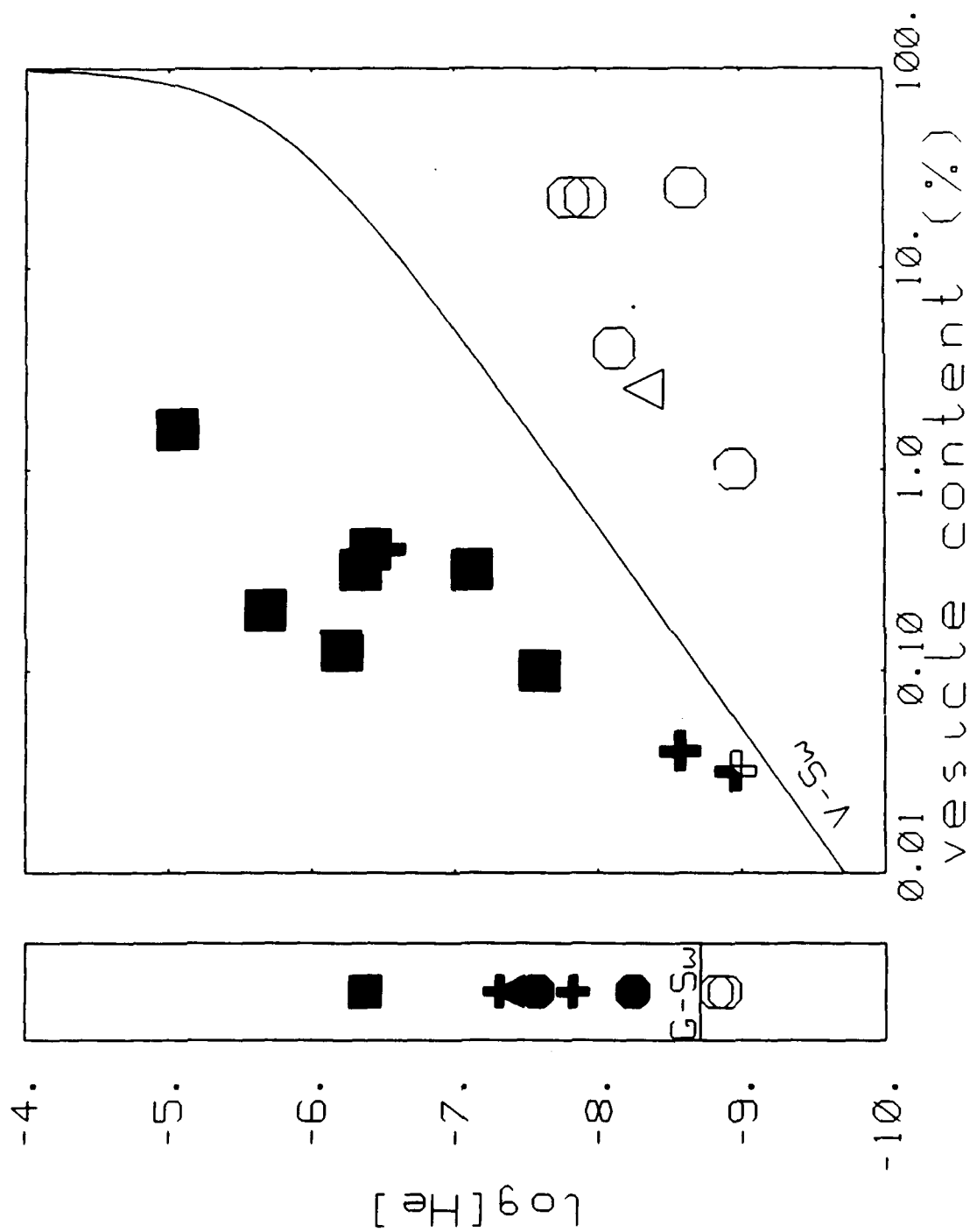
Figure 6.7

(figure 6.4). The amount of helium released by crushing was very small and close to the seawater equilibrium curve for the sample's vesicle content (figure 6.7), suggesting possible contamination. Step-heating of the powder released helium of three distinct isotopic compositions (figure 6.8). A small amount of helium released at high temperature has a ^{3}He/^{4}He ratio higher than (but within 2 sigma) of the isotopic compositions of other NaTi samples and may be released from microphenocrysts of pyroxene within the glass. Intermediate temperatures released most of the helium with an isotopic composition like that released by bulk melting. At low temperature the helium isotopic composition is similar to that obtained by crushing: both methods probably release helium from spherulitic zones (visible in thin section) that have been contaminated by helium from seawater. Diffusive contamination by helium in this situation appears to be much rapider than alteration because Sr and oxygen isotope compositions were not affected.

The rate of addition of helium to glasses and vesicles by diffusion is highly dependent on grain geometry and the size and distribution of vesicles. Applying a membrane diffusion model parameterized to represent glasses with abundant (10%), large (1mm), thin-walled (100um) vesicles, suggests an influx of helium to vesicles on the order of 10^{-8} cc/g per million years. This estimate assumes equilibrium with seawater at the external boundary, as defined by [He] = K_H x P^{SW}_{He}, where K_H is the Henry's law coefficient derived from vesicle – glass partitioning in MORB (Kurz and Jenkins, 1981), and a diffussion coefficient of 10^{-15} cm^2/s (Jambon, Weber and Begemann, 1985; Trull, 1988). The model is probably an upper limit based on the small membrane thickness, the high vesicularity, and the assumption of no helium in the vesicle even as diffusive contamination proceeds, and because lower estimates of the helium diffusivity have been made (Kurz and Jenkins, 1981). At this rate, diffusive contamination of the samples with low ratios in figure 6.7 requires 10^5 to 10^6 years.

Figure 6.8 Histograms show the amounts and isotopic compositions of helium released by crushing and melting (a.), and step-heating experiments (b.) for spherulitic glass sample 32-9. One sigma errors are given. See discussion in text.

Figure 6.8
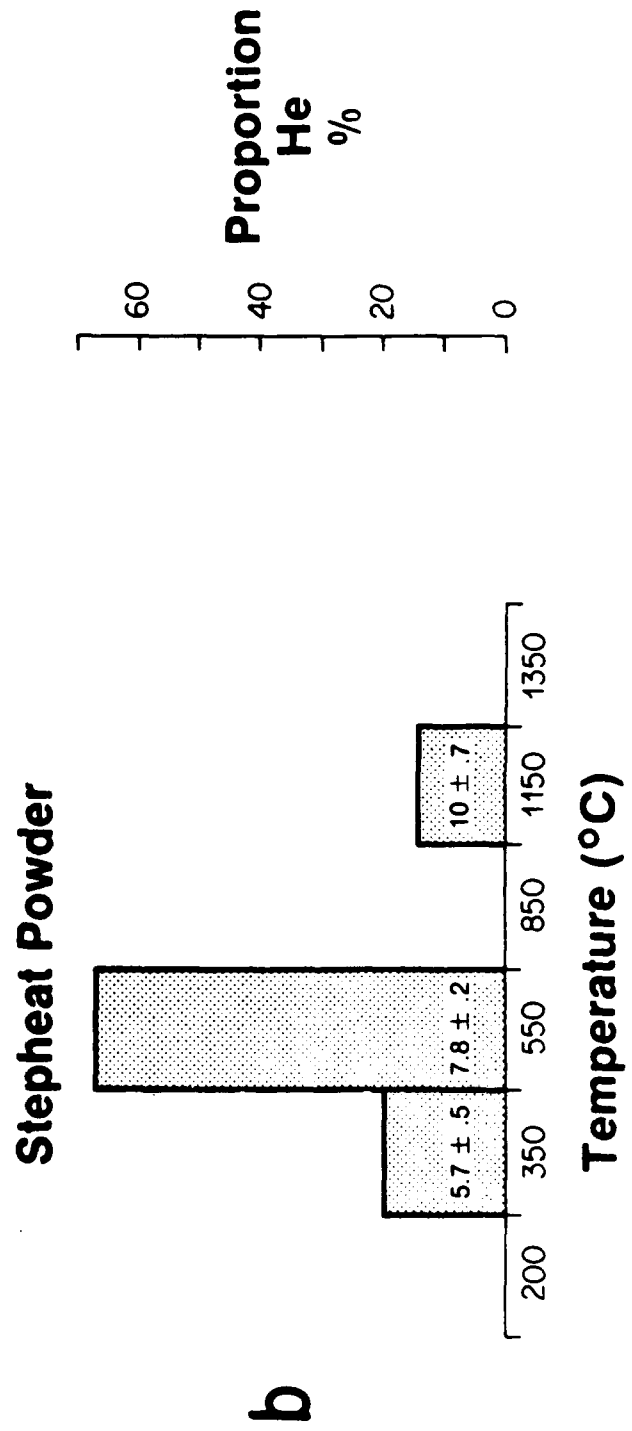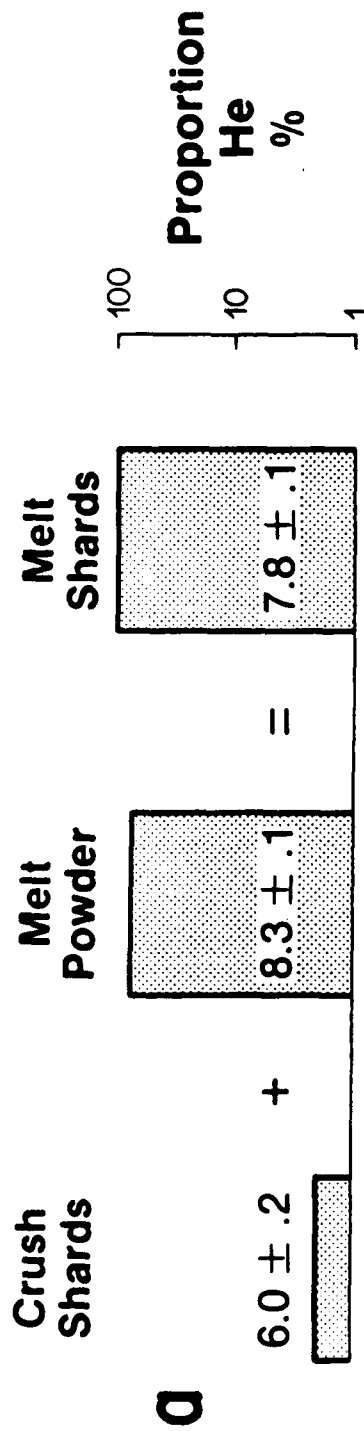
b) Summary of the origins of He isotopic variabilty.

Combined analyses by crushing and melting revealed that a large portion of the overall helium isotopic variability is produced by post-eruptive processes. Moreover, we have derived criteria to conservatively identify samples contaminated in this fashion, which may be applied generally in the study of helium isotopic variability in island arcs and other terrains where sample ages are uncertain and helium concentrations are low. These include the assessment of radiogenic and diffusive helium addition through concentration and internal disequilibrium systematics (as well as cautions on the generally unreliable nature of groundmass samples). The results are summarized in figure 6.9, in which symbols distinguish compromised samples from those that reliably reveal magmatic $^3He/^4He$ ratios. Many samples with low $^3He/^4He$ ratios do not represent magmatic values. In particular, groundmass samples, glasses with low He concentrations, and many phenocrysts are contaminated by diffusive helium loss and radiogenic helium addition. Unfortunately, most of the samples from the forearc and triple junction area are compromised, and none of the "boninite" samples can be assumed to be contamination free, so the role of slab-derived fluids in generating this rock type cannot be addressed. In this context, it is important to note that previous boninite analyses, which revealed low $^3He/^4He$ ratios, (Poreda, 1983) may not represent magmatic ratios, because groundmass samples were used, and radiogenic ^4He was not accounted for. This figure also displays the smooth spatial variations in Sr isotopic and Sr/Zr elemental ratios in the Woodlark Basin – Solomon Islands region.

Almost all of the WSC samples were confirmed to display magmatic $^3He/^4He$ ratios. As mentioned above, WSC samples are erupted with similar He isotopic compositions to mid-ocean-ridge basalts, including one sample with slight chemical enrichments similar to basalts from back-arc basins, and the unusual NaTi basalts of dredge 32. This suggests that the upper mantle materials which supply the spreading center are very similar to those beneath open ocean spreading ridges, despite the small size of the Woodlark Basin and its location amidst arc and continental terrains.

While some samples from Kavachi Volcano have been compromised by radiogenic He addition, the magmatic $^3He/^4He$ ratio can be recovered for most samples, and is uniform at 6.9 $\pm$ .2 R_a. This is significantly lower than $^3He/^4He$ ratios observed in normal MORB and in the basalts from the nearby WSC, although it is within the total range observed in MORB (Kurz, 1982; Kurz et al, 1982). This result is free of the ambiguity associated with hot spring and fumarole samples. That is, the observation of lowered $^3He/^4He$ ratios in arcs can be confidently attributed to the magmas themselves, rather than processes affecting the exsolved gases.

It is important to note that the WSC data are derived from glass analyses, while the Kavachi analyses were on mineral separates. While isotopic exchange between crystals and liquid is rapid (decades), closure temperatures for phenocrysts may be below the solidus if magma cooling is slow, allowing helium loss from phenocrysts and perhaps isotopic fractionation to occur (Hart, 1984). For arc rocks, which often show signs of multiple magmatic episodes (in general: Gill, 1981; for Kavachi rocks: Johnson et al, 1987) it is necessary to assess whether long residence at elevated temperatures contributes to the lower $^3He/^4He$ ratios observed in Kavachi phenocrysts. Two simple tests can be used to assess the relevance of this process. If it were significant, mineral separates should exhibit positive correlations between $^3He/^4He$ ratios and grain sizes, since smaller crystals will have lost more helium. Similarly, pyroxenes should be more affected than olivine, since He diffusion in pyroxene is roughly 100 times faster at magmatic temperatures (Gramlich and Naughton, 1972; Trull, 1988). Our data for olivine/pyroxene pairs display isotopic equilibrium and are therefore not consistent with helium loss by this process. Lowering the $^3He/^4He$ ratio of 1mm spherical olivine grains from 8.4 to 6.9 R_a in this manner would yield a ratio of less than 5 R_a in pyroxenes grains of similar size, for a $^3He/^4He$ isotopic diffusivity ratio of 1.08 in both olivine and pyroxene (Trull, 1988), but the result is not highly sensitive to the choice of isotopic diffusivity ratio, and the classical approximation of 1.15 (the inverse ratio of the square roots of the atomic masses) predicts a similar result. We did not systematically

investigate correlations with grain size, but Kavachi mineral separates ranging from .4 to 1 mm in grain size yielded indistinguishable $^3He/^4He$ ratios. While this process does not appear important here, it deserves more study, and in some cases, such as the study of xenoliths, could perhaps be used to constrain cooling histories (compare Gramlich and Naughton, 1972).

6.3.2 Strontium Isotopic Variability.

The rocks recovered from the Woodlark Basin - Solomon Islands region can be divided into three groups based on their $^{87}Sr/^{86}Sr$ values: MORB with ratios from 0.702580 to 0.702910, island arc lavas with ratios from 0.703468 to 0.704038 (ratios up to .705186 have been measured, Perfit et al, in preparation, but are not reported here) and basaltic andesites with ratios between 0.7031 and 0.7034 and transitional chemical characteristics (Table 6.2 and unpublished data). Incompatible element depleted tholeiitic basalts (n-type MORB) from the WSC have low $^{87}Sr/^{86}Sr$ ratios and Sr concentrations typical of MORB from the major oceanic ridges. A few samples with back-arc-basin-basalt (BABB) chemical characteristics have slightly higher Sr contents and $^{87}Sr/^{86}Sr$ ratios (greater than 0.7027) that could not be lowered by acid leaching. The unusual NaTi basalts have high Sr contents (. 230ppm) but Rb/Sr and $^{87}Sr/^{86}Sr$ ratios typical of MORB (less than 0.7030; Table 6.2 and Staudigel et al, 1987).

Island arc basalts and related lavas from the forearc region, Kana Keoki seamount, and Kavachi submarine volcano exhibit the greatest Sr isotopic variability and have the highest Sr contents. These values (Table 6.2) are typical of a wide variety of island arc volcanic rocks from the western Melanesian arcs (DePaolo and Johnson, 1979; Perfit et al, 1982; Gill, 1984; Johnson et al, 1985). The highest isotopic ratios (approximately 0.7045) tend to be in the most alkalic and large-ion-lithophile-(LIL)-enriched rocks resulting in positive correlations between $^{87}Sr/^{86}Sr$ ratios and LIL abundances. The Sr isotopic heterogeneity of the samples is not unusual for arcs and corresponds to that measured in lavas from the Solomon Islands (0.70352 - 0.70417;

Table 2. Sr-isotope and trace element data

Sample[1]	Rock Type[2]	$^{87}Sr/^{86}Sr$	±2σ	Sr ppm	Zr ppm
26-5	MORB	0.702580	20	120	100
26-11	MORB	0.702600	20	–	–
29-A	MORB	0.702657	18	–	–
29-B	MORB	0.702910	16	154	115
29-C	MORB	0.702686	20	–	–
29-H	BABB	0.702826	20	142	100
30-5	Basaltic andesite	0.703281	16	199	87
30-6	Basaltic andesite	0.703134[3]	24	191	73
31-1	High-Mg andesite	0.703503	20	486	54
31-13	High-Mg andesite	0.703468	18	580	64
31-10	High-SiO$_2$ andesite	0.703493	22	468	50
32-8	NaTi basalt	0.702660	18	–	–
32-9	NaTi basalt	0.702666	14	243	247
32-10	NaTi basalt	0.702707	20	243	219
32-16[4]	Basaltic andesite	0.703317	20	221[5]	43
32-16[4]	Basaltic andesite	0.703311	14	217	43
33-B	Dacite	0.704038	16	371	82
34-1	Quartz tholeiite	0.703518	20	402	–
34-7	Quartz tholeiite	0.703699	24	323	–
34-8	Quartz tholeiite	0.703738	18	342	40
34-9	Quartz tholeiite	0.703728	16	342	40
35-2	Low-SiO$_2$ andesite	0.703724	9	732	54
35-6	Quartz tholeiite	0.703710	9	850	42
KK4-sed 3	sediment	0.706513	16	732	54
KK4-sed 4	sediment	0.708190	20	850	42
24-4	Trachy-basalt	0.703687	16	590	100
24-12	Low-SiO$_2$ andesite	0.703916	20	491	41

[1] All samples have a KK4- prefix, the first # is the dredge#.
[2] Sample descriptions from Johnson et al (1987).
[3] From Staudigel et al (1987).
[4] Duplicate run from separate sample splits.
[5] Measured by isotope dilution; all others by XRF or DCP (see Johnson et al, 1987, Perfit et al, 1987).
– Not determined.

Staudigel et al, 1987; Perfit et al, in preparation). In this study the highest $^{87}Sr/^{86}Sr$ ratio was measured in a glassy, LIL-enriched dacite from Kana Keoki seamount in the complex triple-junction area.

The $^{87}Sr/^{86}Sr$ values of low-K basaltic andesites from the Simbo-Ghizo Ridge in the triple junction region are intermediate between those of MORB from the WSC and island-arc-basalts (IAB) from Kavachi. This is in striking agreement with the chemical characteristics of these lavas, which are transitional between MORB and island arc tholeiites.

A few sediments from the Woodlark Basin have been analyzed and have Sr isotope ratios from 0.70651 to 0.70819 and relatively high Sr contents, greater than 400ppm, (Table 6.2 and unpublished data). Additionally, Staudigel et al (1987) found that highly altered basaltic rocks from the northern Woodlark Basin, close to the subduction zone, have relatively high $^{87}Sr/^{86}Sr$ values (approximately 0.7051) and low Sr contents.

Fairly systematic variations in $^{87}Sr/^{86}Sr$ ratios, Sr concentrations, and incompatible element ratios such as Sr/Zr and Ba/La occur with distance from the trench (Perfit et al, 1987; Staudigel et al, 1987). Increasing $^{87}Sr/^{86}Sr$ correlates with decreasing $^{3}He/^{4}He$ and both correspond to the increasing arc-like character of magmas erupted near the trench (figure 6.9). Arc lavas contain relatively high concentrations of Sr, however the absolute amounts are largely controlled by the extents of plagioclase-dominated crystal fractionation that occured prior to eruption (Perfit, in preparation).

6.4 DISCUSSION

6.4.1 Magma degassing and chamber residence times.

What is the significance of the lower $^{3}He/^{4}He$ and higher $^{87}Sr/^{86}Sr$ ratios observed in the IAB erupted in the Solomon Island arc as compared to the basalts in the WSC? The difference may arise either from source characteristics or from processes that occur during magma transport and eruption. In the latter case, the helium isotopic composition difference may reflect the different degassing processes between arc and

Figure 6.9 ^{3}He/^{4}He (by crushing), ^{87}Sr/^{86}Sr, and Sr/Zr versus distance from the trench. Dredge numbers are shown at the top of the figure. To the left are forearc dredges, and to the right the dredges from further west in the Woodlark Basin. Filled symbols represent samples for which the observed ^{3}He/^{4}He ratio represents the isotopic composition of the erupted magma. Open triangles indicate that the observed ^{3}He/^{4}He ratios are considered suspect because of the presence of significant radiogenic He. Crosses indicate samples that are probably contaminated by helium from seawater. Asterixes mark groundmass samples. Error bars are shown only for filled symbols.

Figure 6.9
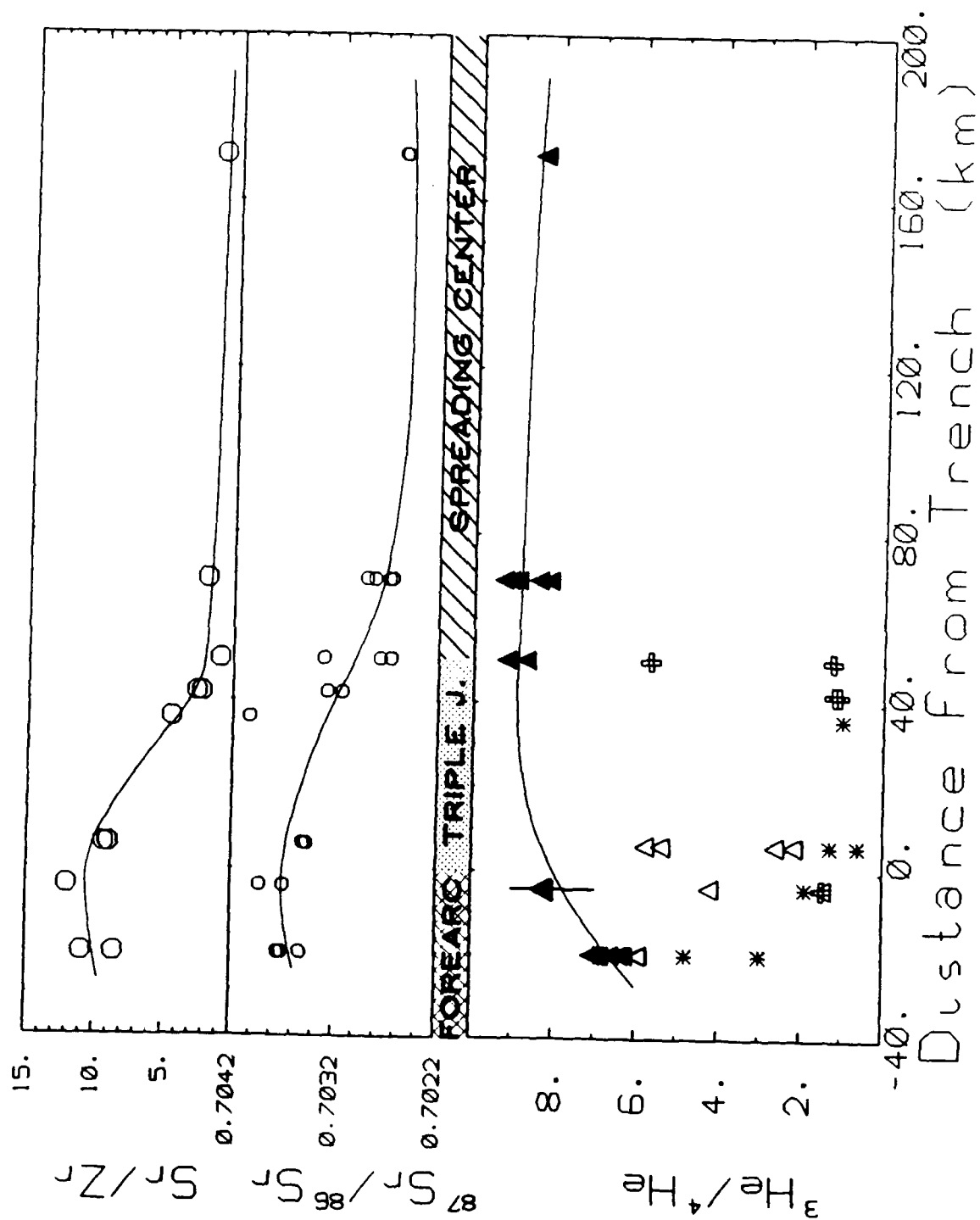
spreading ridge environments. Degassing may lead to lowered ^{3}He/^{4}He ratios in two ways. First, if He is lost by diffusion, mass fractionation may occur. Limits on this effect can be obtained from a Rayleigh fractionation model (e.g. Kaneoka, 1980; Condomines et al, 1983). Isotopic diffusion rates have been demonstrated to be roughly inversely proportional to the square root of the isotopic masses for neon (Frank, Swets, and Lee, 1961; Rama and Hart, 1965) and helium in silica glasses (Shelby, 1971). This 15% difference for ^{3}He vs. ^{4}He diffusion is probably a maximum for basaltic magma (Trull, 1988). Using this model, 90% helium loss is required to reduce a magma's initial ratio by 25% (Hart, 1984). This corresponds to reduction of a parental magma composition of 9.2 R_a, the high value in WSC basalts, to 6.9 R_a, the Kavachi Volcano average.

How long would this take? Lux (1987) has measured the diffusion coefficient for helium in tholeitic melt at 1350 ^{0}C to be 5 x 10^{-5} cm^2/s, in good agreement with extrapolation of glass data measured at lower temperatures (Kurz and Jenkins, 1981). Combining this diffusion coefficient with the diffusive loss equation for spherical bodies (Crank, 1975) yields estimates of longer than 150,000 years for a 1 km diameter magma body, or 50,000 years for a .5 km body, to achieve such large helium losses. Other magma geometries or magma convection will reduce these times, however boundary processes, such as helium loss to surrounding rock, may be rate limiting. Exhalative degassing and/or magma solidification probably occur on much shorter timescales. Phase separation of CO_2 or H_2O fractionates helium isotopes only minimally, if at all, at least in MORB magmas where isotopic equilibrium is observed between helium in vesicles and dissolved in glass (Kurz and Jenkins, 1981).

The second effect of degassing is increased U,Th/He elemental ratios, allowing radiogenic helium to lower a magma's ^{3}He/^{4}He ratio over relatively "short" times (Condomines et al, 1983; Zindler and Hart, 1986). Using the helium content of Kavachi phenocrysts (1 x 10^{-8} cc/g) and measured whole rock uranium contents (0.08 ppm, Johnson et al, 1987) as representative of magmatic concentrations to calculate radiogenic helium production suggests that greater than 10^5 years are required to

lower a parental magmatic ^{3}He/^{4}He ratio from 9.2 R_a to 6.9 R_a. Since glass/phenocryst partition coefficients for He are much less than 1 (Hiyagon and Ozima, 1986; Kurz, 1982), this is undoubtably a minimum estimate.

In summary, if lower ^{3}He/^{4}He ratios in island arc magmas reflect differing degassing processes in arcs as compared to spreading ridge environments, then magma residence timescales must be quite long (approximately 10^5yrs). Thermal models show that such long times require low temperature contrasts, as might characterize magma chambers at mantle depths or replenished chambers (compare Zindler and Hart, 1986; Graham et al, 1987; Usselman and Hodge, 1978). It is possible that these processes could lead to temporal trends in the helium isotopic compositions of Kavachi lavas in the future. Changes in ^{3}He/^{4}He ratios with time have been observed at single volcanos in Hawaii, and appear to be related to plate motion across a mantle plume (Kurz et al, 1983).

6.4.2 Sources of radiogenic Sr and He to Woodlark Basin - Solomon Islands magmas.

Addition of ^{4}He to arc magmas or their source regions could also be responsible for the lower ^{3}He/^{4}He ratios observed in many arc gas samples and most clearly in the rock samples from Kavachi volcano. Possible radiogenic helium sources include subducted materials (seawater, sediments, oceanic crust and lithosphere) as well as older arc basement rocks. The helium content of these materials is poorly known, but is essentially governed by age, uranium and thorium content, and the extent of radiogenic helium retention (Kurz, 1982).

We have investigated the role of these potential radiogenic He sources in the petrogenesis of Kavachi volcano lavas through ^{3}He/^{4}He - ^{87}Sr/^{86}Sr systematics. The correlation observed between increasing ^{87}Sr/^{86}Sr and LIL elemental abundances in rocks from the Solomon islands and the Woodlark Basin suggests mixing between long-term depleted mantle sources like those beneath the Woodlark Basin and some LIL enriched source or contaminant. This hypothesis is further supported by good

correlation between Sr, Nd, and Pb isotopic compositions (Staudigel et al, 1987; Perfit et al, in preparation). However, the nature of this enriched component is most problematical and elusive to determine. Petrogenetic mixing calculations (see Staudigel et al, 1987) point out the difficulties in producing the observed isotope and elemental ratios by simple binary mixing of a MORB source with sediments. These results indicate that although minor amounts of sediment involvement are possible, multiple components and more complex processes (e.g. metasomatism) must be involved in island arc magmagenesis.

If the Kavachi magmas are produced by mixing of WSC type source materials with a more radiogenic "contaminant", then their He–Sr compositions should lie along mixing lines between these isotopic endmembers. Figure 6.10 shows that such an origin requires that the contaminant have a lower He/Sr elemental ratio (R less than 1)than the WSC endmember, at least for closed system mixing with materials such as evolved arc rocks or altered oceanic crust of 10 to 100 Ma age. Melts, fluids, and solid materials from old oceanic crust probably all fulfill this requirement because of the comparatively high He contents of the WSC rocks and their MORB-type source. It is difficult to compare these possible contaminants more quantitatively without experimental study of fluids and melts of altered crust for He and Sr contents. This would be in keeping with contamination in the form of solids or melts, but perhaps not by C-O-H fluids which might have relatively high He/Sr ratios. Also shown are mixing lines (R = 1) for contamination by seawater or an average sediment composition. Contamination by seawater or sediments is unlikely because this would require large contributions that are not consistent with other trace element and isotopic compositions (Perfit et al, 1987; Staudigel et al, 1987).

For any of the endmembers, mixing requires that large fractions of the Sr be contributed by the contaminant. This suggests that contamination probably occurs in the source region, where addition of small amounts of a melt or fluid derived from subducted materials can produce large changes in incompatible element compositions of subsequently derived magmas, rather than by contamination of magmas at crustal depths, which would require much larger bulk contamination.

Figure 6.10 ^{3}He/^{4}He versus ^{87}Sr/^{86}Sr for Woodlark Basin samples. Only those samples for which magmatic ^{3}He/^{4}He ratios were reliably determined are shown. Fields for normal and enriched MORB are from Kurz, Jenkins, and Hart (1982). Two component mixing curves are shown between WSC basalts (^{87}Sr/^{86}Sr = .7027, ^{3}He/^{4}He = 8.8) and young arc rocks (YAR: ^{87}Sr/^{86}Sr = .7045, ^{3}He/^{4}He = 3 R$_a$). R values on these curves represent the ratio (He/Sr)^{YAR}/(He/Sr)^{WSC}. Tick marks represent the fraction of Sr contributed to the mix by the 'contaminant'. Other possible contaminants are marked: OAR = old arc rocks, YOC = young oceanic crust, OOC = old oceanic crust. Also shown are R=1 mixing lines between WSC and seawater and sediments (^{87}Sr/^{86}Sr = .7065, ^{3}He/^{4}He = 3.0). Symbols: open circles - WSC, (dredges 26, 29 and NaTi basalts from dredge 32), filled squares - Kavachi volcano (dredges 34 and 35), open triangle - forearc sample 24-4.

Figure 6.10

345
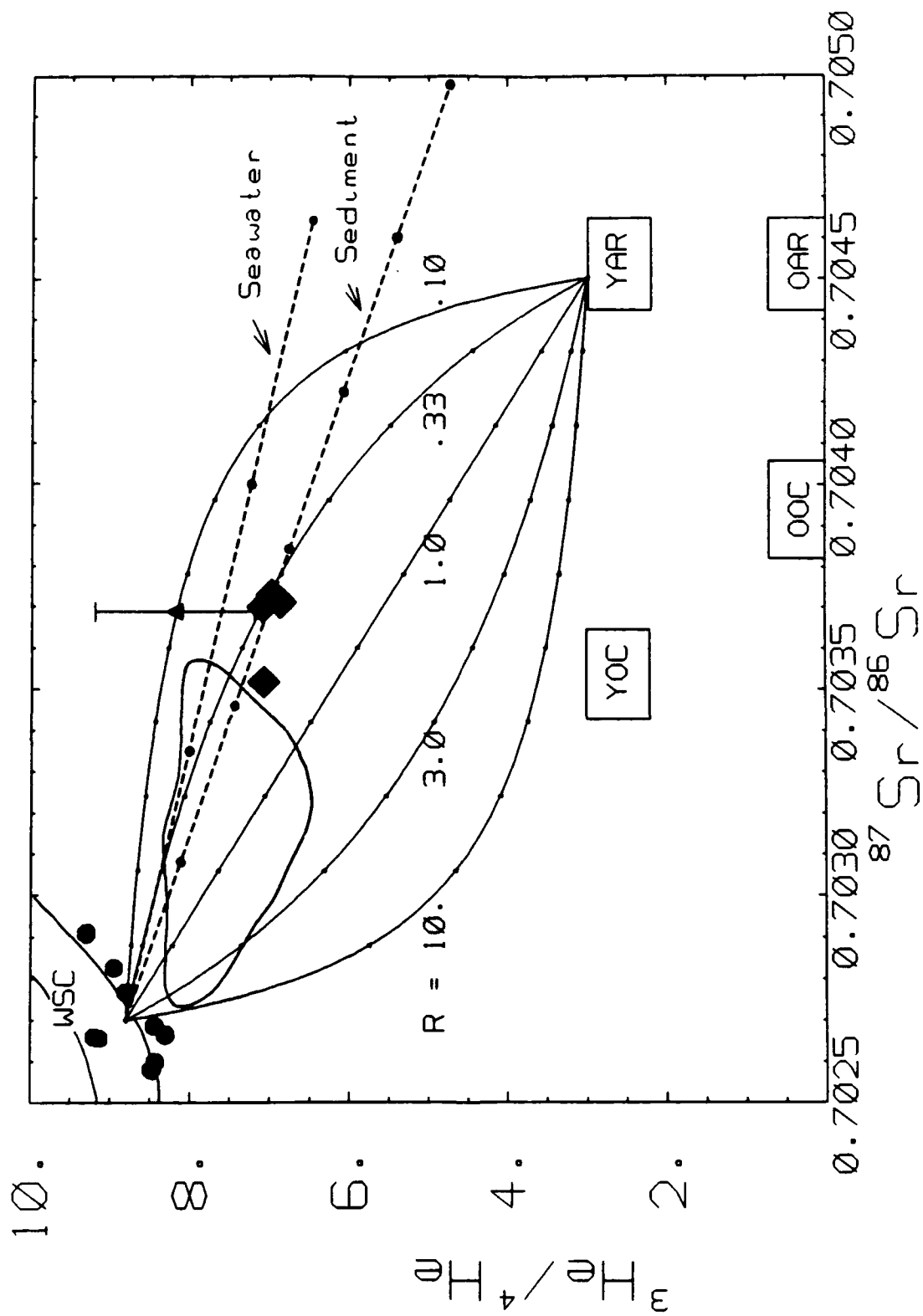
This conclusion is in keeping with oxygen isotope compositions which range from +5.7 to +6.3 per mil in the transistional and arc rocks (Perfit, unpublished data), indicating minimal assimilation of crustal rock or sediments. The mixing curves are relatively insensitive to variation in the $^3He/^4He$ ratio of the radiogenic endmember, and thus do not discriminate between young (10Ma, R/Ra=3) and old (100Ma, R/Ra=.2) subducted lithosphere as likely contaminants. However, contamination of the source region by older, more altered, sediment rich lithosphere, such as was probably subducted from the east in the past, can account for the radiogenic nature of Kavachi magmas through much smaller contributions than can the younger, less altered, sediment poor WSC lithosphere.

In summary, the He-Sr data demonstrate that upwelling of depleted upper mantle beneath the WSC does not extend unimpeded as the spreading center is subducted beneath the Solomon Islands forearc. Rocks erupted at Kavachi submarine volcano contain radiogenic helium and strontium, in contrast to basalts from the WSC. This difference can be explained by the presence of enriched materials beneath the arc that derive from subduction of oceanic crust altered by seawater and time. Ancient Pacific lithosphere is a more probable candidate than the Woodlark plate or assimilation of altered arc crust. Distinguishing the petrogenetic model of Abbot and Fisk (1986) from the "thermal trigger" hypothesis (Perfit et al, 1987; Staudigel et al, 1987) is difficult because many samples were contaminated by post-eruptive processes, preventing the comparison of similar rock types from different locations. However, the helium isotopic compositions of Kavachi volcano basalts, while distinctly different from WSC samples and normal MORB, are not predominantly radiogenic, as might be likely if crustally-derived fluids were directly involved in their generation. For example, magmatic $^3He/^4He$ ratios of approximately .1 (the production ratio) to 1 R_a (seawater) were not observed.

6.5 CONCLUSIONS

In conclusion, three points should be emphasized.

1. Extension of helium isotopic analyses to island arc environments requires careful examination of contamination processes. Groundmass samples and vesicular glasses with low helium contents are particularly susceptible to diffusive and radiogenic contamination, and phenocrysts cannot necessarily be relied upon to yield magmatic $^3He/^4He$ ratios without detailed study involving gas extraction by in vacuo crushing and melting.

2. The Woodlark Spreading Center erupts lavas with helium and strontium isotopic compositions typical of mid-ocean-ridges, despite its location in a region marked by extremely high returns of crustal materials to the mantle (Parsons, 1981). This suggests vigorous mantle convection, or that the WSC basalts derive from a mantle diapir originating at depths unaffected by these lithospheric inputs.

3. Island arc magmas, as represented by Kavachi submarine volcano samples, were confirmed to exhibit $^3He/^4He$ ratios significantly lower than most basalts from spreading centers and mid-ocean-ridges. This solidifies the results of island arc fumarole and hot-spring studies, and suggests that the radiogenic helium (and strontium) contributions derive from sub-crustal sources related to subduction. The He and Sr isotopic compositions, however, are not predominantly radiogenic and probably derive in large part from upper mantle materials similar to those beneath ocean ridges. Involvement of a fluid phase distinct from silicate melt in their formation may occur in the source region, but does not appear to be directly related to magmagenesis.

REFERENCES

ABBOT D. and FISK M. (1986) Tectonically controlled origin of three
    unusual rock suites in the Woodlark Basin. Tectonics 5, 1145-1160.

CAMERON W. E., McCULLOCH M. T. and WALKER D. A. (1983) Boninite
    petrogenesis: chemical and Nd-Sr isotopic constraints. Earth
    Planet. Sci. Lett. 65, 75-89.

CONDOMINES M., GRNVOLD K., HOOKER P. J., MUEHLENBACK K., O'NIONS R. K.,
    O'SKARSON N. and OXBURGH E. R. (1983) Helium, oxygen, strontium
    and neodymium isotopic relationships in Icelandic volcanics. Earth
    Planet. Sci. Lett. 66, 125-136.

COOPER P. A. and TAYLOR B. (1985) Polarity reversal in the Solomon
    Islands arc. Nature 314, 428-430.

COX K. G. and BELL J. D. (1972) A crystal fractionation model for the
    basaltic rocks of the New Georgia Group, British Solomon Islands.
    Contrib. Mineral.Petrol. 37, 1-13.

CRAIG H., LUPTON J. W. and HORIBE Y. (1978) A mantle helium component in
    circum-Pacific volcanic glasses: Hakone, Marianas, Mt. Lassen. In
    Advances in Planetary Sciences 3, Terrestrial Rare Gases (eds. E. C.
    ALEXANDER and M. OZIMA) pp. 3-16. Centre for Academic Publications,
    Japan Scientific Press, Tokyo,

CRANK J. (1975) The Mathematics of Diffusion, 2nd edition, Oxford Press.

DAVIDSON J. P. (1987) Crustal contamination versus subduction zone
    enrichment: Examples from the Lesser Antilles and implications for
    mantle source compositions of island arc rocks. Geochim. Cosmochim.
    Acta 51, 2185-2198.

DePAOLO D. and JOHNSON R. W. (1979) Magma genesis in the New Britain
    island-arc: constraints from Nd and Sr isotopes and trace element
    patterns. Contrib. Mineral. Petrol. 70, 367-379.

DUNKLEY P. N. (1984) Volcanism and evolution of the ensimatic Solomon
    Islands Arc. In Arc Volcanism: Physics and Tectonics, proceedings
    of a 1981 IAVCEI symposium, Tokyo and Hakone (eds. D. SHIMOZURU and
    I. YOKOYAMA) Advances in Earth and Planetary Sciences,
    TERRAPUB/REIDEL.

FLYNN R. T. and BURNHAM C. W. (1978) An experimental determination of rare earth partition coefficients between a chloride containing vapor phase and silicate melts. Geochim. Cosmochim. Acta 42, 685-702.

FRANK R. C., SWETS D. E. and LEE R. W. (1961) Diffusion of neon isotopes in fused quartz. J. Chem. Phys. 35, 1451-1459.

FUNKHOUSER J. G., FISHER D. E. and BONATTI E. (1968) Excess argon in deep sea rocks. Earth Planet. Sci. Lett. 5, 95-100.

GILL J. B. (1981) Orogenic Andesites and Plate Tectonics, Minerals and Rocks series #16, Springer Verlag.

GILL J. B. (1984) Sr-Pb-Nd isotopic evidence that both MORB and OIB sources contribute to oceanic island arc magmas in Fiji. Earth Planet. Sci. Lett. 68, 443-458.

GRAHAM D., JENKINS W. J., KURZ M. D. and BATIZA R. (1987) Helium isotope disequilibrium and geochronology of glassy submarine basalts. Nature 326, 384-386.

GRAMLICH J. W. and NAUGHTON J. J. (1972) Nature of source material for ultra-mafic minerals from Salt Lake Crater, Hawaii, from measurement of helium and argon diffusion. J. Geophys. Res. 77, 3032-3042.

HART S. R. (1984) He diffusion in olivine. Earth Planet. Sci. Lett. 70, 297-302.

HIYAGON and OZIMA (1986) Partition of noble gases between olivine and basalt melt. Geochim. Cosmochim. Acta 50, 2045-57.

JAMBON A., WEBER H. W. and BEGEMANN F. (1985) Helium and argon from an Atlantic MORB glass: concentration, distribution and isotopic composition. Earth Planet. Sci. Lett. 73, 255-267.

JOHNSON R. W., JACQUES A. L., LANGMUIR C. H., PERFIT M. R., STAUDIGEL H., DUNKLEY P. N., CHAPPEL B. W., TAYLOR S. R and BAEKISAPA M. (1987) Ridge subduction and forearc volcanism: petrology and geochemistry of rocks dredged from the western Solomon Arc and Woodlark Basin. In Circum-Pacific Council for Energy and Mineral Resources Earth Science Series vol. 7. 155-226, publ. Circum-Pacific Council for Energy and Mineral Resources, Houston, Texas.

JOHNSON R. W., JAQUES A. L., HICKEY R. L., McKEE C. O. and CHAPPELL B.
W. (1985) Manum Island, Papua New Guinea: petrology and
geochemistry of a low-TiO$_2$ basaltic island-arc volcano. J. Petrol.
26, 283-323.

KANEOKA I. (1980) Rare gas isotopes and mass fractionation: an
indicator of gas transport into or from a magma. Earth Planet.
Sci. Lett. 48, 284-292.

KAY R. W. (1980) Volcanic arc magmas: Implications of a melting-mixing
model for element recycling in the crust-upper mantle system. J.
Geol. 88, 497-522.

KURZ M. D. (1982) Helium isotope geochemistry of oceanic volcanic rocks
implications for mantle heterogeneity and degassing, Ph.D.
dissertation, WHOI/MIT Joint Program in Oceanography.

KURZ M. D. (1986a) Cosmogenic helium in a terrestrial igneous rock.
Nature 320, 435-439.

KURZ M. D. (1986b) In situ production of terrestrial cosmogenic helium
and some applications to geochronology. Geochim. Cosmochim. Acta
50, 2855- 2862.

KURZ M. D. and JENKINS W. J. Jenkins (1981) The distribution of helium
in oceanic basalt glasses. Earth Planet. Sci. Lett. 53, 41-54.

KURZ M. D., JENKINS W. J. and HART S. R. (1982) Helium isotopic
systematics of oceanic islands and mantle hererogeneity. Nature
29, 43-47.

KURZ M. D., JENKINS W. J., SCHILLING J. G. and HART S. R. (1982) Helium
isotopic variations in the mantle beneath the central North
Atlantic Ocean. Earth Planet. Sci. Lett. 58, 1-14.

KURZ M. D., JENKINS W. J., HART S. R. and CLAGUE D. (1983) Helium
isotopic variations in volcanic rocks from Loihi Seamount and the
island of Hawaii. Earth Planet. Sci. Lett. 66, 388-406.

KURZ M. D., GURNEY J. J., JENKINS W. J. and LOTT III D. E. (1987) Helium
isotopic variability within single diamonds from the Orapa
kimberlite pipe. Earth Planet. Sci. Lett. 86, 57-68.

KUSHIRO I. (1975) On the nature of silicate melt and its significance in magma genesis: regularities in the shift of the liquidus boundaries involving olivine, pyroxene, and silica minerals. Amer. Jour. Sci. 275, 411-431.

LUX G (1987) The behavior of noble gases in silicate liquids: solution, diffusion, and surface effects, with applications to natural samples. Geochim. Cosmochim. Acta 51, 1549-1560.

MORRIS J. D. and HART S. R. (1983) Isotopic and incompatible element constraints on the genesis of island arc volcanics from Cold Bay and Amok Islands, Aleutians, and implications for mantle structure. Geochim. Cosmochim. Acta 47, 2015-2030.

PARSONS B. (1981) The rates of plate creation and consumption. Geophys. J. R. astr. Soc. 67, 437-448.

PERFIT M., LANGMUIR C. M., BAEKISAPA M., CHAPPELL B., JOHNSON R. W., STAUDIGEL H. and TAYLOR S. R. (1987) Geochemistry and Petrology of rocks fron the Woodlark Basin: addressing questions of ridge subduction. In Circum-Pacific Council for Energy and Mineral Resources Earth Science Series vol. 7. 113-154, publ. Circum-Pacific Council for Energy and Mineral Resources, Houston, Texas.

PERFIT M. R., GUST D. A., BENCE A. E., ARCULUS R. T. and TAYLOR S. R. (1980) Chemical characteristics of island-arc basalts: implications for mantle sources. Chem. Geol. 30, 227-256.

PERFIT M. R., McCULLOCH M. T. and JOHNSON R. W. (1982) Isotopic and trace element differences in late Cenozoic volcanic rocks from west Melanesia. Geol. Soc. Amer. Abs. 14, 586.

POLVE M. and KURZ M. D. (1988) ^{3}He/^{4}He systematics in spinel-lherzolite nodules, in preparation.

POLVE M. (1985) Fission track mapping of U in alkali basalts: Implications for U behavior during crystallization. EOS 66, 404.

POREDA R. (1983) Helium, neon, water, and carbon in volcanic rocks and gases. Ph.D. dissertation, Scripps Institution of Oceanography.

POREDA R. (1985) Helium-3 and deuterium in back-arc basalts: Lau basin and the Mariana Trough. Earth Planet. Sci. Lett. 73, 244-254.

RAMA S. N. I. and HART S. R. (1965) Neon isotope fractionation during transient permeation. Science 147, 737-738.

RAMSAY W. R. H., CRAWFORD A. J. and FODEN J. D. (1984) Field setting, mineralogy, chemistry, and genesis of arc picrites, New Georgia, Solomon Islands. Contrib. Mineral. Petrol. 88, 386-402.

RINGWOOD A. E. (1974) The petrological evolution of island arc systems. J. Geol. Soc. Lond. 130, 183-204.

SANO Y. and WAKITA H. (1985) Geographical distribution of ^{3}He/^{4}He ratios in Japan: implications for arc tectonics and incipient magmatism. J. Geophys. Res. 90, 8729-8741.

SANO Y., WAKITA H. and GIGGENBACH W. F. (1987) Island arc tectonics of New Zealand manifested in helium isotope ratios. Geochim. Cosmochim. Acta 51, 1855-1860.

SHELBY J. E (1971) Diffusion of helium isotopes in vitreous silica. Phys. Rev.B. 4, 2681-2686.

STAUDIGEL H., McCULLOCH M., ZINDLER A. and PERFIT M.R. (1987) Complex ridge subduction and island arc magmatism: an isotopic study of the New Georgia forearc and the Woodlark Basin. In Circum-Pacific Council for Energy and Mineral Resources Earth Science Series vol. 7. 227-240, publ. Circum-Pacific Council for Energy and Mineral Resources, Houston, Texas.

TAYLOR B. (1987) Geophysical survey of the Woodlark-Solomon region. In Circum-Pacific Council for Energy and Mineral Resources Earth Science Series vol. 7. 25-48, publ. Circum-Pacific Council for Energy and Mineral Resources, Houston, Texas.

TRULL T. W. (1988) Diffusion of helium isotopes in silicate glasses and minerals: Implications for igneous petrogenesis and geochronolgy. Ph.D. dissertation, WHOI/MIT Joint Program in Oceanography, in preparation.

USSELMAN T. M. and HODGE D. S. (1978) Thermal control of low
    pressurefractionation processes. J. Volc. Geotherm. Res. 4, 265–
    281.

WYLLIE P. (1982) Subduction products according to experimental
    prediction. Geol. Soc. Am. Bull. 93, 468–476.

ZINDLER and HART (1986) Helium: problematic primordial signals. Earth
    Planet. Sci. Lett. 79, 1–8.

APPENDIX A: Fortran77 programs for calculating diffusion coefficients from helium emanation data using the refined model presented in chapter 2.

Main program:

DIFPRO

Calculates fractional release data from aliquot measurements. The errors in F were derived as follows, where x and s are aliquot helium contents and associated errors and N is the number of aliquots:

$$F_i = \sum_1^i x_i \pm s_i \Big/ \sum_1^N x_i \pm s_i$$

which when differentiated with respect to x_i, gives for the variance in

F: $(1/\sum_1^N x_i)^4 \left[\left(\sum_{i+1}^N x_i \right)^2 \sum_1^i (s_i)^2 + \left(\sum_1^i x_i \right)^2 \sum_{i+1}^N (s_i)^2 \right]$

Subroutines:

DIFPRO calls SPHAPRX to obtain diffusion coefficient estimates from the spherical approximation equations (2.9a,b,c), which are then refined by calling the subroutine DADJST.

DADJST:

Calculates D_i and D_{i-1} by successively calling subroutine DPIPED, calculates $D_{\Delta i}$ from equation 2.15.

DPIPED:

Calculates D by iterative calls to FPIPED. D is first bracketed by a factor of 10, and then the desired precision is obtained by bisection of the bounded interval.

FPIPED:

Calculates the fractional release from a collection of pipeds using equation 2.11, given a diffusion coefficient, elapsed time and grain size parameters.

```
       PROGRAM DIFPRO
C      Tom Trull July 8, 1988
C      modified from DIFNEW.for for improved I/O and to allow the
C      use of measured grain size distributions in calculating
C      diffusion coefficients.
C      Purpose:
C      Calculates diffusion coefficients from gas release data
C      Requires:
C      Subroutines: SPAPRX (contains SPH1,SPH3,SPH3)
C                   DADJST,DPIPED,FPIPED
C      Input Parameters:
C      V4     - CC 4He measured in aliquot
C      V4B    - corrected form daily blank
C      sV4B   - 1 sigma error
C      RAT    - 3He/4He ratio normalized to atmospheric ratio (RA)
C      sRAT   - 1 sigma error estimated in program HEMAN5.for
C      DIFTIM - time (s from noon) at which the aliquotting valve closed.
C      TEMPC  - temperature of gas release during the aliquot.
C      SAMNAM - sample name
C      NANAL,IHR,IMIN - number and time of analysis.
C      grainR - radius of equivalent sphere characterizing grain size
C      sigmaR - 1 sigma
C
C      Internal Parameters:     (x is either 3 or 4)
C      ET     - elapsed time in step i
C      TET    - total elapsed time to and through step i
C      V3B    - volume of 3He in aliquot, calculated from ratio and 4He
C      sV3B   - 1 sigma
C      VxL    - gas volume corrected for background leak
C      sVxL   - 1 sigma on leak corrected gas volume
C      VARx   - variance of gas volume = sVxl**2
C      RATL   - leak corrected ratio
C      sRATL  - 1 sigma
C      SUMx   - total of gas release through aliquot i
C      TVARx  - variance on Sumx
C      RTOT   - ratio of total 3He to total 4He
C      SRTOT  - 1 sigma
C      FRACx  - fraction of gas released in aliquot i
C      TFRACx - fraction of gas in all steps up to and through i
C      VTFRCx - variance on Tfracx (CAUTION: VTFRCx(I) are not independent!)
C
C      rDSx   - diffusion coefficient from spherical approximations (1/s)
C      rsDSx  - 1 sigma
C      DSx    - spherical D converted to cm2/s units
C      sDSx   - 1 sigma from fractional loss error only
C      TsDSx  - 1 sigma error including equivalent sphere size uncertainty
C      DPx    - Refined D value using size distribution of parallelpipeds.
C      sDPx   - 1 sigma
C      QS     - isotopic diffusivity ratio (DS3/DS4)
C      sQS    - 1 sigma
C      QP     - isotopic diffusivity ratio (DP3/DP4)
C      sQP    - 1 sigma
C
C      sTEMPC - error in heating temp - specified file by file
C      RTEMPK - reciprocal kelvin temperature
C      sRTMPK - 1 sigma
C
C         Note: the log (base 10) of a variable is denoted by the suffix L
C               or Log.
C
C      I/O file names:
```

```
C       FILNAM -   input file containing helium analyses and times
C       OUTDAT -   calculated diffusion coefficients
C       OUTTWO -   release systematics data
C       OUTAPX -   measurements and D values for publication
C       GRNAME -   File contains grain size data for use with DADJST routines.
C
C******************************************************************************
C
      PARAMETER (nsam=101,ndatin=1,ndat=2,ntwo=3,napx=22,zero=0.)
         PARAMETER (jout=7,jin=5)
      DIMENSION
      &           NANAL(nsam),IHR(nsam),IMIN(nsam),
      & DIFTIM(0:nsam),ET(nsam),TET(0:nsam),
      & TEMPC(nsam),sTEMPC(nsam),RTEMPK(nsam),sRTMPK(nsam),
      & RAT(nsam),sRAT(nsam),RATL(nsam),sRATL(nsam),
      &           V4(nsam),V4B(nsam),sV4B(nsam),V4L(nsam),sV4L(nsam),
      & VAR4(0:nsam),TVAR4(0:nsam),SUM4(0:nsam),
      &           FRAC4(nsam),sFRAC4(nsam),TFRAC4(0:nsam),VTFRC4(0:nsam),
      & rDS4(nsam),DS4(nsam),sDS4(nsam),DP4(nsam),sDP4(nsam),
      & REL4(nsam),
      &           V3B(nsam),sV3B(nsam),V3L(nsam),sV3L(nsam),
      & VAR3(nsam),TVAR3(0:nsam),SUM3(0:nsam),
      &           FRAC3(nsam),sFRAC3(nsam),TFRAC3(0:nsam),VTFRC3(0:nsam),
      & rDS3(nsam),DS3(nsam),sDS3(nsam),DP3(nsam),sDP3(nsam)
C
      CHARACTER
      & FILNAM*10,OUTDAT*10,OUTTWO*10,OUTAPX*10,GRNAME*10,
      & SAMNAM(nsam)*22,HEADER(5)*125
C
      DATA RA,PI/1.38E-06,3.14159/
C
C     Initialize
C
      DATA DIFTIM(0),TET(0),SUM4(0),SUM3(0),TVAR4(0),TVAR3(0)/6*0./
         DATA TFRAC4(0),TFRAC3(0),VTFRC4(0),VTFRC3(0)/4*0./
      DATA STEMPC/nsam*0/
C
C************   File name and data input   *****************************
C
      WRITE(jout,1000)
1000  FORMAT(2X,'ENTER NAME OF FILE containing Helium data')
      READ(jin,1010)FILNAM
      WRITE(jout,1005)
1005  FORMAT(2X,'ENTER FILENAM FOR OUTPUT')
      READ(jin,1010)OUTDAT
1010  FORMAT(A10)
C
      OUTTWO=OUTDAT
      OUTAPX=OUTDAT
      OUTTWO(8:10)='TWO'
      OUTAPX(8:10)='APX'
      GRNAME=FILNAM
      GRNAME(1:2)='GR'
      OPEN(UNIT=ndatin,FILE=FILNAM,STATUS='OLD')
      OPEN(UNIT=ndat,FILE=OUTDAT,STATUS='NEW')
      OPEN(UNIT=ntwo,FILE=OUTTWO,STATUS='NEW')
      OPEN(UNIT=napx,FILE=OUTAPX,STATUS='NEW')
C
C     Special input process for synthetic data.
C
      IF(FILNAM.EQ.'DFMOD1.DAT')THEN
              WRITE(jout,*)FILNAM
              READ(ndatin,1012)(HEADER(i),i=1,5)
```

357

```fortran
              WRITE(jout,*)(HEADER(i),i=1,5)
              READ(ndatin,*)grainR,sigmaR
              WRITE(jout,*)grainR,sigmaR
C
              I=1
5             READ(ndatin,1015,END=100) DIFTIM(I),V4B(I),RAT(I),REL4(I)
1015          FORMAT(F20.2,3F14.6)
              WRITE(jout,*)DIFTIM(I),V4B(I),RAT(I)
C
              sV4B(I)=.005*V4B(I)
              SRAT(I)=.01*RAT(I)
              TEMPC(I)=0.
C
C             Discard data to simulate prior loss
C             Rel4 is the total fractional loss.
C
              RLOST=0.0                  !approx. amount of prior loss.
              IF(REL4(I).LE.RLOST)THEN
                      DIFTIM(0)=DIFTIM(I)
                      I=1
                      WRITE(jout,*)REL4(I),I
              ELSE
                    I=I+1
              ENDIF
              GO TO 5
      ENDIF
C
C     Input for experimental data
C
      READ(ndatin,1012)(HEADER(i),i=1,5)
1012  FORMAT(4(a125,/),a125)
      WRITE(jout,1014)(header(i),i=1,5)
1014  FORMAT(4(A125,/))
      READ(ndatin,*)grainR,sigmaR
      WRITE(jout,*)grainR,sigmaR
C
      I=1
6        READ(ndatin,1011,END = 100) NANAL(I),IHR(I),IMIN(I),DIFTIM(I),
     &           V4(I),V4B(I),sV4B(I),RAT(I),sRAT(I),SAMNAM(I),TEMPC(I)
         I=I+1
      GO TO 6
1011     FORMAT(2X,I2,2X,I3,1X,I2,2X,0PF12.1,3(2X,1PE11.5),
     &           2(2X,0PF11.5),5X,A22,F8.1)
C
 100  CONTINUE
      CLOSE(UNIT=1)
      IMAX=I-1
      WRITE(jout,*)' NUMBER OF ALIQUOTS = ',IMAX
C
C************** UNITS CONVERSIONS ********************************
C
      grainR=grainR/10000.                  !data in microns
      sigmaR=sigmaR/10000.                  !conversion to cm.
C
C***************COMPUTE ELAPSED TIME FOR EACH STEP*******************
C
      DO 45 I=1,Imax,1
      ET(I)=DIFTIM(I)-DIFTIM(I-1)
      IF(ET(I).LE.zero)ET(I)=ET(I) + 86400.    !ET greater than 24 hours.
      If(FILNAM.NE.'DFMOD1.DAT')ET(1)=1920.  !FIRST SAMPLE HEATED 1 CYCLE.
45    Continue
C
```

```fortran
C
C**********    Leak corrections.    ***********************************
C
      Rleak4=8.3E-16                                !leak rate in cc/s
      Rleak3=leak4*Ra                               !atmospheric leak
C
      IF(FILNAM.EQ.'DFMOD1.DAT')THEN
              RLEAK4=ZERO
              RLEAK3=ZERO
      ENDIF
C
      DO 55 I=1,IMAX,1
         V3B(I)=RAT(I)*V4B(I)*RA
      sV3B(I)=(sRAT(I)*V4B(I)*RA)**2+(RAT(I)*sV4B(I)*RA)**2    !variance 3He
      sV3B(I)=sV3B(I)**.5                           !sigma 3He
      V4L(I)=V4B(I)-ET(I)*Rleak4                    !LEAK  CORRECT
      V3L(I)=V3B(I)-ET(I)*Rleak3                    !LEAK  CORRECT
      sV4L(I)=sV4B(I)                   !Error in leak rate not considered.
      sV3L(I)=sV3B(I)
      sRATL(I)=sRAT(I)
      IF (V4L(I).LE.zero)THEN
         V4L(I)=0.
         RATL(I)=0
      ENDIF
         IF (V3L(I).LE.zero)THEN
           V3L(I)=0.
             RATL(I)=0
      ENDIF
      IF(V4L(I).GT.zero)RATL(I)=V3L(I)/V4L(I)/RA
 55   CONTINUE
C
C*************    Special section *********************************
C
C     Powder release systematics can be back-corrected to the time of
C     sample crushing (rather than the start of analysis) to examine
C     the time dependence of loss.
C
*             IF(FILNAM.EQ.'TV0525.DAT')THEN
*                     write(jout,*)filnam
*                     TET(0)=1036800.             !time since crushing
*             ENDIF
*             IF(FILNAM.EQ.'TV0715.DAT')THEN
*                     write(jout,*)filnam
*                     TET(0)=4752000.             !Time since crushing
*             ENDIF
C
C*****************  summation of of step releases  *******************
C
      DO 65,I=1,IMAX,1
      TET(I)=TET(I-1)+ET(I)
      SUM4(I)=SUM4(I-1)+V4L(I)
      SUM3(I)=SUM3(I-1)+V3L(I)
      VAR4(I)=sV4L(I)**2
      TVAR4(I)=TVAR4(I-1)+VAR4(I)
      VAR3(I)=sV3L(I)**2
      TVAR3(I)=TVAR3(I-1)+VAR3(I)
 65   CONTINUE
C
C****************  Bulk composition calculation  ***********************
C
      RTOT=SUM3(IMAX)/SUM4(IMAX)/RA
      SRTOT=1./RA*(TVAR3(IMAX)/SUM4(IMAX)**2
     &         +TVAR4(IMAX)*(SUM3(IMAX)/SUM4(IMAX)**2)**2)**.5
```

```
      WRITE(jout,*)' TOTAL HELIUM =',SUM4(IMAX)
      WRITE(jout,*)' BULK RATIO = ',RTOT,'  1 sigma = ',SRTOT
C
C******          EXPRESS GAS LOSS FRACTIONALLY FOR EACH STEP *****************
C
      DO 75 I=1,IMAX,1
      FRAC4(I)=V4L(I)/SUM4(IMAX)
      FRAC3(I)=V3L(I)/SUM3(IMAX)
      SFRAC4(I)=sV4L(I)/SUM4(IMAX)
      SFRAC3(I)=sV3L(I)/SUM3(IMAX)
C
      TFRAC4(I)=SUM4(I)/SUM4(IMAX)
      TFRAC3(I)=SUM3(I)/SUM3(IMAX)
C
      VTFRC4(I)=TVAR4(I)*( (SUM4(IMAX)-SUM4(I))/SUM4(IMAX) )**2
     &                   +(TVAR4(IMAX)-TVAR4(I))*( SUM4(I)/SUM4(IMAX) )**2
        VTFRC4(I)=VTFRC4(I)/SUM4(IMAX)**2
C
      VTFRC3(I)=TVAR3(I)*( (SUM3(IMAX)-SUM3(I))/SUM3(IMAX) )**2
     &                   +(TVAR3(IMAX)-TVAR3(I))*( SUM3(I)/SUM3(IMAX) )**2
        VTFRC3(I)=VTFRC3(I)/SUM3(IMAX)**2
C
 75   CONTINUE
C
C********** COMPUTE DIFFUSION COEFFICIENTS **********************
C
C            4He calculations
C
      DO 85 I=1,IMAX-1,1              !SKIP LAST FRACTION
C
      Ksigma=1                       !ERROR LOOP INDEX
333   CONTINUE                       !ENTRY POINT FOR ERROR LOOP
C
C     Calculate approximate 4He diffusion coefficents assuming equisized
C     spheres using 3 approximation equations
C     (units are 1/s, i.e. D/R**2).
C
        WRITE(jout,*)' DIFPRO:I= ',I
        WRITE(jout,*)' TFRAC4(I)= ',TFRAC4(I),'  VTFRC4(I)= ',VTFRC4(I)
C
      IF(FRAC4(I).EQ.zero) GO TO 85     !Skip steps that released no 4He.
C
       IF (TFRAC4(I).LE.0.04) THEN
         CALL SPH1(ET(I),TFRAC4(I-1),TFRAC4(I),VTFRC4(I-1),VTFRC4(I),
     &  rDS4(I))
        ELSEIF ((TFRAC4(I).GT.0.04).AND.(TFRAC4(I).LE.0.86)) THEN
         CALL SPH2(ET(I),TFRAC4(I-1),TFRAC4(I),VTFRC4(I-1),VTFRC4(I),
     &  rDS4(I))
        ELSEIF ((TFRAC4(I).GT.0.86).AND.(TFRAC4(I).LT.1.0)) THEN
         CALL SPH3(ET(I),TFRAC4(I-1),TFRAC4(I),VTFRC4(I-1),VTFRC4(I),
     &  rDS4(I))
        ENDIF
C
      DS4(I)=rDS4(I)*grainR**2                        !CONVERT TO CM**2/S
C
C     Calculate refined 4He diffusion coefficents from measured
C     grain size distributions and parallelpiped geometry by iteration.
C     (units are cm**2/s). Spherical D value is the initial guess.
C
             CALL DADJST(GRNAME,TET(I-1),ET(I),DS4(I),
     &                   TFRAC4(I-1),TFRAC4(I),DP4(I))
C
C     Approximate error by calculating D at 1 sigma offsets.
```

360

```
C
        IF(Ksigma.EQ.1)THEN
          Ksigma=Ksigma+1
          DS4M=DS4(I)                                      !midpoint
          DP4M=DP4(I)                                      !midpoint
            TFRAC4(I)=TFRAC4(I)+SQRT(VTFRC4(I))            !offset 1s above
          GO TO 333                                        !recalculate
        ENDIF
C
        IF(Ksigma.EQ.2)THEN
            Ksigma=Ksigma+1
          DS4A=DS4(I)                                      !1s above
          DP4A=DP4(I)                                      !1s above
          TFRAC4(I)=TFRAC4(I)-2*SQRT(VTFRC4(I))     !offset 1s below
            GO TO 333                                      !recalculate
        ENDIF
C
        DS4B=DS4(I)                                        !1s below
        DP4B=DP4(I)                                        !1s below
        sDS4(I)=(DS4A-DS4B)/2.                             !halve offset value
s
        sDP4(I)=(DP4A-DP4B)/2.                             !to obtain error
C
        TFRAC4(I)=TFRAC4(I)+SQRT(VTFRC4(I))     !return to midpoint
        DS4(I)=DS4M                                   !retain values in arrays
        DP4(I)=DP4M
C
        WRITE(jout,*)' I= ',I
        WRITE(jout,*)' SPHERE APPROX: D4 = ',DS4(I),'  sD4(I) = ',sDS4(I)
        WRITE(jout,*)' PIPEDS APPROX: D4 = ',DP4(I),'  sD4(I) = ',sDP4(I)
C
 85     CONTINUE

C
C             3He calculations
C

        IF(FILNAM.EQ.'TV0519.DAT')THEN
                WRITE(jout,*)FILNAM
                GO TO 500        !skip 3He section for *4He expts.
        ENDIF
        IF(FILNAM.EQ.'TV1109.DAT')THEN
                WRITE(jout,*)FILNAM
                GO TO 500        !skip 3He section for *4He expts.
        ENDIF
C
C
        DO 95 I=1,IMAX-1,1             !SKIP LAST FRACTION
C
        IF((FILNAM.EQ.'TV0901.DAT').AND.(J.GT.33))THEN
                WRITE(jout,*)FILNAM
                GO TO 500        !skip 3He section for aliquots
        ENDIF                                 !with no remaining 3He.
C
        Ksigma=1                       !ERROR LOOP INDEX
444     CONTINUE                       !ENTRY POINT FOR ERROR LOOP
C
C  Calculate approximate 3He diffusion coefficents assuming equisized
C  spheres using 3 approximation equations
C  (units are 1/s, i.e. D/R**2).
C
          WRITE(jout,*)' DIFPRO:I= ',I
          WRITE(jout,*)' TFRAC3(I)= ',TFRAC3(I),'  VTFRC3(I)= ',VTFRC3(I)
```

```
C
      IF(FRAC3(I).EQ.zero) GO TO 95           !Skip steps that released no 3He.
C
      IF (TFRAC4(I).LE.0.04) THEN
        CALL SPH1(ET(I),TFRAC3(I-1),TFRAC3(I),VTFRC3(I-1),VTFRC3(I),
     &  rDS3(I))
      ELSEIF ((TFRAC4(I).GT.0.04).AND.(TFRAC4(I).LE.0.86)) THEN
        CALL SPH2(ET(I),TFRAC3(I-1),TFRAC3(I),VTFRC3(I-1),VTFRC3(I),
     &  rDS3(I))
      ELSEIF ((TFRAC4(I).GT.0.86).AND.(TFRAC4(I).LT.1.0)) THEN
        CALL SPH3(ET(I),TFRAC3(I-1),TFRAC3(I),VTFRC3(I-1),VTFRC3(I),
     &  rDS3(I))
      ENDIF
C
      DS3(I)=rDS3(I)*grainR**2                          !CONVERT TO CM**2/S
C
C    Calculate refined 3He diffusion coefficents from measured
C    grain size distributions and parallelpiped geometry by iteration.
C    (units are cm**2/s). Spherical D value is the initial guess.
C
          CALL DADJST(GRNAME,TET(I-1),ET(I),DS3(I),
     &                  TFRAC3(I-1),TFRAC3(I),DP3(I))
C
C    Approximate error by calculating D at 1 sigma offsets.
C
      IF(Ksigma.EQ.1)THEN
        Ksigma=Ksigma+1
        DS3M=DS3(I)                                  !midpoint
        DP3M=DP3(I)                                  !midpoint
          TFRAC3(I)=TFRAC3(I)+SQRT(VTFRC3(I))        !offset 1s above
        GO TO 444                                    !recalculate
      ENDIF
C
      IF(Ksigma.EQ.2)THEN
          Ksigma=Ksigma+1
        DS3A=DS3(I)                                  !1s above
        DP3A=DP3(I)                                  !1s above
        TFRAC3(I)=TFRAC3(I)-2*SQRT(VTFRC3(I))    !offset 1s below
          GO TO 444                                  !recalculate
      ENDIF
C
      DS3B=DS3(I)                                     !1s below
      DP3B=DP3(I)                                     !1s below
      sDS3(I)=(DS3A-DS3B)/2.                          !halve offset value
s
      sDP3(I)=(DP3A-DP3B)/2.                          !to obtain error
C
      TFRAC3(I)=TFRAC3(I)+SQRT(VTFRC3(I))    !return to midpoint
      DS3(I)=DS3M                                  !retain values in arrays
      DP3(I)=DP3M
C
      WRITE(jout,*)' I = ',I
        WRITE(jout,*)' SPHERE APPROX: D3 = ',DS3(I),'  sD3(I) = ',sDS3(I)
        WRITE(jout,*)' PIPEDS APPROX: D3 = ',DP3(I),'  sD3(I) = ',sDP3(I)
C
 95   CONTINUE
C
 500  CONTINUE
C
C*************** OUTPUT *********************************************
C
C    Write headers in files
C
```

362

```
      WRITE(ndat,1014)(HEADER(I),I=1,4)
      WRITE(ntwo,1014)(HEADER(I),I=1,4)
      WRITE(nAPX,1014)(HEADER(I),I=1,4)
      WRITE(ndat,1013)SUM4(IMAX),RTOT,SRTOT
      WRITE(ntwo,1013)SUM4(IMAX),RTOT,SRTOT
      WRITE(napx,1013)SUM4(IMAX),RTOT,SRTOT
1013 FORMAT(/,'CC HE TOTAL = ',1PE9.2,2X,'RTOT = ',OPF5.2,2X
     & ,'SRTOT = ',OPF5.2)
C
C     WRITE(ndat,1016)
1016 FORMAT('OUTPUT VARIABLE LIST:'/
     1,'(1,tfrac4)','(2,stfrac4)','(3,tfrac3)','(4,stfrac3)'
     2,'(5,log10D4)','(6,slog10D4)','(7,log10grD4)','(8,slog10grD4)
     3','(9,D3/D4)',,'(10,sD3/D4)','(11,R/Ra)','(12,sR/Ra)'
     4,'(13,tempc)','(14,rtempk)','(15,TgrSD4)','(16,samnam)')
C     WRITE(napx,1017)
1017 FORMAT(/,1x,'#',2x,'oC',2x,'Elapsed',4x,'He(b)',7x,'He(1)'
     &          ,'1s',4x,'R/Ra',2x,'R/Ra(1)',2x,'1s',6x,'F4',8x,'D4/r2'
     & ,6x,'1s',' D4',9x,'1s',6x,'D3/D4',3x,'1s ',/,10x,'time(hr)',5x
     & ,'cc',8x,'cc',41x,'cm2/s',7X,'cm2/s',/)
C
C     Calculate and write output parameters for each aliquot
C               (except last step)
C
      DO 105 I=1,IMAX-1,1
C
C     4He output parameters
C
              TsDS4=((sDS4(I)*grainR)**2+(DS4(I)*2.*sigmaR/grainR)**2)**.5
              rsDS4=sDS4(I)/grainR**2
C
      IF(V4(I).NE.zero)THEN
              V4LOG=ALOG10(V4(I))
      ENDIF
      IF(V4L(I).NE.zero)THEN
              V4LLOG=ALOG10(V4L(I))
              sV4LLG=sV4L(I)/V4L(I)/ALOG(10.)
      ENDIF
C
      IF(DS4(I).NE.zero)THEN
              DS4L=alog10(DS4(I))
              sDS4L=sDS4(I)/DS4(I)/ALOG(10.)
              TsDS4L=TsDS4/DS4(I)/ALOG(10.)
              rDS4L=alog10(rDS4(I))
              rsDS4L=sDS4L
              DP4L=alog10(DP4(I))
              sDP4L=sDP4(I)/DP4(I)/ALOG(10.)
      ENDIF
C
C     3He output parameters
C
              TsDS3=((sDS3(I)*grainR)**2+(DS3(I)*2.*sigmaR/grainR)**2)**.5
              rsDS3=sDS3(I)/grainR**2
C
      IF(V3L(I).NE.zero)THEN
              V3LLOG=ALOG10(V3L(I))
              sV3LLG=sV3L(I)/V3L(I)/ALOG(10.)
      ENDIF
C
      IF(DS3(I).NE.zero)THEN
              DS3L=alog10(DS3(I))
              sDS3L=sDS3(I)/DS3(I)/ALOG(10.)
              TsDS3L=TsDS3/DS3(I)/ALOG(10.)
```

363

```fortran
                  rDS3L=alog10(rDS3(I))
                  rsDS3L=sDS3L
                  DP3L=alog10(DP3(I))
                  sDP3L=sDP3(I)/DP3(I)/ALOG(10.)
          ENDIF
C
C       Isotopic Ratio output parameters
C
          IF(DS4(I).NE.zero)THEN
            QS=DS3(I)/DS4(I)
            sQS=((sDS3(I)/DS4(I))**2
     &            +(sDS4(I)/DS4(I))**2*(DS3(I)/DS4(I))**2)**.5
            QP=DP3(I)/DP4(I)
            sQP=((sDP3(I)/DP4(I))**2
     &            +(sDP4(I)/DP4(I))**2*(DP3(I)/DP4(I))**2)**.5
          ENDIF
C
          IF(QS.NE.zero)THEN
            QSL=ALOG10(QS)
            sQSL=sQS/QS/ALOG(10.)
          ENDIF
C
          IF(QP.NE.zero)THEN
            QPL=ALOG10(QP)
            sQPL=sQP/QP/ALOG(10.)
          ENDIF
C
C       Temperature parameters
C
          RTEMPK(I)=1./(273.+TEMPC(I))
          sRTMPK(I)=sTEMPC(I)*RTEMPK(I)**2
C
C       Write to files
C
            WRITE(ndat,1050)TFRAC4(I),VTFRC4(I)**.5,TFRAC3(I),VTFRC3(I)**.5,
     & rDS4L,sDS4L,DS4L,TsDS4L,
     & QS,sQS,RATL(I),sRATL(I),TEMPC(I),RTEMPK(I)*1000.,TsDS4L,
     & sRTMPK(I)*1000.,DP4L,sDP4L,QP,sQP,SAMNAM(I)
C
            WRITE(ntwo,1060)ET(I)/1000,TET(I)/1000,
     &          V4LOG,V4LLOG,sV4LLG,V3LLOG,sV3LLG,
     &    FRAC4(I),SFRAC4(I),FRAC3(I),SFRAC3(I),
     &    TFRAC4(I),VTFRC4(I)**.5,TFRAC3(I),VTFRC3(I)**.5,
     &          V4L(I)/ET(I),SQRT(TET(I))/100,TET(I)/3600, SAMNAM(I)
C
            WRITE(napx,1070)I,TEMPC(I),ET(I)/3600,V4B(I),V4L(I),SV4L(I),
     & RAT(I),RATL(I),sRATL(I),TFRAC4(I),rDS4(I),rsDS4,DS4(I),TsDS4,
     & QS,sQS,QSL,sQSL,QPL,sQPL,1000.*RTEMPK(I),SAMNAM(I)
C
  105 CONTINUE
C
C       Last aliquot output
C
      IF(V4(IMAX).NE.zero)THEN
                  V4LOG=ALOG10(V4(IMAX))
      ENDIF
      IF(V4L(IMAX).NE.zero)THEN
                  V4LLOG=ALOG10(V4L(IMAX))
                  sV4LLG=sV4L(IMAX)/V4L(IMAX)/ALOG(10.)
      ENDIF
      IF(V3L(IMAX).NE.zero)THEN
                  V3LLOG=ALOG10(V3L(IMAX))
                  sV3LLG=sV3L(IMAX)/V3L(IMAX)/ALOG(10.)
```

364

```fortran
      ENDIF
C
      WRITE(ndat,1050)TFRAC4(IMAX),VTFRC4(IMAX)**.5,TFRAC4(IMAX),
     & VTFRC4(IMAX)**.5,ZERO,ZERO,ZERO,ZERO,ZERO,ZERO,
     & ZERO,ZERO,ZERO,ZERO,ZERO,ZERO,ZERO,ZERO,ZERO,ZERO,SAMNAM(IMAX)
C
      WRITE(ntwo,1060)ET(IMAX)/1000,TET(IMAX)/1000,
     &        V4LOG,V4LLOG,sV4LLG,V3LLOG,sV3LLG,
     & FRAC4(IMAX),SFRAC4(IMAX),FRAC3(IMAX),SFRAC3(IMAX),
     & TFRAC4(IMAX),VTFRC4(IMAX)**.5,TFRAC3(IMAX),VTFRC3(IMAX)**.5,
     &        V4L(IMAX)/ET(IMAX),SQRT(TET(IMAX))/100,TET(IMAX)/3600,
     & SAMNAM(IMAX)
C
      I=IMAX
      WRITE(napx,1070)I,TEMPC(I),ET(I)/3600,V4B(I),V4L(I),SV4L(I),
     & RAT(I),RATL(I),sRATL(I),TFRAC4(I),ZERO,ZERO,ZERO,ZERO,ZERO,
     & ZERO,ZERO,ZERO,ZERO,ZERO,1000.*RTEMPK(I),SAMNAM(I)
C
C*************** Output Format Statements *******************************
C
1050    FORMAT(12(1X,F10.5),2X,f5.0,2X,F7.3,2X,
     & F9.5,2x,F7.3,2x,4(1x,F10.5),2x,A22)
C
1060 FORMAT(2(3X,F12.4),5(3X,F8.4),8(3X,0PF9.5),3X,
     & 1PE10.4,2(3X,0pf10.4),3x,A22)
C
1070 FORMAT(I2,1X,F5.0,1X,F6.2,2X,2(1PE9.2,1X),1PE7.0,2(0PF7.2,1X),
     &        F5.2,1X,F7.4,1X,2(1PE9.2,1X,1PE8.1,1X),2(0PF8.4,1X),
     &        4(f8.5,1x),f6.3,2X,A22)
C
C**********************************************************************
C
C
      STOP
      END




!!!!!!!!!!!!!!!!!!!!!!!!!!!!!!!!!!!!!!!!!!!!!!!!!!!!!!!!!!!!!!!!!!!!!!!!!!!!!!!!!!!!


      Subroutine Dadjst (Grname,TET,ET,Difco,TF1,TF2,Dprime)
C
C     TOM TRULL July 5,1988
C
C     PURPOSE
C     Calculates a refined diffusion coefficient (Dprime) for step-
C     release I, using a measured grain size distribution and a
C     parallelpiped model.  The method is iterative determination of the
C     effective diffusion coefficents (Dbar) at total fractional releases
C     F(I-1) and F(I).  An initial diffusivity estimate is required.
C     The routine is structured to be used with error estimation offsets
C     in TF2 as called by DIFPRO.FOR.
C     PARAMETERS
C     supplied:
C     Grname - source file for grain side lengths, with 3 line header and
C              3 side lengths for each grain.
C     Tet    - total elapsed time at end of heating step i-1.
C     Et     - length of heating step i.
C     Difco  - estimate of diffusion coefficient .
C     TF1    - total fraction He emitted through step i-1.
C        TF2    - total fraction He emitted through step i.
```

```
C     calculated:
C     Dprime   - revised 4He diffusion coefficient for step i.
C     Internal:
C     Dbar1 and Dbar2 are the effective (mean value theorem) diffusivities
C     at total release fractions TF1 and TF2.
C     DlastI retains the step I-1 Dbar2 values for use at step I as Dbar1.
C     TlastI is used to distinguish between subroutine calls for error
C     estimates at any one step, from calls for the next aliquot
C     Requires:
C     Subroutine Dpiped, Function Subroutine Fpiped.
C
      PARAMETER(jout=7)
         CHARACTER Grname*10
      SAVE DBAR1,DLASTI,TLASTI
C
      Time=TET+ET
C
C     compute effective (mean) value for D through step i. (Dbar2)
C
      Call Dpiped(Grname,Time,Difco,TF2,Dbar2)
C
C     Compute effective (mean) value for D through step i-1. (Dbar1)
C     Dbar1 is 0 for the first step, updated from DlastI for each
C     new step (DlastI retains the value of Dbar2 from the previous
C     step), and is SAVED for error estimation multiple calls within
C     each step.
C
      IF(TF1.EQ.0) THEN
               Dbar1=0
               DlastI=0
               TlastI=0
      ENDIF
C
      IF(TF1.GT.0) THEN
               If(TlastI.LT.Time)Dbar1=DlastI
      ENDIF
C
C     Calculate Dprime from the relation:
C     Dbar2*Time = Dbar1*TET + Dprime*ET
C
      Dprime = (Dbar2*Time-Dbar1*TET)/ET
C
D     WRITE(jout,*)' DADJST:DPRIME = ', DPRIME
C
C     Update DlastI at each time step - new aliquot.
C
      If(TlastI.lt.Time)DlastI=Dbar2
C
      RETURN
      END



!!!!!!!!!!!!!!!!!!!!!!!!!!!!!!!!!!!!!!!!!!!!!!!!!!!!!!!!!!!!!!!!!!!!!!!!!!!!!!!!!!!!


      Subroutine Dpiped (Grname,Tet,Difco,TF,Dnew)
C
C     TOM TRULL July 5,1988
C
C     PURPOSE
C     Calculates diffusion coefficient from fractional release data for a
C     collection of parallelpipeds by iteration.  Requires an initial D
C     estimate.
```

```
C       PARAMETERS
C       supplied:
C       Grname - source file for grain side lengths, with 3 line header and
C                  3 side lengths for each grain.
C       Tet    - total elapsed time in seconds.
C       Difco  - estimate of diffusion coefficient.
C       TF     - total fraction He emitted
C       calculated:
C       Dnew   - revised 4He diffusion coefficient.
C       ADJUSTABLE LIMITS:
C       Relative precision on Dnew is specified by Rerror
C       maximum bisection steps given by NTRY
C
C       Requires:
C       Function subroutine Fpiped
C
C
C
        PARAMETER (NTRY=50,Rerror=.00001,jout=7)
        DOUBLE PRECISION D1,D2,DF1,DF2,Dmid,DFmid
        CHARACTER Grname*10
C
C       Find diffusivities that bracket the Dnew value within a factor of 10.
C       (Note:throughout the search routines D2 is less than D1)

        D1=Difco                          !upper limit
        D2=Difco/10.d+00                  !initial search range: factor of 10

        DF1=Fpiped(Grname,Tet,D1)-TF
        DF2=Fpiped(Grname,Tet,D2)-TF
C
C       Check if D is a bad overestimate
C
5       If(((DF1+TF).eq.1).and.((DF2+TF).eq.1))then
                D1=D1/10.
                D2=D2/10.
                GOTO 5
        Endif
           DO 100 J=1,NTRY
                IF(DF1*DF2.LT.0.)THEN
                    GOTO 100
                    ELSIF(DF1.EQ.0.)THEN
                       DNEW = D1
                       GOTO 116
                     ELSEIF(DF2.EQ.0)THEN
                        DNEW = D2
                        GOTO 116
                 ELSEIF(ABS(DF1).GT.ABS(DF2))THEN
                   D1=D2
                   D2=D2/10.
                     DF1=DF2
                    DF2=Fpiped(Grname,Tet,D2)-TF
                 ELSEIF(ABS(DF1).LT.ABS(DF2))THEN
                   D2=D1
                   D1=D2*10.
                     DF2=DF1
                     DF1=Fpiped(Grname,Tet,D1)-TF
                   ELSEIF(ABS(DF1).EQ.ABS(DF2))THEN
                       WRITE(jout,*)'HELP',DF1,DF2,D1,D2      !DEBUGGING AID
                       STOP'  Equal offsets'
                   ELSE
                       WRITE(jout,*)'HELP',DF1,DF2,D1,D2      !DEBUGGING AID
                       STOP'  Cannot bracket Dnew'
```

367

```
                ENDIF
 100    CONTINUE
C
C       Refine Dnew by bisection
C
        DO 110 J=1,NTRY
          Dmid=D2+(D1-D2)*.5
          DFmid=Fpiped(Grname,Tet,Dmid)-TF
          IF(DFmid.LT.0.)D2=Dmid
          IF(DFmid.GT.0.)D1=Dmid
          IF((D1-D2).LT.(2*Rerror*DMID) .OR. DFMID.EQ.0.)GOTO 115
 110    CONTINUE
        Stop ' Unable to obtain Dnew by bisection'
 115    Dnew=Dmid
 116    WRITE(jout,*)'  DPIPED: FPIPED VALUE IS  ',(DFMID+TF)
 D      Write(jout,*)'  DPIPED: Dnew estimate is ',Dnew
        RETURN
            END



   !!!!!!!!!!!!!!!!!!!!!!!!!!!!!!!!!!!!!!!!!!!!!!!!!!!!!!!!!!!!!!!!!!!!!!!!!!!!!!!!!!!!


        Function Fpiped (Grname,Tet,Difco)
C
C       TOM TRULL July 5,1988
C
C       PURPOSE
C       Calculates total fractional loss by diffusion from a collection of
C       parallelpipeds.
C
C       ARGUMENTS
C       supplied:
C       Grname - source file for grain side lengths, with 3 line header and
C                3 side lengths for each grain (in um).
C       Tet    - total elapsed time in seconds
C       Difco  - Diffusion coefficient
C       calculated:
C       Fpiped - total fraction released
C
C       Adjustable limits:
C       Ngrmax - maximum # of grains
C       nGrdat  - unit # for data input from Grname.dat
C          Cmax   - maximum terms in series is 2**Cmax
C          Error  - absolute error allowed for series convergence.
C
C       Notes: REM(J) contains the fractional loss for each individual grain.
C               Each time Fpiped is called, the result is written to a status
C               file for aid in debugging and tracking detached jobs.
C               Alternative grain description input allowed (one bin size
C               and number of grains in bin) - search on d(j). Grain geometry
C               can be specified in this routine as desired.
C
        Parameter(Ngrmax=101,nGrdat=1,nstat=6,jout=7,Cmax=40)
C
        DOUBLE PRECISION TERMR,TERMB,TERMC,SUM,SUMR,SUMB,SUMC
       1,CONV(Cmax),REALT,REALI,RMIN,RMAX,PI,R,B,C,DIFCO,TLOSS
       2,TOTVOL,VOL,Ax(Ngrmax),Bx(Ngrmax),Cx(Ngrmax),REM(Ngrmax)
       3,Q,ERROR,ONE,TWO,EIGHT,d(Ngrmax)
C
        INTEGER COUNTR
        SAVE COUNTR,SAVEF
        DATA COUNTR/0./
```

```fortran
C
          CHARACTER Grname*10,Header(3)*80,STATUS*10
C
C     The following statement function calculates the terms in the
C     infinite series for release from a parallelpiped.
C
               TERMP(z)=EIGHT/PI/PI/(TWO*REALI-ONE)**2
     &               *DEXP(-(TWO*REALI-ONE)**2*PI*PI*DIFCO/z/z*REALT)
C
      ERROR=1.D-06                              !always less than 1% of F
      ONE=1.0D+00                               !or F(i)-F(i-1).
      TWO=2.0D+00
      EIGHT=8.0D+00
      PI=4.0D+00*DATAN(ONE)                     !Calculates Doub. pres. PI
C
      OPEN(UNIT=nGrdat,File=Grname,STATUS='old')
      Read(nGrdat,1012)(header(i),i=1,3)
 1012 format(2(a80,/),a80)
      j=1
   15 Read(nGrdat,*,end=16)Cx(j),Bx(j),Ax(j)    !A is largest side.
      j=j+1
      GOTO 15
   16    Ngrain=j-1
C
C     Alternative data input format, for one bin size parameter and
C     bin degeneracy (number of grains in bin)
C
D        j=1
D   15   Read(nGrdat,*,end=16)Ax(j),d(j)
D        j=j+1
D        Bx(j)=g1*Ax(j)                         !geometry specification
D        Cx(j)=g2*Ax(j)
D        Goto 15
C
C
      IF(COUNTR.EQ.0)WRITE(jout,*)' FPIPED: NGRAIN = ', NGRAIN
      COUNTR=COUNTR+1
C
      Close(unit=nGrdat)
C
      TLOSS=0.D+00                              !INITIALIZE for Grain Assemb
ly
      TOTVOL=0.0
      RealT=Tet
      DO 300 J=1,Ngrain,1                       !MULTIGRAIN LOOP
D            WRITE(jout,*)'GRAIN # ',J
C
             REM(J)=1.                          !INITIALIZE for each grain.
             CONV(IMAX)=0.0D+00
             CONV(IMAX-1)=0.0D+00
             SUMR=0.0
             SUMB=0.0
             SUMC=0.0
C
             IMAX=4                             !CONVERGENCE LOOP INDEX
             RMAX=2.0D+00**IMAX                 !POWER INCREASE IN #TERMS
             RMIN=1.0D+00                       !COMPUTED.
C
             R=Ax(J)/1.D+04                     !data in um
             B=Bx(J)/1.D+04                     !convert to cm
             C=Cx(J)/1.D+04
C
   50        SUM=0.0                            !ENTRY POINT FOR MORE TERMS
```

369

```
              DO 100 REALI=RMIN,RMAX,1                    !LOOP FOR SERIES TERMS
                      TERMR=TERMP(R)
                      TERMB=TERMP(B)
                      TERMC=TERMP(C)
                      SUMR=SUMR+TERMR
                      SUMB=SUMB+TERMB
                      SUMC=SUMC+TERMC
                      SUM=SUMR*SUMB*SUMC
   100 CONTINUE
C                                                          !AVOID OVERFLOW FOR HIGH D
              IF(SUM.LT.1.E-20)THEN
                      SUM=0.
              ENDIF
D                      WRITE(jout,*)' # OF TERMS = 2**',IMAX
D                      WRITE(jout,*)' SUM = ',SUM
C                                                          !CONVERGENCE CRITERION
              CONV(IMAX)=SUM
              Q=(CONV(IMAX)-CONV(IMAX-1))
C
              IF(Q.GT.ERROR)THEN             !CHECK CONVERGENCE
                      RMIN=RMAX+1
                      IMAX=IMAX+1
                      IF(IMAX.GT.CMAX)THEN
                      WRITE(jout,*)' FPIPED: CAN NOT CONVERGE',IMAX
                      ENDIF
                      RMAX=2.D+00**IMAX
                      GO TO 50               !DO MORE TERMS IF NEEDED
              ENDIF
C
              REM(J)=CONV(IMAX)              !SAVE FINAL SUM
C
              VOL=R*B*C                      !NORMALIZE TO GRAIN SIZE
              TOTVOL=TOTVOL+VOL
D              TOTVOL=TOTVOL+VOL*d(J)                     !for use with bin data
              TLOSS=TLOSS+(1.D+00-REM(J))*VOL
D               TLOSS=TLOSS+(1.D+00-REM(J))*VOL*d(j) !for use with bin data
C
C
C************** STATUS FILE FOR RUNNING AS DETACHED JOB *****************
C
      STATUS=GRNAME
      STATUS(1:2)='NV'
      STATUS(8:10)='RUN'
      OPEN(UNIT=nstat,FILE=STATUS,STATUS='Unknown')
      WRITE(nstat,*)' SUM = ',SUM
      WRITE(nstat,*)' FPIPED = ',SAVEF
      CLOSE(UNIT=nstat)
C
C********************************************************************************
C
  300           CONTINUE                    !END MULTIGRAIN LOOP
C
      Fpiped=TLOSS/TOTVOL                    !total fraction lost
         SAVEF=Fpiped                                     !retain value for status fil
e
      RETURN
      END


!!!!!!!!!!!!!!!!!!!!!!!!!!!!!!!!!!!!!!!!!!!!!!!!!!!!!!!!!!!!!!!!!!!!!!!!!!!!!!!!!!!

      SUBROUTINE SPH1(ET,TF1,TF2,VTF1,VTF2,D)
C
```

```
C     Tom Trull,  July 10
C
C     PURPOSE:  Calculate diffusivity from emanation data using
C     approximation equation for equisized spheres at low F.
C     PARAMETERS
C     supplied:
C        ET     -  elapsed time for emanation step i
C        TF1    -  total fraction released through step i-1
C        TF2    -  total fraction released through step i
C        VTFx   -  variance in TFx
C     calculated:
C        D         -  diffusion coefficient (D/R**2)
C
      PARAMETER (R=1.,PI=3.14159265)
C
      G=PI*R**2/36.
      D=G/ET*(TF2**2-TF1**2)
C
      RETURN
      END
C
C*********************************************************************
C
      SUBROUTINE SPH2(ET,TF1,TF2,VTF1,VTF2,D)
C
C     Tom Trull,  July 10
C
C     PURPOSE:  Calculate diffusivity from emanation data using
C     approximation equation for equisized spheres at mid F.
C     PARAMETERS
C     supplied:
C        ET     -  elapsed time for emanation step i
C        TF1    -  total fraction released through step i-1
C        TF2    -  total fraction released through step i
C        VTFx   -  variance in TFx
C     calculated:
C        D         -  diffusion coefficient (D/R**2)
C
      PARAMETER (R=1.,PI=3.14159265)
C
      G=R**2/PI
      H=PI/3.
      D=G/ET*( -H*(TF2-TF1)-2.*(SQRT(1-H*TF2)-SQRT(1-H*TF1)) )
C
      RETURN
      END
C
C*********************************************************************
C
      SUBROUTINE SPH3(ET,TF1,TF2,VTF1,VTF2,D)
C
C     Tom Trull,  July 10
C
C     PURPOSE:  Calculate diffusivity from emanation data using
C     approximation equation for equisized spheres at high F.
C     PARAMETERS
C     supplied:
C        ET     -  elapsed time for emanation step i
C        TF1    -  total fraction released through step i-1
C        TF2    -  total fraction released through step i
C        VTFx   -  variance in TFx
C     calculated:
C        D         -  diffusion coefficient (D/R**2)
```

```
C
      PARAMETER (R=1.,PI=3.14159265)
C
      G=R**2/PI**2
         D=G/ET*ALOG( (1.-TF1)/(1.-TF2) )
C
      RETURN
      END
C
*************************************************************************
```

APPENDIX B: Helium emanation data and diffusivity results for
basaltic glasses (experiments #1-11, chap. 3).

Key to the column headings:

1. The error in the measured ^{4}He amount is given in units of parts per thousand. A value of 0 does not imply no error, but less than .5% at 1 sigma.

2. $\underline{Sm}$ designates values calculated using the equisized sphere model and $\underline{Rm}$ the refined model results.

3. The errors in F are not given but were generally less than .1% for ^{4}He and a few tenths of a percent for ^{3}He.

Experiment #1

Alv892-1a MORB tholeiite glass
1 tabular grain, 7.26mg

Grain size data (um): short side, "visual average", long side.
1397 2032 2057

Bulk helium contents: He = 6.02E-08 ccSTP   3He/4He = 8.56 +0.03 x Ra

Sequential release data:

#	Temp. C	Time hr	4He ccSTP	1s 3He o/oo	3He/4He Ra	1s Ra	F(4He) total	Dsm cm2/s	Drm cm2/s	1s cm2/s	D3/D4 sm	D3/D4 rm	1s rm
1	Ramp	0.53	1.05E-10	10.	1.17	0.41	0.0018	6.83E-13	1.09E-12	2.3E-14	0.019	0.019	0.013
2	253.	1.07	1.71E-09	6.	8.64	0.10	0.0302	1.01E-10	1.65E-10	2.2E-12	0.920	0.919	0.028
3	253.	0.53	5.96E-10	7.	8.68	0.18	0.0401	1.59E-10	2.57E-10	6.5E-12	0.978	0.978	0.056
4	253.	0.53	4.99E-10	8.	8.62	0.19	0.0484	1.69E-10	2.73E-10	8.4E-12	0.980	0.980	0.070
5	253.	0.53	4.38E-10	7.	8.64	0.26	0.0557	1.76E-10	2.84E-10	1.0E-11	0.988	0.987	0.086
6	Ramp	1.07	2.04E-09	5.	8.84	0.08	0.0896	5.84E-10	9.48E-10	1.2E-11	1.026	1.026	0.028
7	311.	0.53	1.27E-09	7.	8.97	0.11	0.1107	1.02E-09	1.67E-09	3.4E-11	1.054	1.054	0.045
8	311.	0.53	1.07E-09	7.	9.06	0.17	0.1285	1.05E-09	1.71E-09	4.4E-11	1.074	1.074	0.058
9	311.	0.53	9.36E-10	7.	9.02	0.12	0.1440	1.06E-09	1.74E-09	5.3E-11	1.075	1.075	0.068
10	Ramp	1.07	5.91E-09	7.	8.96	0.05	0.2422	5.02E-09	8.38E-09	8.4E-11	1.081	1.082	0.020
11	405.	0.53	3.34E-09	6.	8.89	0.07	0.2977	8.55E-09	1.45E-08	2.4E-10	1.082	1.084	0.033
12	405.	0.53	2.69E-09	7.	9.07	0.09	0.3425	8.62E-09	1.48E-08	3.2E-10	1.109	1.112	0.042
13	405.	0.53	2.27E-09	9.	9.06	0.09	0.3802	8.62E-09	1.50E-08	3.9E-10	1.115	1.119	0.051
14	Ramp	1.07	1.41E-08	6.	8.47	0.05	0.6145	4.55E-08	8.26E-08	4.8E-10	1.037	1.041	0.011
15	517.	0.53	4.42E-09	7.	8.80	0.07	0.6879	4.85E-08	9.18E-08	1.1E-09	1.080	1.085	0.025
16	518.	0.53	3.31E-09	6.	8.73	0.07	0.7429	4.68E-08	9.02E-08	1.3E-09	1.085	1.090	0.030
17	517.	0.53	2.57E-09	8.	8.56	0.08	0.7856	4.51E-08	8.83E-08	1.4E-09	1.075	1.079	0.034
18	517.	1.07	3.77E-09	8.	8.55	0.08	0.8481	4.38E-08	8.70E-08	7.9E-10	1.095	1.098	0.020
19	517.	0.53	1.38E-09	7.	8.33	0.10	0.8710	4.22E-08	8.42E-08	1.7E-09	1.086	1.092	0.046
20	517.	0.53	1.13E-09	7.	8.17	0.12	0.8897	4.05E-08	8.15E-08	1.9E-09	1.079	1.085	0.052
21	517.	1.07	1.77E-09	6.	8.21	0.10	0.9192	4.02E-08	8.15E-08	1.0E-09	1.109	1.113	0.031
22	517.	0.53	6.75E-10	7.	7.82	0.18	0.9304	3.86E-08	7.88E-08	2.3E-09	1.081	1.084	0.068
23	517.	0.53	5.53E-10	7.	8.19	0.16	0.9396	3.66E-08	7.48E-08	2.6E-09	1.152	1.155	0.080
24	Ramp	1.07	2.34E-09	9.	7.50	0.07	0.9785	1.34E-07	2.75E-07	1.3E-09	1.124	1.125	0.019
25	620.	0.53	5.44E-10	7.	6.94	0.13	0.9876	1.41E-07	2.91E-07	3.1E-09	1.170	1.171	0.058
26	620.	0.53	7.90E-10	7.	6.60	0.23	0.9924	1.27E-07	2.62E-07	4.0E-09	1.233	1.233	0.099
27	620.	1.07	2.60E-10	8.	6.29	0.30	0.9967	1.09E-07	2.24E-07	3.4E-09	1.479	1.479	0.138
28	620.	0.53	4.71E-11	15.	5.57	1.12	0.9975	7.05E-08	1.45E-07	8.6E-09	1.850	1.849	0.492
29	620.	2.22	1.50E-10	13.	2.66	0.33	1.0000						

Experiment #2

Alv892-1a MORB tholeiite glass
13 chips, 90.1 mg

Grain size data (um): short side, "visual average", long side.
1461 1270 1346 1372 1448 1092 965 1016 1295 1219 1143 1524 1829
1715 2159 2057 1930 1676 2134 1270 1499 1981 1321 1981 2032 1981 2134
2159 2489 2946 2769 1880 2438 2388 2591 2184 2388 2083 2235

Bulk helium contents: He = 7.75E-07 ccSTP   3He/4He = 8.35 +0.01 x Ra

Sequential release data:

#	Temp. C	Time hr	4He ccSTP	1s 3He/4He o/oo	3He/4He Ra	1s Ra	F(4He) (total)	Dsm cm2/s	Drm cm2/s	1s cm2/s	D3/D4 sm	D3/D4 rm	1s rm
1	Ramp	0.53	5.49E-11	9.	9.00	2.04	0.0001	9.62E-16	1.73E-15	2.9E-17	1.161	1.160	0.542
2	113.	0.54	2.25E-10	4.	8.68	0.64	0.0004	2.37E-14	4.26E-14	3.4E-16	1.092	1.092	0.174
3	113.	3.78	1.45E-09	3.	8.76	0.13	0.0022	1.32E-13	2.37E-13	1.4E-15	1.100	1.100	0.040
4	113.	10.25	2.66E-09	2.	8.41	0.09	0.0057	2.71E-13	4.88E-13	1.7E-15	1.038	1.038	0.024
5	113.	27.35	4.69E-09	2.	8.65	0.07	0.0117	3.94E-13	7.15E-13	2.5E-15	1.064	1.065	0.018
6	Ramp	0.54	2.51E-09	2.	8.92	0.10	0.0150	1.64E-11	2.98E-11	1.8E-13	1.104	1.105	0.032
7	209.	1.62	1.07E-08	2.	8.81	0.06	0.0287	3.81E-11	6.99E-11	2.2E-13	1.100	1.101	0.014
8	209.	2.16	9.89E-09	2.	8.76	0.05	0.0415	4.37E-11	7.91E-11	3.1E-13	1.099	1.099	0.017
9	209.	2.70	9.41E-09	2.	8.68	0.05	0.0536	4.56E-11	8.26E-11	3.8E-13	1.089	1.089	0.020
10	209.	2.70	7.91E-09	3.	8.71	0.07	0.0638	4.78E-11	8.68E-11	4.9E-13	1.092	1.092	0.025
11	209.	3.24	7.97E-09	3.	8.62	0.05	0.0741	4.75E-11	8.64E-11	5.2E-13	1.079	1.080	0.026
12	209.	3.78	8.37E-09	2.	8.57	0.06	0.0849	4.97E-11	9.06E-11	5.5E-13	1.071	1.072	0.026
13	Ramp	1.08	4.76E-09	2.	8.89	0.08	0.0911	1.10E-10	2.01E-10	2.1E-12	1.113	1.113	0.046
14	311.	0.54	1.97E-08	2.	8.66	0.05	0.1165	1.09E-09	2.00E-09	7.1E-12	1.084	1.085	0.015
15	311.	1.08	3.13E-08	1.	8.73	0.07	0.1568	1.17E-09	2.17E-09	5.7E-12	1.095	1.096	0.013
16	311.	0.54	1.23E-08	2.	8.73	0.07	0.1727	1.14E-09	2.12E-09	1.3E-11	1.097	1.099	0.031
17	311.	0.54	1.09E-08	1.	8.77	0.07	0.1867	1.12E-09	2.08E-09	1.5E-11	1.103	1.105	0.037
18	311.	3.54	9.90E-09	1.	8.58	0.07	0.1995	1.11E-09	2.07E-09	1.6E-11	1.079	1.081	0.041
19	311.	1.08	1.78E-08	1.	8.68	0.07	0.2224	1.10E-09	2.07E-09	9.5E-12	1.093	1.095	0.025
20	311.	0.54	8.04E-09	1.	8.72	0.08	0.2328	1.10E-09	2.06E-09	2.0E-11	1.099	1.101	0.055
21	311.	1.08	1.50E-08	1.	8.64	0.06	0.2521	1.10E-09	2.08E-09	1.2E-11	1.089	1.092	0.031
22	311.	1.08	1.36E-08	1.	8.68	0.06	0.2696	1.10E-09	2.08E-09	1.3E-11	1.095	1.097	0.035
23	Ramp	1.10	3.93E-08	1.	8.71	0.06	0.3203	3.67E-09	7.01E-09	1.8E-11	1.101	1.104	0.015
24	421.	0.54	4.56E-08	1.	8.62	0.06	0.3791	1.09E-08	2.11E-08	5.2E-11	1.093	1.097	0.014
25	421.	0.54	3.61E-08	1.	8.65	0.06	0.4256	1.06E-08	2.08E-08	6.4E-11	1.100	1.104	0.018
26	421.	0.54	2.99E-08	1.	8.67	0.06	0.4642	1.03E-08	2.04E-08	7.5E-11	1.107	1.112	0.022
27	421.	1.08	4.89E-08	1.	8.52	0.06	0.5273	1.01E-08	2.03E-08	5.0E-11	1.091	1.097	0.015
28	421.	0.54	2.04E-08	1.	8.57	0.06	0.5537	9.91E-09	2.01E-08	1.1E-10	1.102	1.108	0.033

continued

376

Experiment #2 (continued)

#	Temp. C	Time hr	4He ccSTP	1s o/oo	3He/4He Ra	1s Ra	F(4He) (total)	Dsm cm2/s	Drm cm2/s	1s cm2/s	D3/D4 sm	D3/D4 rm	1s rm
29	Ramp	0.54	5.46E-08	1.	8.45	0.06	0.6241	3.15E-08	6.48E-08	1.4E-10	1.090	1.097	0.013
30	519.	0.54	5.84E-08	1.	8.31	0.06	0.6994	4.41E-08	9.28E-08	1.8E-10	1.079	1.086	0.012
31	519.	0.54	4.27E-08	1.	8.24	0.06	0.7545	4.19E-08	9.01E-08	2.1E-10	1.079	1.087	0.014
32	519.	0.54	3.29E-08	1.	8.18	0.06	0.7969	4.03E-08	8.83E-08	2.5E-10	1.082	1.091	0.017
33	519.	1.08	4.74E-08	1.	7.93	0.05	0.8580	3.89E-08	8.71E-08	1.5E-10	1.066	1.073	0.010
34	Ramp	0.54	4.07E-08	1.	7.86	0.05	0.9105	1.02E-07	2.35E-07	1.5E-10	1.079	1.091	0.009
35	620.	0.54	3.16E-08	1.	7.56	0.05	0.9514	1.34E-07	3.22E-07	3.7E-10	1.081	1.092	0.008
36	620.	0.54	1.66E-08	1.	7.17	0.05	0.9728	1.28E-07	3.17E-07	3.9E-10	1.076	1.087	0.011
37	620.	0.54	9.03E-09	1.	6.91	0.07	0.9845	1.23E-07	3.13E-07	4.3E-10	1.084	1.095	0.014
38	620.	0.54	5.06E-09	1.	6.62	0.07	0.9910	1.20E-07	3.12E-07	5.3E-10	1.090	1.102	0.019
39	620.	1.08	4.60E-09	1.	6.10	0.07	0.9969	1.18E-07	3.16E-07	2.6E-10	1.059	1.072	0.019
40	620.	0.54	9.78E-10	1.	6.11	0.19	0.9982	1.16E-07	3.18E-07	6.3E-10	1.137	1.152	0.050
41	620.	0.54	5.61E-10	1.	5.69	0.26	0.9989	1.12E-07	3.12E-07	9.3E-10	1.137	1.153	0.060
42	620.	4.32	8.46E-10	1.	4.82	0.14	1.0000						

Experiment #3

Alv892-1a MORB variolitic glass
2 chips, 28.2mg

Grain size data (um): short side, "visual average", long side.
1575 2692 3962
1676 2235 3988

Bulk helium contents: He = 2.17E-07 ccSTP   3He/4He = 8.55 +0.04 x Ra

Sequential release data:

#	Temp. C	Time hr	4He ccSTP	1s o/oo	3He/4He Ra	1s Ra	F (4He) (total)	Dsm cm2/s	Drm cm2/s	1s cm2/s	D3/D4 sm	D3/D4 rm	1s rm
1	Ramp	0.53	5.62E-10	1.	9.03	0.22	0.0026	2.00E-12	4.21E-12	6.8E-15	1.116	1.116	0.057
2	211.	0.54	1.04E-09	0.	8.64	0.14	0.0074	1.41E-11	2.96E-11	4.4E-14	1.045	1.045	0.035
3	211.	4.87	5.20E-09	0.	8.72	0.06	0.0313	3.03E-11	6.49E-11	8.4E-14	1.044	1.045	0.017
4	211.	4.88	3.35E-09	0.	8.65	0.07	0.0467	4.07E-11	8.58E-11	1.8E-13	1.033	1.033	0.026
5	211.	6.50	3.55E-09	0.	8.56	0.06	0.0630	4.60E-11	9.73E-11	2.5E-13	1.019	1.019	0.028
6	211.	7.58	3.53E-09	3.	9.15	0.20	0.0793	5.16E-11	1.09E-10	4.3E-13	1.095	1.095	0.041
7	Ramp	0.54	2.00E-09	3.	9.62	0.22	0.0884	4.87E-10	1.04E-09	7.6E-12	1.164	1.165	0.078
8	311.	0.54	3.98E-09	3.	9.31	0.20	0.1068	1.14E-09	2.44E-09	1.2E-11	1.138	1.139	0.051
9	311.	1.08	6.80E-09	3.	9.27	0.20	0.1380	1.25E-09	2.68E-09	1.1E-11	1.146	1.147	0.043
10	311.	1.63	8.14E-09	2.	9.03	0.19	0.1755	1.32E-09	2.84E-09	1.2E-11	1.124	1.126	0.045
11	311.	1.63	6.69E-09	3.	9.01	0.19	0.2062	1.36E-09	2.95E-09	1.7E-11	1.124	1.126	0.059
12	311.	1.63	5.72E-09	2.	8.97	0.20	0.2325	1.38E-09	2.99E-09	2.1E-11	1.120	1.122	0.073
13	Ramp	0.54	7.17E-09	3.	9.06	0.19	0.2655	6.06E-09	1.32E-08	8.3E-11	1.130	1.137	0.064
14	415.	0.54	1.17E-08	3.	8.88	0.19	0.3192	1.21E-08	2.67E-08	1.2E-10	1.114	1.117	0.047
15	415.	0.54	9.44E-09	2.	8.94	0.19	0.3625	1.21E-08	2.68E-08	1.6E-10	1.124	1.128	0.060
16	415.	1.08	1.53E-08	3.	8.85	0.19	0.4329	1.23E-08	2.75E-08	1.2E-10	1.116	1.120	0.042
17	415.	0.54	6.25E-09	3.	8.81	0.20	0.4616	1.20E-08	2.72E-08	2.6E-10	1.115	1.119	0.098
18	Ramp	0.54	1.58E-08	3.	8.72	0.19	0.5342	3.65E-08	8.33E-08	3.5E-10	1.107	1.111	0.043
19	517.	0.54	1.89E-08	3.	8.65	0.18	0.6210	5.80E-08	1.34E-07	4.8E-10	1.104	1.108	0.036
20	517.	1.08	2.48E-08	2.	8.47	0.18	0.7350	5.57E-08	1.30E-07	2.9E-10	1.093	1.096	0.022
21	517.	0.54	8.45E-09	2.	8.48	0.19	0.7739	5.19E-08	1.22E-07	6.5E-10	1.110	1.113	0.052
22	517.	0.54	6.90E-09	3.	8.23	0.18	0.8056	5.03E-08	1.19E-07	7.1E-10	1.090	1.092	0.059
23	517.	1.08	1.08E-08	3.	8.09	0.18	0.8551	4.97E-08	1.18E-07	3.9E-10	1.090	1.089	0.032
24	517.	0.54	4.09E-09	2.	8.17	0.19	0.8740	4.77E-08	1.13E-07	8.3E-10	1.113	1.121	0.072
25	517.	0.54	3.49E-09	3.	7.95	0.18	0.8900	4.67E-08	1.12E-07	9.0E-10	1.100	1.106	0.080
26	517.	1.08	5.69E-09	2.	7.77	0.18	0.9162	4.65E-08	1.12E-07	5.1E-10	1.095	1.101	0.045
27	Ramp	0.54	5.13E-09	2.	7.60	0.17	0.9398	1.13E-07	2.75E-07	1.1E-09	1.104	1.108	0.043
28	619.	0.54	5.09E-09	2.	7.34	0.17	0.9632	1.68E-07	4.12E-07	1.4E-09	1.114	1.117	0.035
29	619.	1.08	5.04E-09	2.	6.78	0.16	0.9863	1.70E-07	4.19E-07	6.3E-10	1.110	1.110	0.020
30	619.	0.54	1.14E-09	3.	6.04	0.19	0.9916	1.66E-07	4.10E-07	4.4E-09	1.067	1.068	0.049
31	619.	0.54	6.96E-10	3.	5.86	0.22	0.9948	1.64E-07	4.05E-07	1.7E-09	1.071	1.072	0.063
32	619.	1.08	7.15E-10	3.	5.44	0.19	0.9981	1.70E-07	4.22E-07	1.1E-09	1.022	1.022	0.054
33	619.	1.63	3.42E-10	3.	5.15	0.22	0.9996	1.92E-07	4.75E-07	1.1E-09	0.949	0.949	0.121
34	619.	1.63	7.85E-11	4.	5.73	1.08	1.0000						

378

Experiment #4

Alv892-1a MORB tholeiite glass
300-355 um sieve fraction, 55.8mg

Grain size data (um): short side, "visual average", long side.
493 462 385 431 462 339 462 308 308 462 308
539 770 385 462 462 462 462 308 616 616
601 924 1540 1078 770 739 924 924 462 616 770

Bulk helium contents: He = 4.48E-07 ccSTP   3He/4He = 8.32 +0.02 x Ra
prior loss corrected: He = 4.61E-07 ccSTP   3He/4He = 8.34 +0.02 x Ra
2.6% with 3He/4He release ratio of 1.056.

Bulk helium contents:

Sequential release data:

#	Temp. C	Time hr	4He ccSTP	1s o/oo	3He/4He Ra	1s Ra	F (4He) (total)	Dsm cm2/s	Drm cm2/s	1s cm2/s	D3/D4 sm	D3/D4 rm	1s rm
1	Ramp	1.08	3.25E-10	1.	8.16	0.29	0.0279	Prior loss corrected fractional release.		2.2E-16	0.993	1.013	0.047
2	123.	0.54	6.45E-10	1.	8.45	0.21	0.0293	9.63E-13	1.33E-13	1.3E-15	1.027	1.063	0.017
3	123.	6.51	9.09E-09	0.	8.62	0.07	0.0490	1.60E-12	1.34E-12	2.9E-15	1.052	1.080	0.021
4	123.	6.50	6.10E-09	0.	8.71	0.08	0.0623	1.54E-12	2.18E-12	3.9E-15	1.047	1.068	0.015
5	123.	11.69	8.92E-09	1.	8.60	0.06	0.0816	1.65E-12	2.83E-12	1.5E-13	1.070	1.088	0.018
6	Ramp	0.54	9.92E-09	1.	8.74	0.08	0.1031	5.16E-11	1.01E-10	3.4E-13	1.073	1.087	0.014
7	236.	0.54	1.76E-08	1.	8.70	0.06	0.1413	1.24E-10	2.69E-10	4.5E-13	1.083	1.094	0.011
8	236.	1.08	3.14E-08	1.	8.71	0.06	0.2094	1.67E-10	4.00E-10	1.1E-12	1.077	1.086	0.025
9	236.	0.54	1.27E-08	1.	8.62	0.06	0.2369	1.79E-10	4.49E-10	8.7E-13	1.075	1.083	0.016
10	236.	1.08	2.14E-08	0.	8.59	0.05	0.2833	1.84E-10	4.73E-10	2.0E-12	1.088	1.096	0.037
11	236.	0.54	9.05E-09	1.	8.69	0.07	0.3029	1.81E-10	4.77E-10	2.3E-12	1.085	1.092	0.041
12	236.	0.54	8.30E-09	1.	8.65	0.08	0.3209	1.81E-10	4.80E-10	1.4E-12	1.086	1.093	0.024
13	236.	1.08	1.51E-08	1.	8.64	0.06	0.3537	1.83E-10	4.93E-10	3.2E-12	1.089	1.096	0.052
14	236.	0.54	6.83E-09	1.	8.65	0.06	0.3685	1.82E-10	4.96E-10	3.5E-12	1.081	1.088	0.055
15	236.	0.54	6.50E-09	1.	8.58	0.06	0.3827	1.84E-10	5.03E-10	2.0E-12	1.077	1.084	0.031
16	236.	1.08	1.22E-08	1.	8.54	0.06	0.4091	1.86E-10	5.15E-10	2.4E-12	1.084	1.091	0.034
17	236.	1.08	1.11E-08	1.	8.58	0.06	0.4331	1.86E-10	5.19E-10	2.7E-12	1.071	1.078	0.038
18	236.	1.08	1.00E-08	1.	8.47	0.06	0.4548	1.83E-10	5.16E-10	3.0E-12	1.076	1.083	0.043
19	236.	1.08	9.12E-09	1.	8.51	0.07	0.4746	1.80E-10	5.11E-10	3.4E-12	1.077	1.083	0.048
20	236.	1.08	8.20E-09	1.	8.50	0.08	0.4924	1.73E-10	4.95E-10	3.7E-12	1.077	1.084	0.052
21	236.	1.08	7.65E-09	1.	8.42	0.07	0.5090	1.72E-10	5.08E-10	4.0E-12	1.068	1.075	0.055
22	236.	1.08	7.38E-09	1.	8.42	0.07	0.5250	1.75E-10	4.97E-10	4.4E-12	1.068	1.075	0.060
23	236.	1.08	6.81E-09	1.	8.48	0.06	0.5397	1.71E-10	5.14E-10	4.7E-12	1.077	1.084	0.062
24	236.	1.08	6.64E-09	1.	8.44	0.06	0.5541	1.75E-10	5.12E-10	5.2E-12	1.072	1.079	0.066
25	236.	1.08	6.27E-09	1.	8.45	0.05	0.5677	1.74E-10	5.23E-10	3.8E-12	1.075	1.082	0.048
26	236.	1.63	8.99E-09	1.	8.34	0.04	0.5872	1.76E-10	5.10E-10	4.2E-12	1.063	1.069	0.053
27	236.	1.63	8.16E-09	1.	8.46	0.08	0.6049	1.71E-10	5.03E-10	4.5E-12	1.079	1.086	0.058
28	236.	1.63	7.52E-09	1.			0.6213	1.68E-10					

continued

Experiment #4

#	Temp. C	Time hr	4He ccSTP	1s o/oo	3He/4He Ra	1s Ra	F(4He) (total)	Dsm cm2/s	Drm cm2/s	1s cm2/s	D3/D4 sm	D3/D4 rm	1s rm
29	236.	1.63	7.06E-09	1.	8.40	0.07	0.6366	1.67E-10	5.04E-10	4.9E-12	1.074	1.080	0.063
30	236.	1.63	6.64E-09	1.	8.47	0.06	0.6510	1.66E-10	5.03E-10	5.5E-12	1.084	1.091	0.068
31	236.	1.63	6.13E-09	1.	8.34	0.05	0.6643	1.61E-10	4.92E-10	5.8E-12	1.069	1.076	0.074
32	236.	1.63	5.83E-09	1.	8.41	0.07	0.6769	1.61E-10	4.94E-10	6.2E-12	1.079	1.087	0.079
33	236.	1.63	5.47E-09	1.	8.39	0.06	0.6888	1.59E-10	4.89E-10	6.7E-12	1.079	1.087	0.084
34	236.	1.63	5.15E-09	1.	8.46	0.08	0.6999	1.57E-10	4.84E-10	7.0E-12	1.090	1.098	0.091
35	236.	1.63	4.91E-09	1.	8.38	0.06	0.7106	1.56E-10	4.84E-10	7.4E-12	1.082	1.090	0.096
36	236.	1.63	4.64E-09	1.	8.41	0.06	0.7207	1.54E-10	4.80E-10	8.0E-12	1.087	1.095	0.103
37	236.	1.63	4.35E-09	1.	8.25	0.07	0.7301	1.50E-10	4.70E-10	8.6E-12	1.068	1.076	0.110
38	236.	1.63	4.09E-09	1.	8.43	0.07	0.7390	1.47E-10	4.61E-10	9.1E-12	1.095	1.103	0.119
39	236.	1.63	3.82E-09	1.	8.23	0.07	0.7473	1.42E-10	4.49E-10	9.4E-12	1.071	1.080	0.127
40	236.	1.63	3.72E-09	1.	8.41	0.08	0.7553	1.44E-10	4.56E-10	9.9E-12	1.095	1.103	0.132
41	236.	2.69	6.04E-09	0.	8.16	0.05	0.7684	1.49E-10	4.73E-10	6.6E-12	1.066	1.075	0.084
42	236.	2.71	5.56E-09	0.	8.17	0.06	0.7805	1.44E-10	4.61E-10	7.0E-12	1.069	1.077	0.092
43	236.	2.71	5.19E-09	0.	8.20	0.07	0.7917	1.43E-10	4.59E-10	7.7E-12	1.076	1.085	0.100
44	236.	2.71	4.80E-09	0.	8.31	0.06	0.8022	1.39E-10	4.51E-10	8.1E-12	1.095	1.104	0.109
45	236.	2.71	4.36E-09	0.	8.30	0.07	0.8116	1.34E-10	4.34E-10	8.6E-12	1.098	1.107	0.121
46	236.	2.71	4.18E-09	0.	8.20	0.06	0.8207	1.35E-10	4.41E-10	9.4E-12	1.090	1.098	0.128
47	236.	2.71	3.94E-09	0.	8.27	0.07	0.8292	1.35E-10	4.41E-10	1.0E-11	1.104	1.113	0.137
48	236.	3.25	4.41E-09	0.	8.21	0.07	0.8388	1.32E-10	4.36E-10	9.0E-12	1.102	1.110	0.125
49	236.	2.71	3.65E-09	1.	8.17	0.09	0.8467	1.40E-10	4.61E-10	1.2E-11	1.103	1.109	0.152
50	Ramp	0.54	7.03E-09	1.	7.46	0.06	0.9993	7.51E-08	2.97E-07	1.0E-10	1.067	1.081	0.014
51	620.	0.54	3.24E-10	2.	5.20	0.35	1.0000						

Experiment #5

Alv892-1a MORB tholeiite glass
75-106um sieve fraction, 259.2 mg

Grain size data (um):
100 "mean diameter" measurements grouped by size (um)
Side lengths approximated from inspection as : x,.75x,.75x
Bin size:30 36 48 54 60 66 72 78 84 90 96 102 108 114 120 126 138
in bin: 1 2 2 2 6 7 6 11 19 26 6 7 1 1 1 1 1

Bulk helium contents: He = 2.00E-06 ccSTP   3He/4He = 8.23 +0.01 x Ra
prior loss corrected: He = 2.13E-06 ccSTP   3He/4He = 8.26 +0.01 x Ra
5.8% with 3He/4He diffusivity ratio of 1.056.

Sequential release data:

#	Temp. C	Time hr	4He ccSTP	1s o/oo	3He/4He Ra	1s Ra	F(4He) (total)	Dsm cm2/s	Drm cm2/s	1s cm2/s	D3/D4 sm	D3/D4 rm	1s rm
1	21.	16.22	8.22E-10	1.	7.97	0.18	0.0582	Prior loss corrected fractional release.		2.2E-17	1.172	1.165	0.820
2	21.	11.90	5.72E-10	1.	9.06	0.17	0.0585	1.35E-15	9.08E-16	1.6E-17	1.102	1.095	0.626
3	21.	16.22	7.52E-10	1.	8.52	0.20	0.0589	1.31E-15	8.80E-16	9.8E-18	1.087	1.093	0.391
4	21.	26.50	1.21E-09	0.	8.50	0.15	0.0594	1.31E-15	8.72E-16	9.8E-18	1.079	1.076	0.362
5	21.	28.66	1.30E-09	0.	8.37	0.12	0.0600	1.32E-15	8.81E-16	9.5E-18	1.082	1.078	0.358
6	21.	29.78	1.32E-09	1.	8.39	0.14	0.0607	1.29E-15	8.68E-16	1.0E-17	1.063	1.068	0.367
7	21.	28.13	1.29E-09	1.	8.33	0.11	0.0613	1.35E-15	9.05E-16	1.3E-17	1.092	1.091	0.447
8	21.	22.72	1.06E-09	1.	8.51	0.13	0.0618	1.39E-15	9.31E-16	1.3E-16	1.117	1.116	1.016
9	Ramp	2.16	4.64E-10	1.	8.72	0.18	0.0620	6.46E-15	4.32E-15	5.2E-16	1.066	1.082	1.250
10	47.	0.54	3.36E-10	1.	8.39	0.32	0.0621	1.89E-14	1.25E-14	3.3E-17	1.097	1.098	0.076
11	47.	9.74	6.34E-10	0.	8.56	0.05	0.0651	2.01E-14	1.35E-14	3.3E-17	1.096	1.096	0.066
12	47.	12.98	7.48E-10	0.	8.55	0.06	0.0686	1.88E-14	1.26E-14	2.8E-17	1.087	1.089	0.070
13	47.	11.90	7.04E-10	1.	8.50	0.07	0.0720	2.03E-14	1.36E-14	3.5E-17	1.070	1.070	0.072
14	47.	12.98	6.83E-10	0.	8.36	0.07	0.0752	1.90E-14	1.27E-14	3.7E-17	1.100	1.105	0.452
15	Ramp	0.54	1.07E-09	1.	8.65	0.19	0.0757	7.38E-14	4.94E-14	8.9E-16	1.097	1.098	0.034
16	77.	4.33	1.52E-08	0.	8.59	0.05	0.0828	1.37E-13	9.20E-14	1.4E-16	1.088	1.090	0.038
17	77.	3.79	1.36E-08	0.	8.53	0.05	0.0892	1.53E-13	1.03E-13	1.9E-16	1.098	1.099	0.041
18	77.	4.3;	1.28E-08	0.	8.61	0.05	0.0952	1.36E-13	9.18E-14	1.8E-16	1.072	1.074	0.036
19	77.	5.41	1.52E-08	0.	8.68	0.05	0.1024	1.39E-13	9.42E-14	1.8E-16	1.027	1.028	0.035
20	77.	6.49	1.58E-08	0.	8.42	0.04	0.1098	1.30E-13	8.81E-14	1.7E-16	1.097	1.099	0.105
21	Ramp	0.53	5.15E-09	0.	8.07	0.07	0.1122	5.47E-13	3.71E-13	2.2E-15	1.091	1.093	0.053
22	112.	0.54	1.04E-08	0.	8.63	0.04	0.1171	1.12E-12	7.57E-13	2.3E-15	1.095	1.097	0.019
23	112.	1.62	3.09E-08	0.	8.58	0.03	0.1317	1.21E-12	8.26E-13	1.0E-15	1.093	1.093	0.022
24	112.	1.62	2.80E-08	1.	8.61	0.05	0.1448	1.24E-12	8.46E-13	1.3E-15	1.097	1.097	0.036
25	112.	1.08	1.73E-08	1.	8.62	0.06	0.1530	1.25E-12	8.55E-13	2.1E-15	1.099	1.099	0.039
26	112.	1.08	1.63E-08	1.	8.56	0.06	0.1606	1.24E-12	8.53E-13	2.4E-15	1.090	1.092	0.039
27	112.	1.08	1.58E-08	1.	8.57	0.06	0.1681	1.27E-12	8.77E-13	2.6E-15	1.091	1.093	0.041

continued

Experiment #5 (continued)

#	Temp. C	Time hr	4He ccSTP	1s o/oo	3He/4He Ra	1s Ra	F(4He) (total)	Dsm cm2/s	Drm cm2/s	1s cm2/s	D3/D4 sm	D3/D4 rm	1s rm
28	Ramp	1.08	3.29E-08	1.	8.68	0.06	0.1835	2.86E-12	1.98E-12	3.3E-15	1.105	1.108	0.021
29	150.	0.54	5.60E-08	1.	8.55	0.05	0.2099	1.12E-11	7.76E-12	9.1E-15	1.090	1.093	0.015
30	150.	0.54	4.82E-08	1.	8.62	0.05	0.2325	1.11E-11	7.73E-12	1.1E-14	1.100	1.103	0.018
31	150.	1.08	8.05E-08	1.	8.48	0.05	0.2704	1.08E-11	7.65E-12	8.1E-15	1.083	1.086	0.012
32	150.	0.54	3.49E-08	1.	8.57	0.05	0.2868	1.07E-11	7.62E-12	1.8E-14	1.094	1.098	0.027
33	150.	0.54	3.19E-08	1.	8.54	0.06	0.3018	1.05E-11	7.53E-12	2.0E-14	1.091	1.095	0.030
34	Cool	11.90	1.60E-08	1.	8.40	0.06	0.3093	2.52E-13	1.81E-13	9.9E-16	1.073	1.078	0.060
35	Ramp	0.53	6.00E-08	0.	8.66	0.05	0.3375	2.30E-13	1.66E-13	2.6E-14	1.108	1.113	0.017
36	210.	0.54	1.69E-07	1.	8.50	0.04	0.4168	7.87E-11	5.80E-11	4.5E-14	1.091	1.097	0.008
37	210.	1.08	2.15E-07	0.	8.40	0.03	0.5178	7.02E-11	5.36E-11	3.3E-14	1.081	1.089	0.006
38	210.	0.54	8.60E-08	1.	8.20	0.05	0.5582	7.20E-11	5.66E-11	7.9E-14	1.058	1.067	0.014
39	210.	0.54	7.57E-08	1.	8.26	0.05	0.5938	7.25E-11	5.80E-11	8.7E-14	0.966	1.075	0.016
40	210.	1.08	1.22E-07	1.	7.84	0.05	0.6510	6.90E-11	5.65E-11	5.2E-14	1.008	1.016	0.009
41	210.	1.08	9.82E-08	1.	8.05	0.05	0.6972	6.76E-11	5.70E-11	5.9E-14	1.031	1.039	0.010
42	210.	1.22	2.90E-08	1.	8.18	0.05	0.7390	6.50E-11	5.62E-11	5.7E-14	1.031	1.039	0.010
43	210.	0.54	3.39E-08	1.	8.15	0.06	0.7549	6.31E-11	5.56E-11	1.3E-13	1.049	1.058	0.023
44	210.	0.54	3.13E-08	1.	8.08	0.05	0.7697	6.26E-11	5.57E-11	1.4E-13	1.047	1.056	0.024
45	210.	1.08	5.56E-08	1.	8.11	0.05	0.7958	6.14E-11	5.55E-11	6.6E-14	1.040	1.049	0.013
46	210.	0.54	2.43E-08	1.	8.07	0.05	0.8073	5.93E-11	5.43E-11	1.5E-13	1.047	1.056	0.027
47	210.	1.08	2.26E-08	1.	7.92	0.05	0.8373	5.84E-11	5.39E-11	1.4E-13	1.027	1.036	0.028
48	210.	0.54	4.13E-08	1.	7.99	0.06	0.8458	5.86E-11	5.47E-11	7.2E-14	1.039	1.046	0.014
49	210.	0.54	1.81E-08	1.	8.04	0.06	0.8537	5.63E-11	5.31E-11	1.4E-13	1.048	1.055	0.030
50	210.	1.08	1.68E-08	1.	7.98	0.06	0.8676	5.51E-11	5.22E-11	1.5E-13	1.039	1.051	0.032
51	210.	0.54	2.94E-08	1.	8.05	0.05	0.8737	5.23E-11	5.00E-11	7.4E-14	1.051	1.062	0.017
52	210.	0.54	1.30E-08	1.	8.01	0.07	0.8795	4.99E-11	4.82E-11	1.6E-13	1.048	1.060	0.037
53	210.	1.08	1.23E-08	1.	7.94	0.07	0.8904	5.02E-11	4.94E-11	1.7E-13	1.051	1.054	0.019
54	210.	0.54	2.33E-08	0.	8.00	0.05	0.8954	4.89E-11	4.86E-11	8.2E-14	1.040	1.066	0.040
55	210.	0.54	1.06E-08	1.	7.91	0.06	0.9001	4.83E-11	4.83E-11	1.7E-13	1.053	1.056	0.041
56	210.	1.08	9.97E-09	1.	7.86	0.07	0.9089	4.89E-11	4.93E-11	1.8E-13	1.044	1.052	0.021
57	210.	0.54	1.88E-08	1.	7.85	0.05	0.9130	4.76E-11	4.85E-11	9.0E-14	1.043	1.055	0.044
58	210.	0.54	8.56E-09	1.	7.86	0.07	0.9168	4.76E-11	4.88E-11	1.7E-13	1.045	1.056	0.044
59	210.	1.08	8.19E-09	1.	7.79	0.05	0.9240	4.80E-11	4.95E-11	1.9E-13	1.039	1.053	0.023
60	210.	0.54	1.54E-08	1.	7.77	0.08	0.9273	4.63E-11	4.83E-11	7.9E-14	1.039	1.051	0.048
61	210.	0.54	6.94E-09	1.	7.91	0.07	0.9304	4.53E-11	4.74E-11	1.8E-13	1.059	1.073	0.051
62	210.	1.08	6.50E-09	1.	7.76	0.06	0.9361	4.56E-11	4.81E-11	8.8E-14	1.043	1.057	0.026
63	210.	0.54	1.23E-08	1.	7.74	0.07	0.9388	4.44E-11	4.73E-11	2.1E-13	1.044	1.057	0.055
64	210.	0.54	5.61E-09	1.	7.79	0.07	0.9413	4.50E-11	4.82E-11	1.2E-13	1.052	1.065	0.056
65	210.	1.08	5.44E-09	1.	7.63	0.06	0.9462	4.56E-11	4.91E-11	1.9E-13	1.034	1.048	0.029
66	210.	0.54	1.03E-08	1.	7.69	0.06	0.9484	4.36E-11	4.73E-11	2.0E-13	1.044	1.059	0.061

continued

Experiment #5 (continued)

#	Temp. C	Time hr	4He ccSTP	1s o/oo	3He/4He Ra	1s Ra	F (4He) (total)	Dsm cm2/s	Drm cm2/s	1s cm2/s	D3/D4 sm	D3/D4 rm	1s rm
68	Ramp	0.54	7.96E-09	1.	7.75	0.08	0.9521	7.92E-11	8.67E-11	2.4E-13	1.055	1.069	0.035
69	240.	0.54	1.13E-08	1.	7.63	0.06	0.9574	1.24E-10	1.37E-10	2.3E-13	1.044	1.060	0.023
70	240.	1.08	1.88E-08	1.	7.50	0.05	0.9663	1.23E-10	1.39E-10	1.1E-13	1.033	1.048	0.013
71	240.	0.54	7.60E-09	1.	7.45	0.06	0.9699	1.18E-10	1.36E-10	2.3E-13	1.031	1.047	0.028
72	Ramp	1.08	1.42E-08	0.	7.52	0.04	0.9766	1.32E-10	1.56E-10	1.1E-13	1.048	1.066	0.015
73	270.	0.54	1.21E-08	0.	7.42	0.06	0.9822	2.93E-10	3.57E-10	2.4E-13	1.048	1.069	0.014
74	270.	0.54	8.86E-09	0.	7.28	0.04	0.9864	2.82E-10	3.55E-10	2.5E-13	1.040	1.062	0.018
75	270.	1.62	1.53E-08	0.	7.07	0.05	0.9936	2.64E-10	3.54E-10	9.8E-14	1.024	1.047	0.009
76	270.	0.54	2.72E-09	0.	6.91	0.10	0.9949	2.35E-10	3.33E-10	3.5E-13	1.013	1.036	0.033
77	Ramp	1.08	4.49E-09	0.	6.65	0.07	0.9970	2.80E-10	4.15E-10	1.9E-13	0.970	0.989	0.019
78	299.	0.54	2.01E-09	0.	6.55	0.10	0.9979	3.96E-10	6.16E-10	4.7E-13	0.935	0.950	0.032
79	299.	0.54	1.18E-09	1.	6.36	0.12	0.9985	3.29E-10	5.29E-10	5.8E-13	0.881	0.891	0.046
80	299.	1.08	1.17E-09	0.	6.37	0.14	0.9990	2.38E-10	3.96E-10	4.0E-13	0.836	0.841	0.040
81	299.	0.54	2.82E-10	1.	7.30	0.31	0.9992	1.56E-10	2.65E-10	9.0E-13	0.914	0.917	0.133
82	299.	0.54	1.89E-10	2.	7.14	0.72	0.9993	1.19E-10	2.04E-10	8.2E-13	0.883	0.885	0.167
83	Ramp	1.08	1.09E-09	0.	8.25	0.19	0.9998	6.13E-10	1.09E-09	1.1E-12	1.028	1.030	0.030
84	425.	0.54	2.74E-10	1.	7.85	0.33	0.9999	8.58E-10	1.60E-09	3.2E-12	0.995	0.997	0.070
85	425.	2.16	2.18E-10	2.	7.90	0.43	1.0000						

Additional steps at 600C released no measurable helium.

Experiment #6

Alv892-1a MORB tholeiite glass
38-53 um sieve fraction, 110.6mg

Grain size data (um):
100 "mean diameter" measurements grouped by size
Side lengths approximated from inspection as : x,.75x,.75x
Bin size:18 24 30 36 42 48 54 60 66 72
in bin: 2 8 16 25 13 17 9 6 1 3

Bulk helium contents: He = 8.87E-07 ccSTP   3He/4He = 8.31 +0.01 x Ra
prior loss corrected: He = 9.78E-07 ccSTP   3He/4He = 8.35 +0.01
9.3% with 3He/4He diffusivity ratio of 1.054.

Sequential release data:

Prior loss corrected fractional release.

#	Temp. C	Time hr	4He ccSTP	1s o/oo	3He/4He Ra	1s Ra	F(4He) (total)	Dsm cm2/s	Drm cm2/s	1s cm2/s	D3/D4 sm	D3/D4 rm	1s rm
1	26.	3.25	5.22E-10	0.	8.82	0.30	0.0935	3.57E-15	2.89E-15	2.3E-17	1.095	1.098	0.264
2	26.	11.39	1.66E-09	1.	8.65	0.11	0.0952	4.25E-15	3.44E-15	2.3E-17	1.064	1.066	0.207
3	26.	12.47	2.12E-09	0.	8.40	0.11	0.0974	3.37E-15	2.73E-15	2.2E-17	1.112	1.113	0.266
4	26.	12.47	1.64E-09	0.	8.79	0.09	0.0991	4.05E-15	3.28E-15	2.2E-17	1.107	1.109	0.209
5	26.	13.57	2.10E-09	0.	8.75	0.09	0.1012	3.98E-15	3.23E-15	2.0E-17	1.059	1.060	0.189
6	26.	15.64	2.33E-09	0.	8.37	0.18	0.1036	3.91E-14	3.18E-14	6.0E-16	1.079	1.081	0.561
7	Ramp	0.54	7.79E-10	1.	8.53	0.11	0.1044	6.49E-14	5.28E-14	3.2E-16	1.095	1.098	0.174
8	50.	1.08	2.54E-09	0.	8.67	0.11	0.1070	7.17E-14	5.83E-14	1.8E-16	1.087	1.089	0.083
9	50.	2.17	5.39E-09	0.	8.61	0.08	0.1125	6.50E-14	5.31E-14	1.6E-16	1.096	1.098	0.078
10	50.	2.71	5.78E-09	1.	8.68	0.08	0.1184	5.47E-14	4.47E-14	1.7E-16	1.080	1.083	0.097
11	50.	2.71	4.63E-09	0.	8.56	0.08	0.1232	5.46E-14	4.47E-14	1.1E-16	1.067	1.068	0.058
12	50.	4.88	7.85E-09	0.	8.46	0.06	0.1312	5.60E-14	4.60E-14	1.3E-16	1.079	1.081	0.061
13	50.	4.88	7.54E-09	0.	8.57	0.07	0.1389	1.35E-12	1.11E-12	1.5E-15	1.102	1.104	0.027
14	Ramp	0.54	1.82E-08	0.	8.75	0.05	0.1575	2.34E-12	1.95E-12	2.2E-15	1.084	1.087	0.020
15	118.	0.54	2.66E-08	0.	8.61	0.05	0.1847	2.26E-12	1.90E-12	1.8E-15	1.072	1.076	0.014
16	118.	1.08	4.14E-08	0.	8.53	0.05	0.2270	2.10E-12	1.78E-12	4.2E-15	1.074	1.077	0.033
17	118.	0.54	1.63E-08	0.	8.56	0.05	0.2437	2.02E-12	1.72E-12	4.8E-15	1.067	1.072	0.037
18	118.	1.09	1.45E-08	0.	8.51	0.05	0.2585	1.98E-12	1.71E-12	3.0E-15	1.057	1.061	0.022
19	118.	0.54	2.57E-08	0.	8.43	0.05	0.2848	1.88E-12	1.63E-12	6.7E-15	1.067	1.072	0.050
20	118.	0.54	1.12E-08	0.	8.53	0.06	0.2962	1.01E-11	8.86E-12	9.8E-15	1.078	1.083	0.013
21	Ramp	0.54	5.19E-08	1.	8.60	0.05	0.3494	1.90E-11	1.71E-11	2.0E-14	1.029	1.034	0.010
22	150.	0.54	7.51E-08	0.	8.24	0.05	0.4262	1.65E-11	1.56E-11	1.3E-14	1.053	1.059	0.008
23	150.	1.08	9.48E-08	0.	8.45	0.04	0.5232	1.64E-11	1.61E-11	2.9E-14	1.056	1.064	0.017
24	150.	0.54	3.73E-08	1.	8.45	0.05	0.5614	1.54E-11	1.56E-11	1.6E-14	1.045	1.054	0.011
25	150.	1.08	5.86E-08	0.	8.35	0.05	0.6213	1.46E-11	1.52E-11	3.6E-14	1.059	1.069	0.024
26	150.	0.54	2.39E-08	0.	8.45	0.05	0.6458	1.40E-11	1.49E-11	2.0E-14	1.050	1.061	0.014
27	150.	1.08	4.03E-08	0.	8.35	0.05	0.6870						

continued

Experiment #6 (continued)

#	Temp. C	Time hr	4He ccSTP	1s o/oo	3He/4He Ra	1s Ra	F (4He) (total)	Dsm cm2/s	Drm cm2/s	1s cm2/s	D3/D4 sm	D3/D4 rm	1s rm
28	Ramp	13.01	4.71E-08	0.	8.31	0.05	0.7351	1.63E-12	1.80E-12	1.9E-15	1.049	1.061	0.012
29	211.	0.54	4.01E-08	0.	8.33	0.05	0.7761	4.04E-11	4.68E-11	5.0E-14	1.057	1.071	0.012
30	211.	0.54	3.86E-08	0.	8.24	0.04	0.8157	4.76E-11	5.77E-11	5.6E-14	1.053	1.068	0.012
31	211.	1.08	5.53E-08	0.	8.10	0.04	0.8722	4.60E-11	5.89E-11	3.4E-14	1.042	1.062	0.007
32	211.	1.08	3.60E-08	0.	7.97	0.04	0.9090	4.27E-11	5.94E-11	3.6E-14	1.042	1.061	0.008
33	211.	0.54	1.30E-08	0.	7.94	0.05	0.9223	3.96E-11	5.78E-11	7.6E-14	1.049	1.068	0.017
34	211.	0.54	1.07E-08	0.	7.82	0.05	0.9332	3.81E-11	5.70E-11	7.9E-14	1.041	1.059	0.019
35	211.	1.08	1.67E-08	0.	7.71	0.04	0.9503	3.71E-11	5.76E-11	4.5E-14	1.034	1.052	0.011
36	211.	1.08	1.19E-08	0.	7.65	0.04	0.9625	3.52E-11	5.70E-11	5.1E-14	1.037	1.054	0.014
37	211.	1.08	8.50E-09	0.	7.56	0.06	0.9711	3.31E-11	5.54E-11	6.2E-14	1.035	1.051	0.018
38	211.	1.08	6.11E-09	0.	7.59	0.07	0.9774	3.07E-11	5.29E-11	7.4E-14	1.050	1.067	0.021
39	Ramp	2.71	1.79E-08	0.	7.32	0.04	0.9957	8.36E-11	1.58E-10	4.0E-14	1.052	1.068	0.010
40	310.	0.54	2.93E-09	0.	6.58	0.08	0.9987	3.02E-10	6.24E-10	4.6E-13	0.996	1.007	0.037
41	310.	0.54	4.47E-10	1.	6.88	0.27	0.9992	1.10E-10	2.36E-10	6.5E-13	1.050	1.059	0.147
42	310.	1.08	2.00E-10	1.	7.46	0.47	0.9994	3.55E-11	7.70E-11	4.1E-13	1.180	1.189	0.304
43	310.	0.54	4.59E-11	4.	7.99	1.76	0.9994	1.97E-11	4.28E-11	8.7E-13	1.311	1.323	1.175
44	310.	0.54	2.91E-11	10.	9.06	3.41	0.9995	1.33E-11	2.90E-11	8.8E-13	1.523	1.538	1.697
45	310.	1.08	5.84E-11	7.	10.99	1.57	0.9995	1.45E-11	3.16E-11	4.3E-13	1.991	2.015	0.969
46	310.	1.63	6.02E-11	5.	10.00	1.63	0.9996	1.13E-11	2.48E-11	3.1E-13	2.058	2.084	1.011
47	310.	1.63	4.77E-11	6.	5.95	1.73	0.9996	1.02E-11	2.25E-11	3.2E-13	1.346	1.361	1.230
48	310.	1.63	3.37E-11	9.	7.37	2.00	0.9997	8.00E-12	1.76E-11	3.1E-13	1.765	1.790	1.759
49	Ramp	2.17	3.18E-10	1.	4.17	0.22	1.0000	1.85E-10	4.19E-10	3.4E-12	1.363	1.378	0.685
50	619.	0.54	7.35E-12	54.	0.00	21.97	1.0000	1.36E-10	3.13E-10	1.3E-11	0.000	0.000	0.000
51	619.	1.08	1.03E-11	19.	2.37	5.23	1.0000				0.000	0.000	0.000

Experiment #7

Charco98-11T MORB tholeiitic glass
8 chips, 15.7mg

Grain size data (um): short side, "visual average", long side.
914 787 406 711 1016 965 889 889
1321 940 1067 1524 1016 1143 1270 1270
1651 2134 1930 2667 2235 1626 1727 2083

Bulk helium contents: He = 1.52E-07 ccSTP   3He/4He = 8.77 +0.04 x Ra

Sequential release data:

#	Temp. C	Time hr	4He ccSTP	1s o/oo	3He/4He Ra	1s Ra	F(4He) (total)	Dsm cm2/s	Drm cm2/s	1s cm2/s	D3/D4 sm	D3/D4 rm	1s rm
1	106.	0.53	1.62E-10	2.	7.11	0.56	0.0011	8.70E-14	1.78E-13	9.3E-16	0.657	0.657	0.104
2	106.	7.03	9.15E-10	1.	8.96	0.16	0.0071	2.84E-13	5.82E-13	1.1E-15	0.987	0.987	0.038
3	106.	17.85	1.05E-09	1.	9.20	0.19	0.0140	3.33E-13	6.86E-13	1.5E-15	1.059	1.059	0.042
4	106.	25.42	9.13E-10	19.	9.38	4.66	0.0200	3.27E-13	6.78E-13	8.6E-14	1.099	1.100	0.715
5	Cool	21.64	1.58E-09	1.	7.02	0.10	0.0304	9.89E-13	2.07E-12	1.5E-13	0.789	0.788	0.384
6	Ramp	0.54	2.08E-11	14.	12.26	3.07	0.0306	6.27E-12	1.31E-11	3.8E-12	1.335	1.334	13.930
7	151.	0.54	1.57E-10	3.	10.45	0.71	0.0316	4.84E-12	1.02E-11	6.4E-12	1.144	1.143	2.393
8	151.	18.39	4.08E-09	0.	8.86	0.08	0.0584	5.55E-12	1.14E-11	3.4E-13	0.986	0.986	0.163
9	151.	17.72	2.63E-09	1.	9.08	0.10	0.0757	5.64E-12	1.16E-11	4.6E-13	1.025	1.025	0.219
10	151.	28.55	3.26E-09	0.	8.97	0.06	0.0972	5.68E-12	1.17E-11	3.7E-13	1.022	1.022	0.173
11	151.	28.01	2.62E-09	0.	9.04	0.06	0.1144	5.80E-12	1.20E-11	4.4E-13	1.036	1.036	0.204
12	Ramp	1.08	3.99E-10	1.	9.33	0.27	0.1171	2.52E-11	5.23E-11	1.2E-11	1.072	1.073	1.181
13	223.	6.39	6.12E-09	0.	9.21	0.06	0.1573	7.91E-11	1.65E-10	2.7E-12	1.067	1.067	0.091
14	223.	8.65	5.80E-09	0.	8.83	0.07	0.1955	7.38E-11	1.55E-10	2.4E-12	1.027	1.028	0.089
15	223.	8.65	4.55E-09	0.	8.97	0.07	0.2254	7.14E-11	1.50E-10	2.8E-12	1.043	1.043	0.106
16	223.	11.35	4.94E-09	0.	8.94	0.07	0.2578	6.99E-11	1.48E-10	2.4E-12	1.041	1.042	0.094
17	223.	11.90	4.60E-09	0.	9.04	0.08	0.2881	7.27E-11	1.55E-10	2.6E-12	1.054	1.055	0.096
18	Ramp	1.08	1.06E-08	1.	9.30	0.06	0.3581	2.31E-11	4.98E-09	3.5E-11	1.095	1.097	0.042
19	413.	1.08	2.54E-08	0.	9.05	0.05	0.5250	8.85E-09	1.95E-08	5.0E-11	1.080	1.083	0.016
20	413.	0.54	8.02E-09	0.	8.97	0.07	0.5778	8.19E-09	1.84E-08	1.1E-10	1.080	1.085	0.039
21	413.	0.54	6.44E-09	0.	8.86	0.07	0.6201	7.79E-09	1.77E-08	1.2E-10	1.072	1.077	0.044
22	413.	1.62	1.45E-08	1.	8.83	0.05	0.7152	7.57E-09	1.76E-08	4.6E-11	1.075	1.081	0.019
23	Ramp	0.54	2.47E-08	1.	8.52	0.05	0.8776	7.38E-08	1.76E-07	1.6E-10	1.053	1.064	0.008
24	617.	0.54	1.17E-08	1.	7.82	0.06	0.9544	8.64E-08	2.21E-07	1.6E-10	0.987	0.991	0.008
25	617.	0.54	2.46E-09	0.	7.09	0.07	0.9706	3.84E-08	1.00E-07	1.7E-10	0.864	0.865	0.020
26	617.	1.08	1.15E-09	1.	7.81	0.11	0.9782	1.30E-08	3.42E-08	8.8E-11	0.910	0.910	0.034
27	617.	1.62	7.97E-10	1.	9.25	0.15	0.9834	8.01E-09	2.11E-08	6.4E-11	1.074	1.074	0.043
28	617.	6.49	1.72E-09	1.	8.72	0.10	0.9947	8.31E-09	2.21E-08	1.8E-11	1.043	1.043	0.024
29	617.	9.10	8.07E-10	1.	8.12	0.21	1.0000						

Aftermath D9 alkali basalt glass
17 chips, 49.1mg

Grain size data (um): short side, "visual average", long side.
864 1397 838 1016 1016 711 1219 1041 889 965 1067 813 838 635 1016 965 1245
1600 1473 1651 1067 1422 1194 1346 1321 1524 1143 1270 1067 1067 1727 1422 1295 1372
1880 1499 1829 1905 1626 1981 1473 1422 1651 1727 1549 2083 2032 17781880 1753 1803

Bulk helium contents: He = 3.99E-08 ccSTP 3He/4He = 7.23 +0.02 x Ra

Sequential release data:

#	Temp. C	Time hr	4He ccSTP	1s 3He/4He o/oo	3He/4He Ra	1s Ra	F(4He) (total)	Dsm cm2/s	Drm cm2/s	1s cm2/s	D3/D4 sm	D3/D4 rm	1s rm
1	Ramp	0.53	3.72E-10	1.	7.09	0.28	0.0093	9.48E-12	1.60E-11	3.7E-14	0.960	0.960	0.076
2	150.	2.71	7.45E-10	1.	7.32	0.25	0.0280	1.50E-11	2.56E-11	4.0E-14	1.009	1.009	0.060
3	150.	3.79	9.18E-10	1.	7.52	0.15	0.0511	2.89E-11	4.87E-11	7.3E-14	1.054	1.054	0.050
4	150.	4.87	7.92E-10	1.	7.54	0.13	0.0709	3.04E-11	5.14E-11	9.5E-14	1.068	1.068	0.057
5	150.	4.87	5.90E-10	1.	7.80	0.13	0.0857	2.95E-11	5.01E-11	1.3E-13	1.113	1.114	0.074
6	150.	4.87	5.24E-10	1.	7.32	0.18	0.0989	3.13E-11	5.32E-11	1.6E-13	1.049	1.050	0.084
7	Ramp	0.54	5.52E-10	1.	7.23	0.18	0.1127	3.44E-10	5.86E-10	1.8E-12	1.033	1.034	0.083
8	278.	2.17	5.16E-09	0.	7.54	0.08	0.2420	1.45E-09	2.51E-09	1.6E-12	1.085	1.086	0.017
9	278.	3.25	4.96E-09	0.	7.43	0.07	0.3665	1.81E-09	3.23E-09	2.2E-12	1.076	1.078	0.017
10	Ramp	0.54	2.80E-09	1.	7.33	0.07	0.4367	9.09E-09	1.65E-08	1.7E-11	1.063	1.067	0.027
11	414.	1.08	7.05E-09	0.	7.35	0.05	0.6134	1.81E-08	3.39E-08	1.6E-11	1.072	1.076	0.013
12	414.	1.08	3.75E-09	0.	7.00	0.07	0.7075	1.56E-08	3.03E-08	2.2E-11	1.024	1.029	0.019
13	414.	2.16	3.55E-09	0.	6.78	0.07	0.7967	1.08E-08	2.17E-08	1.6E-11	0.984	0.987	0.019
14	414.	3.25	2.16E-09	0.	6.77	0.09	0.8508	6.35E-09	1.31E-08	1.4E-11	0.970	0.973	0.026
15	414.	6.50	1.75E-09	0.	6.93	0.10	0.8947	3.62E-09	7.63E-09	9.7E-12	0.982	0.984	0.029
16	414.	4.87	6.78E-10	1.	7.11	0.25	0.9117	2.44E-09	5.26E-09	1.6E-11	1.006	1.007	0.059
17	Ramp	0.54	6.68E-10	1.	7.77	0.17	0.9284	2.62E-08	5.72E-08	1.6E-10	1.111	1.114	0.057
18	618.	1.63	1.33E-09	1.	7.27	0.13	0.9617	2.59E-08	5.79E-08	8.1E-11	1.074	1.078	0.028
19	618.	13.47	1.45E-09	1.	6.74	0.11	0.9980	1.49E-08	3.56E-08	4.3E-11	1.189	1.202	0.080
20	618.	8.12	7.83E-11	4.	3.76	0.63	1.0000						

Experiment #9

Aftermath D9 alkali basalt glass
26 chips, 44.5mg

Grain size data (um): short side, "visual average", long side.

```
1397 1219 1321 1270 838 991 1016 813 965 991 787 1067
889 1168 838 1143 965 787 1016 813 889 965 889 1143 889

1524 1245 1422 1372 1219 1168 1143 1219 1067 1270 1270 1016 1143
1143 1321 1295 1270 1041 1473 1143 1295 1295 1397 889 1397 1346

2159 1346 1854 1397 1880 1778 1346 1397 1676 1600 1372 1473 1372
1930 1778 1321 1473 1346 1778 1270 1753 1575 1676 1295 1473 1524
```

Bulk helium contents: He = 7.39E-08 ccSTP   3He/4He = 7.25 +0.07 x Ra

Sequential release data:

#	Temp. °C	Time hr	4He ccSTP	1s o/oo	3He/4He Ra	1s Ra	F(4He) total	Dsm cm2/s	Drm cm2/s	1s cm2/s	D3/D4 sm	D3/D4 rm	1s rm
1	53.	41.24	1.25E-10	4.	8.81	0.25	0.0017	5.62E-15	6.44E-15	4.8E-17	1.478	1.478	0.169
2	53.	29.28	8.72E-11	8.	10.18	0.60	0.0029	1.50E-14	1.72E-14	2.1E-16	1.775	1.776	0.317
3	Ramp	1.63	3.31E-11	15.	8.23	2.23	0.0033	1.39E-13	1.59E-13	5.2E-15	1.456	1.457	0.851
4	125.	15.73	1.29E-09	3.	7.61	0.13	0.0208	2.18E-12	2.53E-12	1.4E-14	1.166	1.167	0.051
5	125.	23.71	1.07E-09	7.	7.20	0.16	0.0353	2.80E-12	3.30E-12	3.1E-14	1.053	1.055	0.059
6	Ramp	1.63	7.21E-11	6.	4.77	1.19	0.0363	3.49E-12	4.15E-12	4.6E-13	0.686	0.687	0.708
7	152.	6.51	7.43E-10	1.	7.56	0.17	0.0463	1.07E-11	1.24E-11	1.5E-13	1.084	1.084	0.088
8	151.	14.10	1.32E-09	2.	7.46	0.11	0.0641	1.19E-11	1.38E-11	1.1E-13	1.069	1.069	0.062
9	151.	3.25	2.55E-10	3.	6.65	0.36	0.0676	1.20E-11	1.39E-11	5.0E-13	0.949	0.950	0.288
10	Ramp	1.63	2.19E-10	3.	6.62	0.38	0.0705	2.17E-11	2.52E-11	1.1E-12	0.940	0.941	0.341
11	189.	10.85	2.31E-09	3.	7.36	0.08	0.1018	4.35E-11	5.08E-11	3.0E-13	1.041	1.041	0.048
12	189.	9.25	1.47E-09	3.	7.21	0.12	0.1217	4.30E-11	5.05E-11	4.7E-13	1.016	1.017	0.079
13	Ramp	1.63	5.08E-10	2.	7.30	0.27	0.1286	9.57E-11	1.13E-10	2.9E-12	1.026	1.027	0.225
14	240.	8.14	3.80E-09	1.	7.53	0.09	0.1799	1.81E-10	2.15E-10	1.0E-12	1.063	1.064	0.047
15	240.	13.02	3.79E-09	1.	7.33	0.07	0.2312	1.58E-10	1.90E-10	1.0E-12	1.038	1.039	0.056
16	Ramp	1.63	1.45E-09	1.	7.43	0.14	0.2508	5.88E-10	7.12E-10	9.7E-12	1.053	1.054	0.142
17	329.	3.26	4.13E-09	2.	7.38	0.07	0.3068	1.01E-09	1.23E-09	7.7E-12	1.045	1.047	0.065
18	329.	4.88	3.41E-09	2.	7.29	0.06	0.3528	6.94E-10	8.60E-10	7.1E-12	1.033	1.035	0.086
19	328.	13.02	3.75E-09	3.	6.70	0.06	0.4036	3.49E-10	4.38E-10	3.7E-12	0.941	0.942	0.086
20	Ramp	1.63	8.75E-09	2.	7.63	0.05	0.5219	8.95E-09	1.77E-08	5.7E-11	1.076	1.078	0.054
21	618.	3.80	1.58E-08	3.	7.56	0.26	0.7358	1.29E-08	1.77E-08	5.1E-11	1.102	1.108	0.034
22	618.	0.54	1.50E-09	3.	7.27	0.28	0.7562	1.33E-08	1.90E-08	4.0E-10	1.090	1.100	0.243
23	618.	5.97	9.98E-09	3.	7.04	0.24	0.8911	1.28E-08	1.89E-08	4.9E-11	1.078	1.095	0.030
24	618.	5.97	4.45E-09	2.	6.65	0.23	0.9513	1.28E-08	2.08E-08	6.2E-11	1.087	1.105	0.035
25	618.	7.05	2.15E-09	3.	6.22	0.23	0.9805	1.23E-08	2.15E-08	7.7E-11	1.101	1.123	0.033
26	618.	11.50	1.08E-09	4.	5.62	0.12	0.9951	1.14E-08	2.19E-08	7.6E-11	1.115	1.146	0.076
27	618.	13.01	3.39E-10	6.	4.83	0.35	0.9997	2.05E-08	4.47E-08	3.5E-10	1.818	1.924	1.152
28	618.	1.63	2.14E-11	19.	0.45	3.36	1.0000						

388

Experiment #10

Alv1389-1854B alkalic basalt glass
Radiogenic *He
9 chips, 44.0mg

Grain size data (um): short side, "visual average", long side.
1626 1524 1270 1194 787 1270 737 1270 813
1728 1854 1956 1880 1702 1549 1905 1829 1575
2896 2235 2032 3480 2235 2362 2667 2413 2007

Bulk helium contents: He = 1.03E-08 ccSTP   3He/4He = 0.08 +0.04 x Ra

Sequential release data:

#	Temp. C	Time hr	4He ccSTP	1s o/oo	3He/4He Ra	1s Ra	F (4He) (total)	Dsm cm2/s	Drm cm2/s	1s cm2/s
1	123.	16.81	9.63E-11	3.	0.01	0.57	0.0094	4.27E-13	8.80E-13	6.0E-15
2	Ramp	0.54	2.71E-11	11.	0.00	3.09	0.0120	8.53E-12	1.76E-11	3.2E-13
3	220.	0.54	8.11E-11	4.	0.00	0.89	0.0199	3.80E-11	7.91E-11	6.7E-13
4	220.	2.71	7.30E-10	1.	0.42	0.12	0.0912	2.51E-10	5.19E-10	7.8E-13
5	220.	2.71	4.98E-10	1.	0.80	0.21	0.1397	3.72E-10	7.76E-10	1.5E-12
6	220.	2.71	3.78E-10	1.	0.00	0.14	0.1765	4.01E-10	8.45E-10	2.0E-12
7	220.	2.71	2.97E-10	1.	0.00	0.22	0.2055	3.93E-10	8.33E-10	2.5E-12
8	Ramp	0.54	1.03E-09	0.	0.00	0.06	0.3060	9.78E-10	2.10E-08	2.3E-11
9	312.	0.54	1.69E-09	0.	0.02	0.04	0.4709	2.86E-08	6.32E-08	4.8E-11
10	312.	1.08	2.96E-09	0.	0.00	0.02	0.7600	5.97E-08	1.41E-07	7.2E-11
11	312.	0.54	6.01E-10	0.	0.00	0.12	0.8186	4.75E-08	1.21E-07	1.9E-10
12	Ramp	9.76	2.00E-10	1.	0.02	0.32	0.8381	1.09E-09	2.84E-09	1.2E-11
13	312.	0.54	2.47E-10	1.	0.01	0.36	0.8622	2.81E-08	7.40E-08	2.5E-10
14	312.	1.08	3.09E-10	1.	0.00	0.18	0.8923	2.16E-08	5.84E-08	1.5E-10
15	312.	1.63	2.05E-10	1.	0.08	0.41	0.9123	1.19E-08	3.31E-08	1.2E-10
16	Ramp	0.54	3.91E-10	1.	0.00	0.34	0.9504	9.97E-08	2.86E-07	5.8E-10
17	416.	0.54	1.21E-10	2.	0.04	0.57	0.9622	4.76E-08	1.40E-07	6.2E-10
18	416.	1.08	9.20E-11	3.	0.00	0.88	0.9712	2.37E-08	7.05E-08	3.5E-10
19	Ramp	0.54	2.95E-10	1.	0.27	0.29	1.0000			

389

Experiment #11

ALV1389-1854B Alkali Basalt glass
Radiogenic *4He

Grain size data (um): short side, "visual average", long side.
246 216 293 169 185 185 277 231 169 185
308 308 308 200 308 185 308 308 262 231
339 323 339 493 354 462 339 308 354

Bulk helium contents: He = 4.10E-09 ccSTP   3He/4He = 0.81 +0.06 x Ra

Sequential release data:

#	Temp. C	Time hr	4He ccSTP	1s o/oo	3He/4He Ra	1s Ra	F (4He) (total)	Dsm cm2/s	Drm cm2/s	1s cm2/s
1	Ramp	2.20	3.13E-11	13.	2.18	1.48	0.0076	8.49E-14	1.18E-13	3.5E-15
2	127.	49.94	1.26E-10	4.	5.41	0.27	0.0385	9.12E-14	1.30E-13	1.6E-15
3	Cool	26.88	1.04E-11	67.	16.48	0.65	0.0410	2.48E-14	3.47E-14	4.0E-15
4	Ramp	1.63	below detection limit							
5	127.	63.11	5.12E-11	20.	7.82	0.35	0.0535	6.22E-14	8.47E-14	3.2E-15
6	Ramp	1.61	1.53E-11	20.	0.96	4.67	0.0572	8.60E-13	1.21E-12	1.4E-13
7	162.	36.89	2.76E-10	7.	1.97	0.10	0.1245	1.15E-12	1.63E-12	2.4E-14
8	162.	16.81	6.62E-11	12.	4.92	0.65	0.1407	9.12E-13	1.30E-12	6.6E-14
9	Ramp	2.17	3.53E-09	6.	0.31	0.03	1.0000			

Additional steps at 600C released no measurable helium.

APPENDIX C: Helium emanation data and diffusivity results
              for olivine and pyroxene at high temperature
              (experiments #1-8, chapter 4).

Experiment #1
113987-107 olivine
500-710um sieve fraction, 127.0mg, r=303.(27.)um
Bulk helium contents: He = 2.24E-08 ccSTP   3He/4He = 8.89 +0.07 x Ra
Sequential release data:

#	Temp. C	1s C	Time hr	4He ccSTP	1s ccSTP	3He/4He Ra	1s Ra	F(4He) (total)	Dsm cm2/s	1s cm2/s	D3/D4 sm	1s sm
1 Load	-		1.63	1.56E-10	2.E-12	11.40	1.03	0.0070	6.64E-13	1.2E-13	1.64	0.30
2 965.	10.		12.48	1.76E-10	2.E-12	9.38	0.96	0.0148	3.06E-13	5.4E-14	1.27	0.24
3 965.	10.		27.09	1.71E-10	6.E-13	8.69	0.54	0.0225	2.34E-13	4.2E-14	1.10	0.22
4 965.	10.		26.04	1.64E-10	5.E-13	8.72	0.50	0.0298	3.26E-13	5.8E-14	1.06	0.22
5 Melt	-		1.63	2.17E-08	9.E-11	8.88	0.05	0.9984				
6 Left	-		1.63	3.68E-11	4.E-13	4.86	1.83	1.0000				

Experiment #2
113987-107 olivine
500-710um sieve fraction, 93.3mg,r=303(27.)
Bulk helium contents: He = 2.68E-08 ccSTP   3He/4He = 8.83 +0.08 x Ra
Sequential release data:

#	Temp. C	1s C	Time hr	4He ccSTP	1s ccSTP	3He/4He Ra	1s Ra	F(4He) (total)	Dsm cm2/s	1s cm2/s	D3/D4 sm	1s sm
1 Load	-		0.5?	2.62E-10	4.E-13	8.78	0.39	0.0098	4.00E-12	7.1E-13	0.99	0.09
2 1084.	20.		20.62	1.44E-09	9.E-13	9.21	0.13	0.0636	4.42E-12	7.9E-13	1.08	0.04
3 1084.	20.		24.96	1.61E-09	8.E-12	9.44	0.13	0.1239	1.09E-11	1.9E-12	1.12	0.04
4 1084.	20.		26.51	1.10E-09	7.E-12	9.36	0.12	0.1650	1.13E-11	2.0E-12	1.12	0.06
5 Melt	-		1.69	2.23E-08	1.E-10	8.74	0.06	0.9980				
6 Left	-		1.63	5.48E-11	7.E-13	7.13	1.98	1.0000				

Experiment #3
113987-107 olivine
500-710um sieve fraction,101.5mg,r=303.(27)um
Bulk helium contents: He = 3.23E-08 ccSTP   3He/4He = 8.93 +0.03 x Ra
Sequential release data:

#	Temp. C	1s C	Time hr	4He ccSTP	1s ccSTP	3He/4He Ra	1s Ra	F(4He) (total)	Dsm cm2/s	1s cm2/s	D3/D4 sm	1s sm
1 Load	-	-	0.53	4.76E-09	1.E-11	9.22	0.06	0.1475	9.86E-10	1.8E-10	1.07	0.02
2 1255.	20.	20.	1.63	4.78E-09	1.E-11	9.20	0.07	0.2955	1.10E-09	2.0E-10	1.07	0.02
3 1255.	20.	20.	3.26	5.87E-09	2.E-11	9.06	0.07	0.4773	1.43E-09	2.5E-10	1.06	0.02
4 1255.	20.	20.	4.88	4.82E-09	1.E-11	9.01	0.09	0.6265	1.42E-09	2.5E-10	1.06	0.02
5 1255.	20.	20.	8.14	3.91E-09	1.E-11	8.85	0.07	0.7476	1.14E-09	2.0E-10	1.04	0.02
6 Melt	-	-	1.63	8.15E-09	4.E-11	8.49	0.05	1.0000				

Experiment #4
113987-107 olivine
500-710um sieve fraction,approx.80mg (partial load), r=303(27)um
Gold in crucible
Bulk helium contents: He = 2.51E-08 ccSTP   3He/4He = 8.81 +0.03 x Ra
Sequential release data:

#	Temp. C	1s C	Time hr	4He ccSTP	1s ccSTP	3He/4He Ra	1s Ra	F(4He) (total)	Dsm cm2/s	1s cm2/s	D3/D4 sm	1s sm
1 Load	-	-	0.53	9.84E-11	6.E-13	6.84	0.94	0.0039	6.41E-13	1.1E-13	0.60	0.17
2 1095.	10.	10.	0.54	7.80E-11	5.E-13	11.45	1.24	0.0070	1.40E-12	2.5E-13	1.20	0.25
3 1095.	10.	10.	6.47	7.32E-10	2.E-12	9.28	0.20	0.0362	4.33E-12	7.7E-13	1.09	0.05
4 1095.	10.	10.	11.86	1.05E-09	4.E-12	9.24	0.22	0.0780	9.39E-12	1.7E-12	1.10	0.05
5 1095.	10.	10.	23.11	1.76E-09	3.E-12	9.08	0.11	0.1480	1.68E-11	3.0E-12	1.08	0.03
6 1095.	10.	10.	23.58	1.36E-09	6.E-12	9.04	0.13	0.2023	2.09E-11	3.7E-12	1.07	0.04
7 1095.	10.	10.	1.08	5.63E-11	6.E-13	10.25	0.98	0.2045	2.25E-11	4.0E-12	1.21	0.75
8 Cool	-	-	4.28	7.14E-11	4.E-13	9.27	1.48	0.2073	7.29E-12	1.3E-12	1.10	0.61
9 Ramp	-	-	0.54	2.82E-09	2.E-12	9.09	0.09	0.3195	3.12E-09	5.6E-10	1.08	0.02
10 1385.	30.	30.	0.54	3.19E-09	2.E-12	8.92	0.05	0.4467	5.91E-09	1.1E-09	1.06	0.02
11 1385.	30.	30.	1.08	4.04E-09	3.E-12	8.91	0.06	0.6074	6.34E-09	1.1E-09	1.06	0.01
12 1385.	30.	30.	2.67	4.14E-09	3.E-12	8.67	0.07	0.7725	4.84E-09	8.6E-10	1.04	0.01
13 Melt	-	-	0.54	5.71E-09	4.E-12	8.34	0.04	1.0000				

Experiment #5
69sal219 clinopyroxine
500-710um sieve fraction,29.9mg,r=303.(27)
23/83 grains trapped in crack
Bulk helium contents: He = 2.14E-08 ccSTP 3He/4He = 8.66 +0.08 x Ra
Sequential release data:

#	Temp. C	1s C	Time hr	4He ccSTP	1s ccSTP	3He/4He Ra	1s Ra	F(4He) (total)	Dsm cm2/s	1s cm2/s	D3/D4 sm	1s sm
1 Load	-	-	0.53	1.17E-09	4.E-12	8.24	0.13	0.0549	1.30E-10	2.3E-11	0.90	0.03
2	965.	10.	0.54	4.73E-10	2.E-12	9.04	0.36	0.0770	1.26E-10	2.2E-11	1.01	0.07
3	965.	10.	5.43	2.35E-09	8.E-12	9.03	0.12	0.1870	1.34E-10	2.4E-11	1.05	0.03
4	965.	10.	6.51	1.52E-09	5.E-12	8.47	0.12	0.2581	1.32E-10	2.4E-11	0.99	0.05
5	965.	10.	7.60	1.15E-09	5.E-12	8.86	0.16	0.3119	1.17E-10	2.1E-11	1.03	0.07
6 Melt	-		1.63	1.47E-08	6.E-11	8.64	0.10	0.9987				
7 Left	-		0.54	2.72E-11	4.E-13	1.44	3.17	1.0000				

Experiment #6
69sal219 clinopyroxine
500-710um sieve fraction,29.2mg,r=303.(27)
7/50 grains trapped in crack
Bulk helium contents: He = 1.32E-08 ccSTP 3He/4He = 8.77 +0.04 x Ra
Sequential release data:

#	Temp. C	1s C	Time hr	4He ccSTP	1s ccSTP	3He/4He Ra	1s Ra	F(4He) (total)	Dsm cm2/s	1s cm2/s	D3/D4 sm	1s sm
1 Load	-	-	0.53	1.46E-09	6.E-12	8.67	0.09	0.1106	5.42E-10	9.7E-11	0.98	0.02
2	1070.	20.	0.54	7.44E-10	3.E-12	8.32	0.15	0.1671	7.24E-10	1.3E-10	0.93	0.03
3	1070.	20.	5.43	3.59E-09	1.E-11	9.00	0.07	0.4399	9.29E-10	1.7E-10	1.02	0.02
4	1070.	20.	8.69	2.19E-09	9.E-12	8.81	0.10	0.6063	8.04E-10	1.4E-10	1.02	0.02
5	1070.	20.	9.77	1.25E-09	3.E-12	8.59	0.16	0.7016	6.52E-10	1.2E-10	0.99	0.03
6 Melt	-		1.63	3.93E-09	8.E-12	8.72	0.08	1.0000				

Experiment #7
69sal219 clinopyroxine
500-710um sieve fraction,38.8mg,r=303.(27)
Bulk helium contents: He = 2.69E-08 ccSTP   3He/4He = 8.65 +0.04 x Ra
Sequential release data:

#	Temp. C	1s C	Time hr	4He ccSTP	1s ccSTP	3He/4He Ra	1s Ra	F(4He) (total)	Dsm cm2/s	1s cm2/s	D3/D4 sm	1s sm
1	Load	-	0.53	1.64E-08	6.E-11	8.71	0.04	0.6097	2.42E-08	4.3E-09	1.02	0.01
2	1170.	30.	0.54	3.06E-09	1.E-11	8.82	0.09	0.7234	1.47E-08	2.6E-09	1.04	0.02
3	1170.	30.	0.54	2.06E-09	8.E-12	8.71	0.13	0.7999	1.48E-08	2.6E-09	1.04	0.03
4	1170.	30.	2.17	2.90E-09	1.E-11	8.47	0.11	0.9076	9.19E-09	1.6E-09	1.02	0.01
5	1170.	30.	5.43	1.63E-09	6.E-12	8.42	0.10	0.9681	5.06E-09	9.0E-10	1.04	0.02
6	1170.	30.	6.64	5.60E-10	1.E-12	7.70	0.19	0.9889	4.12E-09	7.3E-10	0.96	0.03
7	Melt	-	24.00	2.98E-10	8.E-13	8.21	0.24	1.0000				

Experiment #8
69SAL219 Clinopyroxene
.5-1.mm sieve fraction,72.1mg, r=375(125)um
Sample in Ta boat at 770C, loose at 1110C

Bulk helium contents: He = 4.47E-08 ccSTP   3He/4He = 8.68 +0.03 x Ra
Sequential release data:

#	Temp. C	1s C	Time hr	4He ccSTP	1s ccSTP	3He/4He Ra	1s Ra	F(4He) (total)	Dsm cm2/s	1s cm2/s	D3/D4 sm	1s sm
1	Load	-	0.53	4.67E-10	1.E-12	6.70	0.30	0.0104	6.97E-12	4.6E-12	0.60	0.05
2	770.	20.	2.57	2.95E-10	1.E-12	7.78	0.45	0.0170	2.41E-12	1.6E-12	0.72	0.08
3	770.	20.	2.69	1.63E-10	6.E-13	8.75	0.52	0.0207	1.74E-12	1.2E-12	0.84	0.14
4	770.	20.	2.69	1.35E-10	5.E-13	8.77	0.63	0.0237	1.69E-12	1.1E-12	0.87	0.18
5	Ramp	-	21.57	7.06E-09	3.E-11	8.78	0.05	0.1817	5.69E-11	3.8E-11	0.99	0.01
6	1110.	20.	0.53	3.12E-09	1.E-11	8.75	0.07	0.2514	2.36E-09	1.6E-09	1.00	0.02
7	1110.	20.	1.62	5.22E-09	2.E-11	8.79	0.07	0.3681	2.05E-09	1.4E-09	1.01	0.02
8	1110.	20.	1.08	2.47E-09	9.E-12	8.87	0.11	0.4233	2.05E-09	1.4E-09	1.03	0.03
9	1110.	20.	1.08	1.89E-09	7.E-12	8.78	0.09	0.4655	1.87E-09	1.2E-09	1.02	0.04
10	1110.	20.	4.85	5.81E-09	2.E-11	8.76	0.07	0.5954	1.76E-09	1.2E-09	1.02	0.02
11	1110.	20.	4.85	3.34E-09	1.E-11	8.83	0.11	0.6700	1.45E-09	9.7E-10	1.03	0.03
12	1110.	20.	5.55	2.31E-09	3.E-12	8.71	0.10	0.7217	1.12E-09	7.5E-10	1.02	0.03
13	Cool	-	4.22	9.92E-11	4.E-13	9.18	0.62	0.7239	7.05E-11	4.7E-11	1.08	0.73
14	Melt	-	6.17	1.23E-08	7.E-12	8.52	0.06	1.0000				

APPENDIX D: Finite difference determination of the fraction of
helium remaining in a spherical grain undergoing
constant production and volume diffusion loss.

For a mineral grain undergoing both diffusive loss and constant production by cosmic ray spallation the helium concentration is governed by:

$$dC/dt = D \nabla^2 C + P \qquad \text{(AD5.1)}$$

where P is the production rate (per unit volume). The fraction of produced helium which remains at time t can then be written:

$$F_t = C/Pt = \{ Pt - \int_0^t (dC/dt)dt \} / Pt \qquad \text{(AD5.2)}$$

Equation 5.1 was solved numerically using an explicit, spatially centered, finite-difference approach to obtain concentration, C, as a function of time and radial distance within the quartz grains. F_t was then obtained by integrating these curves over the crystal volume (these routines are provided, in Fortran 77, in the program "Findif". The numerical solution was verified by comparison to an infinite series analytical solution for F_t (Tilton, 1960) and has the advantage of easily determining concentration profiles.

```
              Program Findif
c             Tom Trull    Nov. 14, 1988
c             Findif uses an explicit, spatially-centered finite difference
c             algorithm to obtain the time-dependent solution for a sphere
c             undergoing constant production and volume diffusion loss of
c             3He.  It calculates a radial concentration profile as a function
c                 of time which is then integrated to obtain the helium content of
c             the crystal.  As with diffusion alone, the problem can be
c             scaled with D/a2, where D is the diffusion coefficient and a the
c             radius of the sphere, i.e. the solution is independent of production
c             rate.
c
              Parameter(ngrid=500,ngridp=501,daysec=86400.,yrday=365.,pi=3.14159)
              Dimension cold(ngridp),cnew(ngridp)
              Open(unit=1,file='FDFp12.dat',status='new')

              Difco=5.E-20               !Diffusion coefficient in cm2/s.
              rho=2.5                    !density in g/cc
              Pgy=360.                   !production rate in atoms/gr/yr
d             Pgy=0                      !zero production test option
              Pvs=Pgy/yrday/daysec/rho   !production rate in atoms/cc/s
              a=.0250                    !radius in cm
              vspher=4./3.*pi*a**3       !crystal volume
c
              yrs=1.E+06                 !time in years
              diftim=daysec*yrday*yrs    !time in seconds
                nlooks=4                 !# looks at profile during diftim
              dr=a/(ngrid-1)             !grid spacing
              dt=dr**2/Difco/100.        !numeric stability
              dc=Difco*dt/dr**2          !flux increment
              ntstep=diftim/dt/nlooks    !# of time steps between looks
c
              Write(5,*)diftim,ntstep,dt,dr,dc,Pvs
c
              Do 50 nr=1,ngrid           !boundary conditions
                cold(nr)=0.
d               cold(nr)=1.              !0 prod., diffusive loss option
                cnew(nr)=0.
       50 Continue
              cold(ngrid+1)=0.
              cnew(ngrid+1)=0.
c
              Do 300 nlook=1,nlooks      !obtain profiles at various points
              Do 200 nt=1,ntstep
c
              Do 100 nr=2,ngrid          !time step concentration
                cnew(nr)=cold(nr)+dc/nr
              &            *((nr+1)*cold(nr+1)-2*nr*cold(nr)+(nr-1)*cold(nr-1))
              &                   +Pvs*dt
      100     Continue
```

```
           cnew(1)=cold(1)+6*dc*(cold(2)-cold(1))+Pvs*dt     !center point
C
       Do 150 nr=1,ngrid                    !reset old and new, step again
          cold(nr)=cnew(nr)
  150 Continue
C
  200 Continue
C
*************Sum loss, write to files *********************************
C
           time=(nlook)*ntstep*dt/daysec/yrday              !years
           write(1,1000)nlook,time
             totrem=0.
C
       Do 250 nr=1,ngrid   !use conc. at shell midpoint to integrate
           posn=(nr-1)*dr
           fposn=posn/a
           vshell=4./3.*pi*( ((nr-1)*dr+.5*dr)**3 - ((nr-1)*dr-.5*dr)**3 )
           IF(nr.eq.1)vshell=4./3.*pi*(.5*dr)**3
           IF(nr.eq.ngrid)vshell=4./3.*pi*
     &     (((nr-1)*dr)**3 - ((nr-1)*dr-.5*dr)**3 )
d          cnew(nr)=1                       !volume integration test option
           amount=cnew(nr)*vshell          !amount remaining in shell
           totrem=totrem+amount            !total remaining
           write(5,*)(nr-1)*dr,totrem,amount,vshell,cnew(nr)
C
           write(1,2000)nr,posn,cnew(nr)/(Pvs*nlook*ntstep*dt)
d          write(1,2000)nr,Fposn,cnew(nr)       !0 prod. option
  250      Continue
           Totprd=Pvs*(nlook*ntstep*dt)*vspher  !total prod. in sphere
           flost=1.-(totrem/totprd)
d          flost=1.-(totrem/vspher)             !0 prod. option
           IF (flost.lt.(0.00001)) THEN
             flost=0.
           ENDIF
           write(5,*)time,totprd,vspher,totrem,flost
           write(1,3000)time,flost
C
  300 Continue
C
 1000 Format(1x,'findif output',/,1x,'nlook= ',I3,2x,'years= ',F10.1)
 2000 Format(1x,I4,1x,F10.5,1x,F10.5)
 3000 Format(1x,'years= ',F10.1,1x,'flost=   ',F8.4)
      Stop
      End
```

Attn: Stella Sanchez-Wade
Documents Section
Scripps Institution of Oceanography
Library, Mail Code C-075C
La Jolla, CA 92093

Hancock Library of Biology &
    Oceanography
Alan Hancock Laboratory
University of Southern California
University Park
Los Angeles, CA 90089-0371

Gifts & Exchanges
Library
Bedford Institute of Oceanography
P.O. Box 1006
Dartmouth, NS, B2Y 4A2, CANADA

Office of the International
    Ice Patrol
c/o Coast Guard R & D Center
Avery Point
Groton, CT 06340

Library
Physical Oceanographic Laboratory
Nova University
8000 N. Ocean Drive
Dania, FL 33304

NOAA/NESDIS Miami Library Center
4301 Rickenbacker Causeway
Miami, FL 33149

Library
Skidaway Institute of Oceanography
P.O. Box 13687
Savannah, GA 31416

Institute of Geophysics
University of Hawaii
Library Room 252
2525 Correa Road
Honolulu, HI 96822

Library
Chesapeake Bay Institute
4800 Atwell Road
Shady Side, MD 20876

MIT Libraries
Serial Journal Room 14E-210
Cambridge, MA 02139

Director, Ralph M. Parsons Laboratory
Room 48-311
MIT
Cambridge, MA 02139

Marine Resources Information Center
Building E38-320
MIT
Cambridge, MA 02139

Library
Lamont-Doherty Geological
    Observatory
Colombia University
Palisades, NY 10964

Library
Serials Department
Oregon State University
Corvallis, OR 97331

Pell Marine Science Library
University of Rhode Island
Narragansett Bay Campus
Narragansett, RI 02882

Working Collection
Texas A&M University
Dept. of Oceanography
College Station, TX 77843

Library
Virginia Institute of Marine Science
Gloucester Point, VA 23062

Fisheries-Oceanography Library
151 Oceanography Teaching Bldg.
University of Washington
Seattle, WA 98195

Library
R.S.M.A.S.
University of Miami
4600 Rickenbacker Causeway
Miami, FL 33149

Maury Oceanographic Library
Naval Oceanographic Office
Bay St. Louis
NSTL, MS 39522-5001

Marine Sciences Collection
Mayaguez Campus Library
University of Puerto Rico
Mayagues, Puerto Rico 00708

50272-101

REPORT DOCUMENTATION PAGE	1. REPORT NO. WHOI-89-15	2.	3. Recipient's Accession No.

4. Title and Subtitle Diffusion of Helium Isotopes in Silicate Glasses and Minerals: Implications for Petrogenesis and Geochronology	5. Report Date June 1989
	6.

7. Author(s) Thomas W. Trull	8. Performing Organization Rept. No. WHOI-89-15

9. Performing Organization Name and Address The Woods Hole Oceanographic Institution Woods Hole, Massachusetts 02543, and The Massachusetts Institute of Technology Cambridge, Massachusetts 02139	10. Project/Task/Work Unit No.
	11. Contract(C) or Grant(G) No. (C) (G) OCE 85-16082 OCE 87-16970; EAR 88-3783

12. Sponsoring Organization Name and Address The National Science Foundation	13. Type of Report & Period Covered Ph.D. Thesis
	14.

16. Abstract (Limit: 200 words)

Helium diffusivities in basaltic glasses at seafloor temperatures are about 10^{-16} cm^2/s, suggesting only very low concentration samples will be compromised, and that U/He geochronology of submarine basalts may be feasible. Helium diffusivities at magmatic temperatures are 10^{-11}, to 10^{-8} cm^2/s in silicate minerals, too low to regionally homogenize helium in the mantle. Helium exchange rates limit xenolith origin depths and transport times. Faster He diffusion in pyroxene than olivine allows diffusive loss to be evaluated.

Diffusivities of ^{3}He produced by cosmic rays in surface rocks are less than 10^{-20} cm^2/s in olivine and quartz, suggesting exposure dating will not be limited by helium loss for ages up to 10^7 years. Similar conclusions were found for U/^{4}He dating of quartz.

Part of the ^{3}He/^{4}He variability (.01 to 9 R$_a$) of island arc basalts from the western Pacific reflects post-eruptive helium addition. In unaltered samples, Kavachi submarine volcano has different ^{3}He/^{4}He (6.9±.2 R$_a$) than the Woodlark Spreading Center (8-9 R$_a$). A contribution from subducted Pacific lithosphere may explain this and ^{87}Sr/^{86}Sr variations.

17. Document Analysis   a. Descriptors

1. Helium
2. Diffusion
3. Silicates

b. Identifiers/Open-Ended Terms

c. COSATI Field/Group

18. Availability Statement Approved for publication; distribution unlimited.	19. Security Class (This Report) UNCLASSIFIED	21. No. of Pages 399
	20. Security Class (This Page)	22. Price

(See ANSI-Z39.18)	See Instructions on Reverse	OPTIONAL FORM 272 (4-77) (Formerly NTIS-35) Department of Commerce